



# Journal of Engineering

ISSN 1726-4073



A Scientific Refereed Journal  
Published by College of  
Engineering University of  
Baghdad

October

٢٠١٣

Number 10

Volume 19

ISSN 1726-4073

# مجلة الهندسة



مجلة علمية محكمة تصدرها  
كلية الهندسة - جامعة بغداد

العدد ٤

المجلد ١٩

# ENGINEERING

College of Engineering

Baghdad University

Baghdad

## List of Contents

### English Section:

### Page

**Prediction of Compressive Strength of Reinforced Concrete Structural Elements by Using Combined Non-Destructive Tests** 1189 – 1211

*Prof.Dr. Nada Mahdi. Fawzi*

*Asst.Prof.Dr. AbdMuttalib Issa. Said*

*Ali Khalid Jassim*

**Exact Stiffness Matrix for Nonprismatic Beams with Parabolic Varying Depth** 1212 - 1225

*Dr.Musab Aied Qissab Al-Janabi*

**Compressive Behavior of Fiber Reinforced Concrete Columns Rehabilitated with CFRP Warps** 1226 - 1242

*Asst. Prof. Dr. Wasan Ismail Khali*

**Potential Use of Recycled Asphalt Pavement (RAP) in Hot MixAsphalt** 1243 - 1255

*Asst. Prof. Namir Ghani Ahmed*

*Asst. Lect. Abbaas Inaayah Kareem*

*Asst. Lect. Alaa Saadi Abbas*

**The use of Prepared Zeolite Y from Iraqi kaolin for Fluid Catalytic Cracking of Vacuum Gas Oil** 1256 - 1270

*Abdul Halim Abdul Karim Mohammed*

*Ibtehal Kareem Shakir*

*Karim Khalifa Esgair*

**Isolated Word Speech Recognition Using Mixed Transform** 1271 - 1286

*Assist. Prof. Dr. Sadiq Jassim Abou-Loukh*

*Eng. Shahad Mujeeb Abdul-Razzaq*

**A Fuzzy Logic Controller Based Vector Control of IPMSM Drives** 1287 -1299

*Asst. Prof. Afaneen Anwer Abboud*

**Simulation and Modeling of Detailed Load flow Analysis for the 400kVA and 132kVA Iraqi Grid** 1300 - 1313

*Dr. Ahmed Abdul Sahib Hashim*

**Hydrogenation of Nitrobenzene in Trickle Bed Reactor over Ni/SiO<sub>2</sub> Catalyst** 1313 - 1326

*Majid I. Abdulwahab*

**Removal of Cu<sup>2+</sup>, Pb<sup>2+</sup>, And Ni<sup>2+</sup> Ions From Simulated Waste Water By Ion Exchange Method On Zeolite And Purolite C105 Resin** 1327 1340

*Dr. Ahmed Abed Mohammed  
Haidar Shukur Mahmood*

**Neural Network Geometric Correction Method for High Resolution Satellites Images** 1341 -1353

*Alaa Soud Mahdi  
Bushra Hassan Ali*

## Prediction of Compressive Strength of Reinforced Concrete Structural Elements by Using Combined Non-Destructive Tests

Prof.Dr. Nada Mahdi. Fawzi

Asst.Prof.Dr. AbdMuttalib Issa. Said

Ali Khalid Jassim

University of Baghdad

University of Baghdad

University of Baghdad

College of Engineering

College of Engineering

College of Engineering

Civil Engineering Department

Civil Engineering Department

Civil Engineering Department

nalgalawi@yahoo.com

abdmusawi@yahoo.com

ali\_khalid94@yahoo.com

### ABSTRACT

This research is devoted to investigate relationship between both Ultrasonic Pulse Velocity and Rebound Number (Hammer Test) with cube compressive strength and also to study the effect of steel reinforcement on these relationships.

A study was carried out on 32 scale model reinforced concrete elements. Non destructive testing campaign (mainly ultrasonic and rebound hammer tests) made on the same elements. About 72 concrete cubes (15 X 15 X15) were taken from the concrete mixes to check the compressive strength.. Data analyzed. Include the possible correlations between non destructive testing (NDT) and compressive strength (DT) Statistical approach is used for this purpose. A new relationships obtained from correlations results is given.

**Keywords:** Non-destructive investigations, concrete, SonReb Methods, Combined Methods

استنباط مقاومة انضغاط الاعضاء الخرسانية المسلحة باستخدام الفحوص اللااتلافية المدمجة

أ.د ندى مهدي فوزي

أ.م.د عبد المطلب عيسى سعيد

علي خالد جاسم

جامعة بغداد/ كلية الهندسة/قسم الهندسة المدنية

جامعة بغداد/ كلية الهندسة/قسم الهندسة المدنية

جامعة بغداد/ كلية الهندسة/قسم الهندسة المدنية

### الخلاصة

ان الغرض من هذا البحث هو ايجاد علاقة رياضية بين كل من سرعة الامواج فوق الصوتية ورقم ريبوند مع مقاومة انضغاط المكعبات الخرسانية وكذلك دراسة تأثير حديد التسليح على مثل هذا النوع من العلاقات

اجريت الدراسة على 32 نموذجا خرسانيا مسلحا بابعاد مختلفة. اخذت مجموعة من الفحوص اللااتلافية على نفس النماذج. تم اخذ 72 مكعبا خرسانيا اثناء عملية الصب للتأكد من المقاومة التصميمية للخلطات الخرسانية بعد ذلك ربطت النتائج المستحصلة من كل من الفحوص اللااتلافية ومقاومة الانضغاط الخاصة بالمكعبات الخرسانية بعلاقة رياضية بواسطة برنامج الاكسل . تم التوصل الى علاقات جديدة خاصة بموضوع استنباط مقاومة انضغاط الخرسانة المسلحة بواسطة دمج عدة من الفحوص اللااتلافية.

الكلمات الرئيسية: الفحوص اللااتلافية، الخرسانة، طريقة سونرب، الطريقة المشتركة

## INTRODUCTION

With good care in the design and production of concrete mixture, many variations may happen in the conditions of mixing, degree of compaction or curing conditions which make affect the final production. Usually, concrete produced have been assessed by standard tests to find the strength of the hardened concrete. Concrete is a non-homogeneous material and even if a uniform distribution of its component is assumed. It is very difficult to develop a model correctly to evaluate its onsite mechanical behaviour. Compressive tests of concrete cores also gives results affected by uncertainty and strongly dependent on reference standard used. Several non-destructive testing methods have been developed in the past for onsite concrete strength assessment. Among them Rebound Hammer and Ultrasonic Pulse Velocity (UPV) tests are the most commonly used in practice though their reliability and usefulness is quite controversial [Nash't et al., 2005]. A good calibration of the methods is only possible if a good knowledge of the concrete properties is already achieved, i.e. it is necessary to use some destructive tests to obtain such information. When assessing wide non-homogeneous structure such limit can be crucial from an economical and practical point of view. An improvement of the reliability of non-destructive tests could be obtained by their combination as well as in the SONEB method (both ultrasonic pulse velocity and Hammer test). Depending on a wide number of experimental determinations under laboratory condition different regression models have been proposed here. It was evidenced that a preliminary knowledge of concrete characteristics is of great importance to optimize regression model. [Proverbio and Venturi, 2005].

The need for systematic assessment of in situ concrete strength usually arises when the safety margin of an existing structure has to be evaluated or if there are concerns about hardened concrete quality of new constructions. The choice among which destructive, semi-destructive (e.g. coring) or non-destructive tests (e.g. ultrasonic pulse velocity, rebound number, should be adopted, has to account for precision requirements, survey extension, available time and cost [Nash't et al., 2005]. Briefly, rebound hammer (Schmidt hammer or Swiss hammer, invented in 1948) estimates surface strength as a function of resiliency, measuring the kinetic energy that is not

dissipated by hammer impact, on an arbitrary index; ultrasonic pulse velocity, giving an integral measure over length, exploits the relationship between concrete stiffness and strength, since stress waves velocity is also related to concrete Young modulus [Nash't et al., 2005].

The estimate of a single concrete strength value by means of more than one test type, commonly referred to as "combined method" [Mantegazza et al., 2002].

### 1.2 Objective of the Study

The main objectives of this investigation is to find a relationship between ultrasonic pulse velocity and cube compressive strength, Rebound Number and cube compressive strength and both ultrasonic pulse velocity and Rebound Number with cube compressive strength. The main goal of this study is to investigate the effect of reinforcement on these relationships.

## EXPERIMENTAL PROGRAM

The details of the experimental program includes details of the materials used, mix proportions, preparations, curing, and testing of specimens.

These experimental works is carried out to find a fitting equation between non-destructive testing and the compressive strength of reinforced concrete in structural member.

### Materials

The properties of materials used in any structure are of considerable importance [Neville 1995, and ACI 211]. Standard tests according to the American Society for Testing and Materials (ASTM) and Iraqi specifications (I.Q.S.) have conducted to determine the properties of materials.

### Cement

Both Ordinary Portland Cement (OPC) and Sulfate Resisting Cement (SRPC) manufactured in Iraq with a commercial name of (Tasluga and Al-jesser) are used for concrete mixes throughout the present work. This cement complied with the Iraqi specification [IQS, No.5:1984]. Testing of cement is conducted in the National Center for Construction Laboratories and research. The physical properties and chemical analysis of the cement used are given in the **Table.1**. Also, the



compounds of cement calculated according to Bogue equations, [Neville, 1995] are listed in **Table (1)**.

### Water

Tap Water is used for both mixing and curing of concrete, and the amount of it is based on concrete mix design.

### Coarse Aggregate

The coarse aggregate is brought from Al-Nibaii area with a maximum size of (19.5) mm. then recombined to satisfy the [Iraqi specification No.45/1984]. The grading and other properties of this type of aggregate are shown in **Table.2**

### Fine Aggregate

Natural sand from Al-Akhaider in Iraq is used for mixes. The physical and chemical properties of the sand are listed in **Table.3**; the sand is complying with Zone (2) according to the [IQS No.45 (1984)].

### Steel Reinforcement

Steel bars are used throughout this work are manufactured in Ukraine. The physical properties are shown in the **Table.4** and the steel bars are grade 75 according to [ASTM – A615].

### Mix Design and Proportions

The concrete mix is designed according to [ACI 211.1-91] standard as shown in **Table.5**.

### Casting Moulds Preparation

Four types of plywood forms are used in this investigation as shown in Plate (3.1). The first type with dimensions (50X30X30) cm is used as beam specimen. The second type with dimension (30X30X50) cm is used as column specimen. The third type with dimension (60X60X40) cm is used as foundation specimen. The fourth type with dimension (60X60X15) cm is used as slab specimen.

### Mixing Procedure

Concrete is mixed in a drum rotating laboratory mixer with a capacity of (0.5 m<sup>3</sup>). The interior surface of the mixer is cleaned before placing the materials. Mixing method is important to obtain the required homogeneity of concrete mix; the mixing was done according [ASTM C192].

### Compressive Strength Test

Compressive strength test is carried out according to [ASTM C-39 -01], using a digital testing machine with a capacity of (2000 kN) as shown in Plate 3-5. Three cubes of (150×150×150 mm) and three core specimens of (100 diameter × different high mm) are tested from each mix.

### Ultrasonic Pulse Velocity Test (U.P.V)

Ultrasonic Pulse transit times are measured by direct and indirect transmission method as shown in **Plate.1**. This test is carried out according to [ASTM C597-02]

### Rebound Hammer Test

Schmidt hammer is used to estimate the surface hardness of concrete specimens by recording the rebound number, which can be considered as a measure of the concrete strength and percentage of voids. Schmidt hammer type (Proceq) is used which is shown in **Plate.2**. The test method is prescribed by [ASTM C 805-02].

### Obtaining Drilled Cores

The coring process (Hilti Diamond Coring System DD-250EE) is carried out according to [ASTM C42-03], set perpendicular to the laid surface of the specimens as shown in **Plate.3**.

## RESULTS AND DISCUSSION

### Ultrasonic Test Results

The research covers four groups of each type of elements (Columns, Beams, Foundations & Slabs) which varies with compressive strength (15, 25, 35, and 40) MPa, each group contains two elements which varies with the details of steel reinforcement (S1, S2)

It can be seen from **Table6** that the pulse velocity and the ratio between indirect pulse and direct pulse increase with the increasing of compressive strength that is because the w/c ratio decreases from 0.790 to 0.395, the density increase from 2395 to 2456 kg/m<sup>3</sup>.

It is clearly seen from **Tables 6, 7 and 8** (case no.1) (the pulse path at the middle of the element) the pulse velocity was approximately similar and there is no significant difference between Columns, Beams and Foundation, that's because the pulse path is far from the steel reinforcement.

While pulse velocity measured in reinforced concrete in the vicinity of reinforcing bars is usually higher than in plain concrete of the same composition. This is because the pulse velocity in steel may be up to twice the velocity in plain concrete and, under certain conditions, the first pulse to arrive at the receiving transducer travels partly in concrete and partly in steel [BS 1881-Part 203].

So at case No.2 **Tables 6, 7 and 8** (pulse path perpendicular to the steel reinforcement) the pulse velocity increase from 2% for members with 15 MPa compressive strength to 6% for members with 40 MPa compressive strength for both Columns and Beams members, while the increment in Foundations was from 2% for members with 15 MPa compressive strength to 4% for members with 40 MPa compressive strength, the increment at case No.2 for Column and Beams was higher than the increment in Foundation because the ratio  $L_s/W$  is equal to (0.160 for S1, 0.167 for S2) for Columns and Beams while its equal to (0.106 for S1, 0.125 for S2) for foundation.

When the pulse path parallel to the steel reinforcement, it indicated from case No.4 [Tables (6) and (7)] that the pulse velocity increase from 3% for members with compressive strength 15 MPa to 8% for members with 40 MPa compressive strength for both columns and beams members [ $(L_s/w)_{\text{Column}} = (L_s/w)_{\text{Beam}} = 0.84$ ].

In spite of  $L_s/w$  Foundation is approximately similar to that ratio in Column and Beam = 0.86, it can indicated from case No.3 **Table.8** that the increment in pulse velocity for Foundation is higher and it start from 4% for members with compressive strength 15 MPa reaching to 10% for members with compressive strength 40 MPa depending on numbers, diameters and the orientation of the steel reinforcement.

The increasing in direct pulse velocity is bigger than the increasing in indirect pulse velocity and that's clearly appears at **Table.6** this is because the propagation of surface waves is restricted to a region near the boundaries that is to the free external surface of the material.

The linear and non-linear simple regression between compressive strength (dependent) with direct and indirect pulse velocity (independent)

was conducted to [ACI 228.2R-98] and the equations fixed at the curves on **Figures.1 to 4**.

### Hammer Test results

Rebound number was taken for all types of element and illustrated in **Table.10**. It is clearly seen from **Figure.5** that is no significant difference in rebound number between all types of elements. On other hand there is a significant difference between the total proposed Equation and Raouf Equation because Raouf equation was done on concrete cubes samples while the total proposed equation was done on concrete scale model samples.

### Combined method

The limitations of a combined method are usually those pertained to the limitation of each component test, except when a variation in the properties of concrete affects the component test results in opposite directions. For example, an increase in moisture content increases pulse velocity but decreases the rebound number. In this case, the errors can be self-correcting. The more information that can be obtained about the concrete ingredients, proportions, age, curing conditions, etc. the more reliable the estimate is likely to be. When testing suspect quality concrete of unknown composition, it is highly desirable to develop a prior correlation relationship.

It is suitable to use the equation which was obtained by linear multi-regression and illustrated in **Table.11**:

### CONCLUSION

- 1- For the pulse path at the middle of the element, the pulse velocity was approximately similar and there is no significant difference between Columns, Beams and Foundation.
- 2- For the pulse path  $3\Phi$  far from the steel reinforcement, the effect of steel reinforcement is approximately disappears for both condition parallel and perpendicular on steel reinforcement.
- 3- For the pulse path perpendicular on steel reinforcement, the pulse velocity increase from (2% for cubes compressive strength equal to 15 MPa) to (7% for cubes compressive strength equal to 40 MPa) with the increasing of number and the diameter of bars (increasing of the ratio between



the length of pulse in steel reinforcement to the total length of pulse in sample) ( $L_s/W$ ).

4- For the pulse velocity parallel to the steel reinforcement, the pulse velocity also increase from (3% for cubes compressive strength equal to 15 MPa) to (10% for cubes compressive strength equal to 40 MPa) with the increasing of number and diameter of steel reinforcement (increasing of the ration between the length of pulse in steel reinforcement to the total length of pulse in sample) ( $L_s/W$ ) but the most effecting factor is the distribution of steel reinforcement with respect to the location of the ultrasonic pulse velocity reading.

5- The increasing of pulse velocity for the pulse path parallel to the steel reinforcement is always higher than the increasing of pulse velocity for pulse path perpendicular to the steel reinforcement ( $L_s/w \text{ parallel} > L_s/W \text{ perpendicular}$ ).

6- The ratio between indirect pulse velocity and direct pulse velocity increase from 0.782 to 0.853 when the compressive strength of cubes increases from 15 to 40 MPa

7-  $R^2$  for combined method Equation is higher than  $R^2$  for both Ultrasonic Pulse Velocity Equation and Hammer Equation, so if the evaluation for existing structure is needed, it is better to used the combined method.

## REFERENCE

- Proverbio and Venturi, (2005), "**Reliability of nondestructive tests for onsite concrete strength assessment**" 10DBMC International Conférence On Durability of Building Materials and Components LYON [France] 17-20 April 2005.
- Nash't I. H., A'bour S.H. and Sadoon A.A.,(2005), "**Finding an Unified Relationship between Crushing Strength of Concrete and Non-destructive Tests**", www.ndt.net - 3rd MENDT - Middle East Nondestructive Testing Conference & Exhibition - 27-30 Nov., Bahrain, Manama.
- Mantegazza, Chiara N. and Sergio S., (2002), ), "**In situ concrete strength testing by non-destructive combined methods with one, two and three variables (rebound number, ultrasonic pulse velocity, Windsor probe)**".
- American Concrete Institute Committee 211.1-21, "**Proportions for Normal, Heavyweight and Mass Concrete**", Reported by ACI committee 211, ACI Manual of Concrete Practice.
- Neville A.M. and Brooks, J.J., "**Concrete Technology**", Second Edition, Longman Group U.K. Limited, 2010.
- Neville A.M., "**Properties of Concrete**", Fourth and Final Edition, Longman Group Limited, England, 1995.
- Newman, J. and Choo, B.S., "**Advanced Concrete Technology: Concrete Properties**", First Edition, Elsevier Ltd., Oxford, 2003.
- Iraqi Organization of Standards, IOS 45: 1984, for **Aggregate**.
- Iraqi Organization of Standards, IOS 5: 1984, for **Portland Cement**.
- ASTM C-617, (2002), "**Standard practice for capping cylindrical concrete specimen**", Annual Book of ASTM Standards American Society for Testing and Materials, vol.04.02.
- ASTM A-615, (2002), "**Standard Specification for Deformed and Plain Billet-Steel Carbon Steel Bars for Concrete Reinforcement**", Annual Book of ASTM Standards American Society for Testing and Materials, vol.04.02.
- ASTM C-192 (2002), "**Making and Curing Concrete Test Specimens in the Laboratory**" Annual Book of ASTM Standards American Society for Testing and Materials, vol.04.02.
- ASTM C-39, (2001), "**Compressive Strength of Concrete Cubes**", Annual Book of ASTM Standards American Society for Testing and Materials, vol.04.02.
- ASTM C-597, (2002), "**Standard Test Method for Pulse Velocity through Concrete**", Annual Book of ASTM Standards American Society for Testing and Materials, vol.04.02.
- ASTM C-805, (2002), "**Standard Test Method for Rebound Number of Hardened Concrete**", Annual Book of ASTM Standards American Society for Testing and Materials, vol.04.02.
- ASTM C-42, (2003), "**Standard Test Method for Obtaining and Testing**

- **Drilled Cores and Sawed Beams of Concrete**, Annual Book of ASTM Standards American Society for Testing and Materials, vol.04.02.
- ACI Committee 228(2003), **“In-Place Methods to Estimate Concrete Strength**

- **(ACI 228.1R-03),**” American Concrete Institute, Farmington Hills, MI.

**Table (1) Physical and Chemical Properties of Cement**

Physical Properties	Test Result		IQS (No.5:1984) limits	
	O.P.C	S.R.P.C	O.P.C	S.R.P.C
Specific Surface area, Blaine method, m <sup>2</sup> /Kg	256	259	≥230	≥ 250
Setting time,Vicat’s Method Initial setting , hr : min Final setting , hr : min	2:30 4:50	1:39 4:20	≥ 45 minutes ≤ 10 hours	
Compressive strength MPa 3-days 7-days	16.0 24.3	19.3 23.5	≥15 ≥23	
Oxides	Percentage (%)		IQS (No.5:1984) limits	
	O.P.C	S.R.P.C	O.P.C	S.R.P.C
CaO	55	60.63	-----	-----
SiO <sub>2</sub>	18.33	21.63	-----	-----
Fe <sub>2</sub> O <sub>3</sub>	3.28	4.76	-----	-----
Al <sub>2</sub> O <sub>3</sub>	5.88	4.19	-----	-----
MgO	1.93	2.72	≤ 5	≤ 5
SO <sub>3</sub>	1.87	2.04	≤ 2.8	≤ 2.5
L.O.I	2.36	1.94	-----	-----
I.R	0.15	0.92	≤ 1.5	≤ 1.5
L.S.F	0.89	0.86	0.66-1.02	0.66-1.022
Compound Composition	Percentage (%)		IQS (No.5:1984) limits	



C <sub>3</sub> S	35	32.60	-----	-----
C <sub>2</sub> S	26.21	29.95	-----	-----
C <sub>3</sub> A	10.03	3.06	-----	3.5
C <sub>4</sub> AF	9.97	14.47	-----	-----

**Table (2) Physical and Chemical Properties for Coarse Aggregate.**

Sieve Size (mm)	% Passing Gravel	% Passing Limits (IQS: No.45) (5-20)
37.5	100	100
19.5	95.1	95-100
9.5	32.6	30-60
4.75	1.02	0-10
IQS (No.45:1984) Limits	Test Results	Properties
≤ 0.1	0.08	Sulphate content SO <sub>3</sub> (%)
-----	2.68	Specific gravity
-----	1	Absorption (%)

**Table (3) Physical and Chemical Properties for Fine Aggregate.**

Sieve Size (mm)	% Passing Sand	% Passing Zone (1) Limits Sand	% Passing Zone (2) Limits Sand	% Passing Zone (3) Limits Sand	% Passing Zone (4) Limits Sand
9.5	100	100	100	100	100
4.75	91.7	90-100	90-100	90-100	95-100
2.36	76.5	60-95	75-100	85-100	95-100
1.18	58.6	30-70	55-90	75-100	90-100
0.60	41.2	15-34	35-59	60-79	80-100
0.3	18.6	5-20	8-30	12-40	15-50
0.15	9.1	0-10	0-10	0-10	0-15
Properties		Test Results		IQS (No.45:1984) Limits	
Sulphate content SO <sub>3</sub> (%)		0.45		≤ 0.5	
Specific gravity		2.62		-----	
Absorption (%)		3.31		-----	
Fineness Modules (F.M.)		3.0		-----	

**Table (4) Physical Properties for Steel Reinforcement**

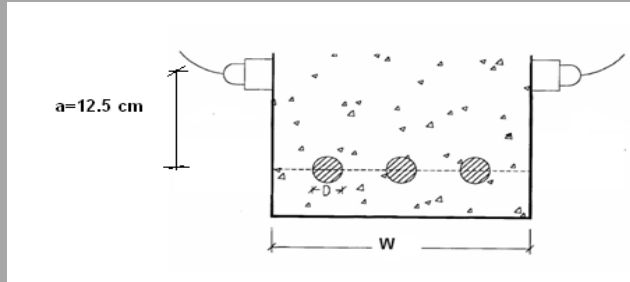
No	Nominal Dia. mm	Weight (kg)/m.l	Dia.(mm)	Yield strength N/mm <sup>2</sup>	Tensile strength N/mm <sup>2</sup>	Elongation	Bend test
1	12	0.859	11.81	685	795	12.0	Pass
2	12	0.859	11.81	682	792	12.2	Pass
3	12	0.859	11.81	681	792	12.3	Pass
1	16	1.571	15.97	634	714	12.7	Pass
2	16	1.571	15.97	631	712	12.8	Pass
3	16	1.571	15.97	632	713	12.8	Pass
1	25	3.778	24.76	633	737	12.5	Pass
2	25	3.778	24.76	631	735	12.6	Pass
3	25	3.778	24.76	630	736	12.6	Pass
ASTM –A615							
Grade		Min Yield strength N/mm <sup>2</sup>		Min Tensile strength N/mm <sup>2</sup>		Elongation %	
Grade 40		280		420		11 % for Bar 10 mm 12 % for Bar $\geq 12$ mm	
Grade 60		420		620		9 % for Bar 10-20 mm 8 % for Bar 22-25 mm 7 % for Bar $\geq 29$ mm	
Grade 75		520		690		7 % for Bar 20-25 mm 6 % for Bar $\geq 29$ mm	

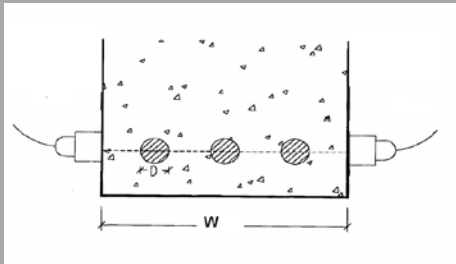
**Table (5) Mix Proportion**

Type	Cement kg/M <sup>3</sup>	Fine agg. kg/M <sup>3</sup>	Coarse agg. kg/M <sup>3</sup>	Water kg/M <sup>3</sup>	w/c	$\Sigma$ amount of mix proportion
C15	210	914	1105	166	0.790	2395
C25	300	880	1075	166	0.533	2421
C35	375	832	1067	166	0.422	2440
C40	420	820	1050	166	0.395	2456

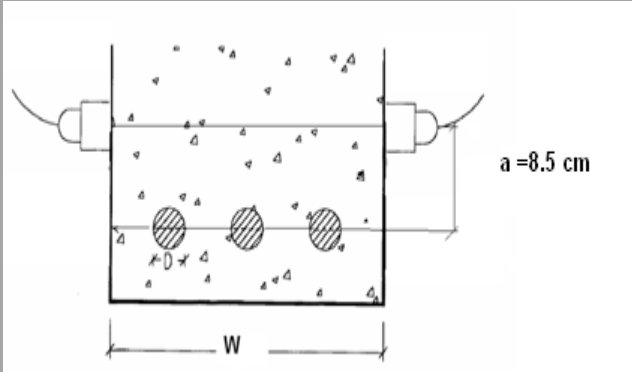
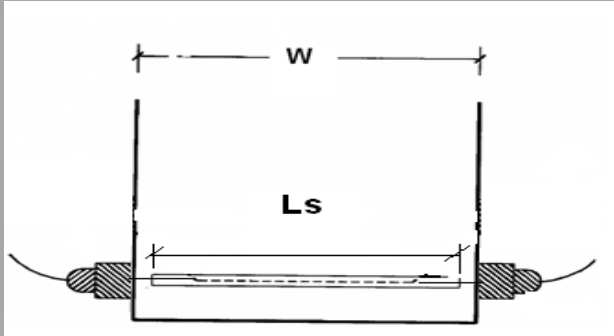


Table (6) Ultrasonic Test Results for Beam

 <p><math>a=12.5</math> cm</p> <p><math>W</math></p> <p><b>B<sub>15</sub>S<sub>1</sub></b>: Beam class 15 MPa compressive strength series No.1 Ls = length of pulse path in steel Ls is equal to zero in case No.1 W = concrete element dimension parallel to the pulse path a= Distance between ultrasonic transducers and steel bars Ls/W = N/A a/W= 0.416</p>	<b>Case no.1</b>	pulse path at the middle of the element	Type	Average Direct pulse Km /sec	Average Indirect pulse Km/sec	Average (Indirect/direct) pulse	Average Compressive strength at 28 days ( MPa)
			B <sub>15</sub> S <sub>1</sub>	3.963	3.163	0.798	16.05
			B <sub>15</sub> S <sub>2</sub>	3.982	3.168	0.796	16.54
			B <sub>25</sub> S <sub>1</sub>	4.395	3.518	0.801	27.00
			B <sub>25</sub> S <sub>2</sub>	4.408	3.562	0.808	27.07
			B <sub>35</sub> S <sub>1</sub>	4.582	3.739	0.816	36.56
			B <sub>35</sub> S <sub>2</sub>	4.613	3.780	0.819	36.62
			B <sub>40</sub> S <sub>1</sub>	4.656	3.816	0.820	42.27
			B <sub>40</sub> S <sub>2</sub>	4.673	3.855	0.825	42.28

 <p><math>W</math></p> <p><b>S1</b>=Beam with 3 <math>\Phi</math> 16 Top &amp; bottom <b>S2</b>=Beam with 2 <math>\Phi</math> 25 Top &amp; bottom <math>L_s = \frac{\pi}{4} \times 3 \times D = 3 \times 1.6 = 4.8</math> cm for S1 <math>L_s = \frac{\pi}{4} \times 2 \times D = 2 \times 2.5 = 5.0</math> cm for S2 W= 30cm Ls/W= 0.160 for S1 Ls/W= 0.167 for S2</p>	<b>Case no.2</b>	pulse path perpendicular on steel reinforcement	Type	Average Direct pulse	$\frac{\text{case No.2}}{\text{Case No.1}}$ (Direct)	Average Indirect pulse	$\frac{\text{case No.2}}{\text{Case No.1}}$ (Indirect)	Average (Indirect/direct) pulse	Average Compressive strength at 28
			B <sub>15</sub> S <sub>1</sub>	4.013	1.013	3.215	1.016	0.801	16.05
			B <sub>15</sub> S <sub>2</sub>	4.063	1.020	3.246	1.025	0.799	16.54
			B <sub>25</sub> S <sub>1</sub>	4.448	1.012	3.600	1.023	0.809	27.00
			B <sub>25</sub> S <sub>2</sub>	4.525	1.026	3.647	1.024	0.806	27.07
			B <sub>35</sub> S <sub>1</sub>	4.789	1.045	3.862	1.033	0.807	36.56
			B <sub>35</sub> S <sub>2</sub>	4.836	1.048	3.924	1.038	0.811	36.62
			B <sub>40</sub> S <sub>1</sub>	4.959	1.065	3.977	1.042	0.802	42.27
			B <sub>40</sub> S <sub>2</sub>	4.984	1.067	4.026	1.044	0.808	42.28

Continuous of Table (6) Ultrasonic Test Results for Beam

 <p><math>a = 8.5 \text{ cm}</math> <math>a/W = 0.283</math></p>	Case no.3  pulse path on 8.5 cm perpendicular on steel reinforcement	Type	Average Direct pulse Km /sec	<u>case No.3</u> <u>Case No.1</u> (Direct)	Average Indirect pulse Km/sec	<u>case No.3</u> <u>Case No.1</u> (Indirect)	Average (Indirect/direct) pulse	Average Compressive strength at 28 days ( MPa)
		B <sub>15</sub> S <sub>1</sub>	3.984	1.005	3.163	0.998	0.794	16.05
		B <sub>15</sub> S <sub>2</sub>	3.996	1.004	3.168	1.002	0.793	16.54
		B <sub>25</sub> S <sub>1</sub>	4.427	1.007	3.518	1.004	0.795	27.00
		B <sub>25</sub> S <sub>2</sub>	4.441	1.008	3.562	1.000	0.802	27.07
		B <sub>35</sub> S <sub>1</sub>	4.562	0.996	3.706	0.991	0.812	36.56
		B <sub>35</sub> S <sub>2</sub>	4.579	0.993	3.717	0.983	0.812	36.62
		B <sub>40</sub> S <sub>1</sub>	4.723	1.014	3.883	1.017	0.822	42.27
		B <sub>40</sub> S <sub>2</sub>	4.740	1.014	3.922	1.017	0.827	42.28
 <p><math>L_s = 42 \text{ cm}</math> <math>W = 50 \text{ cm}</math> <math>L_s/W = 0.84</math></p>	Case no.4  pulse path parallel on steel reinforcement	Type	Average Direct pulse	<u>case No.4</u> <u>Case No.1</u> (Direct)	Average Indirect pulse	<u>case No.4</u> <u>Case No.1</u> (Indirect)	Average (Indirect/direct) pulse	Average Compressive strength at 28 days ( MPa)
		B <sub>15</sub> S <sub>1</sub>	4.051	1.022	3.202	1.012	0.791	16.05
		B <sub>15</sub> S <sub>2</sub>	4.097	1.029	3.212	1.014	0.784	16.54
		B <sub>25</sub> S <sub>1</sub>	4.539	1.033	3.630	1.032	0.800	27.00
		B <sub>25</sub> S <sub>2</sub>	4.562	1.035	3.686	1.035	0.808	27.07
		B <sub>35</sub> S <sub>1</sub>	4.791	1.046	3.867	1.034	0.807	36.56
		B <sub>35</sub> S <sub>2</sub>	4.834	1.048	3.907	1.034	0.808	36.62
		B <sub>40</sub> S <sub>1</sub>	5.004	1.075	4.001	1.048	0.800	42.27
		B <sub>40</sub> S <sub>2</sub>	5.020	1.074	4.030	1.045	0.803	42.28

Continuous of Table (6) Ultrasonic Test Results for Beam





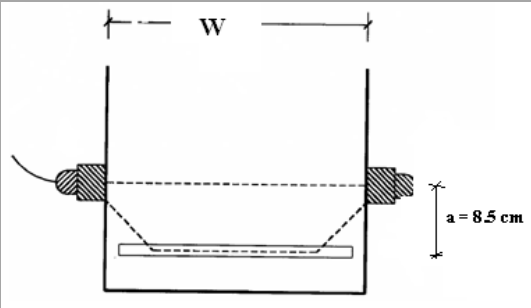
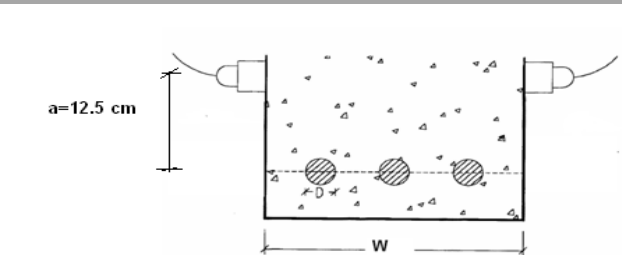
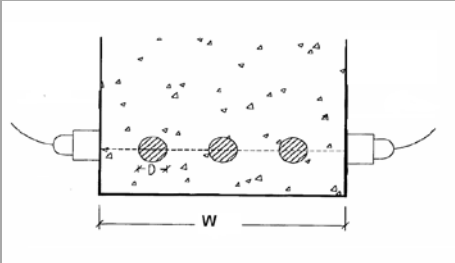
 <p><math>a/W = 0.17</math></p>	Case no.5	pulse path on 8.5 cm parallel on steel reinforcement	Type	Average Direct pulse Km /sec	case No.5 Case No.1 (Direct)	Average Indirect pulse Km/sec	case No.5 Case No.1 (Indirect)	Average (Indirect/direct) pulse	Average Compressive strength at 28 days ( MPa)
			B <sub>15</sub> S <sub>1</sub>	3.996	1.008	3.171	1.002	0.794	16.05
			B <sub>15</sub> S <sub>2</sub>	4.015	1.008	3.201	1.011	0.797	16.54
			B <sub>25</sub> S <sub>1</sub>	4.433	1.009	3.508	0.997	0.791	27.00
			B <sub>25</sub> S <sub>2</sub>	4.462	1.012	3.558	0.999	0.797	27.07
			B <sub>35</sub> S <sub>1</sub>	4.633	1.011	3.743	1.001	0.808	36.56
			B <sub>35</sub> S <sub>2</sub>	4.640	1.006	3.780	1.000	0.815	36.62
			B <sub>40</sub> S <sub>1</sub>	4.735	1.017	3.883	1.017	0.820	42.27
			B <sub>40</sub> S <sub>2</sub>	4.765	1.020	3.907	1.013	0.820	42.28

Table (7) Ultrasonic Test Results for Column

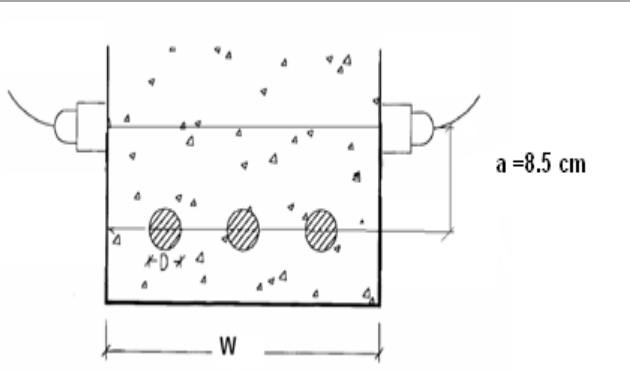
 <p><math>a=12.5\text{ cm}</math></p> <p><math>a/W = 0.416</math></p> <p>C<sub>15</sub>S<sub>1</sub>: Column class 15 MPa compressive strength series No.1  Ls = length of pulse path in steel  Ls is equal to zero in case No.1  W = concrete element dimension parallel to the pulse path  a= Distance between ultrasonic transducers and steel bars  Ls/W = N/A  a/W= 0.416</p>	Case no.1	pulse path at the middle of the element	Type	Average Direct pulse Km /sec	Average Indirect pulse Km/sec	Average (Indirect/direct) pulse	Average Compressive strength at 28 days ( MPa)
			C <sub>15</sub> S <sub>1</sub>	3.836	3.022	0.788	16.05
			C <sub>15</sub> S <sub>2</sub>	3.860	3.080	0.798	16.54
			C <sub>25</sub> S <sub>1</sub>	4.352	3.531	0.811	27.00
			C <sub>25</sub> S <sub>2</sub>	4.366	3.554	0.814	27.07
			C <sub>35</sub> S <sub>1</sub>	4.528	3.747	0.828	36.56
			C <sub>35</sub> S <sub>2</sub>	4.531	3.776	0.833	36.62
			C <sub>40</sub> S <sub>1</sub>	4.620	3.815	0.826	42.27
			C <sub>40</sub> S <sub>2</sub>	4.685	3.892	0.831	42.28

Nada Mahdi. Fawzi  
AbdMuttalib Issa. Said  
Ali Khalid Jassim

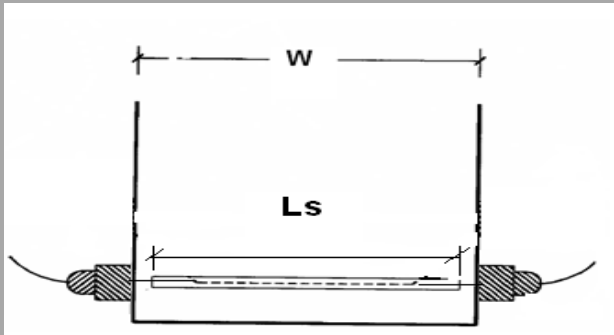
# Prediction of Compressive Strength of Reinforced Concrete Structural Elements by Using Combined Non-Destructive Tests

 <p>S1=Column with 6 <math>\Phi</math> 16 S2=Column with 4 <math>\Phi</math> 25 Ls = <math>\Phi</math> = 3xD = 3x1.6= 4.8 cm for S1 Ls = <math>\Phi</math> = 2xD= 2x2.5 =5.0 cm for S2 W= 30cm Ls/W= 0.160 for S1 Ls/W= 0.167 for S2</p>	Case no.2	pulse path perpendicular on steel reinforcement	Type	Average Direct pulse	<u>case No.2</u> <u>Case No.1</u> (Direct)	Average Indirect pulse	<u>case No.2</u> <u>Case No.1</u> (Indirect)	Average (Indirect/direct) pulse	Average Compressive strength at 28 days (MPa)
			C <sub>15</sub> S <sub>1</sub>	3.907	1.0187	3.057	1.0115	0.782	16.05
			C <sub>15</sub> S <sub>2</sub>	3.934	1.0192	3.123	1.0140	0.794	16.54
			C <sub>25</sub> S <sub>1</sub>	4.489	1.0314	3.620	1.0251	0.807	27.00
			C <sub>25</sub> S <sub>2</sub>	4.530	1.0377	3.631	1.0216	0.802	27.07
			C <sub>35</sub> S <sub>1</sub>	4.716	1.0414	3.839	1.0246	0.814	36.56
			C <sub>35</sub> S <sub>2</sub>	4.723	1.0424	3.877	1.0269	0.821	36.62
			C <sub>40</sub> S <sub>1</sub>	4.881	1.0566	3.935	1.0316	0.806	42.27
			C <sub>40</sub> S <sub>2</sub>	4.977	1.0622	4.013	1.0313	0.806	42.28

Continuuous of Table (7) Ultrasonic Test Results for Colum

 <p>a =8.5 cm a/W = 0.283</p>	Case no.3	pulse path on 8.5 cm perpendicular on steel reinforcement	Type	Average Direct pulse Km /sec	<u>case No.3</u> <u>Case No.1</u> (Direct)	Average Indirect pulse Km/sec	<u>case No.3</u> <u>Case No.1</u> (Indirect)	Average (Indirect/direct) pulse	Average Compressive strength at 28 days (MPa)
			C <sub>15</sub> S <sub>1</sub>	3.821	0.9963	3.030	1.0025	0.793	16.05
			C <sub>15</sub> S <sub>2</sub>	3.814	0.9882	3.063	0.9944	0.803	16.54
			C <sub>25</sub> S <sub>1</sub>	4.327	0.9943	3.473	0.9835	0.803	27.00
			C <sub>25</sub> S <sub>2</sub>	4.303	0.9856	3.470	0.9764	0.807	27.07
			C <sub>35</sub> S <sub>1</sub>	4.535	1.0015	3.702	0.9879	0.816	36.56
			C <sub>35</sub> S <sub>2</sub>	4.572	1.0091	3.734	0.9890	0.817	36.62
			C <sub>40</sub> S <sub>1</sub>	4.675	1.0119	3.790	0.9936	0.811	42.27
			C <sub>40</sub> S <sub>2</sub>	4.784	1.0211	3.881	0.9972	0.812	42.28



 <p> <math>L_s = 42 \text{ cm}</math>  <math>W = 50 \text{ cm}</math>  <math>L_s/W = 0.84</math> </p>	Case no.4  pulse path parallel on steel reinforcement	Type	Average Direct pulse	<u>case No.4</u> <u>Case No.1</u> (Direct)	Average Indirect pulse	<u>case No.4</u> <u>Case No.1</u> (Indirect)	Average (Indirect/direct) pulse	Average Compressive strength at 28 days (MPa)
		C <sub>15</sub> S <sub>1</sub>	3.923	1.0228	3.098	1.0250	0.790	16.05
		C <sub>15</sub> S <sub>2</sub>	3.930	1.0181	3.177	1.0316	0.808	16.54
		C <sub>25</sub> S <sub>1</sub>	4.485	1.0306	3.598	1.0189	0.802	27.00
		C <sub>25</sub> S <sub>2</sub>	4.516	1.0344	3.622	1.0190	0.802	27.07
		C <sub>35</sub> S <sub>1</sub>	4.772	1.0537	3.819	1.0191	0.800	36.56
		C <sub>35</sub> S <sub>2</sub>	4.777	1.0543	3.877	1.0268	0.812	36.62
		C <sub>40</sub> S <sub>1</sub>	5.007	1.0838	4.041	1.0594	0.807	42.27
		C <sub>40</sub> S <sub>2</sub>	5.063	1.0807	4.133	1.0620	0.816	42.28

Continuous of Table (7) Ultrasonic Test Results for Colum

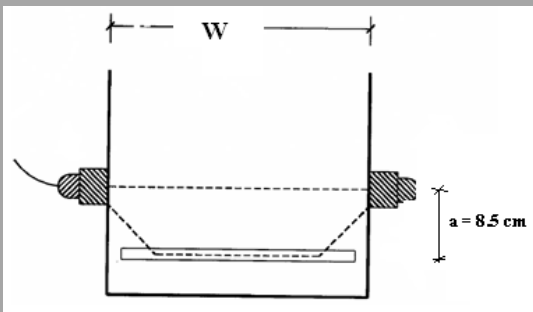
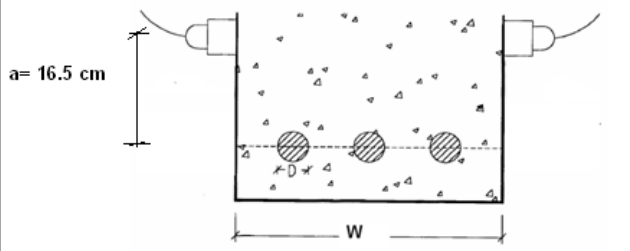
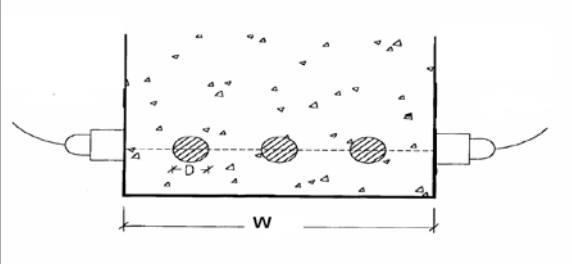
 <p> <math>a = 8.5 \text{ cm}</math>  <math>a/W = 0.17</math> </p>	Case no.5  pulse path on 8.5 cm parallel on steel reinforcement	Type	Average Direct pulse Km /sec	<u>case No.5</u> <u>Case No.1</u> (Direct)	Average Indirect pulse Km/sec	<u>case No.5</u> <u>Case No.1</u> (Indirect)	Average (Indirect/direct) pulse	Average Compressive strength at 28 days (MPa)
		C <sub>15</sub> S <sub>1</sub>	3.930	1.0245	3.081	1.0194	0.784	16.05
		C <sub>15</sub> S <sub>2</sub>	3.930	1.0181	3.123	1.0140	0.795	16.54
		C <sub>25</sub> S <sub>1</sub>	4.463	1.0255	3.604	1.0207	0.808	27.00
		C <sub>25</sub> S <sub>2</sub>	4.453	1.0199	3.604	1.0139	0.810	27.07
		C <sub>35</sub> S <sub>1</sub>	4.630	1.0225	3.781	1.0091	0.817	36.56
		C <sub>35</sub> S <sub>2</sub>	4.658	1.0280	3.871	1.0252	0.831	36.62
		C <sub>40</sub> S <sub>1</sub>	4.717	1.0210	3.956	1.0370	0.839	42.27
		C <sub>40</sub> S <sub>2</sub>	4.784	1.0211	4.034	1.0366	0.843	42.28

Table (8) Ultrasonic Test Results for Foundation

 <p><math>a=16.5\text{ cm}</math></p> <p><math>W</math></p> <p><b>F<sub>15</sub>S<sub>1</sub></b>: Foundation class 15 MPa compressive strength series No.1 Ls = length of pulse path in steel Ls is equal to zero in case No.1 W = concrete element dimension parallel to the pulse path a= Distance between ultrasonic transducers and steel bars <math>L_s/W = N/A</math> <math>a/W= 0.275</math></p>	Case no.1	pulse path at the middle of the element	Type	Average Direct pulse Km /sec		Average Indirect pulse Km/sec		Average (Indirect/direct) pulse	Average Compressive strength at 28 days ( MPa)
			F <sub>15</sub> S <sub>1</sub>	3.901		3.137		0.804	16.05
			F <sub>15</sub> S <sub>2</sub>	3.922		3.148		0.803	16.54
			F <sub>25</sub> S <sub>1</sub>	4.395		3.689		0.839	27.00
			F <sub>25</sub> S <sub>2</sub>	4.420		3.706		0.839	27.07
			F <sub>35</sub> S <sub>1</sub>	4.694		3.932		0.838	36.56
			F <sub>35</sub> S <sub>2</sub>	4.709		3.960		0.841	36.62
			F <sub>40</sub> S <sub>1</sub>	4.768		4.053		0.850	42.27
			F <sub>40</sub> S <sub>2</sub>	4.773		4.071		0.853	42.28

 <p><math>W</math></p> <p>S1=Foundation with 4 <math>\Phi</math> 16 Top &amp; bottom S2=Foundation with 3 <math>\Phi</math> 25 Top &amp; bottom <math>L_s = 4 \times \Phi = 4 \times D = 4 \times 1.6 = 6.4\text{ cm}</math> for S1 <math>L_s = 3 \times \Phi = 3 \times D = 3 \times 2.5 = 7.5\text{ cm}</math> for S2 <math>W= 60\text{ cm}</math> <math>L_s/W= 0.106</math> for S1 <math>L_s/W= 0.125</math> for S2</p>	Case no.2	pulse path perpendicular on steel reinforcement	Type	Average Direct pulse	<u>Case No.2</u> <u>Case No.1</u> (Direct)	Average Indirect pulse	<u>Case No.2</u> <u>Case No.1</u> (Indirect)	Average (Indirect/direct) pulse	Average Compressive strength at 28 days ( MPa)
			F <sub>15</sub> S <sub>1</sub>	3.994	1.0238	3.188	1.0164	0.798	16.05
			F <sub>15</sub> S <sub>2</sub>	4.037	1.0294	3.199	1.0160	0.792	16.54
			F <sub>25</sub> S <sub>1</sub>	4.537	1.0322	3.767	1.0211	0.830	27.00
			F <sub>25</sub> S <sub>2</sub>	4.575	1.0350	3.780	1.0201	0.826	27.07
			F <sub>35</sub> S <sub>1</sub>	4.896	1.0431	4.085	1.0388	0.834	36.56
			F <sub>35</sub> S <sub>2</sub>	4.909	1.0426	4.111	1.0381	0.837	36.62
			F <sub>40</sub> S <sub>1</sub>	4.993	1.0471	4.225	1.0424	0.846	42.27
			F <sub>40</sub> S <sub>2</sub>	4.982	1.0439	4.238	1.0409	0.851	42.28



Continuous of Table (8) Ultrasonic Test Results for Foundation

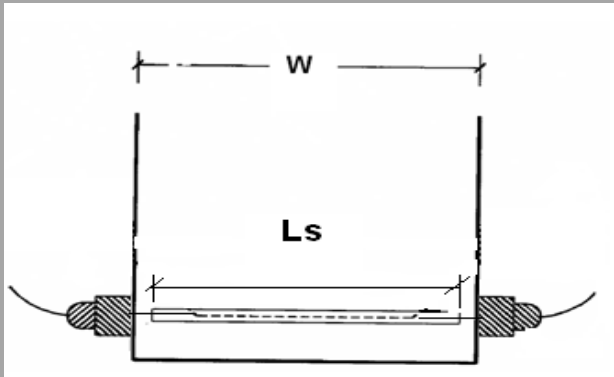
 <p><math>Ls/W = 0.86</math></p>	<b>Case no.3</b>  pulse path parallel to the steel reinforcement	Type	Average Direct pulse Km /sec	<del>case No.3</del> <del>Case No.1</del> (Direct)	Average Indirect pulse Km/sec	<del>case No.3</del> <del>Case No.1</del> (Indirect)	Average (Indirect/direct) pulse	Average Compressive strength at 28 days ( MPa)
		F <sub>15</sub> S <sub>1</sub>	4.053	1.0389	3.253	1.0372	0.803	16.05
		F <sub>15</sub> S <sub>2</sub>	4.060	1.0352	3.246	1.0311	0.800	16.54
		F <sub>25</sub> S <sub>1</sub>	4.581	1.0423	3.833	1.0392	0.837	27.00
		F <sub>25</sub> S <sub>2</sub>	4.602	1.0412	3.880	1.0470	0.843	27.07
		F <sub>35</sub> S <sub>1</sub>	4.985	1.0620	4.111	1.0454	0.825	36.56
		F <sub>35</sub> S <sub>2</sub>	4.991	1.0599	4.152	1.0483	0.832	36.62
		F <sub>40</sub> S <sub>1</sub>	5.254	1.1019	4.334	1.0692	0.825	42.27
		F <sub>40</sub> S <sub>2</sub>	5.245	1.0989	4.370	1.0734	0.833	42.28

Table (9) Ultrasonic Test Results for Slab

	<b>Case no.1</b>	Type	Average Direct pulse Km /sec	Average Indirect pulse Km/sec	Average (Indirect/direct) pulse	Average Compressive strength at 28 days ( MPa)
		S <sub>15</sub> S <sub>1</sub>	3.809	3.119	0.819	16.05
		S <sub>15</sub> S <sub>2</sub>	3.807	3.119	0.820	16.54
		S <sub>25</sub> S <sub>1</sub>	4.333	3.481	0.803	27.00
		S <sub>25</sub> S <sub>2</sub>	4.320	3.470	0.803	27.07
		S <sub>35</sub> S <sub>1</sub>	4.670	3.845	0.823	36.56
		S <sub>35</sub> S <sub>2</sub>	4.685	3.892	0.831	36.62
		S <sub>40</sub> S <sub>1</sub>	4.823	4.052	0.840	42.27
		S <sub>40</sub> S <sub>2</sub>	4.843	4.052	0.837	42.28

**Table 10 Hammer Test Results**

Element	Type	Average of three sets of Rebound Hammer	Average Compressive strength ( MPa)
Column	C <sub>15</sub> S <sub>1</sub>	25	16.05
	C <sub>15</sub> S <sub>2</sub>	26	16.54
	C <sub>25</sub> S <sub>1</sub>	30	27.00
	C <sub>25</sub> S <sub>2</sub>	31	27.07
	C <sub>35</sub> S <sub>1</sub>	36	36.56
	C <sub>35</sub> S <sub>2</sub>	37	36.62
	C <sub>40</sub> S <sub>1</sub>	44	42.27
	C <sub>40</sub> S <sub>2</sub>	44	42.28
Beam	B <sub>15</sub> S <sub>1</sub>	25	16.05
	B <sub>15</sub> S <sub>2</sub>	25	16.54
	B <sub>25</sub> S <sub>1</sub>	30	27.00
	B <sub>25</sub> S <sub>2</sub>	31	27.07
	B <sub>35</sub> S <sub>1</sub>	37	36.56
	B <sub>35</sub> S <sub>2</sub>	37	36.62
	B <sub>40</sub> S <sub>1</sub>	44	42.27
	B <sub>40</sub> S <sub>2</sub>	44	42.28
Foundation	F <sub>15</sub> S <sub>1</sub>	25	16.05
	F <sub>15</sub> S <sub>2</sub>	26	16.54
	F <sub>25</sub> S <sub>1</sub>	30	27.00
	F <sub>25</sub> S <sub>2</sub>	31	27.07
	F <sub>35</sub> S <sub>1</sub>	37	36.56
	F <sub>35</sub> S <sub>2</sub>	38	36.62
	F <sub>40</sub> S <sub>1</sub>	44	42.27
	F <sub>40</sub> S <sub>2</sub>	44	42.28
Slab	S <sub>15</sub> S <sub>1</sub>	25	16.05
	S <sub>15</sub> S <sub>2</sub>	25	16.54
	S <sub>25</sub> S <sub>1</sub>	30	27.00
	S <sub>25</sub> S <sub>2</sub>	30	27.07
	S <sub>35</sub> S <sub>1</sub>	37	36.56
	S <sub>35</sub> S <sub>2</sub>	37	36.62
	S <sub>40</sub> S <sub>1</sub>	44	42.27
	S <sub>40</sub> S <sub>2</sub>	44	42.28



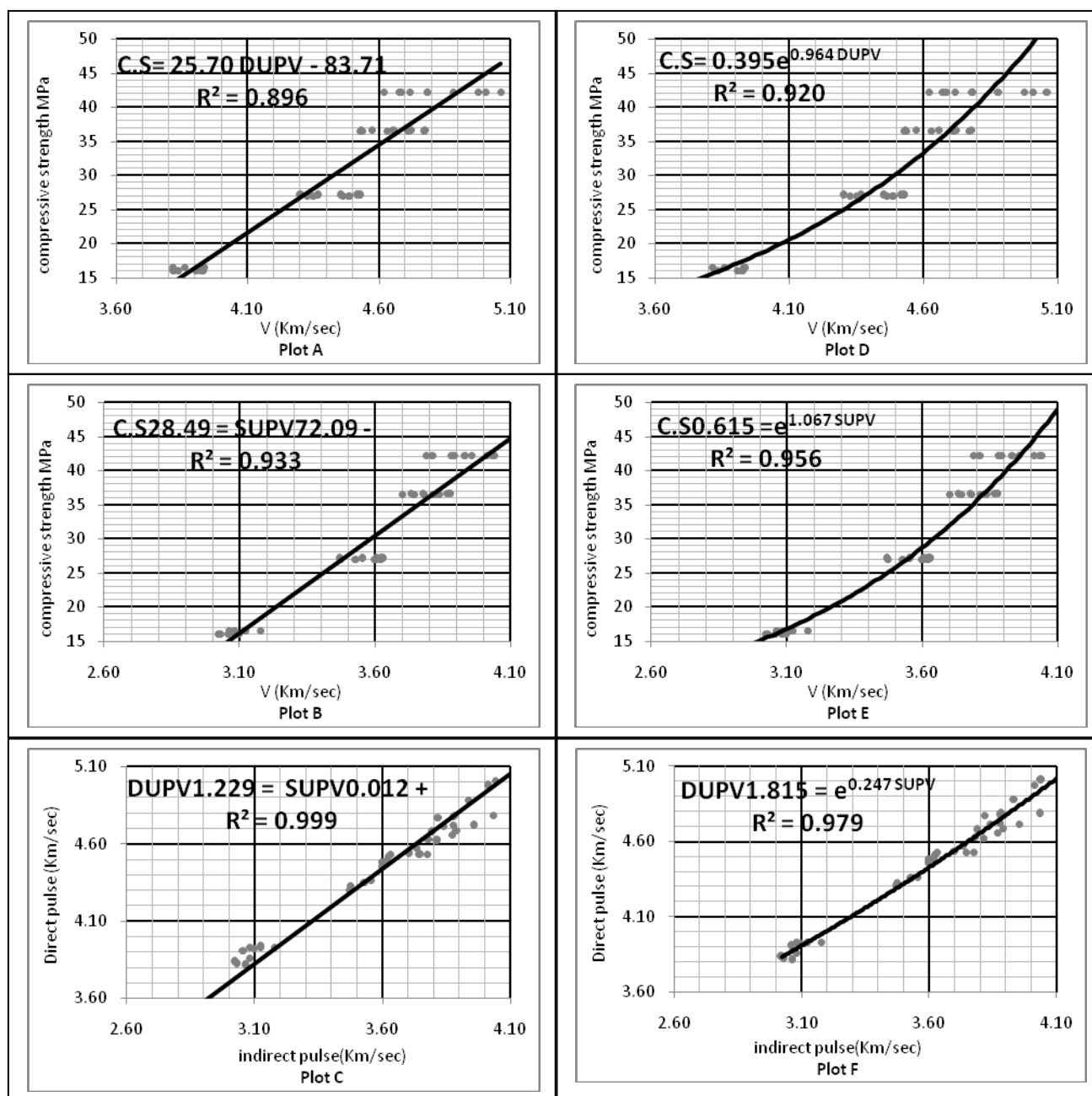


Table 11 Summary of Equation of Combined Method

Element	Equation Name	Type of Pulse Velocity	Equation	R <sup>2</sup>
Column	Total proposed Column equation	DUPV	$y = 10.123 \text{ DUPV} + 0.913 \text{ R} - 45.433$	0.975
		SUPV	$y = 13.502 \text{ SUPV} + 0.789 \text{ R} - 45.036$	0.981
Beam	Total proposed Beam equation	DUPV	$y = 9.166 \text{ DUPV} + 0.987 \text{ R} - 44.367$	0.981
		SUPV	$y = 13.913 \text{ SUPV} + 0.836 \text{ R} - 48.447$	0.985
Foundation	Total proposed Foundation equation	DUPV	$y = 7.293 \text{ DUPV} + 0.995 \text{ R} - 37.197$	0.980
		SUPV	$y = 9.780 \text{ SUPV} + 0.870 \text{ R} - 36.654$	0.987
Slab	Total proposed Slab equation	DUPV	$y = 16.420 \text{ DUPV} + 0.488 \text{ R} - 58.495$	0.999
		SUPV	$y = 26.215 \text{ SUPV} + 0.056 \text{ R} - 66.490$	0.996
Total	Total combined proposed equation	DUPV	$y = 7.666 \text{ DUPV} + 1.017 \text{ R} - 38.653$	0.974
		SUPV	$y = 8.129 \text{ SUPV} + 1.015 \text{ R} - 33.877$	0.974
-	Raouf equation	DUPV	$y = 0.93R^{0.63} e^{0.31\text{DUPV}}$	0.978

Table.12 Summary of Proposed Equations

Item	Equation name	Type	Equation	R <sup>2</sup>
1.	Proposed Total Plain Concrete Equation	DUPV	$y = 0.173 e^{1.157 \text{ DUPV}}$	0.961
		SUPV	$y = 0.460 e^{1.150 \text{ SUPV}}$	0.944
2.	Proposed Total Effect Equation	DUPV	$y = 0.422 e^{0.939 \text{ DUPV}}$	0.888
		SUPV	$y = 0.747 e^{0.997 \text{ SUPV}}$	0.890
3.	Proposed Total Hammer Equation	R	$y = 5.378 e^{0.049 \text{ R}}$	0.899
4.	Proposed Total Combined Equation	DUPV + R	$y = 7.666 \text{ DUPV} + 1.017 \text{ R} - 38.653$	0.974
		SUPV + R	$y = 8.129 \text{ SUPV} + 1.015 \text{ R} - 33.877$	0.974



**Figure (1) Relationships between Pulse Velocity and Compressive Strength Total Case for Column Element**

Plot A Linear relationship between direct pulse and compressive strength

Plot B Linear relationship between indirect pulse and compressive strength

Plot C Linear relationship between indirect pulse and direct pulse

Plot D Non-Linear relationship between direct pulse and compressive strength

Plot E Non-Linear relationship between indirect pulse and compressive strength

Plot F Non-Linear relationship between indirect pulse and direct pulse

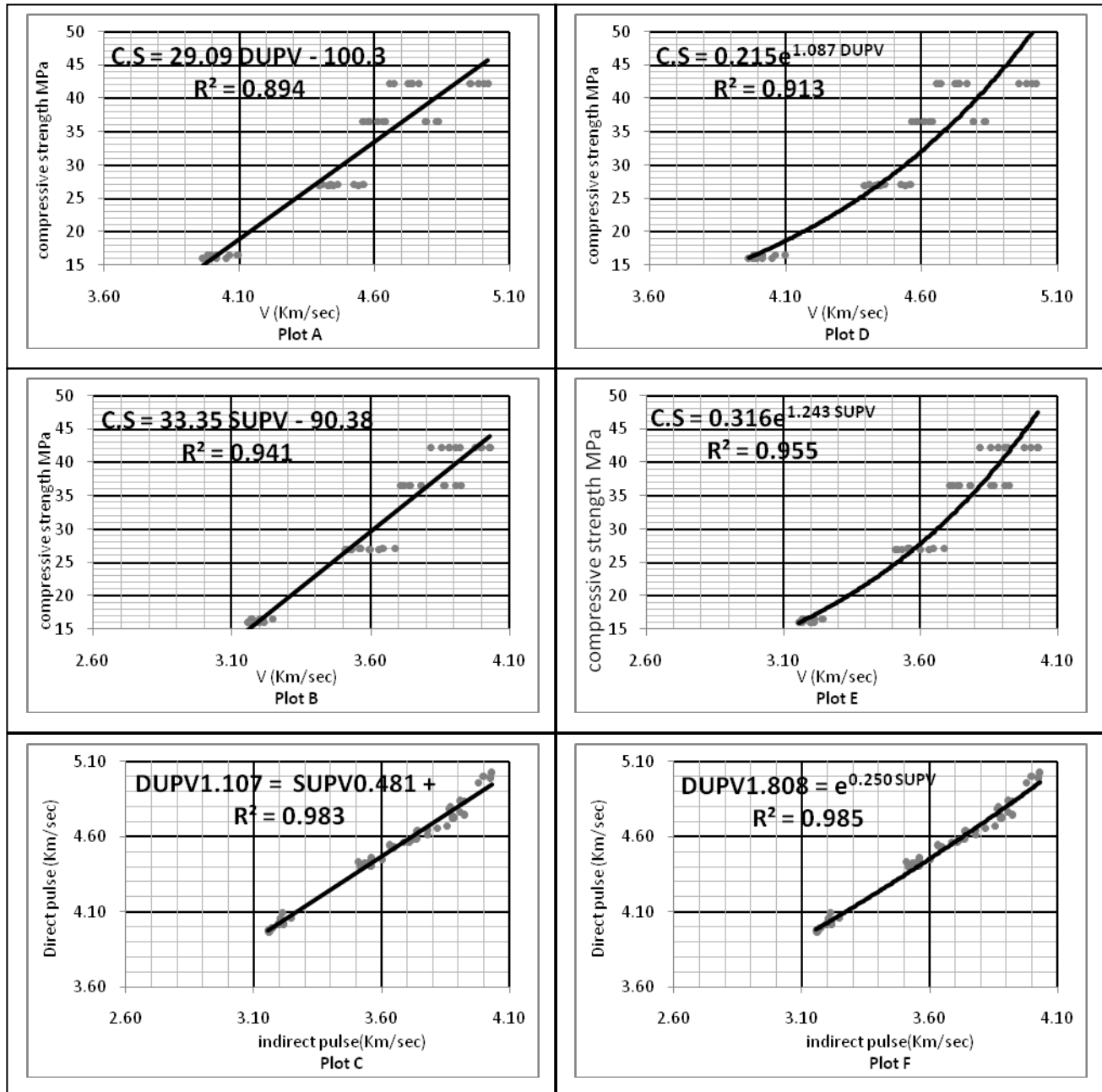


**Figure (2) Relationships between Pulse Velocity and Compressive Strength Total Case for Beam Element**

Plot A Linear relationship between direct pulse and compressive strength

Plot B Linear relationship between indirect pulse and compressive strength

Plot C Linear relationship between indirect pulse and direct pulse

Plot D Non-Linear relationship between direct pulse and compressive strength

Plot E Non-Linear relationship between indirect pulse and compressive strength

Plot F Non-Linear relationship between indirect pulse and direct pulse

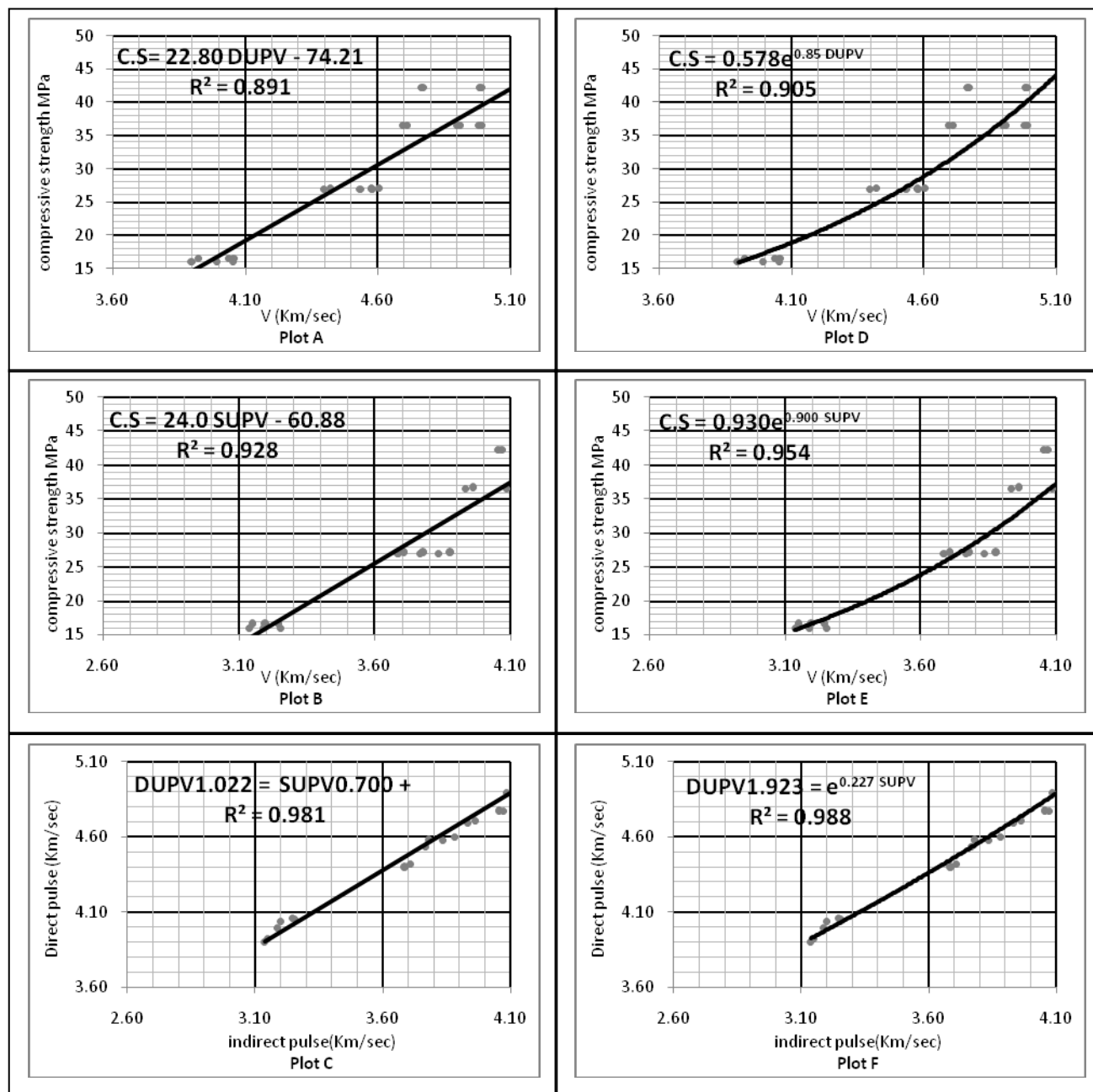


**Figure (3) Relationships between Pulse Velocity and Compressive Strength for Total Case for Foundation Element**

Plot A Linear relationship between direct pulse and compressive strength

Plot B Linear relationship between indirect pulse and compressive strength

Plot C Linear relationship between indirect pulse and direct pulse

Plot D Non-Linear relationship between direct pulse and compressive strength

Plot E Non-Linear relationship between indirect pulse and compressive strength

Plot F Non-Linear relationship between indirect pulse and direct pulse

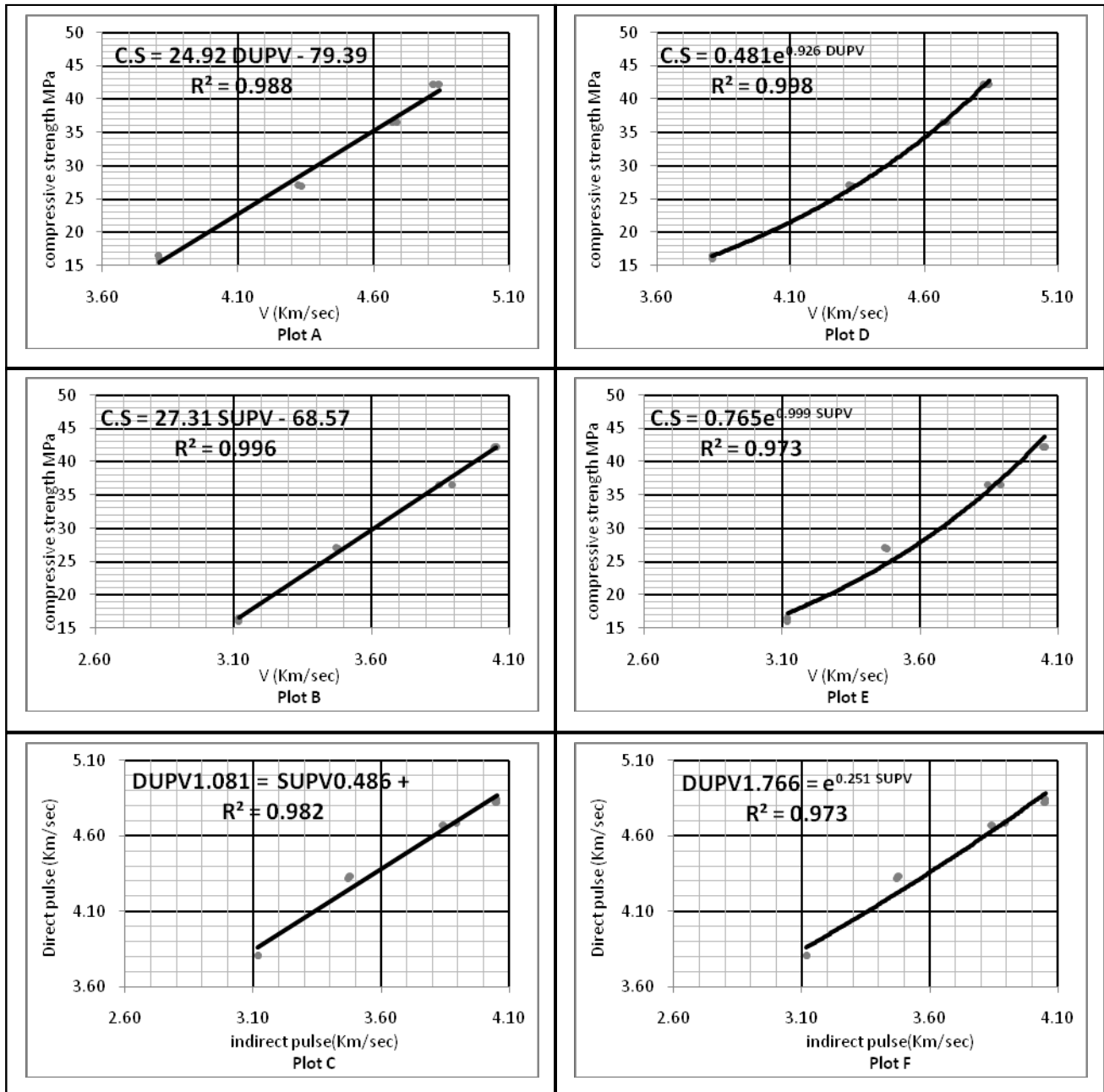


**Figure (4) Relationships between Pulse Velocity and Compressive Strength for Slab Element**

Plot A Linear relationship between direct pulse and compressive strength

Plot B Linear relationship between indirect pulse and compressive strength

Plot C Linear relationship between indirect pulse and direct pulse

Plot D Non-Linear relationship between direct pulse and compressive strength

Plot E Non-Linear relationship between indirect pulse and compressive strength

Plot F Non-Linear relationship between indirect pulse and direct pulse

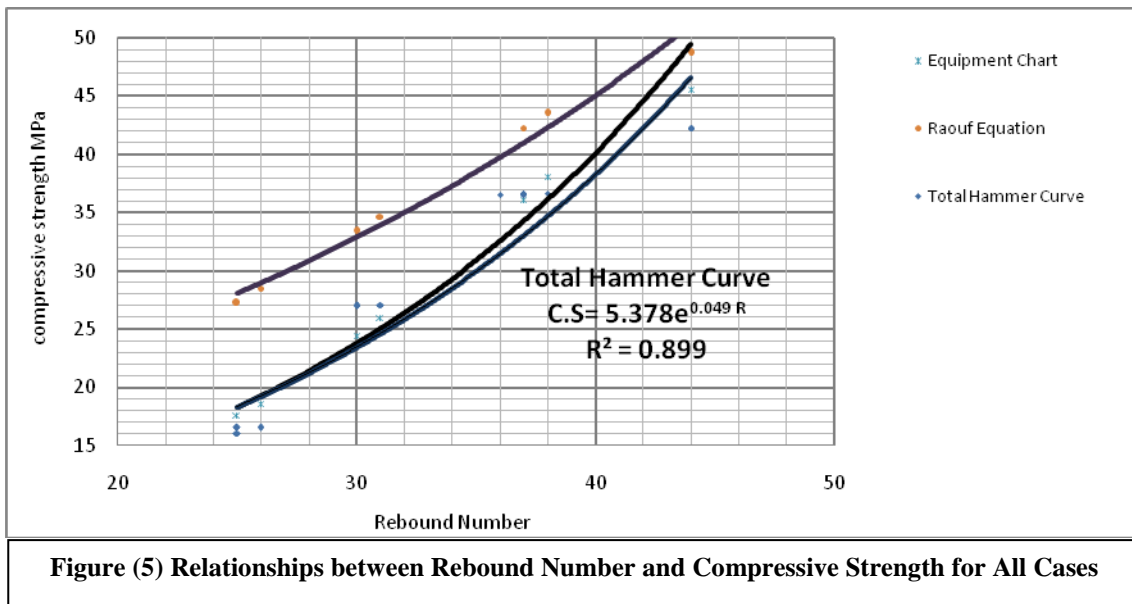


Plate.1 Direct and Indirect Reading of Ultrasonic Pulse Velocity





**Plate.2 Rebound Hammer testers**



**Plate.3 Cutting core specimens from Beam sample**

## Exact Stiffness Matrix for Nonprismatic Beams with Parabolic Varying Depth

Dr.Musab Aied Qissab Al-Janabi

Lecturer/ Department of Civil Engineering  
AL-Nahrain University

### ABSTRACT

In this paper, an exact stiffness matrix and fixed-end load vector for nonprismatic beams having parabolic varying depth are derived. The principle of strain energy is used in the derivation of the stiffness matrix. The effect of both shear deformation and the coupling between axial force and the bending moment are considered in the derivation of stiffness matrix. The fixed-end load vector for elements under uniformly distributed or concentrated loads is also derived. The correctness of the derived matrices is verified by numerical examples. It is found that the coupling effect between axial force and bending moment is significant for elements having axial end restraint. It was found that the decrease in bending moment was in the range of 31.72%-42.29% in case of including the effect of axial force for the studied case. For midspan deflection, the decrease was 46.07% due to the effect of axial force generated at supports as a result of axial restraint.

**KEYWORDS:** Stiffness; Parabolic; Shear deformation; Axial force; Beams

### الخلاصة

في هذا البحث، تم اشتقاق مصفوفة الجساءة و متجه حمل النهايات المثبتة للأعتاب الغير موشورية ذات العمق المتغير لاختبار (قطع مكافئ). تم استعمال مبدأ طاقة الإنفعال في اشتقاق مصفوفة الجساءة مع الأخذ بنظر الإعتبار تأثير تشوهات القص والتأثير المتبادل بين القوة المحورية وعزم الإنحناء. كذلك، تم اشتقاق متجه حمل النهايات المثبتة لعناصر ذات احمال موزعة بانتظام او احمال مركزة. تم اختبار عدة امثلة تطبيقية لغرض اثبات صحة المصفوفات التي تم اشتقاقها. من خلال النتائج التي تم الحصول عليها وجد بأن التأثير المتبادل للقوة المحورية مع عزم الإنحناء ذات فاعلية بالنسبة للأعضاء ذات النهايات المقيدة محوريا. فقد لوحظ تناقصا في مقدار عزم الإنحناء وينسب تناقص من 31.72% الى 42.29% في حال تم ادخال تأثير القوة المحورية بالنسبة للحالة التي تم دراستها. أما بالنسبة للهطول، فقد كان التناقص بنسبة 46.07% في منتصف الفضاء نتيجة لتأثير القوة المحورية المتولدة من تقييد الحركة المحورية للمساند مقارنة مع الحالة التي تم فيها اهمال تأثيرها.

**الكلمات الرئيسية:** الجساءة، قطع مكافئ، تشوهات القص، القوة المحورية، الأعتاب

## INTRODUCTION

Members with variable depth are used in many engineering structures such as highway bridges, buildings, as well as in many mechanical components and aerospace engineering structures. In civil engineering construction, nonprismatic members are frequently used to optimize material distribution and stresses, increase the overall stability and stiffness, reduce the dead load positive moment and deflection, and sometimes to satisfy architectural requirements. Accordingly, the analysis of structures having nonprismatic elements is of interest in structural, mechanical, and aerospace engineering. The analysis of nonprismatic members is covered in several publications (e.g., Timoshenko and Young 1965; AL-Gahtani 1996; Al-Gahtani and Khan 1998; Luo et al 2007). Most of the available publications deal with the analysis of tapered members only. Some particular cases (e.g., Timoshenko and Young 1965; AL-Gahtani 1996) deal with the analysis of nonprismatic beams having parabolic varying depth. However, these cases are limited to the analysis only (no stiffness matrix derivation) of such type of members involving lengthy and tedious calculations which are not applicable for use in the analysis packages in which the analysis is based on matrix operations. In addition, the available analytical solutions do not consider the effect of shear deformation and the axial force-bending moment interaction. The other alternative publications deal with the numerical methods of analysis such as the finite element method (e.g., Bathe 1996) in which the member is discretized to a number of elements and the stiffness matrices of the elements are assembled to obtain the stiffness matrix for the whole member. The main disadvantage resulting from member discretization is the large number of input data required even for simple structures.

The purpose of this paper is to present an exact stiffness matrix for nonprismatic beam elements with parabolic varying depth including the effect of shear deformation and the axial force-bending moment interaction. The correctness of the derived stiffness matrix and the fixed-end load vector is examined through numerical examples.

## PROBLEM STATEMENT

Consider a nonprismatic Euler- Bernoulli beam element of length  $L$  as shown in Fig. 1(a). The element is rectangular in cross-section and has a parabolic varying depth and constant width. Three degrees of freedom are assumed at each node. Only the deformation in the plane of the element and the bending moment about the centroidal main axis are considered. The positive direction of displacements and forces are as shown in Fig. 1(b).

The stiffness components corresponding to the degrees of freedom shown in Fig. 1(b) can be obtained by using Castigliano's second theorem (Boresi, A.P. and Schmidt, R.J. 2003), which states that the deflection caused by an external force is equal to the partial derivative of the strain energy ( $U$ ) with respect to that force. The total strain energy ( $U$ ) for the element shown in Fig. 1(a) including the strain energy caused by bending moment, shear and axial forces can be given by

$$U = \frac{1}{2E} \int_0^L \frac{M_x^2}{I_x} dx + \frac{1.2}{2Gb} \int_0^L \frac{Q_x^2}{h_x^2} dx + \frac{1}{2Eb} \int_0^L \frac{P_x^2}{h_x} dx \quad (1)$$

where  $M_x$ ,  $Q_x$ ,  $P_x$ ,  $I_x$ ,  $h_x$ , are the bending moment, shear force, axial force, moment of inertia and the depth of the element at the distance  $x$  respectively;  $b$ ,  $E$ ,  $G$ , are the width of the element, Young's and shear modulus of elasticity, respectively. The bending moment  $M_x$ , shear force  $Q_x$ , and the axial force  $P_x$  can be found from equilibrium as follows

$$M_x = \frac{1}{2} P_i h_0 (cx^2) + Q_i x - M_i \quad (2a)$$

$$Q_x = Q_i \quad (2b)$$

$$P_x = P_i \quad (2c)$$

The moment of inertia and the depth of the element cross section at a distance  $x$  can be given by

$$I_x = \frac{bh_0^3}{12} (1+cx^2)^3 = I_0 (1+cx^2)^3; h_x = h_0 (1+cx^2)$$

(3)

where  $h_0$ =the minimum depth of the element (at the origin),  $c=(h_l-h_0)/(h_0L^2)$ , and  $h_l$ = the maximum depth of the element.

Substituting eqs. (2a), (2b), (2c), and (3) into eq. (1) and after integrations, the following exact expression for the strain energy can be given as

$$U = \frac{1}{2EI_0} \left[ P_i^2 I_0(a_0) + \frac{P_i^2 h_0^2}{4} (a_1) - P_i M_i h_0(a_2) + M_i^2 (a_3) + P_i Q_i h_0(a_4) - M_i Q_i (a_5) + Q_i^2 (a_6 + 2EI_0 K_v) \right] \quad (4)$$

where

$$a_0 = \frac{\phi_0}{\sqrt{c} A_0} \quad (5a)$$

$$a_1 = \frac{1}{\sqrt{c}} \left[ \frac{3}{4} \left( \frac{1}{2} \phi_0 - \frac{1}{4} \sin(2\phi_0) \right) - \frac{1}{4} \sin^3 \phi_0 \cos \phi_0 \right] \quad (5b)$$

$$a_2 = \frac{1}{4\sqrt{c}} \left[ \frac{1}{2} \phi_0 - \frac{1}{8} \sin(4\phi_0) \right] \quad (5c)$$

$$a_3 = \frac{1}{\sqrt{c}} \left[ \frac{3}{4} \left( \frac{1}{2} \phi_0 + \frac{1}{4} \sin(2\phi_0) \right) + \frac{1}{4} \cos^3 \phi_0 \sin \phi_0 \right] \quad (5d)$$

$$a_4 = \frac{1}{2c} \left[ \frac{1}{2(1+cL^2)^2} - \frac{1}{(1+cL^2)} + \frac{1}{2} \right] \quad (5e)$$

$$a_5 = \frac{1}{2c} \left[ 1 - \frac{1}{(1+cL^2)^2} \right] \quad (5f)$$

$$a_6 = \frac{1}{c} (a_2) \quad (5g)$$

and

$$K_v = \frac{1.2\phi_0}{2GA_0\sqrt{c}}, \phi_0 = \tan^{-1}(\sqrt{c}L), \text{ and } A_0 = bh_0$$

(6)

The partial derivative of the strain energy ( $U$ ) with respect to  $P_i$ ,  $Q_i$ , and  $M_i$  can be given respectively as follows

$$\frac{\partial U}{\partial P_i} = u_i = \frac{1}{2EI_0} \left[ P_i \left( 2I_0 a_0 + \frac{h_0^2}{2} (a_1) \right) + Q_i (h_0(a_4)) - M_i (h_0(a_2)) \right] \quad (7)$$

$$\frac{\partial U}{\partial Q_i} = v_i = \frac{1}{2EI_0} \left[ P_i (h_0(a_4)) + Q_i (2(a_6) + 4EI_0 K_v) - M_i (a_5) \right] \quad (8)$$

$$\frac{\partial U}{\partial M_i} = \theta_i = \frac{1}{2EI_0} \left[ -P_i (h_0(a_2)) - Q_i (a_5) + M_i (2a_3) \right] \quad (9)$$

where  $u_i$ ,  $v_i$ , and  $\theta_i$  are the displacement components in horizontal, vertical directions, and rotation angle at node ( $i$ ) respectively.

The stiffness coefficient ( $k_{ij}$ ) of an element can be defined as the force or moment at node ( $i$ ) required to induce a unit displacement or rotation at node ( $j$ ) with all other displacements equal to zero. Therefore, eqs. (7), (8), and (9) will be used to derive the stiffness matrix of the element.

Writing eqs. (7), (8), and (9) in a matrix form yield the following

$$\begin{bmatrix} (2I_0 a_0 + \frac{h_0^2}{2} (a_1)) & (h_0(a_4)) & -(h_0(a_2)) \\ (h_0(a_4)) & (2(a_6) + 4EI_0 K_v) & -(a_5) \\ -(h_0(a_2)) & -(a_5) & (2a_3) \end{bmatrix} \begin{Bmatrix} P_i \\ Q_i \\ M_i \end{Bmatrix} = 2EI_0 \begin{Bmatrix} u_i \\ v_i \\ \theta_i \end{Bmatrix} \quad (10)$$

or

$$[D] \{F\} = 2EI_0 \{\delta\}; \{F\} = 2EI_0 [D]^{-1} \{\delta\}$$

(11)

where

$$[D] = \begin{bmatrix} d_{11} & d_{12} & d_{13} \\ d_{12} & d_{22} & d_{23} \\ d_{13} & d_{23} & d_{33} \end{bmatrix}$$

$$= \begin{bmatrix} (2I_0 a_0 + \frac{h_0^2}{2}(a_1)) & (h_0(a_4)) & -(h_0(a_2)) \\ (h_0(a_4)) & (2(a_6) + 4EI_0 K_v) & -(a_5) \\ -(h_0(a_2)) & -(a_5) & (2a_3) \end{bmatrix}$$

(12)

$$\{F\} = \begin{Bmatrix} P_i \\ Q_i \\ M_i \end{Bmatrix}; \{\delta\} = 2EI_0 \begin{Bmatrix} u_i \\ v_i \\ \theta_i \end{Bmatrix}$$

(13)

### AXIAL STIFFNESS

Applying a unit axial displacement at node (*i*) with all other displacements equal to zero (i.e. put  $u_i=1$ ,  $v_i=0$ , and  $\theta_i=0$  in the displacements vector  $\delta$ ), the stiffness coefficients corresponding to that displacement can be found by solving eq. (11) for the column matrix  $F$ , hence

$$k_{11} = P_i = \frac{2EI_0}{\lambda}(d_{33}d_{22} - d_{23}^2) \quad (14a)$$

$$k_{21} = Q_i = \frac{-2EI_0}{\lambda}(d_{33}d_{12} - d_{13}d_{23}) \quad (14b)$$

$$k_{31} = M_i = \frac{2EI_0}{\lambda}(d_{23}d_{12} - d_{13}d_{22}) \quad (14c)$$

From equilibrium, the force vector (or stiffness coefficients) at node (*j*) corresponding to the unit axial displacement at node (*i*) can be given as

$$k_{41} = P_j = -k_{11} \quad (14d)$$

$$k_{51} = Q_j = -k_{21} \quad (14e)$$

$$k_{61} = M_j = k_{11}\left(\frac{h_1 - h_0}{2}\right) + k_{21}L - k_{31} \quad (14f)$$

where

$$\lambda = d_{11}(d_{33}d_{22} - d_{23}^2) - d_{12}(d_{33}d_{12} - d_{13}d_{23}) + d_{13}(d_{23}d_{12} - d_{13}d_{22})$$

(15)

### FLEXURAL STIFFNESS

Following the same procedure given for the derivation of axial stiffness, the flexural (translational and rotational) stiffness coefficients can be obtained by applying a unit lateral displacement or a unit rotation (with all other displacements equal to zero) to obtain the translational or rotational stiffness coefficients, respectively.

Hence, by substituting  $u_i=0$ ,  $v_i=1$ , and  $\theta_i=0$  in the displacements vector  $\delta$ , the translational stiffness coefficients can be given as

$$k_{12} = P_i = \frac{-2EI_0}{\lambda}(d_{33}d_{12} - d_{13}d_{23}) \quad (16a)$$

$$k_{22} = Q_i = \frac{2EI_0}{\lambda}(d_{33}d_{11} - d_{13}^2) \quad (16b)$$

$$k_{32} = M_i = \frac{-2EI_0}{\lambda}(d_{23}d_{11} - d_{13}d_{12}) \quad (16c)$$

From equilibrium, the stiffness coefficients or the force vector at node (*j*) corresponding to the unit lateral displacement at node (*i*) (i.e.  $u_i=0$ ,  $v_i=1$ , and  $\theta_i=0$ ) can be given as

$$k_{42} = -k_{12} = P_j \quad (16d)$$

$$k_{52} = Q_j = -k_{22} \quad (16e)$$

$$k_{62} = M_j = k_{12}\left(\frac{h_1 - h_0}{2}\right) + k_{22}L - k_{32} \quad (16f)$$

Similarly, the rotational stiffness coefficients can be obtained by substituting  $u_i=0$ ,  $v_i=0$ , and

$\theta_i = 1$  in the displacement vector  $[\delta]$  and solving eq. (11) as follows

$$k_{13} = P_i = \frac{2EI_0}{\lambda} (d_{23}d_{12} - d_{13}d_{22}) \quad (17a)$$

$$k_{23} = Q_i = \frac{-2EI_0}{\lambda} (d_{23}d_{11} - d_{13}d_{12}) \quad (17b)$$

$$k_{33} = M_i = \frac{2EI_0}{\lambda} (d_{22}d_{11} - d_{12}^2) \quad (17c)$$

and from equilibrium

$$k_{43} = P_j = -k_{13} \quad (17d)$$

$$k_{53} = Q_j = -k_{23} \quad (17e)$$

$$k_{63} = M_j = k_{13} \left( \frac{h_1 - h_0}{2} \right) + k_{23}L - k_{33} \quad (17f)$$

Taking advantage of the symmetry characteristic in the stiffness matrix, and from equilibrium requirements, the other coefficients of the 6\*6 stiffness matrix can be given as follows

$$k_{14} = \frac{-2EI_0}{\lambda} (d_{33}d_{22} - d_{23}^2) \quad (18a)$$

$$k_{24} = \frac{2EI_0}{\lambda} (d_{33}d_{12} - d_{13}d_{23}) \quad (18b)$$

$$k_{34} = \frac{-2EI_0}{\lambda} (d_{23}d_{12} - d_{13}d_{22}) \quad (18c)$$

$$k_{44} = \frac{2EI_0}{\lambda} (d_{33}d_{22} - d_{23}^2) \quad (18d)$$

$$k_{54} = \frac{-2EI_0}{\lambda} (d_{33}d_{12} - d_{13}d_{23}) \quad (18e)$$

$$k_{64} = k_{14} \left( \frac{h_1 - h_0}{2} \right) + k_{24}L - k_{34} \quad (18f)$$

$$k_{15} = \frac{2EI_0}{\lambda} (d_{33}d_{12} - d_{13}d_{23}) \quad (19a)$$

$$k_{25} = \frac{-2EI_0}{\lambda} (d_{33}d_{11} - d_{13}^2) \quad (19b)$$

$$k_{35} = \frac{2EI_0}{\lambda} (d_{23}d_{11} - d_{13}d_{12}) \quad (19c)$$

$$k_{45} = \frac{-2EI_0}{\lambda} (d_{33}d_{12} - d_{13}d_{23}) \quad (19d)$$

$$k_{55} = \frac{2EI_0}{\lambda} (d_{33}d_{11} - d_{13}^2) \quad (19e)$$

$$k_{65} = k_{15} \left( \frac{h_1 - h_0}{2} \right) + k_{25}L - k_{35} \quad (19f)$$

$$k_{16} = k_{11} \left( \frac{h_1 - h_0}{2} \right) + k_{21}L - k_{31} \quad (20a)$$

$$k_{26} = k_{12} \left( \frac{h_1 - h_0}{2} \right) + k_{22}L - k_{32} \quad (20b)$$

$$k_{36} = k_{13} \left( \frac{h_1 - h_0}{2} \right) + k_{23}L - k_{33} \quad (20c)$$

$$k_{46} = -k_{11} \left( \frac{h_1 - h_0}{2} \right) - k_{21}L + k_{31} \quad (20d)$$

$$k_{56} = -k_{12} \left( \frac{h_1 - h_0}{2} \right) - k_{22}L + k_{32} \quad (20e)$$

$$k_{66} = k_{16} \left( \frac{h_1 - h_0}{2} \right) + k_{62}L - k_{36} \quad (20f)$$

where  $\lambda$  is given by eq. (15)

Similar results can be obtained for the stiffness coefficients given by eqs. (18a)-(20f) by using the same procedure presented before. Therefore, substituting for  $M_x$ ,  $Q_x$ , and  $P_x$  in the strain energy expression (eq. (1)) interms of the nodal force vector at node (j) and following the same previous procedure will yield the same expressions given in eqs. (18a)-(20f).

The obtained stiffness coefficients can be written in a matrix form as

$$[K] = \begin{bmatrix} k_{11} & k_{12} & k_{13} & k_{14} & k_{15} & k_{16} \\ & k_{22} & k_{23} & k_{24} & k_{25} & k_{26} \\ & & k_{33} & k_{34} & k_{35} & k_{36} \\ & & & k_{44} & k_{45} & k_{46} \\ & & & & k_{55} & k_{56} \\ & & & & & k_{66} \end{bmatrix} \quad (21)$$

For a beam element having an orientation as shown in Fig. 2, the stiffness coefficients can be



obtained by the same previous procedure. The stiffness matrix for this case can be written in terms of the obtained coefficients (eqs. (14a)-(20f)) of the above stiffness matrix as follows

$$[\bar{K}] = \begin{bmatrix} \bar{k}_{11} & \bar{k}_{12} & \bar{k}_{13} & \bar{k}_{14} & \bar{k}_{15} & \bar{k}_{16} \\ & \bar{k}_{22} & \bar{k}_{23} & \bar{k}_{24} & \bar{k}_{25} & \bar{k}_{26} \\ & & \bar{k}_{33} & \bar{k}_{34} & \bar{k}_{35} & \bar{k}_{36} \\ & & & \bar{k}_{44} & \bar{k}_{45} & \bar{k}_{46} \\ & & & & \bar{k}_{55} & \bar{k}_{56} \\ & & & & & \bar{k}_{66} \end{bmatrix} \quad (22)$$

in which

$$\bar{k}_{11} = \frac{2EI_0}{\lambda} (d_{33}d_{22} - d_{23}^2) \quad (23a)$$

$$\bar{k}_{12} = \frac{2EI_0}{\lambda} (d_{33}d_{12} - d_{13}d_{23}) \quad (23b)$$

$$\bar{k}_{13} = k_{14} \left( \frac{h_1 - h_0}{2} \right) + k_{24}L - k_{34} \quad (23c)$$

$$\bar{k}_{14} = \frac{-2EI_0}{\lambda} (d_{33}d_{22} - d_{23}^2) \quad (23d)$$

$$\bar{k}_{15} = \frac{-2EI_0}{\lambda} (d_{33}d_{12} - d_{13}d_{23}) \quad (23e)$$

$$\bar{k}_{16} = \frac{-2EI_0}{\lambda} (d_{23}d_{12} - d_{13}d_{22}) \quad (23f)$$

$$\bar{k}_{22} = \frac{2EI_0}{\lambda} (d_{33}d_{11} - d_{13}^2) \quad (24a)$$

$$\bar{k}_{23} = k_{12} \left( \frac{h_1 - h_0}{2} \right) + k_{22}L - k_{32} \quad (24b)$$

$$\bar{k}_{24} = \frac{-2EI_0}{\lambda} (d_{33}d_{12} - d_{13}d_{23}) \quad (24c)$$

$$\bar{k}_{25} = \frac{-2EI_0}{\lambda} (d_{33}d_{11} - d_{13}^2) \quad (24d)$$

$$\bar{k}_{26} = \frac{-2EI_0}{\lambda} (d_{23}d_{11} - d_{13}d_{12}) \quad (24e)$$

$$\bar{k}_{33} = k_{16} \left( \frac{h_1 - h_0}{2} \right) + k_{62}L - k_{36} \quad (24f)$$

$$\bar{k}_{34} = -k_{14} \left( \frac{h_1 - h_0}{2} \right) - k_{24}L + k_{34} \quad (25a)$$

$$\bar{k}_{35} = -k_{12} \left( \frac{h_1 - h_0}{2} \right) - k_{22}L + k_{32} \quad (25b)$$

$$\bar{k}_{36} = k_{13} \left( \frac{h_1 - h_0}{2} \right) + k_{23}L - k_{33} \quad (25c)$$

$$\bar{k}_{44} = \frac{2EI_0}{\lambda} (d_{33}d_{22} - d_{23}^2) \quad (25d)$$

$$\bar{k}_{45} = \frac{2EI_0}{\lambda} (d_{33}d_{12} - d_{13}d_{23}) \quad (25e)$$

$$\bar{k}_{46} = \frac{2EI_0}{\lambda} (d_{23}d_{12} - d_{13}d_{22}) \quad (25f)$$

$$\bar{k}_{55} = \frac{2EI_0}{\lambda} (d_{33}d_{11} - d_{13}^2) \quad (26a)$$

$$\bar{k}_{56} = \frac{2EI_0}{\lambda} (d_{23}d_{11} - d_{13}d_{12}) \quad (26b)$$

$$\bar{k}_{66} = \frac{2EI_0}{\lambda} (d_{22}d_{11} - d_{12}^2) \quad (26c)$$

For elements having no axial force-bending moment coupling such as when the centroidal axis of the element is straight (i.e. the element is symmetric about centroidal axis), the obtained coefficients can be modified by substituting the following values for the  $[D]$  matrix coefficients (eq. (12)) such that

$$[D] = \begin{bmatrix} d_{11} & d_{12} & d_{13} \\ d_{12} & d_{22} & d_{23} \\ d_{13} & d_{23} & d_{33} \end{bmatrix} = \begin{bmatrix} (2I_0 a_0) & 0 & 0 \\ 0 & (2(a_6) + 4EI_0 K_v) & -(a_5) \\ 0 & -(a_5) & (2a_3) \end{bmatrix} \quad (27)$$

## FIXED-END LOAD VECTOR DUE TO UNIFORM LOAD

Consider a nonprismatic beam element with a parabolic varying depth under a uniform load  $q$  as shown in Fig. 3(a). By using the principle of superposition and knowing that the sum of all displacement components in each direction at the fixed end must be zero, the flexibility matrix equation corresponding to node ( $i$ ) can be written as

$$\begin{bmatrix} \frac{1}{\sqrt{c}}(\beta_1) & \frac{h_0}{8c}(\gamma) & \frac{-h_0}{2\sqrt{c}}(\gamma_1 - \beta) \\ \frac{h_0}{8c}(\gamma) & \frac{1}{c^{3/2}}(\alpha) & \frac{-1}{4c}\left(1 - \frac{1}{(1+cL^2)^2}\right) \\ \frac{-h_0}{2\sqrt{c}}(\alpha) & \frac{-1}{4c}\left(1 - \frac{1}{(1+cL^2)^2}\right) & \frac{1}{\sqrt{c}}(\beta) \end{bmatrix} \begin{Bmatrix} P_{Fi} \\ Q_{Fi} \\ M_{Fi} \end{Bmatrix} = \frac{q}{c^{3/2}} \begin{Bmatrix} \frac{h_0}{4}(\alpha_1) \\ \frac{\sin^4 \phi_0}{8\sqrt{c}} \\ \frac{-1}{2}(\alpha) \end{Bmatrix} \quad (28)$$

where

$$\alpha = \frac{1}{8}\phi_0 - \frac{1}{32}\sin(4\phi_0) \quad (29)$$

$$\beta = \frac{1}{4}\cos^3 \phi_0 \sin \phi_0 + \frac{3}{4}\left(\frac{1}{2}\phi_0 + \frac{1}{4}\sin(2\phi_0)\right) \quad (30)$$

$$\gamma = \left(1 + \frac{1}{(1+cL^2)^2} - \frac{2}{(1+cL^2)}\right) \quad (31)$$

$$\alpha_1 = \left(\frac{3}{8}\phi_0 - \frac{1}{4}\sin(2\phi_0) + \frac{1}{32}\sin(4\phi_0)\right) \quad (32)$$

$$\beta_1 = \left(\frac{I_0}{A_0} + \frac{h_0^2}{4}\right)\phi_0 + \frac{h_0^2}{4}(\beta - 2\gamma_1) \quad (33)$$

$$\gamma_1 = \frac{1}{2}\left(\phi_0 + \frac{1}{4}\sin(2\phi_0)\right) \quad (34)$$

Writing the flexibility matrix  $[F]$  in eq. (28) in the form

$$[F] = \begin{bmatrix} f_{11} & f_{12} & f_{13} \\ f_{21} & f_{22} & f_{23} \\ f_{31} & f_{32} & f_{33} \end{bmatrix} = \begin{bmatrix} \frac{1}{\sqrt{c}}(\beta_1) & \frac{h_0}{8c}(\gamma) & \frac{-h_0}{2\sqrt{c}}(\gamma_1 - \beta) \\ \frac{h_0}{8c}(\gamma) & \frac{1}{c^{3/2}}(\alpha) & \frac{-1}{4c}\left(1 - \frac{1}{(1+cL^2)^2}\right) \\ \frac{-h_0}{2\sqrt{c}}(\alpha) & \frac{-1}{4c}\left(1 - \frac{1}{(1+cL^2)^2}\right) & \frac{1}{\sqrt{c}}(\beta) \end{bmatrix} \quad (35)$$

and solving eq. (28) for the unknown fixed end reactions  $P_{Fi}$ ,  $Q_{Fi}$ , and  $M_{Fi}$  yields

$$P_{Fi} = \frac{q}{\psi} \left( \frac{h_0\alpha_1}{4c^{3/2}}(f_{33}f_{22} - f_{23}f_{32}) - \frac{\sin^4 \phi_0}{8c^2}(f_{33}f_{12} - f_{32}f_{13}) - \frac{\alpha}{2c^{3/2}}(f_{23}f_{12} - f_{22}f_{13}) \right) \quad (36a)$$

$$Q_{Fi} = \frac{q}{\psi} \left( \frac{-h_0\alpha_1}{4c^{3/2}}(f_{33}f_{21} - f_{31}f_{23}) + \frac{\sin^4 \phi_0}{8c^2}(f_{33}f_{11} - f_{31}f_{13}) + \frac{\alpha}{2c^{3/2}}(f_{23}f_{11} - f_{21}f_{13}) \right) \quad (36b)$$

$$M_{Fi} = \frac{q}{\psi} \left( \frac{h_0\alpha_1}{4c^{3/2}}(f_{32}f_{21} - f_{31}f_{22}) - \frac{\sin^4 \phi_0}{8c^2}(f_{32}f_{11} - f_{31}f_{12}) - \frac{\alpha}{2c^{3/2}}(f_{22}f_{11} - f_{21}f_{12}) \right) \quad (36c)$$

where

$$\psi = f_{11}(f_{22}f_{33} - f_{32}f_{23}) - f_{12}(f_{33}f_{21} - f_{31}f_{23}) + f_{13}(f_{32}f_{21} - f_{31}f_{22}) \quad (37)$$

The right hand side of eq. (28) represents the free-end displacement vector at node ( $i$ ) due to applied load  $q$ .

From equilibrium, the fixed-end reactions at node (j) can be given as

$$P_{Fj} = -P_{Fi}, \quad Q_{Fj} = qL - Q_{Fi}, \quad \text{and}$$

$$M_{Fj} = P_{Fi} \left( \frac{h_1 - h_0}{2} \right) + Q_{Fi} - M_{Fi} - \frac{qL^2}{2} \quad (38)$$

## FIXED-END LOAD VECTOR DUE TO CONCENTRATED LOAD

For a beam element loaded by a concentrated load ( $P$ ) at an arbitrary location defined by a distance ( $L_1$ ) from the left support as shown in Fig. 3(b), the fixed-end load vector can be derived by using the same procedure given before. The flexibility matrix equation for this case can be given as

$$\begin{bmatrix} \frac{1}{\sqrt{c}}(\beta_1) & \frac{h_0}{8c}(\gamma) & \frac{-h_0}{2\sqrt{c}}(\gamma_1 - \beta) \\ \frac{h_0}{8c}(\gamma) & \frac{1}{c^{3/2}}(\alpha) & \frac{-1}{4c} \left( 1 - \frac{1}{(1+cL^2)^2} \right) \\ \frac{-h_0}{2\sqrt{c}}(\alpha) & \frac{-1}{4c} \left( 1 - \frac{1}{(1+cL^2)^2} \right) & \frac{1}{\sqrt{c}}(\beta) \end{bmatrix} \begin{Bmatrix} P_{Fi} \\ Q_{Fi} \\ M_{Fi} \end{Bmatrix} = P \begin{Bmatrix} \delta_1 \\ \delta_2 \\ \delta_3 \end{Bmatrix} \quad (39)$$

where

$$\delta_1 = \frac{-h_0}{8c} \left( 2 \left( \frac{1}{(1+cL_1^2)} - \frac{1}{(1+cL^2)} \right) + \left( \frac{1}{(1+cL^2)^2} - \frac{1}{(1+cL_1^2)^2} \right) + 4L_1\sqrt{c} \left( (\phi_1 + \beta) - (\phi_0 + \bar{\beta}) \right) \right) \quad (40a)$$

$$\delta_2 = \frac{1}{4c^{3/2}} \left( \left( \frac{1}{2}(\phi_0 - \phi_1) - \frac{1}{8}(\sin(4\phi_0) - \sin(4\phi_1)) \right) + L_1\sqrt{c} \left( \frac{1}{(1+cL^2)^2} - \frac{1}{(1+cL_1^2)^2} \right) \right) \quad (40b)$$

$$\delta_3 = \frac{-1}{4c} \left( 4L_1\sqrt{c}(\beta - \bar{\beta}) + \left( \frac{1}{(1+cL_1^2)^2} - \frac{1}{(1+cL^2)^2} \right) \right) \quad (40c)$$

$$\bar{\beta} = \frac{1}{4} \cos^3 \phi_1 \sin \phi_1 + \frac{3}{4} \left( \frac{1}{2} \phi_1 + \frac{1}{4} \sin(2\phi_1) \right),$$

$$\phi_1 = \tan^{-1}(\sqrt{c} L_1) \quad (41)$$

and all other constants are previously defined.

Solving eq. (39) yields the following expressions for the unknowns fixed-end reactions at node (i) in terms of the flexibility matrix coefficients

$$P_{Fi} = \frac{P}{\psi} (\delta_1(f_{33}f_{22} - f_{23}f_{32}) - \delta_2(f_{33}f_{12} - f_{32}f_{13}) + \delta_3(f_{23}f_{12} - f_{22}f_{13})) \quad (42a)$$

$$Q_{Fi} = \frac{P}{\psi} (-\delta_1(f_{33}f_{21} - f_{31}f_{23}) + \delta_2(f_{33}f_{11} - f_{31}f_{13}) - \delta_3(f_{23}f_{11} - f_{21}f_{13})) \quad (42b)$$

$$M_{Fi} = \frac{P}{\psi} (\delta_1(f_{32}f_{21} - f_{31}f_{22}) - \delta_2(f_{32}f_{11} - f_{31}f_{12}) + \delta_3(f_{22}f_{11} - f_{21}f_{12})) \quad (42c)$$

And from equilibrium, the fixed-end reactions at node (j) can be given as

$$P_{Fj} = -P_{Fi}, \quad Q_{Fj} = P - Q_{Fi}, \quad \text{and}$$

$$M_{Fj} = P_{Fi} \left( \frac{h_1 - h_0}{2} \right) + Q_{Fi} - M_{Fi} - P(L - L_1) \quad (43)$$

## NUMERICAL EXAMPLES

To verify the correctness of the derived matrices, the following examples are considered.

### Example 1

Consider the beam shown in Fig. 4 which has a single span of length,  $L=1$  units and fixed at both ends. The beam is carrying a uniformly distributed load,  $q=1$ . The depth of the beam is  $h_0=1$  units at the left end and increase parabolically to  $h_1=2$  units at the right end and has a unit width,  $b=1$  units. The beam was analyzed by Khan and Al-Gahtani (1995) by using the boundary integral method (BIM). Using the same dimensionless data adopted by Al-Gahtani and Khan, the beam is reanalyzed by using the derived expressions for

the fixed-end load vector. The results are presented in Table 1.

### Example 2

Consider a three-span continuous bridge girder having a parabolic varying depth as shown in Fig. 5. The depth of the girder varies from  $h=2.5$  units at both ends and midspan to  $h=7.5$  units at interior supports. This problem has been analyzed by Timoshenko and Young 1965 ; Al-Gahtani and Khan (1998). Using the same dimensionless data, the problem is reanalyzed by using the derived stiffness matrices and the fixed- end load vector. The analysis results (at nodes 1,2,3,4, and 5) are presented in Table 2 together with those obtained by Timoshenko and Young (1965) ; Al-Gahtani and Khan (1998). It can be seen that when the girder is restraint against horizontal (axial) displacement at supports (i.e. all supports are hinges), the results diverge significantly from that obtained by other methods as given in the last column of Table 2. This is due to the coupling effect between the axial force generated from axial restraint and the bending moment which reduces the displacement, rotations, and bending moments.

### Example 3

Finally, consider the beam shown in Fig. 6 which has a span of unit length and a depth varies parabolically from  $h=1.0$  units at left end to  $h=2.0$  units at the right end. The beam is supported at the left end on a translational spring with a stiffness constant of  $K=10$  , fixed at the right end and carrying a concentrated load  $P=1.0$  at the left end. The beam is analyzed by using the derived stiffness matrix in terms of the given dimensionless data. The analysis results are presented in Table 3 in which the third column show the results when the shear deformation is considered. The results show a significant effect for shear deformation. This is due to the large translational stiffness relative to the rotational stiffness for this beam.

## SUMMARY AND CONCLUSIONS

In this paper, an exact stiffness matrix and fixed-end load vector for beams with parabolic varying depth are derived. An exact integrations were carried out to obtain the strain energy equation

including bending, shear, and axial strain energies which is used to obtain the exact expressions for the coefficients of the stiffness matrix. The correctness of the derived expressions is examined through numerical examples. It is found that the derived stiffness matrices and the equivalent load vector are efficient for the analysis of structures having members with parabolic varying depth. Furthermore, the derived matrices can be used in the structural analysis softwares as compared to the available analytical solutions. The obtained results show a significant effect for axial force-bending moment coupling in continuous beams with axial restraint.

## REFERENCES

- Al-Gahtani, H. J. (1996). "Exact stiffnesses for tapered members" *J. Struct. Eng.*, 122(10), 1234-1239.
- Al-Gahtani, H. J., and Khan, M. S. (1998). "Exact analysis of nonprismatic beams" *J. Eng. Mech.*, 124(11), 1290-1293.
- Bathe, K. J., (1996). "Finite element procedures" Prentice-Hall, New Jersey.
- Boresi, A. P., and Schmidt, R. J. (2003). "Advanced mechanics of materials" 6<sup>th</sup> Ed., Wiley, New York.
- Khan, M. S., and Al-Gahtani, H. J. (1995). "Analysis of continuous non-prismatic beams using boundary procedures" The Fourth Saudi Engineering Conference, V11, 137-145.
- Luo, Y., Xu, X., and Wu, F. (2007). "Accurate stiffness matrix for nonprismatic members" *J. Struct. Eng.*, 133(8), 1168-1175.
- Timoshenko, S. P., and Young, D. H. (1965). "Theory of structures" 2<sup>nd</sup> Ed., McGraw-Hill, New York.
- $h_x$  = depth of beam at any section  $x$ ;
- $I_0, I_x$  = moment of inertia of beam cross-section;
- $K_v$  = coefficient defined in eq. (6);
- $[K], [\bar{K}]$  = stiffness matrices;
- $L$  = length of beam;

$M, P, Q$  = bending moment, axial force, and shear force;

$U$  = total strain energy;

$u, v$  = displacements in  $X$  and  $Y$  directions;

$\alpha, \beta, \gamma, \alpha_1, \beta_1, \gamma_1$  = variables defined in eqs. (29)-(34);

$\delta_1, \delta_2, \delta_3$  = variables defined in eqs. (40a)-(40c);

$\theta_i, \theta_j$  = rotational angles at nodes  $i, j$ ;

$\lambda$  = variable defined in eq. (15);

$\phi_0, \phi_1$  = variables defined by eq. (6) and eq. (41) respectively; and

$\psi$  = variable defined in eq. (37).

## NOTATION

*The following symbols are used in this paper:*

$A_0$  = minimum cross-sectional area of beam element;

$b$  = width of beam cross-section;

$c$  = depth variation variable;

$[D]$  = matrix defined by eq. (12)

$E$  = Young's modulus;

$[F]$  = flexibility matrix defined by eq. (35);

$G$  = shear modulus;

$h_0, h_l$  = minimum ,and maximum depth of beam respectively;

**Table 1.** Fixed-End Actions

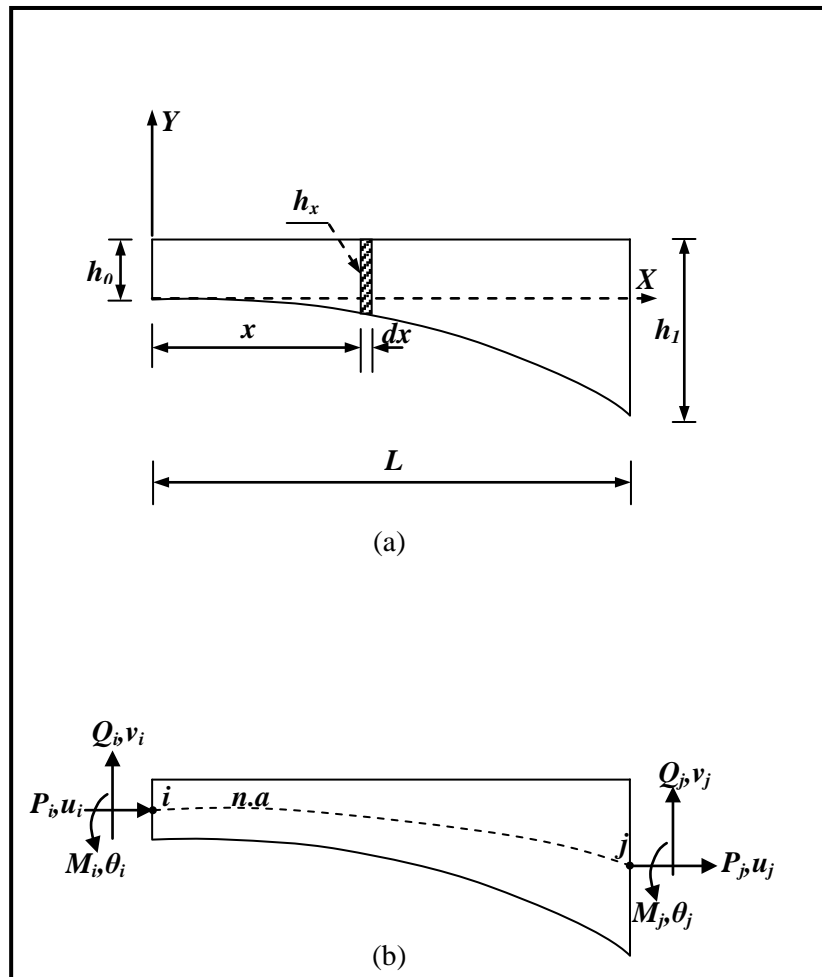
Variable	BIM <sup>a</sup>	Exact <sup>b</sup>
$P_{F1}$	0.0000	0.0088
$Q_{F1}$	0.4267	0.4232
$M_{F1}$	0.0568	0.0564
$P_{F2}$	0.0000	0.0088
$Q_{F2}$	0.5733	0.5768
$M_{F2}$	0.1301	0.1287
<sup>a</sup> Khan and Al-Gahtani (1995)		
<sup>b</sup> Present Analysis		

**Table 2.** Supports Reactions, Midspan Deflection, and Angles of rotation

Variable	BIM <sup>a</sup>	Slop-Deflection <sup>b</sup>	Exact <sup>c</sup> (Free horizontal disp.)	Exact <sup>c</sup> (Horizontal disp. is restraint)
$P_1$	0.000	0.000	0.000	-6.489
$P_2$	0.000	0.000	0.000	98.978
$P_4$	0.000	0.000	0.000	-128.116
$P_5$	0.000	0.000	0.000	35.667
$Q_1$	1.510	1.500	1.337	7.090
$Q_2$	72.450	72.850	72.644	66.165
$Q_4$	46.620	46.150	46.768	40.187
$Q_5$	-12.580	-12.500	-12.732	-5.433
$M_2$	-593.750	-594.000	-598.393	-408.562
$M_3$	124.810	138.600	125.941	72.680
$M_4$	-452.810	-453.000	-458.562	-283.633
$\bar{v}_3$	-	-	-30086.330	-16224.470
$\bar{\theta}_1$	290.250	376.560	387.600	-59.462
$\bar{\theta}_2$	-423.920	-551.880	-560.712	-212.144
$\bar{\theta}_4$	615.500	800.640	809.900	433.410
$\bar{\theta}_5$	-775.540	-1006.200	-1018.890	-502.100
<sup>a</sup> Al-Gahtani and Khan (1998)				
<sup>b</sup> Timoshenko and Young (1965)				
<sup>c</sup> Present Analysis				
$\bar{v}_3 = EI_0 v_3$ , $\bar{\theta}_1 = EI_0 \theta_1$ , $\bar{\theta}_2 = EI_0 \theta_2$ , $\bar{\theta}_4 = EI_0 \theta_4$ , $\bar{\theta}_5 = EI_0 \theta_5$				

**Table 3.** Displacements, rotation, and Support reactions

Variable	Exact (no shear deformation)	Exact (with shear deformation)
$u_l$	-0.01577	-0.00776
$v_l$	-0.04950	-0.07515
$\theta_l$	0.09460	0.04658
$Q_l$	0.4950	0.7515
$Q_2$	0.5050	0.2485
$M_2$	-0.5050	-0.2485

**Fig. 1 .** A beam element with parabolic varying depth:  
(a) typical element; (b) degrees of freedom and nodal forces

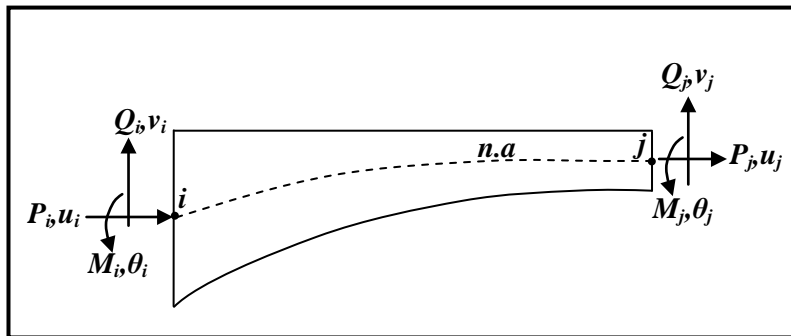


**Fig. 2.** A beam element with parabolic varying depth

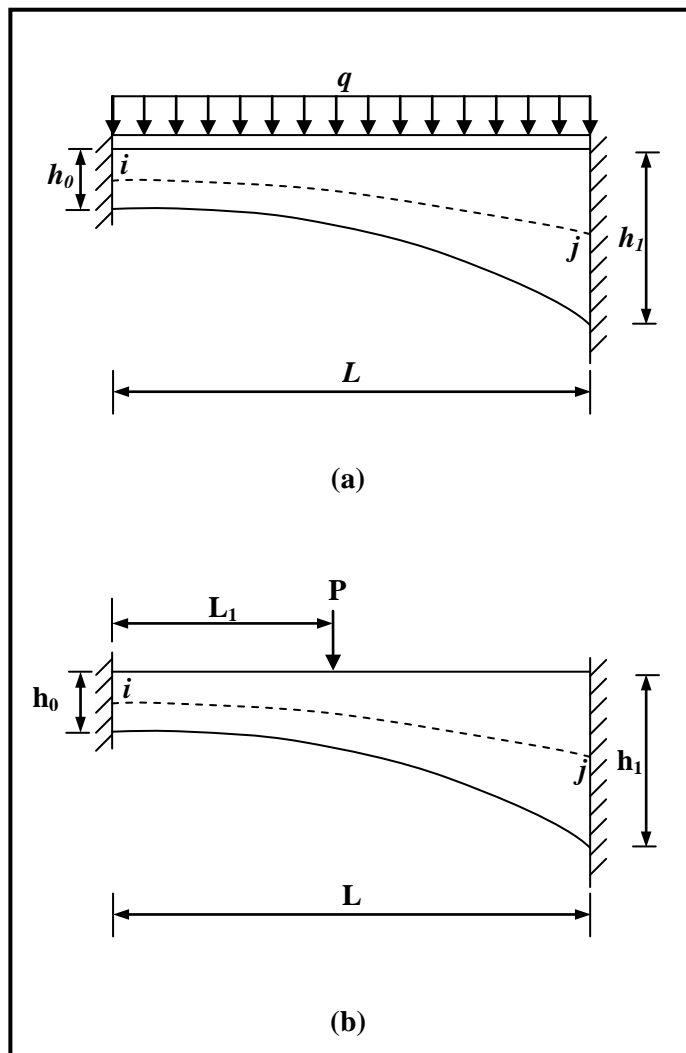


**Fig. 3.** Beam with parabolic varying depth fixed at both ends under the action of:  
(a) uniformly distributed load; (b) concentrated load



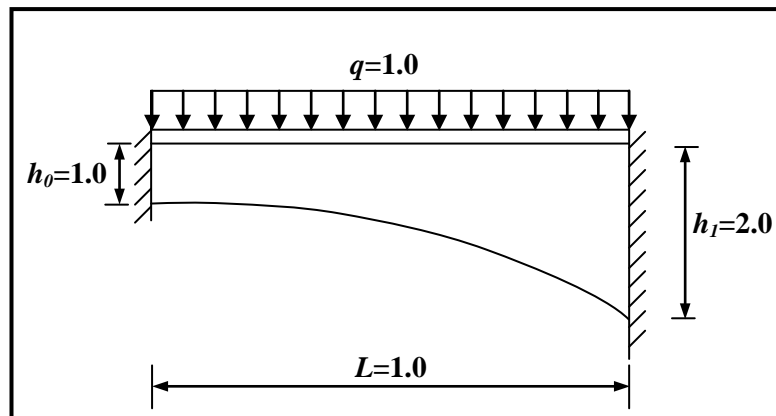


Fig. 4. A Beam with parabolic varying depth (example 1)

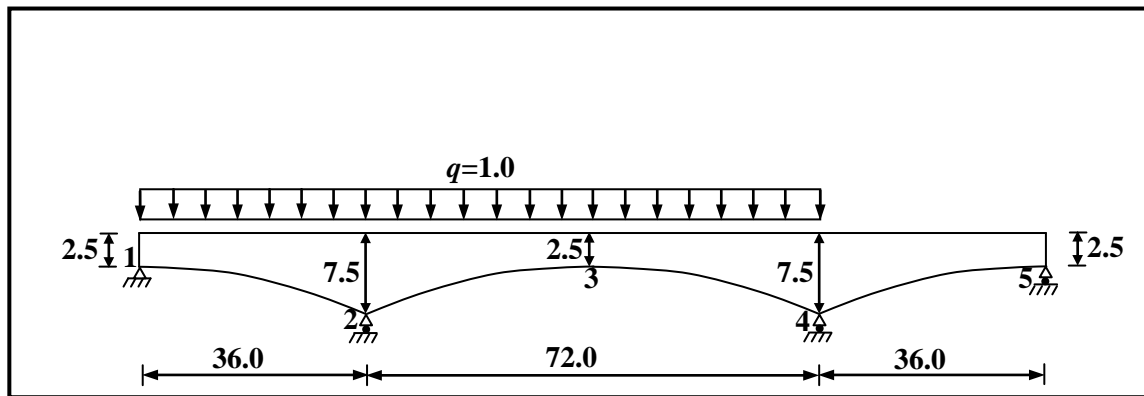


Fig. 5. A three-span continuous bridge girder (example 2)

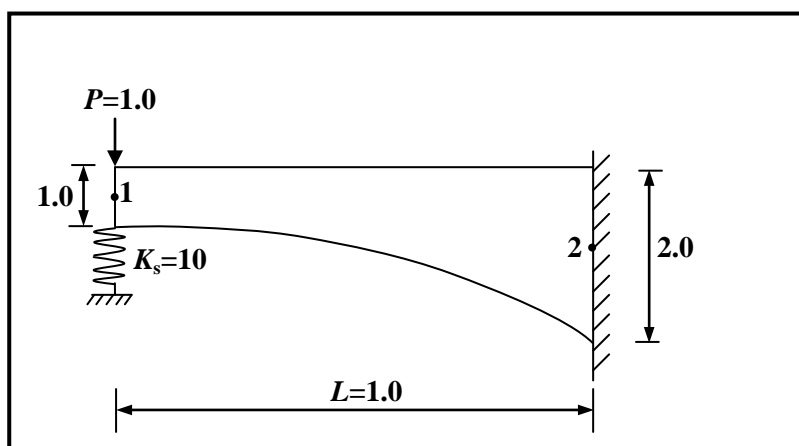


Fig. 6. A Beam with parabolic varying depth elastically supported at one end and fixed at the other end (example 3)

## Compressive Behavior of Fiber Reinforced Concrete Columns Rehabilitated with CFRP Warps

Asst. Prof. Dr. Wasan Ismail Khali

University of Technology- Building & Construction Department –Baghdad-Iraq

[Email-Wasan1959@yahoo.com](mailto:Email-Wasan1959@yahoo.com)

### ABSTRACT

Over the last few years, there has been a worldwide increase in the use of composite materials for rehabilitation of deficient reinforced concrete structures. One important application of this technology is the use of Carbon Fiber Reinforced Polymer (CFRP) jacket to provide external confinement of reinforced concrete columns. Square concrete column specimens  $100 \times 100 \times 1000$  mm with concrete compressive strength of about 30 and 50 MPa, steel fiber volume fraction 0%, 0.5%, 0.75%, and percentage of longitudinal reinforcement 2.01%, 3.14% and 4.52% were tested until failure in previous research. In this research seven tested columns were repaired and rehabilitated using one layer of CFRP flexible wraps and tested to determine their ultimate load carrying capacity. A comparison between the behavior of column specimens before rehabilitation and after rehabilitation was carried out. The result show that high strength concrete (HSC) columns show reduction in the maximum load carrying capacity of about 2% - 21%, while the deflection at maximum load significantly increases relative to concrete columns before rehabilitation.

**KEYWORDS:** Carbon Fiber Reinforced Polymer (CFRP), rehabilitated columns, high strength concrete.

### سلوك الانضغاط للأعمدة الخرسانية المعززة بالألياف والمؤهلة باستخدام لفائف الياف تسليح الكربون البوليمرية

استاذ مساعد د. وسن إسماعيل خليل

#### الخلاصة

لقد ازداد استخدام المواد المركبة في تأهيل المنشآت الخرسانية المتضررة خلال السنوات القليلة الماضية. إن أحد أهم التطبيقات لهذه التقنية هو استخدام التغليف بألياف تسليح الكربون البوليمرية لتوفير تطويق خارجي للأعمدة الخرسانية المسلحة. في بحث سابق تم فحص نماذج لأعمدة خرسانية مربعة المقطع بأبعاد  $100 \times 100 \times 1000$  مم لحين الفشل، حيث كانت مقاومة الانضغاط للخرسانة 30 ، 50 نيوتن/مم<sup>2</sup>، النسبة الحجمية للألياف الفولاذية 0%، 0.5%، 0.75% ونسبة التسليح الطولي 2.01%، 3.14%، 4.52%. تضمن هذا البحث اصلاح وتأهيل سبعة نماذج للأعمدة المفحوصة باستخدام لفائف لدنة من الياف تسليح الكربون البوليمرية ومن ثم إعادة فحص هذه الأعمدة لإيجاد مقاومة تحملها القصوى. تم اجراء مقارنة بين سلوك نماذج الأعمدة قبل وبعد التأهيل. أظهرت النتائج بأن أعمدة الخرسانة عالية المقاومة المؤهلة تبدي إنخفاضا في سعة التحمل القصوى بحدود 2%-21% في حين إزداد الانحراف عند الاجهاد الاقصى بشكل واضح بالمقارنة مع الأعمدة الخرسانية قبل التأهيل.

**الكلمات الرئيسية:** ألياف تسليح الكربون البوليمرية، الأعمدة المؤهلة، الخرسانة عالية المقاومة.

## 1. INTRODUCTION

The use of High Strength Concrete (HSC) members has proved to be most promising in terms strength, stiffness, durability and economy. As the strength of concrete increases, it becomes more brittle. The lack of ductility of HSC columns can result in sudden failure without warning. Previous studies have shown that the strength and ductility can be improved by the use of spiral confinement rectangular and circular lateral ties (Saravanan et al. 2010). In the case of a seismic event, energy dissipation allowed by well confined concrete core can often save lives. On the contrary, a poorly confined concrete column behaves in a brittle manner leading to sudden and catastrophic failures (Sadeghian et al. 2009). Over the last few years, there has been a worldwide increase in the use of composite materials for the rehabilitation of deficient reinforced concrete structures. One important application of this composite retrofitting technology is the use of fiber reinforced polymer (FRP) jacket or sheets to provide external confinement to reinforced concrete columns when the existing internal transverse reinforcement is inadequate (Benzaid et al. 2009). The concept of strengthening reinforced concrete columns by FRP composites is that when concrete is uniaxially compressed due to load, Poisson's effect induces transverse strain that result in radial expansion of the concrete. By confining the concrete using continuous FRP jacket, the fibers resist the transverse expansion of the concrete and provide passive confinement which increases both strength and ductility (Rai). Carbon fiber wrap provided a better solution for repair and strengthening concrete columns due to their well known advantages including, a high strength to weight ratio than traditional reinforcing material such as steel, excellent corrosion resistance and the ability to change the orientation of the fibers which allows the user to strengthen a structure in preferential directions to meet performance requirements, and can result in less labour- intensive work (Wang et al. 2008, Sheikh 2002 and Li et al. 2003). Most of the available studies on the behavior of FRP confined concrete columns have concentrated on the strengthening of circular shaped columns, while relatively few studies have addressed rectangular columns. This partly because the rectangular section is not uniformly confined and

the compressive pressure is unevenly distributed. The higher stress is usually found at the corners (Toutanji et al. 2007, Benzaid et al. 2008). No detail study has been available on the repair and rehabilitation of high strength fiber reinforced concrete rectangular columns after subjected to failure using carbon fiber reinforced polymer (CFRP) wraps.

The effect of corner radius on the performance of CFRP confined square columns were investigated by Wang and Wu 2008. They reported a series of tests on 108 CFRP confined short concrete columns. The primary variables were the corner radius, transverse jacket stiffness, and concrete grade. The test results demonstrated that the corner radius ratio is in direct proportion to the increase in confined concrete strength. Furthermore, it is revealed and explained that confinement provided by a jacket with sharp corners is insignificant in increasing the strength of columns but significant in increasing the ductility of columns.

The main objective of the present investigation is to:

- Rehabilitation failed normal and high strength concrete columns by CFRP flexible wraps.
- To determine the ultimate load carrying capacity of the rehabilitated columns under axial compression.
- To make a comparison between the behavior of conventional concrete columns (before rehabilitation) and the columns after rehabilitation using CFRP flexible wraps.

## 2. EXPERIMENTAL WORK

### 2.1 Materials and Concrete Mixes

In previous research (Khalil et al. 2012) concrete column specimens were manufactured using the following material, ordinary Portland local cement with physical and chemical test results conform to the provisions of Iraqi specification No.5/1984 as shown in Table (1) and (2) respectively. Natural sand of maximum size 4.75 mm and gradation lies in zone (2) was used. The gradation and sulfate content results were within the requirements of the Iraqi specification No. 45/1980, as shown in Table (3). Normal weight crushed aggregate of maximum size 10 mm was also used. Its grading and sulfate content conform to the requirements of Iraqi specification

No. 45/1980, as shown in Table (4). High range water reducing admixture (HRWRA) commercially known as TopFlow SP 703 was used to produce the HPC mix. Its properties are shown in Table (5). The dosage recommended by the manufacturer was (0.75-2) liters/100 kg of cementations material. This type of admixture conforms to the requirement of ASTM C494-04. Silica fume with pozzolanic activity index and the chemical oxide compositions conform to the requirements of ASTM C1240-05 specifications was also used, as shown in Table (6) and (7) respectively. Hooked end steel fiber was used. It is commercially known as Dramix-Type ZC, with 50 mm long and 0.5 mm diameter (aspect ratio,  $l/d = 100$ ), the density of the steel fiber is  $7850 \text{ kg/m}^3$ , and the ultimate tensile strength for individual fiber is 1117 MPa. Deformed steel bars with nominal diameters 8mm, 10mm and 12 mm were used as longitudinal reinforcement. Three specimens for each bar diameter were tested in tension according to ASTM A996M-05 to determine their properties; the results were summarized in Table (8) and Fig. (1).

Reference concrete mix for normal strength concrete (NSC) was designed in accordance with ACI (ACI 211. 1991) to have compressive strength about 35 MPa at 28 days without using any admixtures. The mix proportions are 1: 1.19: 1.8 by weight of cement with cement content  $525 \text{ kg/m}^3$  and w/c ratio of 0.43 to obtain a slump of  $100 \pm 5$  mm. Several trial mixes were carried out to determine the optimum content of silica fume and the optimum dosage of HRWRA to have the same workability (slump  $100 \pm 5$ ) in order to achieve a high strength concrete mix with compressive strength of about 50 MPa. The results indicated that maximum compressive strength obtained was for mixes with 5% silica fume as addition by weight of cement and a dosage of HRWRA 2 liter/100kg of cement. Finally, discrete steel fibers with different volume fractions (0.5% and 0.75%) were added to the concrete mixes. Table (9) indicates the details of concrete mixes used. The column specimens were tested under uniaxial compression till failure.

In this research some tested columns from previous research were repaired using bonding slurry Sika Monotop-610 which was applied to the prepared substrate, then a polymer modified repair mortar Sika Monotop-612 was applied wet by wet to the bonding slurry. After curing period, the repaired concrete columns were wrapped with a

unidirectional carbon fiber fabric SikaWrap-300C/60. The manufacturers guaranteed tensile strength for this carbon fiber fabric is 3900 MPa, with a tensile modulus of 230 GPa, maximum tensile strain 0.006, an ultimate elongation of 1.5% and a fiber thickness of 0.166mm. Two part epoxy resin Sikadur-330 was used to bond the carbon fabrics over the column specimens.

## 2.2 Preparation and Test Procedure of Specimens

In previous research (Khalil et al. 2012) reinforced concrete columns  $100 \times 100 \times 1000$  mm were prepared as indicated in Table (10). To comply with existing reinforced concrete members in any structure, the corners for all prismatic specimens were kept sharp for CFRP application. Four longitudinal reinforcing deformed steel bars one at each corner of column specimen cross section with different diameter (8, 10 and 12) were used. Lateral ties with 8mm diameter were used for all columns specimens as shown in Fig. (2). Concrete cover of 12.5 mm was provided in all columns and a cover of 20 mm was provided between the ends of longitudinal bars at the top and bottom surfaces of the specimens to prevent direct loading on the bars. The columns were continuously cured with water and after that, they were kept in the laboratory to be normally dried until the time of testing.

Universal testing machine with maximum capacity of 2500 kN was used for testing the reinforced concrete columns (conventional columns). The column specimens were externally confined by 5 mm thick and 100 mm height steel collars at both ends of the specimen to avoid premature failure at the end regions of the columns throughout the test. The columns gross deflection was measured by a dial gauge of (0.01mm/div) sensitivity, fixed with the two collars by a steel frame.

## 2.3 Procedure for Repairing and Rehabilitation of Tested Column Specimens

In this research the column specimens tested in previous research were repaired and then wrapped with carbon fiber fabric (rehabilitated columns) using the following procedure:

- The unsound concrete was removed and the surface of the concrete was well cleaned from dust by a steel brush.

- The bonding slurry was mixed with water/powder ratio 0.17-0.18 according to manufacturers. Then it was applied by brush to the prepared (pre-wetted) concrete surface.
- Polymer modified repair mortar was mixed with water/powder ratio 0.11- 0.13 by weight according to manufacturers. The mortar is applied wet on wet to the bonding layer in several layers with thickness not greater than 30mm.
- The repaired part of the column specimens was cured by covering it with burlap and spraying water on it every day, then covering it with polyethylene sheets. The repaired part was cured for 28 days after that the specimens were kept in the laboratory for seven days to be normally dried.
- Two part epoxy impregnation resin was mixed by hand (part A: part B=4:1 by weight according to the manufacturers) and applied to the prepared concrete column surfaces using a brush.
- A unidirectional woven carbon fiber fabric wrapped around the column. A roller used parallel to the fabric direction until the resin is squeezed out between and through the fiber strands and distributed evenly over the whole fabric surface. Carbon fiber layer was wrapped around the column with an overlap of  $\frac{1}{4}$  of the perimeter to avoid sliding or debonding of fibers during test. The wrapped specimens were left at room temperature for seven days before testing. Fig. (3-A) shows one of concrete column specimens before repair and rehabilitation, while Fig. (3-B) shows the same column after repair and rehabilitation with CFRP.

The same testing procedure was followed for wrapped column specimen.

### 3. TEST RESULTS AND DISCUSSION

#### 3.1 Properties of Bonding Slurry and Repair Mortar

The compressive strength and direct tensile strength specimens for the bonding slurry and polymer modified repair mortar used to repair the column specimens was casted cured and tested according to ASTM C-109 and AASHTO T132 respectively.

Table (11) and (12) show the results of the compressive strength and direct tensile strength at different ages for bonding slurry and polymer modified repair mortar respectively used in this research. The results show that both the compressive strength and direct tensile strength increase with age.

#### 3.2 Maximum Load Carrying Capacity and Deflection

The comparison of maximum load carrying capacity and deflection between conventional (tested columns until failure) and rehabilitated columns are shown in Table (13). Generally it can be observed that high strength concrete columns after rehabilitation with CFRP wraps show a reduction in the maximum load carrying capacity of about 2%-21% in comparison with conventional high strength concrete columns. This is because FRP not increases the compressive strength of the square columns with sharp corners, since the confining action is mostly limited at the corners, producing therefore a confining pressure not sufficient to overcome the effect of concrete degradation (Chikh et al. 2012). The deflection at maximum load significantly increases (except for column 0.75SF100-10H100) in comparison with conventional high strength concrete columns. So the application of CFRP wrap improves the ductility of the rehabilitated column specimens. This attributed to the fact that when FRP confined concrete subjected to axial compression, the FRP jackets are loaded mainly in hoop tension while the concrete is subjected to triaxial compression, so that both materials are used to their best advantages. As a result of the confinement, both the strength and the ultimate strain of concrete can be enhanced and instead of the brittle behavior exhibited by both materials, FRP confined concrete possesses an enhanced ductility (Nicolae et al. 2008). The results also show that the percentage decrease in maximum load carrying capacity for rehabilitated fibrous HSC columns relative to the conventional column specimens is higher than that for nonfibrous concrete specimens. The maximum load of rehabilitated normal strength concrete columns (NF-8N100) considerably increases relative to conventional normal strength columns. The percentage increase is about 65%. It can be concluded that rehabilitation of normal strength

concrete columns with CFRP wraps produce higher results in terms of strength than for similar high strength concrete columns.

### 3.3 Stress – Strain Response

The stress-strain relationships for both conventional and rehabilitated column specimens are shown in Figures (4) to (10). All CFRP wrapped specimens showed almost linear stress-strain relationship at the first stage governed by the stiffness of the unconfined tested concrete, no confinement is activated in the CFRP wraps when the lateral strains in the concrete are very small. Then the increase of load produces large lateral expansion in columns, and consequently the CFRP wrap reacts accordingly and a confining action is created on the concrete core. In the cases of square section columns, the confining action is mostly limited at the corners, producing therefore a confining pressure not sufficient to overcome the effect of concrete degradation, thus the ultimate load for rehabilitated high strength columns is lower than that of conventional columns. Also high strength concrete is more brittle than normal strength concrete. Moreover the high slenderness ratio of column specimen tested in this investigation leads on overall to a decrease in load carrying capacity of CFRP wrapped columns (Chikh et al. 2012).

### 3.4 Mode of Failure of Rehabilitated Column Specimens

The summary of mode of failure for rehabilitated column specimens is tabulated in Table (14), also Fig. (11) shows the failure mode of some rehabilitated specimens. Even though the CFRP and reinforced concrete columns combination is a composite action, the most of the load is carried by the CFRP alone. Clicking sounds were heard during various stages of loading which were attributed to the microcracking of the concrete. It was noticed that after the failure of CFRP the ultimate load of column is reached and failure occurred as tensile rupture or snatching of fiber wraps. It was observed that the failure of fiber wraps was mostly concentrated in column specimen end regions (at the head or the base of specimen). This is due to the high slender ratio of column specimens ( $L/h=10$ ) which leads to small rupture area for CFRP wraps (Chikh et al. 2012). For all confined specimens delamination was not observed at the overlap

location of the jacket, which confirmed the adequate stress transfer over the splice.

### 4. CONCLUSIONS

From the experimental results presented in this investigation, the following conclusions can be drawn:

- 1- High strength concrete columns after rehabilitation with CFRP wraps shows a reduction in the maximum load carrying capacity of about 2%-21% relative to HSC columns before rehabilitation.
- 2- The deflection of the rehabilitated HSC columns is significantly increases in comparison with HSC columns before rehabilitation.
- 3- The maximum load of the rehabilitated normal strength concrete columns increases by about 65% relative to concrete column before rehabilitation, so the rehabilitation of normal strength concrete columns produce higher results in terms of strength than for similar HSC columns.
- 4- The failure of the rehabilitated columns occurred as a tensile rupture or snatching of fiber wraps mostly concentrated in column end region.

### 5. REFERENCES

- ACI Committee 211.1, “*Standard Practice for Selecting Proportions for Normal, Heavyweight, and Mass Concrete*”, 1991.
- Benzaid, R., Chikh, N.E. and Mesbah, H., “*Behaviour of Square Concrete Columns Confined with GFRP Composite Warp*”, Journal of Civil Engineering and Management, Vol.14, No.2, 2008, PP.115-120.
- Benzaid, R., Chikh, N.E. and Mesbaah, H., “*Study of the Compressive Behavior of Short Concrete Columns Confined by Fiber Reinforced Composite*”, The Arabian Journal for Science and Engineering, Vol.34, No.113, April 2009, PP.15-26.

Chikh, N., Gahmous, M. and Benzaid, R., ***“Structural Performance of High Strength Concrete Columns Confined with CFRP Sheets”***, Proceedings of the Word Congress on Engineering Vol.III, July, 2012, London, U.K.

Khalil, W.I., Gorgis, I.N. and Mahdi, Z.r., ***“Behavior of High Performance Fiber Reinforced Concrete Columns”***, ARPN Journal of Engineering and Applied Science, Vol.7, No.11, Nov.2012, PP.1455-1467.

Li, G., Kidane, S., Pang, S.S., Helms, S.E., and Stubblefield, M.A., ***“Investigation into FRP Repaired RC Columns”***, Composite Structures, No.62, 2003, PP.83-89.  
[www.ivsl.org](http://www.ivsl.org)

Nicolae, N., Gabriel, O., et al., ***“Fibre Reinforced Polymer Composites as Internal and External Reinforcement for Building Elements”***, Technical University, Jassy, Department of civil and Industrial Engineering, March, 2008.

Rai, G., ***“New and Emerging Technologies for Retrofitting and Repairs”***.  
[www.rminternational.co.in/pdf-folder/New-technologies](http://www.rminternational.co.in/pdf-folder/New-technologies).

Sadeghian, P. and Rahai, A.R., ***“Strength and Ductility of Unreinforced Concrete Columns Confined With CFRP Composites Under Uniaxial Loading”***, Concrete Repair, Rehabilitation and Retrofitting, London, 2009.

Saravanan, J., Suguna, K. and Raghunath, P. N., ***“Confined High Strength Columns: An Experimental Study”***, American Journal of Engineering and Applied Sciences, Vol.3, No.1, 2010, PP.133-137.

Sheikh, S.A., ***“Performance of Concrete Structures Retrofitted with Fiber Reinforced Polymers”***, Engineering Structures, No.24, 2002, PP.869-879.  
[www.ivsl.org](http://www.ivsl.org)

Toutanji, H.A., Han, M., and Matthys, S., ***“Axial Load Behavior of Rectangular Concrete Columns Confined with FRP Composites”***, FRPRCS-8, University of Patras, Patras, Greece, July, 2007, PP.1-10.

Wang, L.M. and Wu, Y.F., ***“Effect of Corner Radius on the Performance of CFRP-Confined Square Concrete Columns: Test”***, Engineering Structures, 30, 2008, PP.493-505.





Table 1 Physical properties of cement\*

Physical properties	Test results	Limits of Iraqi Specification No.5/1984
Specific surface area (Blaine method), $m^2/kg$	372	$\geq 230$
Soundness (Autoclave), %	0.01	$\leq 0.8$
Setting time (Vicat's apparatus)		
Initial setting time, hrs: min.	3:58	$\geq 45$ min
Final setting time, hrs: min.	4:50	$\leq 10$ hrs
Compressive strength		
3days, $N/mm^2$	29.80	$\geq 15$
7days, $N/mm^2$	34.84	$\geq 23$

\* Physical tests were carried out by the National Center for Construction Laboratories and Researches (NCCLR).

Table 2 Chemical composition and main compounds of the cement used throughout this investigation\*

Oxide composition	Abbreviation	Content (percent)	Limit of Iraqi Specification No.5/1984
Lime	CaO	62.44	---
Silica Dioxide	SiO <sub>2</sub>	20.25	---
Alumina Trioxide	Al <sub>2</sub> O <sub>3</sub>	4.73	---
Iron Oxide	Fe <sub>2</sub> O <sub>3</sub>	4.32	---
Magnesia oxide	MgO	1.5	$\leq 5.0\%$
Sulphate	SO <sub>3</sub>	1.88	$\leq 2.8\%$ If C <sub>3</sub> A > 5%
Loss on Ignition	L. O. I.	3	$\leq 4.0\%$
Insoluble residue	I. R.	0.8	$\leq 1.5\%$
Lime saturation factor	L. S. F.	0.93	0.66- 1.02
Main compounds (Bogue's equations)			
Tricalcium Silicate	C <sub>3</sub> S	56.90	---
Dicalcium Silicate	C <sub>2</sub> S	15.21	---
Tricalcium Aluminate	C <sub>3</sub> A	5.23	---
Tetracalcium alumino-Ferrite	C <sub>4</sub> AF	13.13	---

\* Chemical tests were carried out by the National Center for Construction Laboratories and Researches (NCCLR).



**Table 3 Fine aggregate properties\***

Sieve size (mm)	Cumulative passing %	Limits of Iraqi specification No.45/1980, zone 2
4.75	100	90-100
2.36	90.15	75-100
1.18	74.22	55-90
0.60	51.37	35-59
0.30	19.3	8-30
0.15	3.79	0-10
<b>Fineness modulus = 2.61</b>		
<b>Specific gravity = 2.65</b>		
<b>Sulfate content = 0.08%</b> <b>(Iraqi specification requirement <math>\leq 0.5\%</math>)</b>		
<b>Absorption = 0.75%</b>		

\* Properties of fine aggregate were performed by the National Center for Geological Survey and Mines

**Table 4 Coarse aggregate properties\***

Sieve size (mm)	Cumulative passing %	Limits of Iraqi specification No. 45/1980
14	100	100
10	100	85-100
5	15.3	0-25
2.36	0.53	0-5
<b>Specific gravity = 2.66</b>		
<b>Sulfate content = 0.08%</b> <b>(Iraqi specification requirement <math>\leq 0.1\%</math>)</b>		
<b>Absorption = 0.52%</b>		

\* Properties of coarse aggregate were performed

by (NCCLR)

**Table 5 Technical data of the superplasticizer used in this investigation\***

Technical description	Properties
Appearance	Dark Brown/Black liquid
Specific gravity	1.235 at 25 $\pm$ 2°C
Chloride content	Nil.
Storage life	Up to 1 year in unopened containers.

\*According to manufacturer.

**Table 6 Physical requirements and pozzolanic activity index for condensed silica fume(SF)\***

Physical properties	SF	ASTM C1240-05 limits
Specific surface area, min, (m <sup>2</sup> /g)	20	$\geq 15$
Strenght activity Index with Portland cement at 7days, min. percent of control.	122	$\geq 105$
Percent retained on 45 $\mu$ m (No.325), max, %	9	$\leq 10$

\*Tests were carried out by Building Research Center

**Table 7 Chemical composition for silica fume \***

Oxides	content(%)	ASTM C1240-05 limitations
SiO <sub>2</sub>	90.51	≥ 85
Al <sub>2</sub> O <sub>3</sub>	0.60	–
Fe <sub>2</sub> O <sub>3</sub>	2.32	–
Na <sub>2</sub> O	0.15	–
CaO	0.58	–
MgO	0.3	–
TiO <sub>2</sub>	0.01	–
K <sub>2</sub> O	1.26	–
P <sub>2</sub> O <sub>5</sub>	0.10	–
SO <sub>3</sub>	0.35	≤ 4
L.O.I	3.82	≤ 6

\*Test was carried out at by the National Center for Geological Survey and Mines

**Table 8 Properties of steel reinforcing bars**

Nominal bar diameter (mm)	Bar area (mm <sup>2</sup> )	Modulus of elasticity (GPa)	Yield stress (MPa)	Strain at yield stress (mm/mm)	Ultimate stress (MPa)	Strain at ultimate stress (MPa)	Elongation (%)
8	50.27	202	545	0.0027	660	0.18	15.5
10	78.54	202	514	0.00255	625	0.16	14.5
12	113.1	200	503	0.00252	615	0.13	14.5

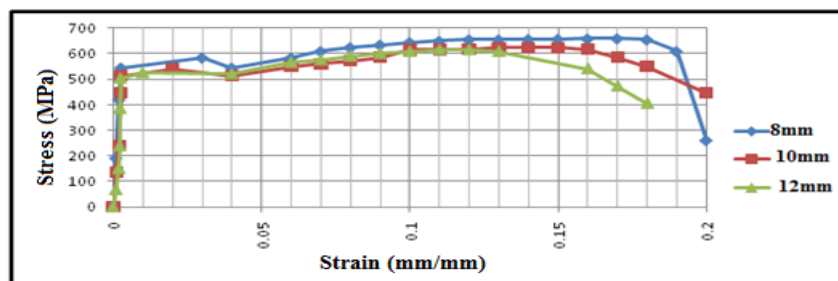
**Fig. 1 Stress-strain curves for steel reinforcement**

Table 9 Details of trail mixes for various volume fractions of steel fiber

Mix proportions by weight	Concrete type	HRWRA (liter/100kg of cement)	Silica fume (% as addition by weight of cement)	w/c ratio	Type of fiber	aspect ratio	Fiber volume fraction	Slump (mm)	Compressive strength at 28days $f_c^*$ (MPa)
1: 1.19: 1.8	HSC	2	5	0.295	-	-	-	105	48.15
					Steel	100	0.5	75	52.73
					steel	100	0.75	65	56.02
	NSC	-	-	0.43	-	-	-	105	29.38

\* Cylinder compressive strength (150×300)

Table 10 Details of the column specimens

Column symbols	Volume fraction of Fibers $V_f$ (%)	Aspect ratio of fibers L/d	Type of concrete	Diameter of long. reinf. (mm) (Percent of long. Reinf.) ( $\rho_l$ %)	Spacing of lateral reinf.(mm) (Percent of lateral reinf.) ( $\rho_s$ %)
NF-8H100	0	--	HSC	8 (2.01)	100 (2.79)
NF-10H100	0	--	HSC	10 (3.14)	100 (2.79)
0.5SF100-10H100	0.5	100			
0.75SF100-10H100	0.75	100			
NF-12H100	0	--	HSC	12 (4.52)	100 (2.79)
0.75SF100-12H100	0.75	100			
NF-8N100	0	--	NSC	8 (2.01)	100 (2.79)

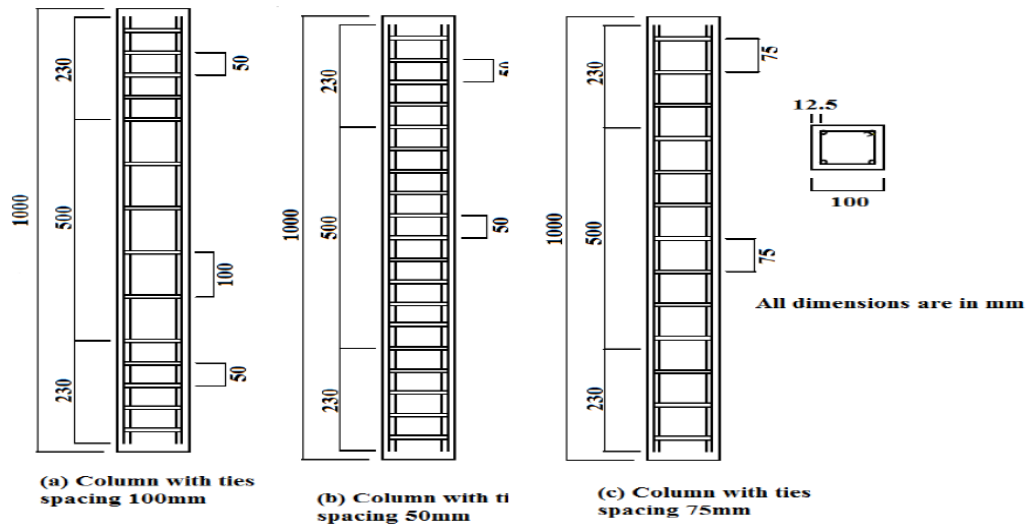


**Fig. 2 Details of columns reinforcement**



A- Conventional column (0.75SF100-12H100)  
before rehabilitation (after testing)



B- Column (0.75SF100-12H100)  
after rehabilitation

**Fig. 3 Column specimen before and after rehabilitation**

**Table 11 Compressive and direct tensile strengths  
for bonding slurry used in this research**

Age (days)	Compressive strength (MPa)	Direct tensile strength (MPa)
1	41.12	1.01
7	48.5	1.37
14	55.59	1.49
28	57.54	1.67

**Table 12 Compressive and direct tensile strengths  
for modified mortar used in this research**

Age (days)	Compressive strength (MPa)	Direct tensile strength (MPa)
1	28.3	0.75
7	42.0	1.59
14	48.6	2.72
28	68.2	2.95

**Table 13 Comparison between conventional and rehabilitated column results**

Specimen	Conventional columns		Rehabilitated columns		Rehab.max.load/Conv. max.load (%)
	Max. load (kN)	Deflection at max. load (mm)	Max. load (kN)	Deflection at max. load (mm)	
NF-8H100	515	1.32	490	3.46	95.2
NF-10H100	481	2.81	470	3.06	97.7
0.5SF100-10H100	560	2.33	440	3.20	78.6
0.75SF100-10H100	575	2.80	520	2.39	90.4
NF-12H100	550	2.35	470	4.74	85.5
0.75SF100-12H100	670	2.03	550	2.72	82.1
NF-8N100	260	0.95	430	1.96	165.4

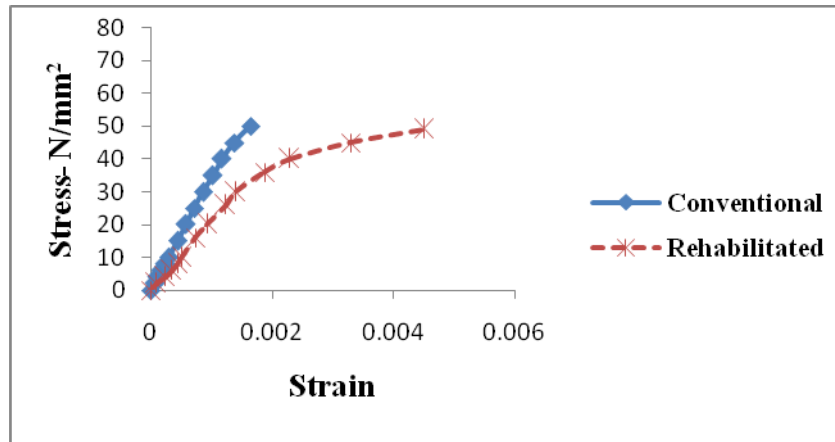


**Fig. 4 Comparison of stress vs strain curve for conventional & rehabilitated column specimen NF-8H100**

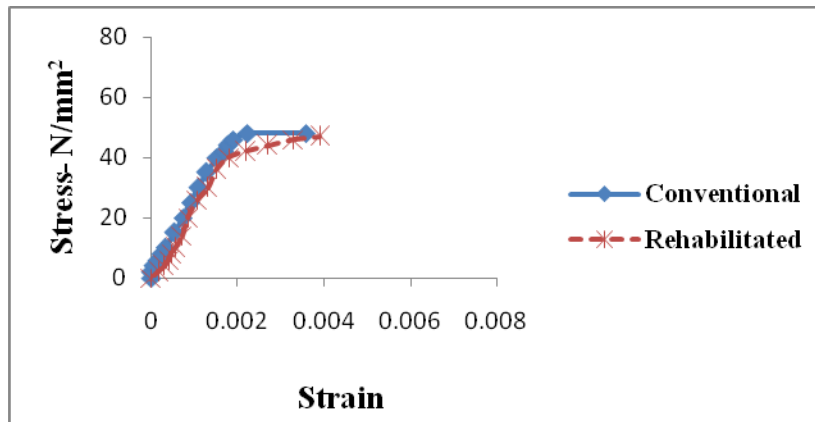


**Fig. 5 Comparison of stress vs strain curve for conventional & rehabilitated column specimen NF-10H100**

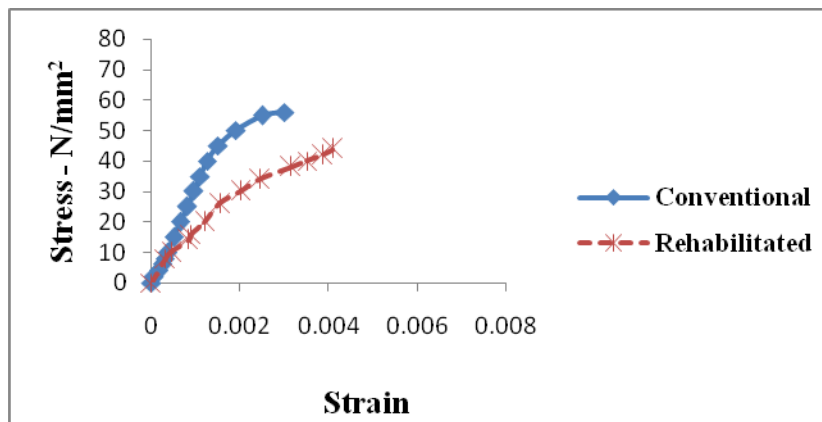


**Fig. 6 Comparison of stress vs strain curve for conventional & rehabilitated column specimen 0.5 SF100-10H100**

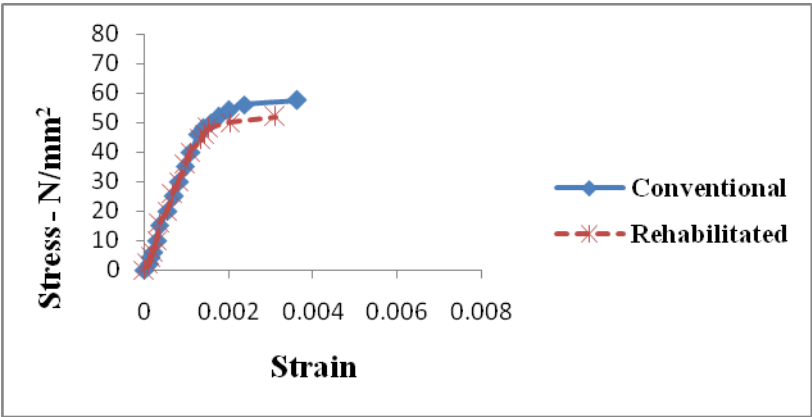


Fig. 7 Comparison of stress vs strain curve for conventional & rehabilitated column specimen 0.75 SF100-10H100

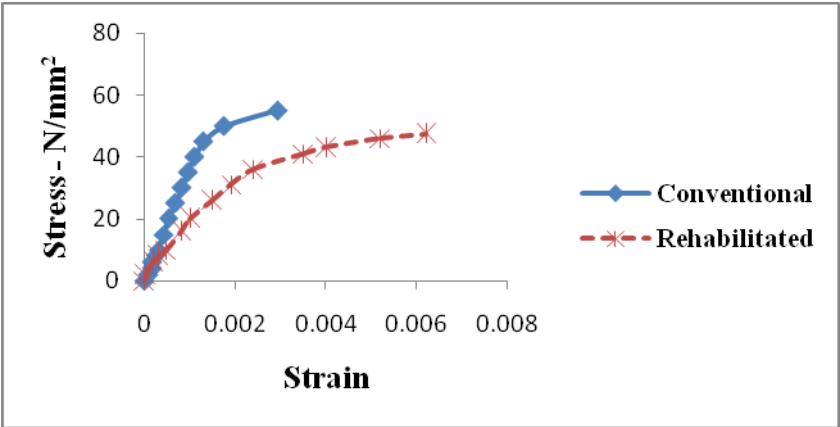


Fig. 8 Comparison of stress vs strain curve for conventional & rehabilitated column specimen NF-12H100

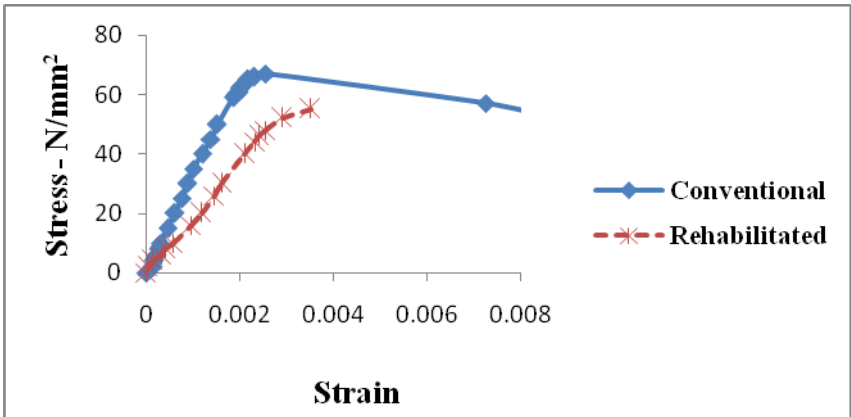
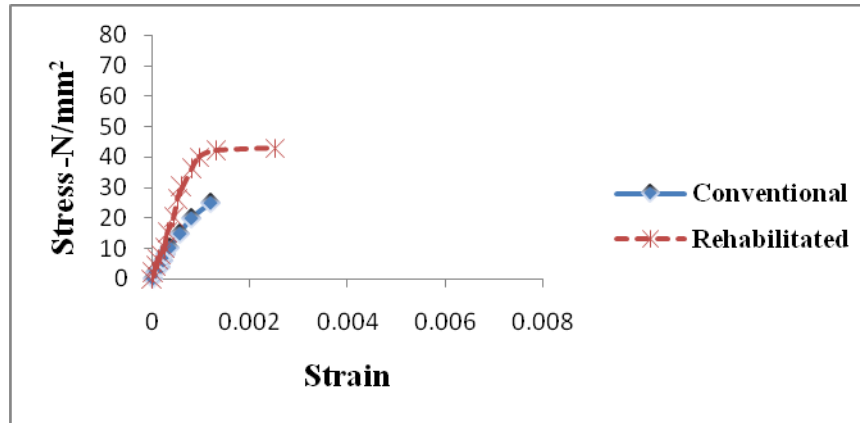


Fig. 9 Comparison of stress vs strain curve for conventional & rehabilitated column specimen 0.75 SF100-12H100



**Fig. 10 Comparison of stress vs strain curve for conventional & rehabilitated column specimen NF-8N100**

**Table 14 Failure mode of rehabilitated concrete columns**

Specimen	Failure mode
NF-8H100	Snatching of fiber with considerable crushing of concrete at the column base
NF-10H100	Snatching of fiber near the column base
0.5SF100-10H100	Snatching of fiber with slight crushing of concrete at the column head
0.75SF100-10H100	Tensile rupture of the fiber in the corner at the column base
NF-12H100	Tensile rupture of fiber near the column base
0.75SF100-12H100	Tensile rupture of fiber in the corner at the column base
NF-8N100	No sign of any tensile rupture or snatching of fiber is appears on the column





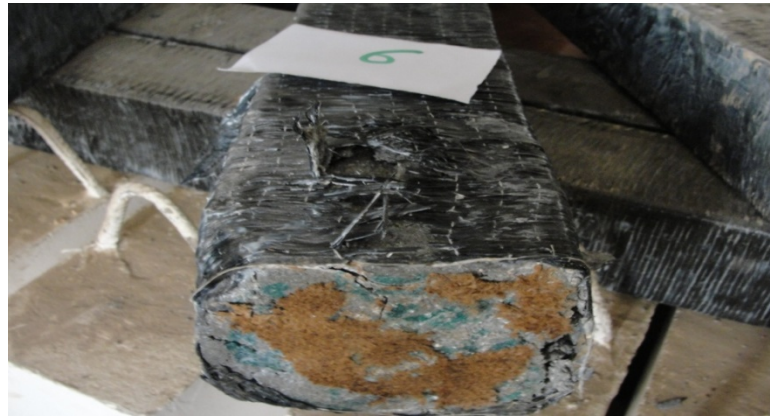
A- Failure mode for specimen **NF-8H100**



B- Failure mode for specimen **NF-10H100**



C- Failure mode for specimen **0.75 SF100-10H100**



D- Failure mode for specimen **NF-12H100**



E- Failure mode for specimen **0.75 SF100-12H100**

**Fig. 11 Failure mode of some rehabilitated concrete column specimens**

## Potential Use of Recycled Asphalt Pavement (RAP) in Hot Mix Asphalt

**Asst. Prof. Namir Ghani Ahmed**  
Department of highway &  
Transportation Engineering  
College of Engineering  
University of Al Mustansiriya  
Email: dr.namir@alsadeemiraq.net

**Asst. Lect. Abbaas Inaayah Kareem**  
Department of highway &  
Transportation Engineering  
College of Engineering  
University of Al Mustansiriya  
email: kkkabbaas@yahoo.com

**Asst. Lect. Alaa Saadi Abbas**  
Department of highway &  
Transportation Engineering  
College of Engineering  
University of Al Mustansiriya  
email: alaa04\_engineer@yahoo.com

### ABSTRACT:

The objective of the present paper is to examine the effect of Recycled Asphalt Pavement (RAP) on marshall properties and indirect tensile strength of HMA through experimental investigation. A mixture with 0% RAP was used as a control mix to evaluate the properties of mixes with 5%, 10%, and 15% RAP. One type of RAP was brought from Bab Al-moadam's road in Baghdad for this purpose. The experimental testing program included Marshall and Indirect Tensile Strength tests. The results indicated that the bulk density, flow and VFA increase with the increasing of the percentage of RAP, while increasing in RAP results decreases in VTM and VMA values. Furthermore, the stability is changed from 10.1 kN for the control mix to 12, 13.6 and 11.7 kN for mixes with 5%, 10% and 15% RAP respectively. The results reveal that the inclusion of RAP into HMA mixtures increases the indirect tensile strength and decreases the values of ITS with the increasing of the test temperature. The results also indicated that increasing the percentage of RAP produces an increasing in temperature susceptibility value. The results of marshall properties and IDT test indicate that the amount of new binder that needs to be added to the RAP mixture can be reduced without significant effects on the quality of the produced mix.

**Keywords:** recycled asphalt pavement (RAP), marshall properties, indirect tensile strength old aggregate, and old asphalt.

### أمكانية استخدام التبييط الاسفلتي المعاد تدويره في الخلطات الاسفلتية

م.م. الاع سعدي عباس  
قسم هندسة الطرق والنقل  
كلية الهندسة/الجامعة المستنصرية

م.م. عباس عناية كريم  
قسم هندسة الطرق والنقل  
كلية الهندسة/الجامعة المستنصرية

أ.م.د. نمير غني احمد  
قسم هندسة الطرق والنقل  
كلية الهندسة/الجامعة المستنصرية

### الخلاصة:

الهدف من البحث الحالي هو التحري عن تأثير الخرسانة الاسفلتية المعاد تدويرها على خواص مارشال و قوة الشد غير المباشر للخلطة الاسفلتية من خلال التحريات المختبرية. تم اعتماد خلطة بنسبة 0% من الخرسانة الاسفلتية المعاد تدويرها استخدمت كخلطة قياسية لتقييم خواص خلطات تم اعدادها مع نسب 5%، 10% و 15% من الخرسانة الاسفلتية المعاد تدويرها. تم توفير نوع واحد من الخرسانة الاسفلتية المعاد تدويرها من منطقة باب المعظم في بغداد لهذا الغرض. تضمن برنامج الفحوصات: فحوصات مارشال و فحوصات قوة الشد غير المباشر. النتائج اشارت الى ان الكثافة و الانسياب و الفراغات المملوءة بالاسفلت تزداد مع الزيادة بنسبة الخرسانة الاسفلتية المعاد تدويرها، بينما الزيادة في نسبة الخرسانة الاسفلتية المعاد تدويرها تنتج نقصان في نسبة الفراغات الهوائية و الفراغات بين حبيبات الركام. علاوة على ذلك، الثبوتية تتغير من 10.1 كيلو نيوتن للخلطة القياسية الى 12، 13.6 و 11.7 كيلو نيوتن للخلطات التي تم اعدادها مع نسب: 5%، 10% و 15% من خرسانة اسفلتية معاد تدويرها وعلى التوالي. بينت النتائج بأن تضمين الخرسانة الاسفلتية المعاد تدويرها بالخرسانة الاسفلتية يزيد من قوة الشد غير المباشر والذي يقل مع زيادة درجة حرارة الفحص. كما اشارت النتائج بأن زيادة نسبة الخرسانة الاسفلتية المعاد تدويرها ينتج زيادة التأثير بدرجة الحرارة. وبينت نتائج فحوصات مارشال وفحص (IDT) الى ان مقدار الاسفلت المضاف للخلطة المحضرة مع خرسانة اسفلتية معاد تدويرها من الممكن أن يقلل من دون التأثير على نوعية الخلطة المنتجة.

**الكلمات الرئيسية:** التبييط الاسفلتي المعاد تدويره، خصائص مارشال، مقاومة الشد الغير مباشر، الركام القديم، الاسفلت القديم.

## 1- INTRODUCTION

The most frequently used by-product in hot mix asphalt is recycled or reclaimed asphalt pavement (RAP) and the most recycled material in the United States. The use of RAP in hot-mix asphalt projects has economic and environmental benefits. The economic benefits from use of RAP materials can provide a great boost to the highway industry by freeing funds for additional highway construction, rehabilitation, preservation, and maintenance. In recent years, the incentive to recycle has grown stronger because of concerns about the environment and sustainability. The use of RAP can result in sustainable development and cost savings by reducing the amount of virgin materials required in the production of the new asphalt mixture (Behnia B. et al., 2011). Most states in the United States have established a limit of 10% to 50% RAP that can be used as part of their regular asphalt concrete (AC) designs. The Virginia Department of Transportation (Virginia DOT) recently increased the threshold of allowable RAP for Superpave mixtures from 20% to 30%. As in Virginia, AC mixtures produced in other parts of the United States may contain up to 30% or more RAP. The effect, therefore, of RAP on pavement performance is of tremendous importance and is receiving much attention as evidenced by numerous recent publications on the subject (Apeagyei A. K. et al., 2011).

A study by Jo Sias Daniel and Aaron Lachance (2005) showed that the voids in mineral aggregate (VMA) and voids filled with asphalt (VFA) of the RAP mixtures increased at the 25% and 40% levels, and there was also an influence of preheating time on the volumetric properties.

Shu X. et al., (2008) conducted a laboratory study to evaluate fatigue characteristics of hot-mix asphalt (HMA) mixtures. In this study, the HMA mixtures containing 0%, 10%, 20%, and 30% of recycled asphalt pavement (RAP) were plant prepared with one source of aggregate, limestone, and one type of binder, PG 64–22. The results from this study indicated that both indirect tensile strength IDT and beam fatigue tests agreed with each other in ranking the fatigue resistance of

mixtures when proper procedures were followed. An experimental study by Valdés G. et al., (2011) to characterize the mechanical behavior of bituminous mixtures containing high rates of reclaimed asphalt pavement (RAP). Two semi-dense mixtures of 12 and 20 mm maximum aggregate size and containing 40% and 60% RAP. Results show that the mixtures with RAP, have very similar values of indirect tensile strength, which are considerably higher than that of the conventional mixture.

Tran b. T. and Hassan R. A., (2011) conducted an experimental program to design and assess the properties of recycled hot dense graded asphalt mixes, the RAP contents in the recycled mixes were 10%, 20%, and 30%. The results from this experimental program proved to be successful in producing recycled mixes with up to 20% RAP that meet specification requirements. Results also indicate that the addition of RAP leads to reduction in required binder content to achieve 4% air voids content, also a reduction in the value of voids in mineral aggregate, voids filled with binder, and film index. Further, the addition of RAP results in a stiffer mix, and this effect increases with increasing RAP content. Intisar M. J., (2011) concluded that RAP materials are not suitable to be used in cold mix alone as base materials without certain processes or treatment to improve their characteristics.

## 2- OBJECTIVES

The objective of the present paper is to evaluate RAP's role and its effect on; bulk density, stability, flow, volumetric properties and the tensile strength of HMA through experimental investigation.

## 3- MATERIALS AND METHODS OF TESTING

### 3-1 Materials

Materials used in this study are locally available and selected from the currently materials used in roads construction in Iraq.

### 3-1-1 Asphalt Cement

One type of asphalt cement is used, (40-50) Penetration grade from Daurah Refinery. The physical properties for the asphalt cement are presented in **Table 1**.

### 3-1-2 Aggregate

The aggregate used in this work was crushed quartz obtained from Al-Nibaie quarry in Taji, north of Baghdad. This aggregate is widely used in Baghdad city for asphaltic mixes. The coarse and fine aggregates used in this work were sieved and recombined in the proper proportions to meet the wearing course gradation as required by SCRB specification (SCRB, R/9 2003). The gradation for the aggregate is shown in **Table (2)** and **Fig1**. Routine tests were performed on the aggregate to evaluate their physical properties. The results together with the specification limits as set by the SCRB are summarized in **Table (3)**. Tests results show that the chosen aggregate met the SCRB specifications.

### 3-1-3 Mineral Filler

One type of mineral filler is used: ordinary Portland cement was brought from local market. It is thoroughly dry and free from lumps or aggregations of fine particles. The physical properties are shown in **Table (4)**.

### 3-1-4 Recycled Asphalt Pavement (RAP)

Recycled asphalt pavement (RAP) was taken from Bab Al-moadam's road in Baghdad. The top 50 mm of the asphalt layer was removed and gathered from the damaged pavement, which represents the surface layer. The gathered RAP was milled, sieved and recombined in predetermined percent with new aggregate and new asphalt grade (40-50). **Table (5)** represented the physical properties of recycled asphalt pavement used in the study. **Plate (1)** shows samples of Recycled Asphalt pavement.

### 3- 2RAP Variability

In order to minimize the RAP aggregate variability, especially in gradation, the RAP aggregate was milled and sieved on standard sieve and the amount of RAP aggregate retained on each sieve was separated.

### 3-3 Mix Design

The Marshall Mix design method was employed to determine the optimum asphalt content (O.A.C) for the mix with zero RAP percent. The optimum asphalt content for HMA mixture with 0%RAP was found to be 4.9%.

### 3-4 SPECIMENS PREPARATION

New aggregate is heated to a temperature of 175<sup>0</sup>C to 190<sup>0</sup>C, the compaction mold assembly and rammer are cleaned and kept pre-heated to a temperature of 100<sup>0</sup>C to 145<sup>0</sup>C. The bitumen is heated to a temperature of 121<sup>0</sup>C to 138<sup>0</sup>C. In case of mixture with RAP, the RAP is heated in special oven at 120<sup>0</sup>C for 60 minutes, before mixing with new aggregate and new asphalt cement. The mixture of new aggregate and new asphalt cement (40-50) and RAP (in case of preparation the mixture with recycled asphalt pavement) is then placed in mixing bowl and mix rapidly until the new aggregates are thoroughly coated. The mix is placed in standard mold and compacted with number of blows specified on each face.

### 3-5 TEST METHODS

#### 3-5-1 Resistance to Plastic Flow of Asphalt Mixture (Marshall Test Method)

This method covers the measurement of the resistance to plastic flow of cylindrical specimens of bituminous paving mixtures loaded on the lateral surface by means of the Marshall apparatus according to ASTM (D 1559). This method includes preparation of cylindrical specimens which are 4 inch (101.6 mm) in diameter and 2.5 ±0.05 inch (63.5 ±1.27 mm) in height.

The Marshall Mold, spatula, and compaction hammer are heated on a hot plate to a temperature



between (120-150 °C). The asphalt mixture is placed in the preheated mold and it is then spaded vigorously with the heated spatula 15 times around the perimeter and 10 times in the interior.

The temperature of the mixture immediately prior to compaction is between (142-146°C) (ASTM D-1559). Then, 75 blows on the top and bottom of the specimen are applied with a compaction hammer of 4.535 kg sliding weight, and a free fall in 18 inch (457.2 mm). The specimen in mold is left to cool at room temperature for 24 hours and then it is removed from the mold.

Marshall stability and flow tests are performed on each specimen. The cylindrical specimen is placed in water bath at 60 °C for 30 to 40 minutes, and then compressed on the lateral surface at constant rate of 2in/min. (50.8mm/min) until the maximum load (failure) is reached.

The maximum load resistance and the corresponding flow value are recorded. Three specimens for each combination are prepared and the average results are reported.

The bulk specific gravity and density ASTM (D 2726), theoretical (maximum) specific gravity of voidless mixture is determined in accordance with ASTM (D 2041). The percent of air voids is then calculated.

### 3-5-2 Indirect Tensile Strength

Specimens are prepared by Marshall method and tested for indirect tensile strength according to ASTM (D 4123). The prepared specimens are cooled at room temperature for 24 hours, immersed in a water bath at different test temperatures (5, 25, and 40 °C) for 30 minutes, then tested by Versa-Tester using a 1/2 in. (12.5mm) wide curved, stainless steel loading strip on both the top and bottom, running parallel to the axis of the cylindrical specimen which are loaded diametrically at a constant rate of 2 in/min. (50.8 mm/min.) until reaching the ultimate loading resistance. Three specimens for each mix combination are tested and the average results are reported. The indirect tensile strength (I.T.S) is calculated, as follows:

$$I.T.S = 2 P_{ult} / \pi t D \quad (eq.1)$$

where:

$P_{ult}$  = Ultimate load upto failure (N).  $t$  = Thickness of specimen (mm), and  $D$  = Diameter of specimen (mm).

The temperature susceptibility is calculated, as below:

$$TS = [(I.T.S)_{t_0} - (I.T.S)_{t_1}] / (t_1 - t_0) \quad (eq.2)$$

where:

$(I.T.S)_{t_0}$  = Indirect tensile strength at  $t_0$  (°C)  
 $(I.T.S)_{t_1}$  = Indirect tensile strength at  $t_1$  (°C)  $t_0 = 25^\circ\text{C}$ ,  $t_1 = 40^\circ\text{C}$ .

## 4- RESULTS AND DISCUSSION

### 4-1 Marshall Test Results

The results of Marshall Tests show typical relationships between Marshall Properties and control mix (0% RAP), mixes with 5% RAP, 10% RAP and 15% RAP. **Fig (2A)** shows the bulk density values for various mixtures as a function of RAP content. In this Fig, the bulk density increases with the increase in RAP content, this indicates that; with the presence of RAP more dense mixes will be produced as compared with no RAP mixes and this effect appears clearly with the increasing in RAP content. **Fig (2B)** shows the Marshall Stability values. It indicates that, stability values for various mixes follow the typical trend in the presence of RAP. Where, the stability values increase with the increase in RAP content until a maximum value is reached after which stability tends to decrease.

This can be attributed to the increase in the stiffness of asphalt by incorporating more RAP which gives high cohesive strength while maintaining the interlocking between coarse crushed aggregate. The decrease in stability after certain RAP content is due to an increase in the thickness of asphalt film coating the coarse aggregate particles, which lower the internal friction. The decrease in internal friction is also

associated with the increased lubrication, which is believed to be the reason for the continuous increase in Marshall Flow values, as shown in **Fig (2C)**.

**Fig (2D)** shows the relationship between the percent of air voids and RAP content. It can be noticed that percent of air voids decreases with the increase in percent of RAP content. This is an indication that the old asphalt in the RAP aggregate do not act as black rock and the old asphalt in the RAP contributed with new asphalt cement (AC) and result in increasing the asphalt percentage in the produced mix. And this leads to a reduction in percent of air voids for compacted specimen and consequently the bulk density of specimen increases.

**Fig (2E)** shows voids in mineral aggregate (VMA) against RAP content. It can be noticed that percent of (VMA) decreases with the increase of RAP content. This reduction in (% VMA) due to the decrease percent of air voids.

**Fig (2F)** shows the values of voids filled with asphalt (VFA) percent against RAP content. It can be noticed that percent of (VFA) increase with the increase of RAP content, and this is prove that the old binder in the RAP contributed with new asphalt cement and increasing the percentage of asphalt in the mix. The (VFA) values are within the S.C.R.B specified limit (70-85) %.

**Fig (3)** shows the effect of RAP content for various mixes on Marshall Stiffness. Marshall Stiffness is defined as the ratio between the Marshall stability and Marshall Flow. The high Marshall Stiffness (stability /flow) means that asphalt mixture has good resistance to plastic flow resulting from traffic loading when this mix is used in pavement. Also, high value of stability of asphalt mixes does not mean that good resistance of plastic flow can be gained from this mix because high flow value will lead to low Marshall Stiffness. This indicates that, stiffness values for various mixes follow the typical trend in their relation with asphalt content where these values increase with the increase in the percent of RAP

content until a maximum value is reached after which stiffness tends to decrease.

#### 4 -2 Indirect Tensile Strength Test Results

The evaluation of tensile strength for asphaltic concrete mixture used in construction of pavement becomes increasingly more important. This is partially due to the fact that pavements during service will be exposed to various traffic loading and climatic conditions. These conditions may cause tensile stresses to be developed within the pavement, and as a result, two types of cracks may be exhibited: one resulting from traffic loading, called fatigue cracking and the other type of crack resulting from climatic conditions and called thermal or shrinkage cracking. The indirect tensile test IDT has been used to evaluate the mixture resistance to low temperature cracking.

In order to evaluate the mixture resistance to variation in temperatures, three different testing temperatures are used (5°C, 25°C and 40°C), at the selected optimum asphalt content (O.A.C) which are obtained previously.

The mechanical responses for four mixtures at three temperatures (5°C, 25°C and 40°C) during the indirect tensile strength tests are shown in **Fig (4)**. The results indicate that, the presence of recycled asphalt pavement (RAP) in a mixture tends to increase the indirect tensile strength of the mix as compared to a mixture without RAP. This may be related to the hardness of the old asphalt in the RAP as compared to the new asphalt cement (40-50) which result in increasing the viscosity of the mix. The results reveal that the values of IDT strength decreases with increase the temperature of the test. At the highest temperature (40°C), the asphalt mixture is more ductile and has a lower peak tensile strength and the high temperature diminish the difference between the four mixes. At the lowest temperature (5°C), the material is brittle and has a higher peak tensile strength. At 25°C, the mixture exhibits an intermediate response. Test results also confirm the significance of temperature on the mixture indirect tensile strength, since indirect tensile strength increased as temperature decreased.

One may be seen that the IDT strength values did not follow a definitive trend at 5°C with 5% RAP, so the behavior of HMA with low RAP percent (less than 15%) at low temperature, need more laboratory investigation.

**Fig. (5)** shows the values of temperature susceptibility for four mixes. The results indicate that any increasing in RAP percent produce increasing in temperature susceptibility value. This may be related to the fact that the old (aged) asphalt cement in the RAP aggregate changes the physical properties of new asphalt cement (40-50) and make it more susceptible to change in temperature.

## 5- SUMMARY AND CONCLUSIONS

A laboratory study was conducted to evaluate RAP's role and its effect on bulk density, stability, flow, volumetric properties and the tensile strength of HMA using marshall test method and ITS. The HMA were prepared with one source of aggregate, Portland cement and one type of asphalt cement (40-50), containing 0%, 5%, 10%, and 15% of RAP.

Based on the findings of this study, the following conclusions can be put forward:

- 1- Marshall stability increases with the increasing of RAP content until a maximum value is reached after which stability tends to decrease.
- 2- Increasing of the percent of RAP content produces decreasing of air voids and VMA. This increasing in RAP would produce an increase in bulk density, flow and VFA with the same increment in RAP content.
- 3- Stiffness of mixes increase with the increasing of the percentage of RAP until a certain value is reached and it then tends to decrease.
- 4- The inclusions of RAP into HMA mixtures (in general) increases the tensile strength, while the values of ITS are decreased with the increasing of temperature test.

- 5- The results indicate that increasing in RAP content produces an increasing in temperature susceptibility.
- 6- Results of marshall properties indicate that the amount of new binder in the RAP mixture can be reduced without any effect on the quality of the produced mixes.
- 7- Finally and based on the tests results, it appeared that 5% of RAP can be recognized as optimal percentage to be added to the HMA of wearing course layer for local pavement within the study limitation. Keeping in mind comprehensive lab and field tests need to be carried out to confirm or revise the mentioned percentage.

## REFERENCES

- "ASTM", (1988), Annual Book of ASTM Standards, Section 4, Volume 04.03, American Society for Testing and Materials, Philadelphia, USA.
- Apeagyei A, Diefenderfer B, and Diefenderfer K., (2011). "Rutting Resistance of Asphalt Concrete Mixtures That Contain Recycled Asphalt Pavement." Journal of the Transportation Research Board, No. 2208, pp. 9-16.
- ASTM, (2000), "Road and Paving Materials", Annual Book of ASTM Standards, Volume 04.03, American Society for Testing and Materials, Philadelphia, USA.
- Behnia B., Dave E., Ahmed S., Buttlar W. and Reis H., (2011). ". "Effects of Recycled Asphalt Pavement Amounts on Low-Temperature Cracking Performance of Asphalt Mixtures Using Acoustic Emissions." Journal of the Transportation Research Board, No. 2208, pp. 64-71.
- Daniel J. and Lachance A., (2005). "Mechanistic and Volumetric Properties of Asphalt Mixtures with Recycled Asphalt Pavement." Journal of the Transportation Research Board, No. 1929, pp. 28-36.





- Intisar M. J. Al-Aakaily,(2011),"Design and Management of Recycled Flexible Pavement in Iraq.",M.Sc.Thesis, Al-Mustansiriya University
- .SCRB/R9, (2003), "General Specification for Roads and Bridges", Section R/9, Hot-Mix Asphalt Concrete Pavement, Revised Edition. State Corporation of Roads and Bridges, Ministry of Housing and Construction, Republic of Iraq.
- Shu X., Huang B and Vukosavljevic D., (2008). "Laboratory evaluation of fatigue characteristics of recycled asphalt mixture." Journal of Construction and Building Materials, Vol. 22, pp. 1323-1330.
- Tran B. and Hassan R., (2011). "Performance of Hot-Mix Asphalt Containing Recycled Asphalt Pavement."Journal of the Transportation Research Board, No. 2205, pp. 121–129.
- Valdés G., Pérez-Jiménez F, MiróR, Martnez A .and, Botella R., (2011). "Experimental study of recycled asphalt mixtures with high percentages of reclaimed asphalt pavement (RAP)." Journal of Construction and Building Materials,Vol.25,pp.1289–1297.

**Table (1): Physical Properties of Asphalt Cement.**

Property	ASTM Designation (ASTM,2000)	Penetration Grade 40-50	
		Test Results	SCRB <sup>(*)</sup> Specification
1-Penetration at 25°C,100 gm,5 sec, (0.1mm)	D-5	41	40-50
2- Softening Point, (°C)	D-36	50	.....
3-Ductility at 25 °C, 5cm/min,( cm)	D-113	>100	>100
4-Flash Point, (°C)	D-92	288	Min.232
5-Specific Gravity	D-70	1.041	.....
6- Residue from thin film oven test	D-1754		
- Retained penetration,% of original	D-5	60	55+
- Ductility at 25°C , 5cm/min,(cm)	D-113	80	25 <sup>+</sup>

(\*): State Commission of Roads and Bridges

**Table (2): Combined Gradation of Aggregate and Mineral Filler.**

Sieve Size	Sieve Opening (mm)	Percentage Passing by Weight of Total Aggregate	
		Surface or Wearing Course	
		Specification Limit (SCRB)	Selected Gradation
3/4"	19	100	100
1/2"	12.5	90-100	96
3/8"	9.5	76-90	82
No.4	4.75	44-74	56
No.8	2.36	28-58	36
No.50	0.3	5-21	12
No.200	0.075	4-10	6

**Table (3): Physical Properties of Aggregate**

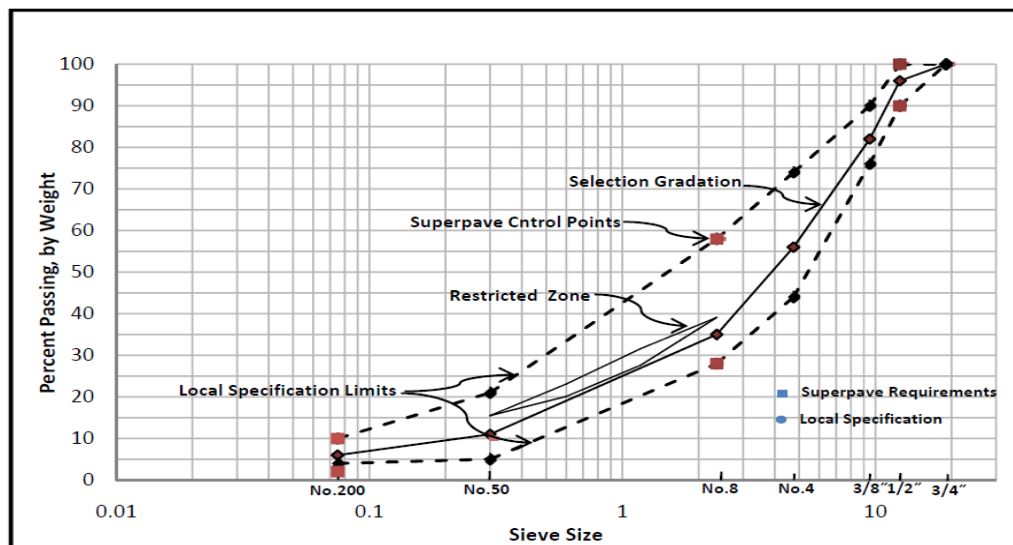
Property	ASTM designation	Test results	SCRB specification
<u>Coarse aggregate</u>			
1. Bulk specific gravity	C-127	2.611	.....
2. Apparent specific gravity		2.687	.....
3. Water absorption,%		0.447	.....
4. Percent wear by Los Angeles abrasion ,%	C-131	19.0	30 Max
5. Soundness loss by sodium sulfate solution,%	C-88	3.2	10 Max
6. Fractured pieces, %		96	95 Min
<u>Fine aggregate</u>			
1. Bulk specific gravity	C-127	2.62	.....
2. Apparent specific gravity		2.69	.....
3. Water absorption,%		0.720	.....
4. Sand equivalent,%	D-2419	55	45 Min.

**Table (4): Physical Properties of Mineral Filler.**

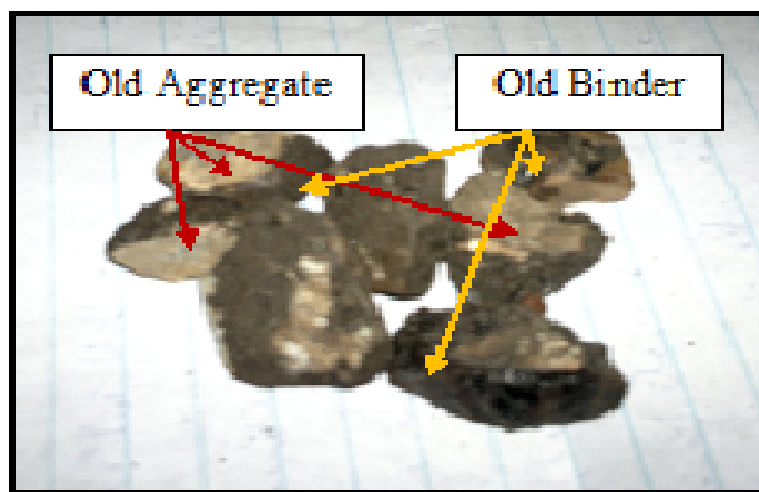
Property	Test results
% Passing Sieve No. 200	100
Specific Gravity	3.13

**Table (5): Physical Properties of Recycled Asphalt Pavement.**

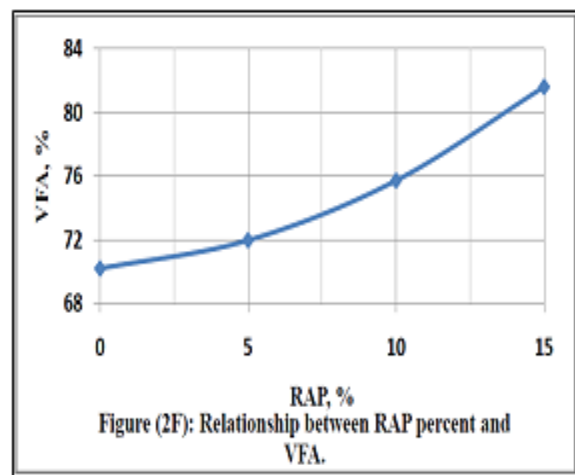
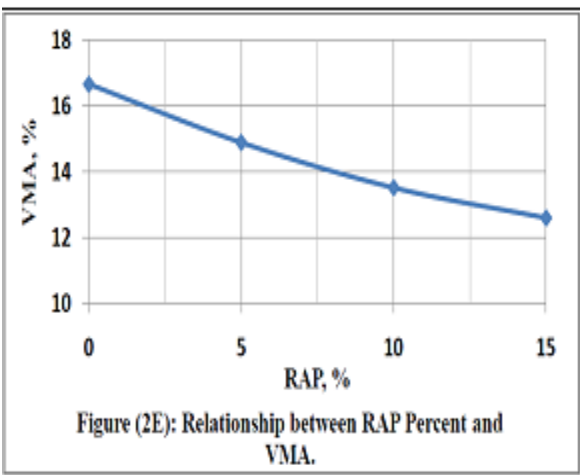
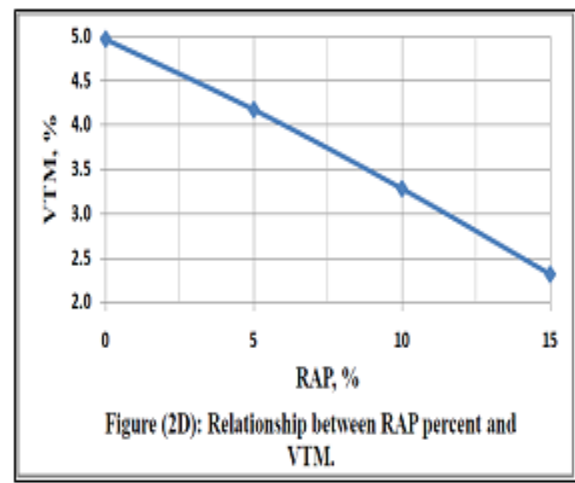
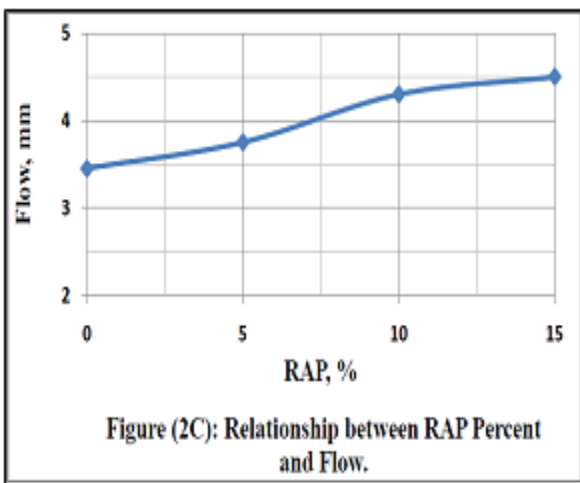
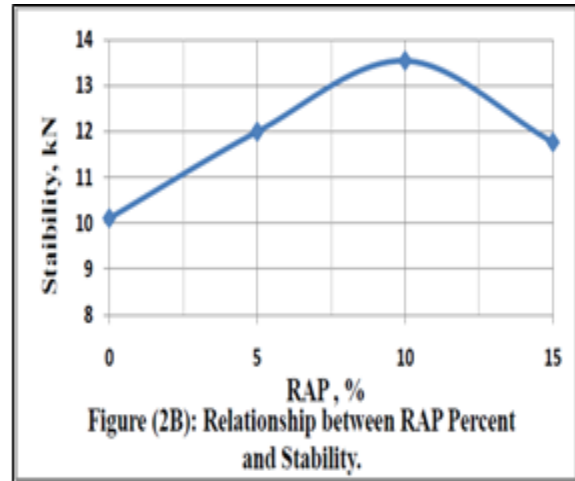
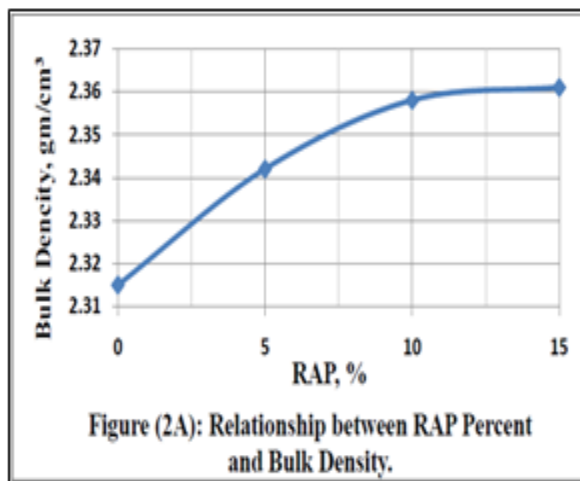
Test Method	ASTM designation	Coarse RAP	Fine RAP
Bulk specific gravity	C- 127& C- 128	2.311	2.078
water absorption, %	C- 127& C- 128	3.811	7.981



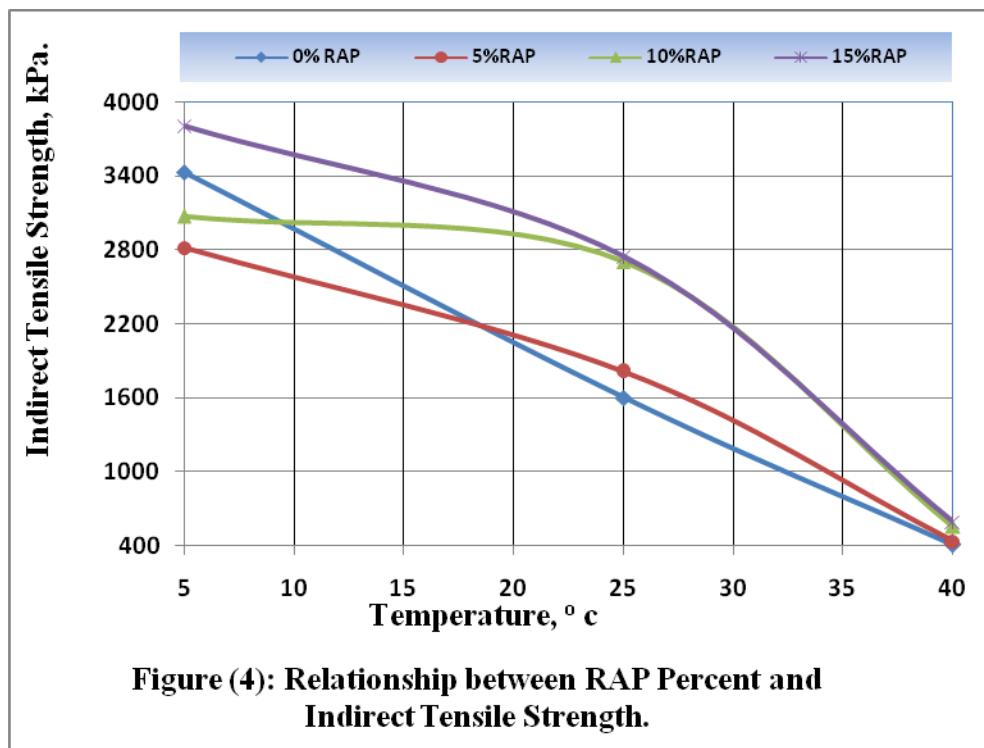
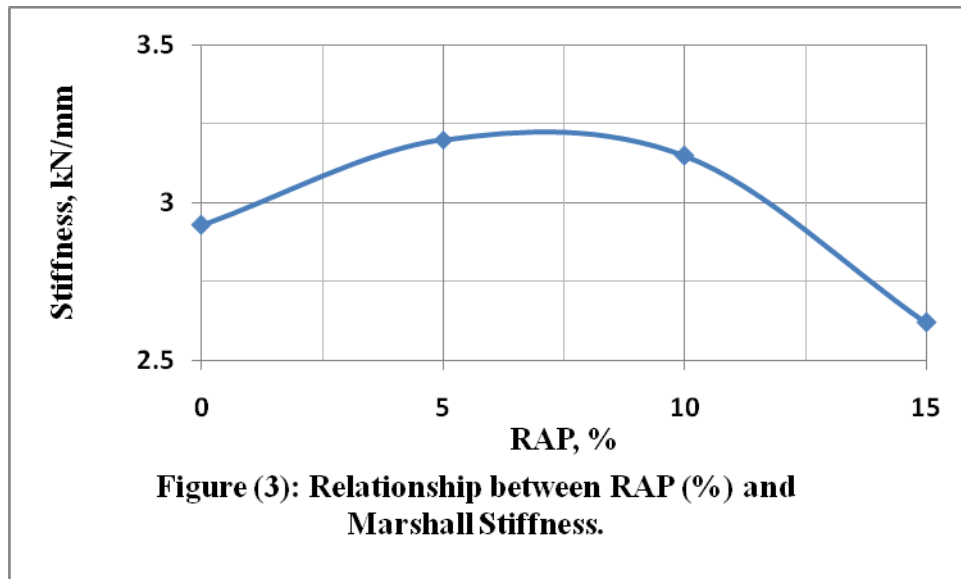
**Fig (1): Aggregate Gradation Curve.**



**Plate (1): Samples of Recycled Asphalt Pavement (RAP).**



**Fig (2): Effect of RAP (%) on Marshall Properties.**



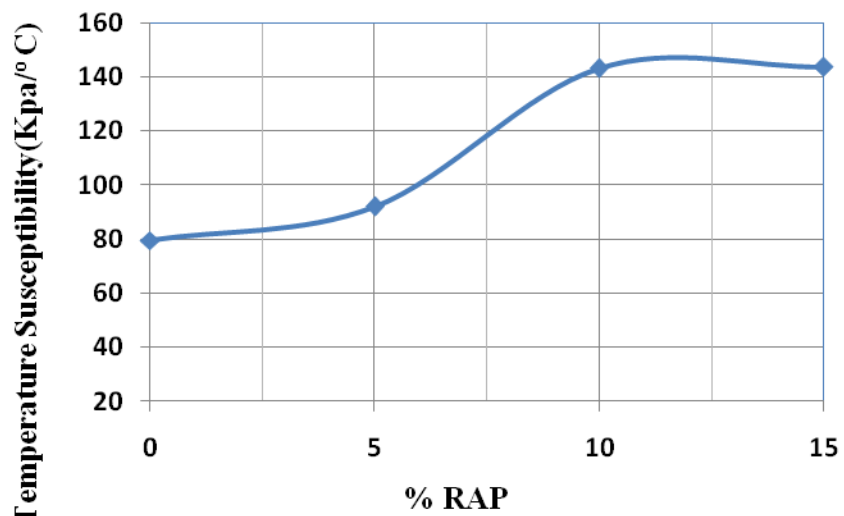


**Figure (5): Relationship between RAP (%) and Temperature Susceptibility.**

## The use of Prepared Zeolite Y from Iraqi kaolin for Fluid Catalytic Cracking of Vacuum Gas Oil

Abdul Halim Abdul Karim Mohammed

imahalim2005@yahoo.com

Ibtehal Kareem Shakir

ibtehal\_27@yahoo.com

Karim Khalifa Esgair\*

[karimkhalifa70@yahoo.com](mailto:karimkhalifa70@yahoo.com)

Chemical Engineering Department, College of Engineering, Baghdad University

\*Foundation of Technical Education.

### ABSTRACT

The faujasite type Y zeolite catalyst was prepared from locally available kaolin. For prepared faujasite type NaY zeolite X-ray, FT-IR, BET pore volume and surface area, and silica/ alumina were determined. The X-ray and FT-IR show the compatibility of prepared catalyst with the general structure of standard zeolite Y. BET test shows that the surface area and pore volume of prepared catalyst were 360 m<sup>2</sup>/g and 0.39 cm<sup>3</sup>/g respectively.

The prepared faujasite type NaY zeolite modified by exchanging sodium ion with ammonium ion using ammonium nitrate and then ammonium ion converted to hydrogen ion. The maximum sodium ion exchange with ammonium ion was 53.6%.

The catalytic activity of prepared faujasite type NaY, NaNH<sub>4</sub>Y and NaHY zeolites was investigated by using the experimental laboratory plant scale of fluidized bed reactor. The cracking process was carried out in the temperature range 440 to 500 °C, weight hourly space velocity (WHSV) range 10 to 25 h<sup>-1</sup>, and atmospheric pressure. The catalytic activities of the prepared faujasite type NaY, NaNH<sub>4</sub>Y and NaHY zeolites were determined in terms of vacuum gas oil (VGO) conversion, and gasoline yield. The conversion at 500°C and WHSV10 hr<sup>-1</sup> by using faujasite type NaY, NaNH<sub>4</sub>Y and NaHY zeolite were 50.2%, 64.1% and 69.5wt% respectively. The gasoline yield using the same operating conditions were 24.8%, 30.5% and 36.8wt% respectively.

**Keywords :** Fluid catalytic cracking ; gasoline production ; vacuum gasoil cracking

### استخدام الزيولايت من نوع Y المحضر من الكاولين العراقي لعملية التكسير الحفازي المائع لمادة زيت الغاز الفراغي

د. عبد الحليم عبد الكريم محمد ، د. ابتهاش كريم شاكر ، د. كريم خليفة أزغير

#### الخلاصة

تم تحضير العامل المساعد الفلوجيسايت نوع Y زيولايت من الكاولين المتوفر محليا. اجريت تحاليل الاشعة السينية ، والاشعة تحت الحمراء ، والمساحة السطحية و الحجم المسامي ، وتحليل نسبة السليكا الى الالومينا للعامل المساعد فلوجيسايت نوع NaY زيولايت. اظهرت تحليلي الاشعة السينية ، والاشعة تحت الحمراء توافق العامل المساعد المحضر مع التركيب العام للزيولايت القياسي و كانت المساحة السطحية 360 م<sup>2</sup>/غم والحجم المسامي 0.39 سم<sup>3</sup>/غم .

طور العامل المساعد المحضر فلوجيسايت نوع NaY زيولايت و ذلك باستبدال ايون الصوديوم بايون الامونيوم باستعمال نترات الامونيوم ومن ثم جرى تحويل ايون الامونيوم الى ايون الهيدروجين . كانت اعلى نسبة استبدال لايون الصوديوم 53.6% .

درست الفعالية الحفازية للفلوجيسايت بصيغة الصوديوم NaY ، و صيغة الامونيوم NaNH<sub>4</sub>Y و صيغة الهيدروجين NaHY زيولايت باستخدام وحدة تجريبية بحدود درجات الحرارة بين 440 – 500 °C وسرعة فراغية بين 10 – 25 سا<sup>-1</sup> .

تم تعيين الفعالية الحفازية للفلوجيسايت بصيغة الصوديوم NaY ، و صيغة الامونيوم NaNH<sub>4</sub>Y و صيغة الهيدروجين NaHY زيولايت بصيغة تحويل المتفاعلات الى مختلف النواتج ونسبة الكازولين الناتج . لقد كانت نسبة تحويل المتفاعلات الى نواتج عند درجة حرارة 500 °C وسرعة فراغية 10 سا<sup>-1</sup> 50.2% و 64.1% و 69.5% على التوالي. وان انتاجية الكازولين لنفس الظروف التشغيلية كانت 24.8% و 30.5% و 36.8% على التوالي .

**الكلمات الرئيسية :** التكسير الحفازي المائع ، انتاج الكازولين ، تكسير زيت الغاز الفراغي .



## INTRODUCTION

Catalysis by zeolites—with focus on hydrocarbon conversion and formation—covers nowadays a broad range of processes related to the upgrading of crude oil and natural gas. This includes, among others, fluid catalytic cracking (FCC), hydrocracking, dewaxing, aliphatic alkylation, isomerisation, oligomerisation, transformation of aromatics, transalkylation, hydrodecyclisation as well as the conversion of methanol to hydrocarbons. All these conversions are catalysed by zeolites or related microporous materials, based both on the acid properties and shape-selective behaviour of this type of materials (Michael Stocker, 2005).

A number of different FCC catalysts exist and catalyst changes in the worldwide about 350 refinery FCC units are made often, depending on the feedstock type and quality available (Ballmoos, et al 1997).

The FCC process produces about 45% of the total gasoline pool either directly or indirectly (Reza Sadeghbeigi, 2000). With the introduction of zeolite (faujasite type) containing cracking catalysts in 1962, replacing the amorphous silica–alumina, a tremendous change concerning FCC technology took place. Zeolite containing catalysts are much more active, show higher gasoline yield performances and produce less coke than the amorphous silica–alumina based catalysts, resulting in higher feedstock conversions and severities as well as enhanced economic benefits of the process ( Corma, et al 2002). The actual FCC technology involves the formulation of proprietary multifunctional cracking catalysts, consisting of different amorphous (catalytically active macroporous matrix, clay type binder) and crystalline acid

functions zeolites like Y-type zeolite containing mesopores due to dealumination

forming the ultra-stable Y zeolite—USY), and a series of additives for metal passivation (mainly V and Ni), sulfur removal, promoters for total combustion and octane enhancing additives ( Corma, et 2002). The matrix plays a critical role in the selective cracking of the (high molecular) bottoms fractions when residue containing feedstocks are processed. The unique pore architecture of Y zeolite is ideal for cracking gas oil components into gasoline molecules. Moreover, it has been observed that the activity of the Y zeolite for gas oil cracking has a maximum for a Si/Al ratio of 5–8, corresponds to a unit cell size (UCS) 2.436– 2.440 nm. This clearly indicates that gas oil cracking requires the presence of strong Brønsted acid sites. Unfortunately, so far it has not been possible to prepare Y zeolite with a framework Si/Al ratio above 4 by direct synthesis. Therefore, highly dealuminated zeolites have to be prepared by dealumination of commercially prepared Y zeolite samples with Si/Al ratios in the range of 2.6. ( Corma, et al 1988).

In this respect, Y zeolites dealuminated by steaming (USY) create a secondary porosity formed during the partial destruction of the zeolite framework and forming mesopores which facilitate diffusion of larger molecules into the zeolitic channels. The obtained USY type zeolites show, in addition, a much better hydrothermal stability, which is a prerequisite of the application as FCC catalyst (Sie et al, 1994). Due to the pore architecture, ZSM-5 increases the octane number of the gasoline by selectively upgrading low octane gasoline components into lower molecular weight compounds with a higher octane number. The concept of using ZSM-5 as co-catalyst to modify the performance of a generic FCC catalyst system can significantly increase the product flexibility in the FCC unit ( Ward, et al 1990).

The present work is aimed to prepare Y zeolite from Iraqi kaolin and study the characteristics and activity of prepared catalyst.

## EXPERIMENTAL

### Kaolin

The Kaolin used is available in Al-Dewekhala Quarry in Al-Enbar region. It is supplied from State Company of Geological Surveying and Mining. Table 1 shows the chemical analysis of this material as determined by State Company of Geological Surveying and Mining.

**Table 1: Chemical analysis of local kaolin**

Component	Weight %
SiO <sub>2</sub>	53.21
Al <sub>2</sub> O <sub>3</sub>	32.13
Fe <sub>2</sub> O <sub>3</sub>	1.41
K <sub>2</sub> O	0.35
Na <sub>2</sub> O	0.21
MgO	0.13
CaO	0.15
TiO <sub>2</sub>	0.41
L.O.I	12.00

LOI = Loss on Ignition

## CATALYST PREPARATION

### Preparation of faujasite type NaY zeolite catalyst

The catalyst is prepared by steps consisting of:

1. Kaolin was finely divided to a particle size < 75 µm
2. Sodium hydroxide solution was prepared at concentration 45% wt and mixed with kaolin at weight ratio  $\left(\frac{\text{Kaolin}}{\text{pureNaOH}} = \frac{1}{1.5}\right)$ .
3. The mixture in step 2 calcines at 850 °C for three hours in a programmable electrical furnace .The resultant from this step called fused kaolin
4. Fused kaolin was sieved to particle size < 75 µm.
5. Fifty grams of fused kaolin powder and 63.35 grams of sodium silicate were dispersed in 750 ml of deionized water in a 1000 ml flask with two necks, one neck connected with water cooling reflux condenser and the other neck with thermometer. Agitation speed and flask temperature were kept constant using regulator attached with electrical

magnetic stirrer. The gel formation step was achieved at temperature 60 °C and atmospheric pressure during 1 hr .

6. The resultant slurry which has pH 13.6 was placed in 1000ml sealed glass jar, and subjected to aging at 50 °C for 24 hr in a programmable electrical furnace, then the gel slurry was subjected to hydrothermal crystallization at 100 °C for 48 hr in the same furnace .
7. The resultant precipitate was separated from the mother liquor by filtration using a Buckner funnel with the aid of a vacuum source. The crystalline mass is then washed with deionized water until a pH of 11.5. The drying of crystalline mass was achieved at 100 °C for 16 hr using a programmable electrical furnace The dried powder was activated by calcination in a programmable electrical furnace at 500 °C for 1hr.

### Ammonium - Zeolite Preparation

Ammonium - form catalyst was prepared by ion exchange method of the prepared catalyst NaY zeolite with 1.0 M ammonium nitrite solution . Thus 100 g NaY zeolite was mixed with 600g of NH<sub>4</sub>NO<sub>3</sub> solution at 80 °C for 6 hr under stirring. This operation was followed by filtration using a Buckner funnel and washing with deionized water until no nitrate ions were detected. The produced ammonium zeolite sample was dried at 90 °C for 2 hr then at 120 °C for 6 hr using a programmable electrical furnace .

## HYDROGEN -ZEOLITE PREPARATION

Hydrogen -form catalyst prepared by calcinations NH<sub>4</sub>-Y at 600 °C for 6 hr. During calcination ammonia and water are liberated and decationized H-form catalyst is formed.

## ANALYSIS AND CHARACTERIZATION

X- Ray diffraction analysis was done in the Research Center of Chemistry and Petrochemical – Ministry of Science and Technology. Analysis was carried out using X- Ray diffractometer type Shimadzu SRD 6000.

The chemical analysis of silica and alumina of prepared calcined powdered faujasite type NaY

**Abdul Halim Abdul Karim Mohammed**  
**Ibtehal Kareem Shakir**  
**Karim Khalifa Esgair**

zeolite was achieved in The State Company for Geological Survey and Mining.

The sodium content of prepared calcined powdered faujasite type NaY zeolite before and after ammonium ion exchange was determined using digital flame analyzer by flame photometer Gallen Kamp in The State Company for Geological Survey and Mining. Sodium is commonly reported as the weight percent of sodium oxide ( $\text{Na}_2\text{O}$ ) on the catalyst.

The Infrared Fourier Transform Spectroscopy (FT-IR) test was done to investigate the synthesized zeolite structure. This test was achieved at University of Baghdad/ College of Science/ Chemical Laboratory, by the device of Shimadzu FTIR 8400S type.

Catalyst surface area was determined using BET method by Thermo Finnegan type, apparatus located at Oil Development and Research Center, Ministry of Oil .

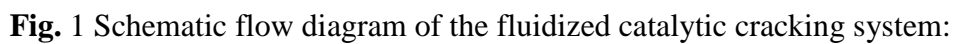
#### **CATALYTIC ACTIVITIES TEST**

The catalytic activities of prepared zeolites NaY,  $\text{NH}_4\text{Y}$  and HY were investigated by using experimental laboratory plant scale of fluidized bed reactor shown in figure 1. The FCC

#### **The use of Prepared Zeolite Y from Iraqi kaolin for Fluid Catalytic Cracking of Vacuum Gas Oil**

experiments were carried out at temperature range 440 to 500 °C, WHSV range 10 to 25h<sup>-1</sup>, and atmospheric pressure using prepared catalyst NaY form,  $\text{NH}_4\text{Y}$  form, and NaH form with particle size between 75 to 150 micrometer.

The effect of catalyst regeneration temperature at temperature 600, 650, 700, and 750°C on equilibrium catalyst activity was carried out at 500 °C, WHSV=10h<sup>-1</sup>, and atmospheric pressure using NaH form catalyst.



1260

## RESULTS AND DISCUSSION

### Characterization of Prepared Catalysts

#### 1. X-ray Powder Diffraction (XRD)

X-ray Powder Diffraction technique is the best method to define the crystallographic structure of zeolite. Each zeolite has their own specific pattern that can be used as references for the determination of solid crystal phase and it is used as fingerprint for every zeolite. This technique can signify whether the solid sample is amorphous or crystalline phase, the degree of crystallinity and identification of phase present. The purity of solid crystal will be measured by comparing the X-ray diffractogram pattern of sample with X-ray diffractogram pattern of standard that can be obtained from International Zeolite Association (West, 1988). The powder X-ray diffraction pattern of the prepared calcined powdered faujasite type NaY zeolite is shown in Figure 2, while Figure 3 shows the standard zeolite Y X-ray analysis with silica to alumina ratio of five. From these Figures, it can be seen that the prepared zeolite in the

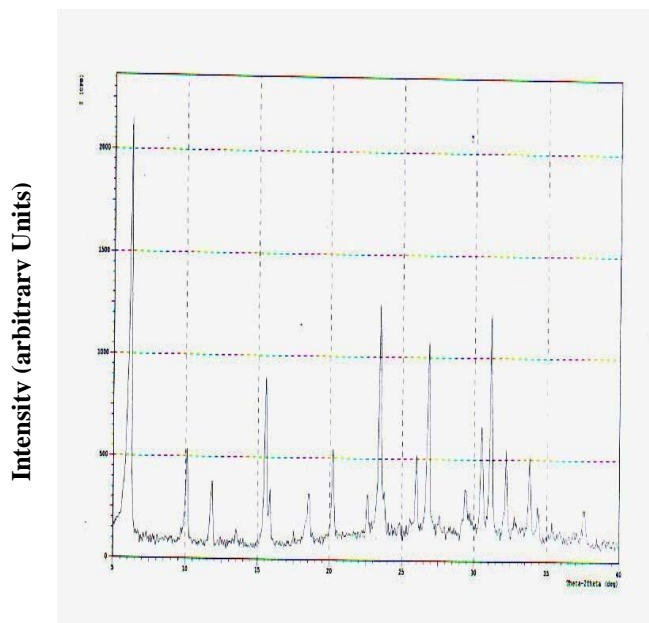


**Fig. 2** X – Ray diffraction Spectrum for the Prepared faujasite type Y zeolite Catalysts

### The use of Prepared Zeolite Y from Iraqi kaolin for Fluid Catalytic Cracking of Vacuum Gas Oil

present work, is approximately comparable with the standard.

The presence or absence of some peaks of the diffractogram indicates the existence of other crystal phase or zeolite contaminated with other phases. The size and shape of unit cell for any crystal are easily determined by using the diffraction of the X-rays.

Some differences are found among the X-ray diffraction data which can be attributed to the distribution of sodium cation, different in silica to alumina mole ratio, and different in a mode of preparation.

A comparison between lattice spacing of prepared calcined powdered faujasite type NaY zeolite with standard synthesis faujasite –Na is illustrated in table 2. It can be noted from this table that the lattice spacing of prepared faujasite-Na sample gave similar lattice spacing of standard synthesis faujasite –Na.

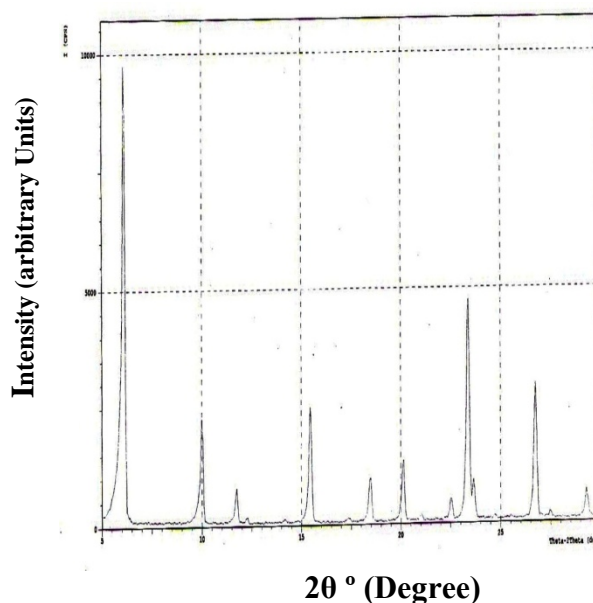


**Fig. 3.** X – Ray diffraction Spectrum for the standard zeolite Y (Treacy et al, 1996).



**Table.2:** Comparison of lattice spacing, between prepared faujasite -Na and standard synthesis faujasite -Na.

prepared faujasite-Na		Standard synthesis faujasite -Na(ICDD, 2009)	
Angle(2-Theta)deg.	d,spacing (Å)	Angle (2-Theta)deg	d,spacing (Å)
6.1042	14.46736	6.181	14.3000
18.5855	4.77028	18.562	4.78000
26.8497	3.31783	26.845	3.32100
32.7971	2.72849	32.817	2.72900
37.5824	2.39134	37.618	2.39100

## 2.FOURIER TRANSFORMS INFRA RED SPECTROSCOPY (FTIR)

FT-IR spectroscopy is used to probe the structure of zeolites and monitor reactions in zeolite pores. Figure 4 shows the FT-IR spectra of prepared calcined powdered faujasite type NaY zeolite. This figure shows that the FT-IR spectra are compatible with categories of zeolites. The double ring opening vibration at  $566\text{ cm}^{-1}$  in the FT-IR spectrum of NaY zeolite is characteristic of faujasite zeolites ( Zhan et al,2002)

The T-O bending vibrations of internal tetrahedra in NaY can be identified by absorption bands around  $500$ ,  $466$  and  $450\text{ cm}^{-1}$  ( Karge,1998). These absorption bands characterizing T-O bending vibrations can be shifted to lower frequencies with decreasing Si/Al ratio in the internal linkages due to the different length of the Al-O ( $1.73\text{ Å}$ ) and Si-O ( $1.62\text{ Å}$ )

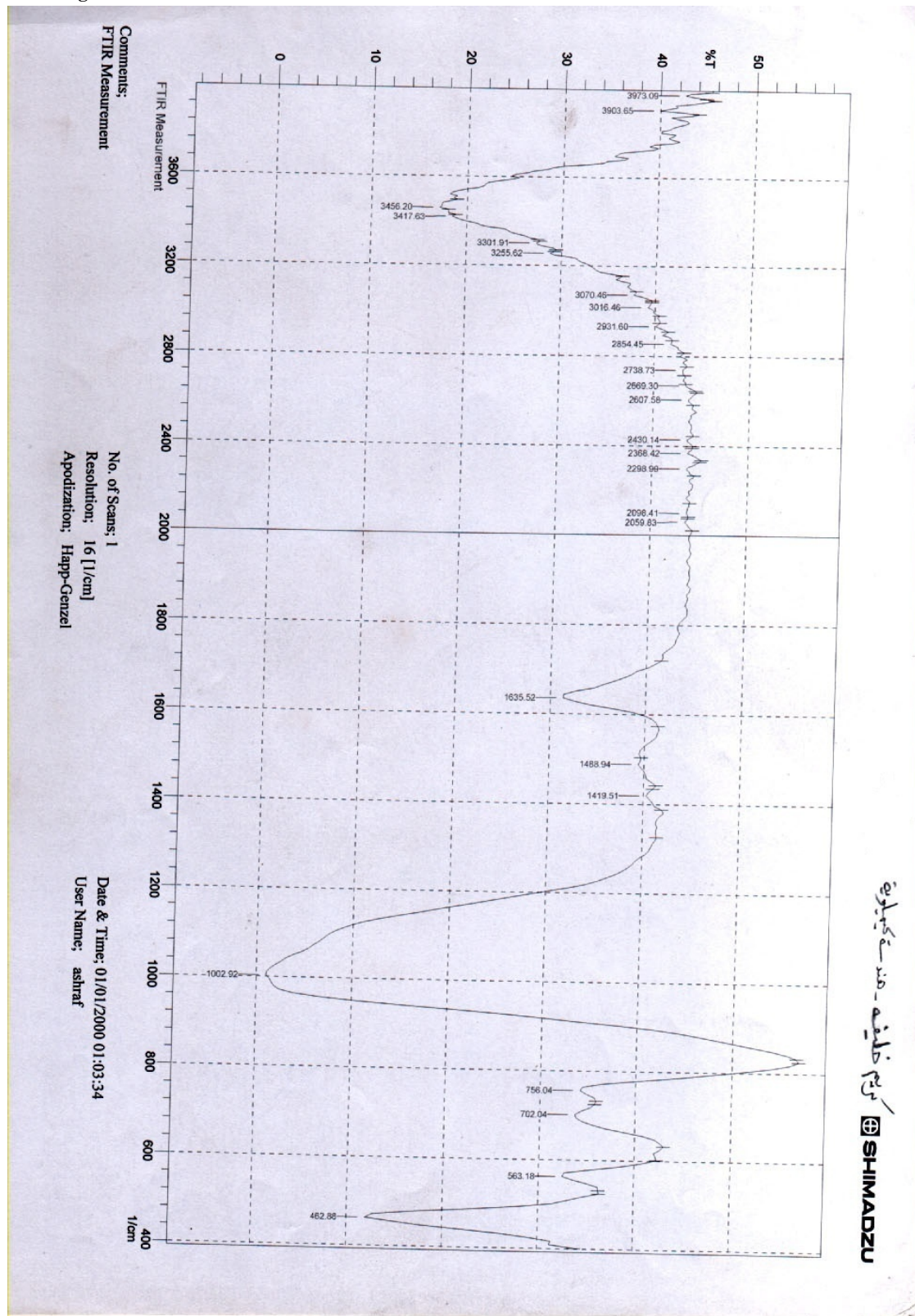
bonds. Three absorptions are observed in the spectral region between  $3765$  and  $3630\text{ cm}^{-1}$ . The most intense and highest frequency band at  $3744\text{ cm}^{-1}$  is assigned to terminal silanol groups that are on the external surface of the zeolite crystals ( Jentys et al, 2001).

The absorption band at  $3695\text{ cm}^{-1}$  is assigned to hydroxyl groups attached to  $\text{Na}^+$  [15]( Fritz et al,1989). An absorption band at  $3656\text{ cm}^{-1}$ , associated with hydroxyl groups attached to extra framework alumina (EFAL) species. In the O-H stretching region, infrared spectra of zeolites provide a wealth of information on hydroxyl groups attached to zeolite structures. The hydroxyl groups are important for the chemistry of zeolite materials ( Khabtou et al,1994).

At least five types of hydroxyl groups are present in zeolite Y, including (i) lattice termination silanol groups ( $\sim 3745\text{ cm}^{-1}$ ), (ii) hydroxyl groups occurring at defect sites, i.e. hydroxyl nests ( $\sim 3720\text{ cm}^{-1}$ ), (iii) OH groups attached to cations which compensate the negative charge of the framework ( $\sim 3695\text{ cm}^{-1}$ ), (iv) OH groups attached to extra framework aluminum (EFAL) species ( $\sim 3655\text{ cm}^{-1}$ ), and (v) for zeolite Y in the H-form, the bridging OH groups with Bronsted acidity ( $\sim 3630$  and  $3560\text{ cm}^{-1}$ ).

The bands at  $1135$  and  $725\text{ cm}^{-1}$  assigned to the asymmetric and symmetric stretching modes of internal tetrahedra, respectively. The bands at  $1020$  and  $792\text{ cm}^{-1}$  are associated with the asymmetric and symmetric stretching modes of external linkages (Szostak, 2001).





Wavenumber  $\text{cm}^{-1}$

Fig. 4. FT-IR spectra of faujasite type Y zeolite

The catalytic performance of the zeolite is strongly affected by its composition and structural characteristics, such as framework  $\text{SiO}_2/\text{Al}_2\text{O}_3$  ratio and unit cell size.

Table 3 shows the effect of additional silica source on the silica to alumina mole ratio of prepared zeolite

**Table 3:** Silica / alumina Ratio of prepared zeolite

No.	Additional source	$\text{SiO}_2$ (wt%)	$\text{Al}_2\text{O}_3$ (wt%)	$\text{SiO}_2/\text{Al}_2\text{O}_3$ mole ratio
1	Na meta silicate	45.96	23.93	3.27
2	Sodium silicate	55.14	24.35	3.85

The above results show that the silica to alumina ratio of prepared samples was affected by type of additional silica source in the mixing step, when using sodium metasilicate as additional silica source gave silica to alumina ratio 3.27 sample 1. While Sample 2 shows higher ratio than sample 1, this may be due to using sodium silicate as additional silica source. One of the important zeolite characterizing items is the silica to alumina ratio, and according to this ratio sodium silicate which gives silica to alumina 3.85 was selected as additional silica source for further preparation of catalyst used in this investigation.

The obtained silica-to-alumina ratio 3.85 ( $\text{Si}/\text{Al}=1.925$ ) of prepared calcined powdered faujasite type NaY zeolite was in a good agreement with those results obtained by Break (Break,1974). Chandrasekhar et al, (Chandrasekhar, 1999), and Zhu et al ( Zhu et al, 1999). They recorded that the silica to alumina ratio of zeolite X is 2 to 3 ( $\text{Si}/\text{Al}=1$  to 1.5) ,

while for zeolite Y this ratio higher than 3 to 6 ( $\text{Si}/\text{Al}=1.5$  to 3) .

Zeolite silica-to-alumina ratio and cationic exchange form have the most significant influence on its thermal and hydrothermal stability. An increase in framework  $\text{SiO}_2/\text{Al}_2\text{O}_3$ , ratio increases zeolite stability, provided a minimum number of vacancies left in the framework as a result of dealumination. It is for that reason the thermal and hydrothermal stability increase in the order  $X < Y < \text{HSY}$  zeolites. Since an increase in framework  $\text{SiO}_2/\text{Al}_2\text{O}_3$  ratio is associated with a corresponding decrease in unit cell size, zeolite stability increases with decreasing unit cell size (Scherzer, 1991) .

#### 4. UNIT CELL SIZE (UCS).

The elementary building block of the zeolite crystal is a unit cell. The UCS is the distance between the repeating cells in the zeolite structure.

The UCS of the prepared calcined powdered faujasite type NaY zeolite was calculated from figure 5, and the result was 24.73 Å.

This result is in agreement with results published by Beck (Break,1974), who recorded that for synthesized powdered zeolite Y in sodium form has a unit cell size from 24.6 to 25 Å .Also this result is in agreement with those results published by Reza (Reza Sadeghbeigi, 2000), who recorded that freshly manufactured NaY zeolite has a UCS in the range of 24.50 Å to 24.75 Å.

The UCS is an indicator of zeolite acidity. The decrease in UCS causes farther apart of acid sites. The strength of the acid sites is determined by the extent of their isolation from the neighboring acid sites.



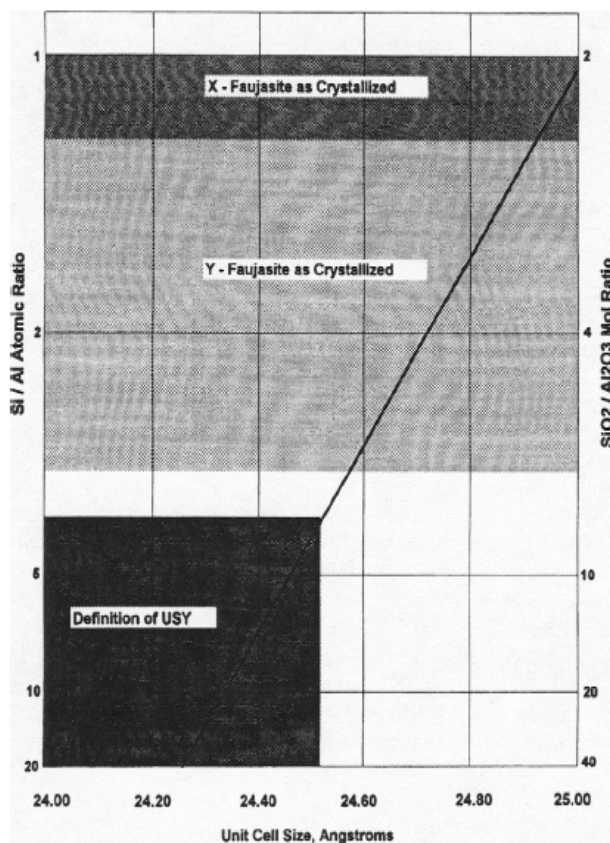


Fig. 5 Silica-alumina ratio versus zeolite unit cell size (Reza Sadeghbeigi, 2000).

Acid distribution of the zeolite is a fundamental factor affecting zeolite activity and selectivity. The UCS measurement can be used to indicate octane potential of the zeolite. A lower UCS presents fewer active sites per unit cell. The fewer acid sites are farther apart and, therefore, inhibit hydrogen transfer reactions, which in turn increase gasoline octane as well as the production of  $C_3$  and lighter components. The octane increase is due to a higher concentration of olefins in the gasoline (Pine et al, 1984).

The number of aluminum atoms per unit cell ( $N_{Al}$ ) can be calculated by equation (1) (Break,1974):

$$N_{Al} = 192 / (1 + R) \quad (1)$$

Where,  $R = N_{Si} / N_{Al}$

The number of aluminum atoms per unit cell of the prepared calcined powdered faujasite type NaY zeolite calculated from equation 2 was equal to 66. This value within the range given by

## The use of Prepared Zeolite Y from Iraqi kaolin for Fluid Catalytic Cracking of Vacuum Gas Oil

Beck (Break,1974), where the number of aluminum atoms per unit cell for zeolite X vary from 96 to 77 and from 76 to 48 for zeolite Y.

### 5. SURFACE AREA

The measured specific surface area and pore volume of the prepared powdered faujasite type NaY zeolite were  $360 \text{ m}^2/\text{g}$  and  $0.39 \text{ cm}^3/\text{g}$  respectively. Such a high surface area is obvious due to the micro porosity of prepared powdered zeolite.

This result is in agreement with the results published by Auerbach et al. (Auerbach et al, 2003).

They recorded that the internal surface of zeolite is highly accessible and can compose more than 98% of the total surface area, and the surface areas are typically of the order of  $300\text{--}700 \text{ m}^2/\text{g}$ .

### 6. SODIUM CONTENT

The Sodium content of prepared calcined powdered faujasite type NaY zeolite was 12.5 wt%. This result is in agreement with the result published by Reza (Reza Sadeghbeigi, 2000). and Jones (Jones, et al 2006). They recorded that a typical NaY zeolite contain approximately 13wt%  $\text{Na}_2\text{O}$ . The sodium on the catalyst originates either from zeolite during its manufacture or from the FCC feedstock, and the sodium content of the zeolite should be minimized for two reasons. First high sodium content is detrimental to zeolite stability, and activity. Sodium decreases the hydrothermal stability of the zeolite. It also reacts with the zeolite acid sites to reduce catalyst activity (Suchuchchai Nuanklai, 2004). Second, high sodium content decreases the gasoline octane number, because the sodium is mobile in the regenerator. Sodium ions tend to neutralize the strongest acid sites, and can have an adverse effect on the gasoline octane. The loss of octane is attributed to the drop in the number of strong acid sites. (Hayward et al 1990).

Sodium content must be reduced. This is accomplished by ionic exchange of the zeolite with ammonium nitrate solutions.

Table 4 shows the effect of duration time of ion exchange on catalyst sodium content ( $\text{Na}_2\text{O}$ ),

from this table shows that the ionic exchange increases with increasing duration time ,after that the increasing of duration time lead to slightly increase of ionic exchange .This means that the ion exchange reaction not far from equilibrium, so the ion exchange process must be repeated for more than one time. The ion exchange process was repeated four times to reach the final result. The sodium content in the prepared calcined powdered faujasite after ionic exchange was reached to 5.8wt%  $\text{Na}_2\text{O}$ . This result represented 53.6 % ionic exchange . The diffusion difficulties during ion exchange inhibits a complete exchange of Na ion by  $\text{NH}_4$  ion as mentioned by Plank( Plank, 1969).

This result of ion exchange is in a good agreement with that obtained by Mu et al (Mu et al, 2008). They reached to 44 percent ionic exchange for NaY Zeolite prepared from kaolin . Also, this result slightly differs from the result obtained by Reza (Reza Sadeghbeigi, 2000), and Jones et al( Jones et al, 2006). They recorded that the exchangeable sodium content is reduced to 3wt%  $\text{Na}_2\text{O}$ . Anyway the results of this work was in agreement with that obtained by Samar (Samar,2008) for zeolite X .The exchangeable sodium content is reduced to less than about 2%.

#### CATALYTIC ACTIVITIES OF PREPARED CATALYST

The activity of prepared catalyst on the VGO conversion and the yield of gasoline, gases, and coke was studied at reaction temperatures range 440 to 500 °C, and weight hour space velocity (WHSV) range 10 to  $25\text{h}^{-1}$ ,

Figures 6, 7, and 8 show the effect of WHSV on the VGO conversion at different reaction temperature for Na form catalyst,  $\text{NaNH}_4$  form catalyst, and NaH form catalyst, respectively. As shown from these figures, the VGO conversion increases with decreasing of WHSV at constant temperature. This means that the conversion of VGO is a function of reaction time for all catalysts, the increasing of the contact time of the feed molecules with the catalyst increases the VGO conversion in direct proportion to the amount of the catalyst and inversely proportional to the feed flow rate. The lower WHSV increases the contact time and favors VGO conversion. The results obtained for the effect of WHSV on the VGO conversion are in a

good agreement with those obtained by Rawet et al(Rawet et al,2001) , and Ancheyta et al(Ancheyta et al 2002).

**Table 4** The effect of duration time of ion exchange on catalyst sodium content.

Duration of ion exchange(hr)	$\text{Na}_2\text{O}(\text{wt}\%)$	$\text{Na}_2\text{O}(\text{wt}\%)$ exchanges
0.0	12.5	0.0
24	9.7	22.4
48	9.2	26.4
72	8.9	28.8
192	7.5	40
240	7.2	42.4
360	5.8	53.6

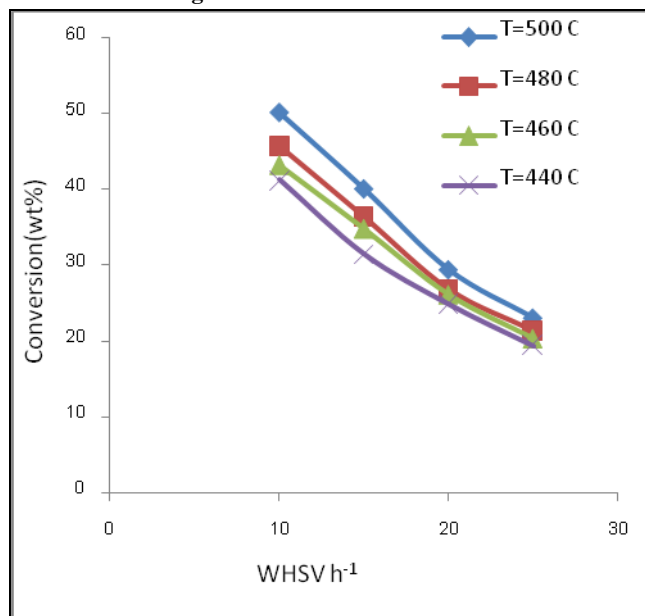


**Fig.6** Effect of WHSV on the VGO conversion at different temperatures for Na-form zeolite catalyst

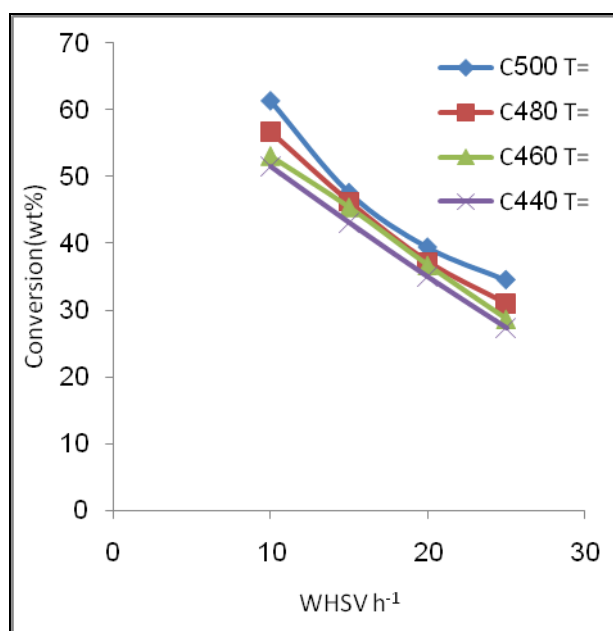


**Fig 7** Effect of WHSV on the VGO conversion at different temperatures for NaNH<sub>4</sub>-form zeolite catalyst

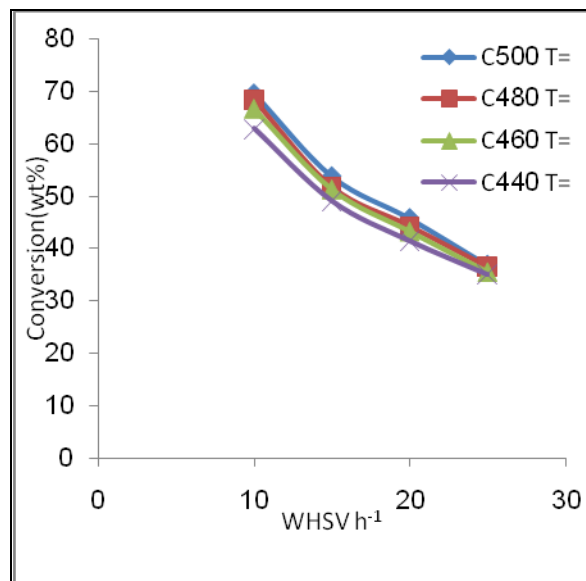


**Fig. 8** Effect of WHSV on the VGO conversion at different temperatures for NaH

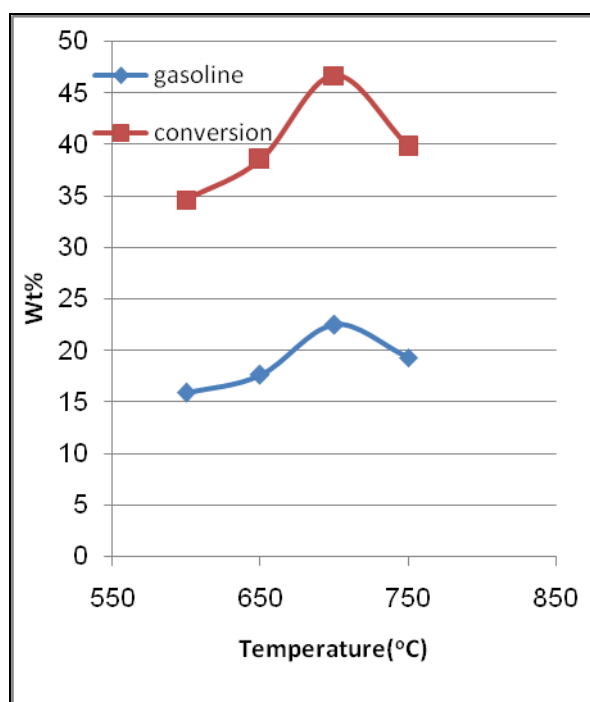
The selectivity of prepared catalyst to produce gasoline was calculated for Na form, NaNH<sub>4</sub> form, and NaH form at 10 WHSV and 500 °C and equals 37.3, 40, and 43.5% respectively. The selectivity increases with increasing conversion. These results agree with those obtained by Ravichander et. al (Ravichander, et al ,2009) and Al-Khattaf (Al-Khattaf 2002) .

Figure 9 shows the effect of regeneration temperature of prepared catalyst NaH form on the conversion and the gasoline yield. The experimental conditions of these tests are WHSV of 10 h<sup>-1</sup>, reaction temperature of 500 °C, and atmospheric pressure.

As shown from this figure, the gasoline yield and the VGO conversion increases with increasing regeneration temperature to a certain limit, after that the gasoline yield and the VGO conversion decrease. The regeneration transformed the coke deposits into carbon monoxide, carbon dioxide, and steam, all of which are gaseous. Thus, the poisoning of catalyst by coke is a reversible process that can be effectively counteracted, when coke removing reach a maximum point, the surface area (active sites) and the activity

reach a maximum level, thus leads to a maximum conversion (46.7wt%) and gasoline yield (22.5wt%). The excessive rise in regeneration temperature decreases the gasoline yield and the VGO conversion because the structure and texture of the catalyst may be irreversibly altered( Danial Decroocq 1984)

The activity of regenerated catalyst gives 61% of original activity. This result was far away from those obtained by Ravichander et al [29] (Ravichander, 2009) .They recorded that the activity of regenerated catalyst is 10% lower than that obtained with fresh catalyst.



**Fig. 9:** Effect of regenerated temperature on the gasoline yield and VGO conversion

## CONCLUSIONS

From the present work using kaolin (clay mineral locally found ) as a raw material for preparation faujasite type Y zeolite and studying the performance of the prepared catalyst in fluidized bed reaction system the following conclusions are deduced:-

- 1- From the X-ray Powder Diffraction, FT-IR spectroscopy , silica-to-alumina mole ratio 3.85(Si/Al=1.925) , unit cell size (UCS) 24.73 Å ,surface area 360m<sup>2</sup>/g , pore volume 0.39 and sodium content 12.5 wt%. for prepared catalyst and the comparison with the standard NaY zeolite ,it is possible to say that the prepared catalyst obtained from locally available kaolin in this work is NaY zeolite.
- 2- Activity of faujasite type Y zeolite NaH form is a highest among Na form, NaNH<sub>4</sub> form and NaH form.
- 3- The appropriate regeneration temperature for prepared catalyst was 700°C, which gives 61% from original activity.
- 4- The experimental results indicate that the effect of WHSV is higher than the effect of temperature on the VGO conversion and gasoline yield within the process variables.

## REFERENCES

Al-Khattaf S., "The influence of Y-zeolite unit cell size on the performance of FCC catalysts during gas oil catalytic cracking" *Applied Catalysis A: General* 231 (2002) 293–306.

Ancheyta, J., and Sotelo, R., "kinetic modeling of vacuum gas oil catalytic cracking" *J. Mexican, chem. society* 46(2002)38-42

Auerbach, Scott M. Kathleen A. Carrado, and Prabir K. Dutta "Handbook of zeolite science and Technology", Marcel Dekker Inc. (2003).

Ballmoos, R. von. D.H. Harris, J.S. Magee, in: G. Ertl, H. Knozinger, J. Weitkamp (Eds.), *Handbook of Heterogeneous Catalysis*, Wiley-VCH, Weinheim, 1997, p. 1955.

Break, D. W., "Zeolite Molecular Sieves Structure Chemistry and Use", John Wiley and Sons, New York, (1974).

Chandrasekhar, S., and, Pramada, P.N., "Investigation on the synthesis of zeolite NaX from Kerala kaolin" *Journal of porous material* 6,(1999), 283-297.

Corma, A. Martinez, A. in: F. Schuth, K.S.W. Sing, J. Weitkamp (Eds.), *Handbook of Porous Solids*, Wiley-VCH, Weinheim 2002, p. 2825

Corma, A. Martinez, A. in: M. Guisnet, J.-P. Gilson (Eds.), *Zeolites for Cleaner Technologies*, Imperial College Press, London, 2002, p. 29.

Corma, A.V. Fornes, A. Martinez, F.V. Melo, O. Pallota, in: P. Grobet, W.J. Mortier, E.F. Vansant, G. Schulz-Ekloff (Eds.), *Innovation in Zeolite Materials Science*, *Studies in Surface Science and Catalysis*, vol. 37, Elsevier, Amsterdam, 1988, p. 495

Daniel Decroocq, "Catalytic Cracking of Heavy Petroleum Fractions", *Imprimerie Louis-Jean*, Paris, (1984)

Fritz, P.O., and Lunsford, J.H., *J. Catal.* (1989), 118, 85.

## **The use of Prepared Zeolite Y from Iraqi kaolin for Fluid Catalytic Cracking of Vacuum Gas Oil**

Hayward, C. M. and Winkler, W. S., "FCC: Matrix/Zeolite", *Hydrocarbon Processing*, February (1990), pp. 55-56.

International center for diffraction data (ICDD), 12 campus boulevard, Newtown square, PA 19073-3273, U.S.A., (2009)

Jentys, A., and Lercher, J.A., "Studies in Surface Science and Catalysis" (Vol. 137), Eds. H. van Bekkum, E.M. Flanigen, P.A. Jacobs and J.C. Jensen. Elsevier Science B.V., Amsterdam. (2001), p 345

Jones, D. S., and Pujad, P. R., "Handbook of Petroleum Processing", Published by Springer, (2006).

H.G. Karge, *Microporous and Mesoporous Materials* Micro. Meso. Mater. (1998), 22, 547.  
Khabtou, S.T. Chevreau and Lavalley J.C., *Microporous and Mesoporous Materials*. 3(1994), 133

Michael Stocker, "Gas phase catalysis by zeolites", *Microporous and Mesoporous Materials*, 82 (2005) 257–292

Mu Mu Htay, and Mya Mya Oo, "Preparation of Zeolite Y Catalyst for Petroleum Cracking", *Pwaset Volume 36 ISSN 2070-3740*, 2008, 859 – 865.

Pine, L.A., Maher, P.J., and Wachter, W.A., "Prediction of cracking catalyst behavior by zeolite unit cell size model" *Journal of catalyst* 85,(1984), 466-476

Plank, C. J., "Conversion of clays to Crystalline Aluminosilicates and Catalysts There from", U.S. Patent, 3,431,218,(1969).

Rawet, R., Cerqueira, H. S., and Pinto, J. C., "The influence of covariances during laboratory evaluation of FCC catalysts" *Applied Catalysis A: General* 207 (2001) 199–209

Ravichander, N., Chiranjeevi, T., Gokak, D.T., Voolapalli, R.K., Choudary, N.V., "FCC catalyst and additive evaluation—A case study" *Catalysis*





Today 141 (2009) 115–119.

Reza Sadeghbeigi, “Fluid Catalytic Cracking Handbook Design, Operation and Troubleshooting of FCC Facilities”, Elsevier Inc., (2000).

Samar.K.Dh, “Catalytic Dealkylation of Cumene”. M.Sc. Thesis, University of Baghdad, (2008).

Scherzer, J., “Designing FCC catalysts with high-silica Y zeolites” *Applied catalysis*, 75 (1991) 1 - 32.

S.T Sie, in: J.C. Jansen, M. Stöcker, H.G. Karge, J. Weitkamp (Eds.), *Advanced Zeolite Science and Applications*, Studies in Surface Science and Catalysis, vol. 85, Elsevier, Amsterdam, 1994, p. 587.

Suchuchchai Nuanklai, “Effects of Particle Size and Hydrothermal Treatment of Y-zeolite on Catalytic Cracking of n-Octane”, M.Sc., University of Chulalongkorn, (2004).

Szostak, R. “Studies in Surface Science and Catalysis” (Vol. 137), Eds. H. van Bekkum, E.M. Flanigen, P.A. Jacobs and J.C. Jensen. Elsevier Science B.V., Amsterdam. 2001, p 261.

Treacy, M.M.J., Higgins, J. B. and Von Bollmoos, R., “Collection of Simulated XRD Powder Patterns for Zeolite.” 3<sup>rd</sup> ed. Amsterdam: Elsevier (1996).

Ward, W. D.L. Trimm, S. Akashah, M. Absi-Halabi, A. Bishara (Eds.), *Catalysis in Petroleum Refining 1989*, Studies in Surface Science and Catalysis, vol. 53, Elsevier, Amsterdam, 1990, p. 417.

West, A.R., “Basic Solid State Chemistry”, New York: John Wiley and Sons Inc., (1988).

B. Zhan, M.A. White, M. Lumsden, J. Mueller-Neuhaus, K.N. Robertson, T.S. Cameron and M. Gharghour, *Chem. Mater.* (2002), 14, 3636.

Zhu, L., and Seff, K. “Reinvestigation of the crystal structure of dehydrated sodium zeolite X” *J. Phys. Chem.* 103(1999) 9512-9518.

# Isolated Word Speech Recognition Using Mixed Transform

Assist. Prof. Dr. Sadiq Jassim Abou-Loukh and Eng. Shahad Mujeeb Abdul-Razzaq

University of Baghdad, College of Engineering, Electrical Engineering Department  
Email: doctor\_sadiq@yahoo.com

## ABSTRACT :

Methods of speech recognition have been the subject of several studies over the past decade. Speech recognition has been one of the most exciting areas of the signal processing. Mixed transform is a useful tool for speech signal processing; it is developed for its abilities of improvement in feature extraction. Speech recognition includes three important stages, preprocessing, feature extraction, and classification. Recognition accuracy is so affected by the features extraction stage; therefore different models of mixed transform for feature extraction were proposed. The properties of the recorded isolated word will be 1-D, which achieve the conversion of each 1-D word into a 2-D form. The second step of the word recognizer requires, the application of 2-D FFT, Radon transform, the 1-D IFFT, and 1-D discrete wavelet transforms were used in the first proposed model, while discrete multicircularlet transform was used in the second proposed model. The final stage of the proposed models includes the use of the dynamic time warping algorithm for recognition tasks. The performance of the proposed systems was evaluated using forty different isolated Arabic words that are recorded fifteen times in a studio for speaker dependant. The result shows recognition accuracy of (91% and 89%) using discrete wavelet transform type Daubechies (Db1) and (Db4) respectively, and the accuracy score between (87%-93%) was achieved using discrete multicircularlet transform for 9 sub bands.

**KEYWORDS:** Mixed Transform, Radon Transform, Discrete Wavelet Transform, Discrete Multicircularlet Transform, Dynamic Time Warping.

## تمييز الكلمات المفصولة باستخدام التحويلات الخليطة

م.م. شهد مجيب عبد الرزاق

أ.م.د. صادق جاسم ابو اللوخ

قسم الهندسة الكهربائية / كلية الهندسة / جامعة بغداد

## الخلاصة:

طرائق تمييز الكلام كان موضوع كثير من الدراسات خلال العقد الماضي. الكلام هو الطريقة الطبيعية للتواصل بين البشر ويعتبر تمييز الكلام واحد من المجالات المهمة في معالجة الإشارة. التحويلات الخليطة هي أداة مفيدة في معالجة إشارة الكلام، وقد تم تطويرها من أجل تحسين تمثيل الإشارة المستخلصة. يتضمن تمييز الكلام ثلاث أجزاء أساسية: معالجة مسبقة للإشارة، استخلاص الميزات، والتصنيف. تتأثر دقة تمييز الكلام بمرحلة استخلاص الميزات لذلك فقد تم اقتراح نماذج مختلفة من التحويلات الخليطة. ان خصائص الكلمات المسجلة ستكون احادية الابعاد (1-D) مما سيمكننا تحويلها الى صيغة ثنائية الابعاد (2-D). المرحلة الثانية في التصنيف تتطلب تطبيق التحويلات الخليطة، تحويل فورير ثنائي الابعاد بطبق على الإشارة ثنائية الابعاد ثم تحويل رادون ثم تحويل فورير المعكوس احادي البعد. بعد ذلك تم استخدام تحويل المويجي المتقطع في النموذج الأول، بينما تم استخدام التحويل الدائري المتعدد في النموذج الثاني. المرحلة النهائية تتضمن استخدام تحويل الزمن الديناميكي لغرض التمييز بين الكلمات. أربعون كلمة عربية مسجلة بخمسة عشر زمن مختلف في الاستوديو بواسطة متكلم واحد استخدمت كقاعدة بيانات في هذا العمل. أداء كل الطرق المستخدمة تم تحليلها وتقييمها بواسطة الحاسوب باستخدام لغة MATLAB (2010a). إن دقة تمييز الكلام في النموذج الأول تساوي (91% and 89%) عندما استعمل التحويل المويجي المتقطع نوع Db1 و Db4 على التوالي بينما كانت الدقة في النموذج الثاني بين (87%-93%) عندما استخدمت تسعة أحزمة مختلفة من التحويل الدائري المتعدد.

**الكلمات الرئيسية:** التحويلات الخليطة، تحويل رادون، التحويل المويجي المتقطع، تحويل الزمن الديناميكي، التحويل الدائري المتعدد

## 1. INTRODUCTION

Speech recognition is the process to recognize speech utterances by a speaker. For human beings, it is a natural and simple task. However, it is an extremely complex and difficult job to make a computer respond to even simple spoken commands. Speech recognition becomes a challenging task to create an intelligent recognizer that emulates a human being's ability in speech perception under all environments (Rabiner, 1993).

Many research works have been done on the recognition of Arabic words. These studies include the use of neural networks and dynamic time warping. Mutasher, 2010, presented different models for speech recognition based on artificial neural network (ANN) and dynamic time wrapping (DTW) algorithm, and in each model, two transformation methods namely, discrete wavelet transform and slantlet transform are used to extract features from speech signal. Qassim, 2006, developed speech feature extraction using a hybrid technique based on discrete wavelet transform which is applied to each Arabic phoneme for single words. He proposed a technique for training and recognition tasks includes the use of feed-forward back propagation neural network.

Speech recognition consists of several stages, that the most significant of them are the feature extraction and recognition stages. Therefore, several feature extraction techniques are evaluated based on discrete wavelet transform (DWT), radon transform, and discrete multicircularlet transform (DMCT).

In this paper, isolated Arabic word recognition system is proposed based on different mixed transform techniques and DTW algorithm as a decision network.

## 2. ISOLATED WORDS DATABASE

A database is created for Arabic language using single speaker. Each word is repeated 15 times. We have used forty different isolated words for creating the database. The samples stored in the database are recorded by using a high quality studio-recording microphone at a sampling rate of 8 KHz. Recognition has been made on these 40 isolated spoken words under the same configuration. Our database consists of a total of 600 utterances of the spoken words.

The spoken words are preprocessed, numbered, and stored in appropriate classes in the database. The general block diagram of the speech recognition system is shown in **Fig.1**. Basic speech recognition system includes three stages: the preprocessing stage, the feature extraction stage, and the classification stage.

**a. Sampling:** the speech signals are sampled to convert it from analog to digital.

**b. Framing and windowing:** at this stage the speech signal is blocked in frames of N sample. Since we deal with speech signal, which is non-stationary signal, the framing process is essential to deal with frame not with the original signal. After this stage the speech signal has many frames and the number of frames depends on the number of samples for each word, so all length of utterances must be resized into a length which is agreed with the proposed length. The main reason behind choosing proposed length, is to get high performance of the algorithms, to get best feature extraction coefficient and also to convert the process from 1D into the 2D process matrix. In this proposed system, after many studies and tests on different data (words), and different lengths, it is found that the suitable (proposed) length of all words is



256, and this choice comes from noting all length of words and finding that this length is very appropriate for all. Windowing includes multiplying each frame of the word by the hamming window; the advantage of the multiplication is to minimize the signal discontinuities at the beginning and the end of each frame. The concept here is to minimize the spectral distortion by using the window to taper the signal to zero at the beginning and the end of each frame. It is clear that the hamming window does not go to zero at the extremes (Mutasher, 2010). In this paper, a mixed transform was used to extract the features from the speech signal, while the DTW algorithm was used to recognize the input speech.

### 3. MIXED TRANSFORM

Transform techniques have proved invaluable in signal analysis and in coding for efficient transmission and storage of signal data. The goal of a transform is to represent as much of the signal information in few transform coefficients as possible. However, a particular transform is only efficient for representing signals which are of the same class as the basis functions of the transform. However, a signal may be represented efficiently only if the basis functions of the selected transform are similar in structure to the signal. Since signals such as speech and images are highly dynamic, consisting of regions with various combinations of narrow and broadband components, a single transform with fixed basis functions is rarely optimal for representing such signals (Albert, 1999).

In this work, the feature extraction of the speech signal will be done using two different mixed transforms, as explained below.

### 3.1 Radon Transform

The Radon transform was utilized for DSP purposes, in a novel procedure known as Finite Radon Transform (FRAT), which converts a matrix of data into a set of independent projections, and it can be reversed to retrieve the original data from the set of projections. This objective is carried out by applying 2D FFT on the matrix, to obtain the frequency-domain version of the data, then reordering the matrix elements through an optimum ordering procedure. Optimum ordering algorithm, which states that, the output matrix always contains principal directions, which are: the first column, the main diagonal, the first row, and the reverse diagonal, respectively. For example 4\*4 matrix the optimum ordering will be shown below (Abdulwahid, 2010):

$$\begin{bmatrix} 1 & 5 & 9 & 13 \\ 2 & 6 & 10 & 14 \\ 3 & 7 & 11 & 15 \\ 4 & 8 & 12 & 16 \end{bmatrix} \Rightarrow \begin{bmatrix} 1 & 1 & 1 & 1 & 1 & 1 \\ 2 & 6 & 5 & 8 & 10 & 7 \\ 3 & 11 & 9 & 0 & 0 & 0 \\ 4 & 16 & 13 & 14 & 12 & 15 \end{bmatrix}$$

### 3.2 Discrete Wavelet Transform

The DWT can be defined as the process of decomposing a signal or function into an expansion in terms of a basis function, usually called mother wavelet, from which two types of filters, low-pass and high-pass, can be generated. These filters can be arranged in a tree structure, called a filter bank, whose outputs will be separate signals, which stand for the signal content in separate bands of frequency.

**Fig. 2** illustrates a two-band filter bank, which consists of a high-pass (details) filter  $h_1(-n)$ , and a low-pass (approximation) filter  $h_0(-n)$ . The outputs  $d_j$  and  $c_j$  are found by the following convolution sums (Trivedi, 2011),

$$c_j(k) = \sum_m h_0(m-2k)c_{j+1}(m) \quad (1)$$

$$d_j(k) = \sum_m h_1(m-2k)c_{j+1}(m) \quad (2)$$

Notice how the convolved filter sequence jumps by two elements instead of one, due to the down sampler (Decimator) step, which takes a signal  $x(n)$  as an input and produces an output of  $y(n) = x(2n)$ .

Further decomposition on the approximation coefficients  $c_j$ , resulting in the new outputs  $d_{j-1}$  and  $c_{j-1}$  (Trivedi, 2011).

Most of the energy of the speech signal lies in the lower frequency bands. The other sub-bands contain more detailed information of the signal and they are discarded, since the frequency band covered by these levels contains much noise and less necessary for representing the approximate shape of the speech signal. Hence take the approximation a3 and discard (d1, d2, d3). **Fig.3** shows 3-levels DWT.

### 3.3 Multiwavelet Transform

As in the scalar wavelet case, the theory of multiwavelets is based on the idea of multiresolution analysis, analyzing the signal at different scales or resolutions. The difference is that multiwavelets have several scaling functions. The standard multiresolution has one scaling function  $\phi(t)$  (Ibraheem, 2010). The multiwavelet two-scale equation resemble those for scalar wavelets:

$$\Phi(t) = \sqrt{2} \sum_{k=-\infty}^{\infty} H_k \Phi(2t-k) \quad (3)$$

$$\Psi(t) = \sqrt{2} \sum_{k=-\infty}^{\infty} G_k \Psi(2t-k) \quad (4)$$

One famous multiwavelet filter is the GHM filter proposed by Geronimo, Hardin, and Massopust (Geronimo, 1994). Their system

contains the two scaling functions and  $\Phi_2(t)$  and the two wavelets  $\Psi_1(t)$  and  $\Psi_2(t)$  (Strela, 1998). According to equations 3 and 4, the GHM two scaling and wavelet functions satisfy the following two-scale dilation equations:

$$\begin{bmatrix} \psi_1(t) \\ \psi_2(t) \end{bmatrix} = \sqrt{2} \sum_k G_k \begin{bmatrix} \psi_1(2t-k) \\ \psi_2(2t-k) \end{bmatrix} \quad (5)$$

$$\begin{bmatrix} \phi_1(t) \\ \phi_2(t) \end{bmatrix} = \sqrt{2} \sum_k H_k \begin{bmatrix} \phi_1(2t-k) \\ \phi_2(2t-k) \end{bmatrix} \quad (6)$$

Where  $H_k$  for GHM system are four scaling matrices  $H_0, H_1, H_2$ , and  $H_3$ .

$$H_0 = \begin{bmatrix} \frac{3}{5\sqrt{2}} & \frac{4}{5} \\ \frac{1}{20} & -\frac{3}{10\sqrt{2}} \end{bmatrix}, H_1 = \begin{bmatrix} \frac{3}{5\sqrt{2}} & 0 \\ \frac{9}{20} & \frac{1}{\sqrt{2}} \end{bmatrix}, \\ H_2 = \begin{bmatrix} 0 & 0 \\ \frac{9}{20} & -\frac{3}{10\sqrt{2}} \end{bmatrix}, H_3 = \begin{bmatrix} 0 & 0 \\ -\frac{1}{20} & 0 \end{bmatrix} \quad (7)$$

Also,  $G_k$  for GHM system are four wavelet matrices  $G_0, G_1, G_2$ , and  $G_3$ .

$$G_0 = \begin{bmatrix} -\frac{1}{20} & -\frac{3}{10\sqrt{2}} \\ \frac{1}{10\sqrt{2}} & \frac{3}{10} \end{bmatrix}, G_1 = \begin{bmatrix} \frac{9}{20} & -\frac{1}{\sqrt{2}} \\ -\frac{9}{10\sqrt{2}} & 0 \end{bmatrix}, \\ G_2 = \begin{bmatrix} \frac{9}{20} & -\frac{3}{10\sqrt{2}} \\ \frac{9}{10\sqrt{2}} & -\frac{3}{10} \end{bmatrix}, G_3 = \begin{bmatrix} -\frac{1}{20} & 0 \\ -\frac{1}{10\sqrt{2}} & 0 \end{bmatrix} \quad (8)$$

### 3.4 Discrete MultiCircularlet Transform

The GHM characteristics offers a combination of orthogonality, symmetry, and compact support, which cannot be achieved by any scalar wavelet basis except for the Haar basis, its basis functions are exploited to generate more efficient basis functions for

compression purposes where the number of zeros is as large as possible.

The GHM basis functions are exploited to generate more efficient basis functions for compression purposes. This can be achieved through the following steps (Alubady, 2009).

1- Taking the 2-D convolution for each basis function matrix with itself to generate new basis functions. This is done as follows:-

a. Write the polynomial representation of the matrix, e.g. for matrix  $G_1(n_1, n_2)$  &  $G_2(n_1, n_2)$  :

$$G_1 = p \begin{bmatrix} a_1 & a_2 \\ a_3 & a_4 \end{bmatrix} \quad (9)$$

$$G_2 = p \begin{bmatrix} b_1 & b_2 \\ b_3 & b_4 \end{bmatrix} \quad (10)$$

The polynomial representation for eq. (9) Will Be

$$G_1(p, q) = a_1 + a_3p + a_2q + a_4pq \quad (11)$$

The polynomial representation for eq. (10) Will Be

$$G_2(p, q) = b_1 + b_3p + b_2q + b_4pq \quad (12)$$

b. Use table lookup method to find the convolution result as follows:

	$a_1$	$a_3p$	$a_2q$	$a_4pq$
$b_1$	$a_1b_1$	$a_3b_1p$	$a_2b_1q$	$a_4b_1pq$
$b_3p$	$a_1b_3p$	$a_3b_3p^2$	$a_2b_3pq$	$a_4b_3p^2q$
$b_2q$	$a_1b_2q$	$a_3b_2pq$	$a_2b_2q^2$	$a_4b_2pq^2$
$b_4pq$	$a_1b_4pq$	$a_3b_4p^2q$	$a_2b_4pq^2$	$a_4b_4p^2q^2$

The output polynomial representation is equal to:

$$a_1b_1$$

$$a_3b_1p + a_1b_3p$$

$$a_2b_1q + a_3b_3p^2 + a_1b_2q$$

$$a_4b_1pq + a_2b_3pq + a_3b_2pq + a_1b_4pq$$

$$a_4b_3p^2q + a_2b_2q^2 + a_3b_4p^2q$$

$$a_4b_2pq^2 + a_2b_4pq^2$$

$$a_4b_4p^2q^2$$

c. Arrange the result in matrix form to which gives:

$$a_1b_1$$

$$a_2b_1 + a_1b_2$$

$$a_2b_2$$

$$a_3b_1 + a_1b_3 \quad a_2b_3 + a_3b_2 + a_1b_4 + a_4b_1 \quad a_4b_2 + a_2b_4$$

$$a_3b_3$$

$$a_4b_3 + a_3b_4$$

$$a_4b_4$$

d. Fold the 3<sup>rd</sup> column on the 1<sup>st</sup> column & next folding the 3<sup>rd</sup> row on the 1<sup>st</sup> row.

i- Folding the 3<sup>rd</sup> column results in

$$\begin{pmatrix} a_1b_1 + a_2b_2 & a_2b_1 + a_1b_2 \\ a_1b_3 + a_3b_1 + a_2b_4 + a_4b_2 & a_1b_4 + a_2b_3 + a_3b_2 + a_4b_1 \\ a_3b_3 + a_4b_4 & a_3b_4 + a_4b_3 \end{pmatrix}$$

ii- Folding the 3<sup>rd</sup> row results in

$$\begin{pmatrix} a_1b_1 + a_2b_2 + a_3b_3 + a_4b_4 & a_1b_2 + a_2b_1 + a_3b_4 + a_4b_3 \\ a_1b_3 + a_2b_4 + a_3b_1 + a_4b_2 & a_1b_4 + a_2b_3 + a_3b_2 + a_4b_1 \end{pmatrix}$$

The individual coefficients values of these matrices are generated using the following procedure (Alubady, 2009):

1- Apply the 2-D convolution between the G's & H's . This can be achieved as follows:

- a) compute  $A_{i1} = H_i \otimes H_i$   
b) compute  $B_{i1} = G_i \otimes G_i$   
where  $i = 0, 1, 2, 3$   
2. Now compute the 2-D Convolution between the resultant of step 1 & the G's & H's. This can be done through the following way:  
a) compute  $A_{i2} = A_{i1} \otimes H_i$   
b) compute  $B_{i2} = B_{i1} \otimes G_i$   
where  $i = 0, 1, 2, 3$

3. The process was repeated several times. It was found that the optimal results was at the third step.

The proposed matrix coefficients A's and B's was obtained by performing the following computations:

- a) compute  $A_i = A_{i2} \otimes H_i$   
b) compute  $B_i = B_{i2} \otimes G_i$   
where  $i = 0, 1, 2, 3$

The proposed new multifilter bases functions which denoted by A's and B's are stated as

$$A_0, A_1, A_2, A_3 \text{ \& } B_0, B_1, B_2, B_3$$

The proposed basis functions are:

The A's 2x2 matrices are:

$$\begin{aligned} A_0 &= \begin{bmatrix} 1.4561 & 1.4131 \\ -1.0265 & -0.9857 \end{bmatrix}, \\ A_1 &= \begin{bmatrix} 1.6896 & 1.5814 \\ 1.4376 & 1.5450 \end{bmatrix}, \\ A_2 &= \begin{bmatrix} 0.0977 & -0.0945 \\ 0 & 0 \end{bmatrix}, \\ A_3 &= 1.0e-005 * \begin{bmatrix} 0.6250 & 0 \\ 0 & 0 \end{bmatrix} \end{aligned} \quad (13)$$

The B's 2x2 matrices are:

$$\begin{aligned} B_0 &= \begin{bmatrix} 0.0460 & 0.0343 \\ -0.0459 & -0.0342 \end{bmatrix}, \\ B_1 &= \begin{bmatrix} 2.7696 & -2.4406 \\ -2.4142 & 2.7225 \end{bmatrix}, \\ B_2 &= \begin{bmatrix} 1.6610 & -1.6066 \\ 1.6581 & -1.6038 \end{bmatrix}, \\ B_3 &= \begin{bmatrix} -0.0302 & -0.0302 \\ 0.0052 & 0.0052 \end{bmatrix} \end{aligned} \quad (14)$$

Due to the good characteristics of the transformed 1-D and 2-D signal by the basis functions obtained from third convolution, it will be adopted as the new transform named "Multicircularlet Transform" (Alubady, 2009). The AB multifilter bank coefficients are 2 by 2 matrices, and during the convolution step they must multiply vectors (instead of scalars). This means that multifilter banks needs 2 input rows. This transformation is called preprocessing. The most obvious way to get two input rows from a given signal is to repeat the signal. Two rows go into the multifilter bank. This procedure is called "Repeated Row" which introduces over sampling of the data by a factor of 2. For computing DMWT, the transformation matrix can be written as follows:

$$W = \begin{bmatrix} A_0 & A_1 & A_2 & A_3 & 0 & 0 & \dots & 0 & 0 & 0 & 0 \\ 0 & 0 & A_0 & A_1 & A_2 & A_3 & \dots & 0 & 0 & 0 & 0 \\ \vdots & \vdots & \vdots & \vdots & \vdots & \vdots & \dots & \vdots & \vdots & \vdots & \vdots \\ A_2 & A_3 & 0 & 0 & 0 & 0 & \dots & 0 & 0 & A_0 & A_1 \\ B_0 & B_1 & B_2 & B_3 & \vdots & \vdots & \dots & 0 & 0 & 0 & 0 \\ 0 & 0 & B_0 & B_1 & B_2 & B_3 & \dots & 0 & 0 & 0 & 0 \\ \vdots & \vdots & \vdots & \vdots & \vdots & \vdots & \dots & \vdots & \vdots & \vdots & \vdots \\ 0 & 0 & 0 & 0 & 0 & 0 & \dots & B_0 & B_1 & B_2 & B_3 \\ B_2 & B_3 & 0 & 0 & 0 & 0 & \dots & 0 & 0 & B_0 & B_1 \end{bmatrix}$$

where  $A_i, B_i$  are the impulse responses of the **AB** multifilter bank, equations 13 and 14.

The organization and statistics of multicircularlet subbands differ from the scalar wavelet case. During a single level of decomposition using a scalar wavelet transform, the 2-D signal data is replaced with four blocks, while in multifilter bank used here, two channels are corresponds for each bank, so there will be two sets of scaling coefficients and two sets of wavelet coefficients.

#### 4. DYNAMIC TIME WARPING

The Dynamic Time Warping (DTW) is the mathematical technique which is used to find the cumulative distance along the optimum path without having to calculate the cumulative distance along all possible paths (Chapaneri,2012). In **Fig.4** consider a point  $i, j$  somewhere in the middle of both words. If this point is on the optimum path, then the constraints of the path necessitate that the immediately preceding point on the path is  $i-1, j$  or  $i-1, j-1$  or  $i, j-1$ . These three points are associated with a horizontal, diagonal or vertical path step respectively. Let  $D(i, j)$  be the cumulative distance along the optimum path from the beginning of the word to point  $i, j$ , thus:

$$D(i,j)= \sum_{x,y=1,1}^{i,j} d(x, y) \quad (15)$$

As there are only the three possibilities for the point before  $i, j$  it follows that:

$$D(i,j)= d(i,j) + \min [D(i-1, j) , D(i-1, j-1), D(i,j-1)] \quad (16)$$

The best way to get to point  $i, j$  is thus to get to one of the immediately preceding points by the best way, and then take the appropriate step to  $i, j$ . The value of  $D(1, 1)$  must be equal to  $d(1, 1)$  as this point is the beginning of all

possible paths. To reach points along the bottom and the left-hand side of **Fig.4** there is only one possible direction (horizontal or vertical, respectively). Therefore, starting with the value of  $D(1, 1)$ , values of  $D(i, 1)$  or values of  $D(1, j)$  can be calculated in turn for increasing values of  $i$  or  $j$ . Let us assume that we calculate the vertical column,  $D(1, j)$ , using a reduced form of eq. (15) that does not have to consider values of  $D(i-1, j)$  or  $D(i-1, j-1)$ . (As the scheme is symmetrical we could equally well have chosen the horizontal direction instead). When the first column values for  $D(1, j)$  are known, eq.(16) can be applied successively to calculate  $D(i, j)$  for columns 2 to  $n$ . The value obtained for  $D(n,m)$  is the score for the best way of matching the two words(Holmes, 2001).

Suppose we have two time series  $Q$  and  $C$ , of length  $n$  and  $m$  respectively, where

$$Q = q_1, q_2, \dots, q_i, \dots, q_n$$

$$C = c_1, c_2, \dots, c_j, \dots, c_m$$

To align two sequences using DTW we construct a  $n$ -by- $m$  matrix where the  $(i, j)$  element of the matrix contains the distance  $d(Q_i, c_j)$  between the two points  $Q_i$  and  $c_j$  (Typically the Euclidean distance is used, so  $d(Q_i, c_j) = (Q_i - c_j)^2$ ). Each matrix element  $(i, j)$  corresponds to the alignment between the points  $Q_i$  and  $c_j$ .

A warping path  $W$  is a contiguous set of matrix elements that defines a mapping between series. The  $k$ th element of  $W$  is defined as  $w_k = (i, j)_k$  so we have:

$$W = (w_1, w_2, \dots, w_j, \dots, w_k)$$

The best warp (the shortest) path could be found by exhaustively searching all possible paths and selecting that path having the minimum measure. This, however, is not a practical solution, because the number of possible paths is large and exponentially related to the size of the lattice.

If a point  $(Q_i, c_j)$  lies on the optimal path, then the sub path from  $(q_1, c_1)$  to  $(Q_i, c_j)$  is

also locally optimized. This means that the best path from (q1, c1) to (qn, cm) can be recursively found by locally optimizing paths one grid unit with time-beginning at (q1, c1) and ending at (qn, cm). This is done in practice by running the recurrence relation in eq. (16) which defines the cumulative distance D (I, j) for each point , i.e. assigning a partial sum to each grid (Li Dong, 2006).

The global warp cost of the two sequences is defined as shown below:

$$GC = \frac{1}{P} \sum_{i=1}^P w_i \quad (17)$$

Where  $w_i$  are those elements that belong to warping path, and p is the number of them. There are three conditions imposed on the DTW algorithm that ensure them a quick convergence (Furtuna, 2008):

1. Monotony – the path never returns, that means that both indices I and j used for crossing through sequences never decrease.
2. Continuity – the path advances gradually, step by step; indices I and j increase by maximum 1 unit on a step.
3. Boundary – the path starts in left-down corner and ends in a right-up corner in the distance matrix.

## 5. PROPOSED SPEECH RECOGNITION SYSTEM

The general block diagram for the proposed speech recognition system is shown in Fig. 5

### 5.1 Speech Signal

The proposed models have been applied on forty Arabic words; these words were recorded by a microphone in the studio by one speaker and stored as files, the format of these files is wave format. The type of digital speech signal is (PCM), and the sampling rate is 8 KHz. These words are:

(اشارة، لندن، افتح، الخير، تصميم، نبيل، مربع، رازق، رحمن، شارع، صباح، صديق، عمودي، كامل، محمد،

معلومات، نظام، وفاء، ياسين، ورود، بغداد، خشب، ثلاثون، ابراهيم، تردد، واحد، عباس، جبل، مصعد، قادر، زائد، قلم، خاص، محمول، سيارات، هاتف، كتاب، دفتر، صالح، مستقبل)

### 5.2 Sampling

The speech signals are sampled to convert it from analog to digital. The sampling rate has been down sampled from 44 KHz to 8 KHz.

### 5.3 Framing

At this stage the continuous speech signal is blocked in frames of N samples. Since we deal with speech signal, which is non stationary signal (vary with time), the framing process is essential to deal with frame not with the whole signal. After this stage the speech signal has many frames and the number of frames depends on the number of samples for each word. The number of samples for each frame is 265 samples.

### 5.4 Hamming Windowing

Each frame of the word was multiplied by the Hamming window; the advantage of the multiplication is to minimize the signal discontinuities at the beginning and the end of each frame.

### 5.5 Feature Extraction

Since speech recognition is so affected by the feature extraction stage, therefore two different mixed transforms are used in this work.

#### 5.5.1 The First Mixed Transform

The first mixed transform consist of applying 2-D FFT for each frame after resizing it into 16×16 matrix, then find the best sequence of direction for each frame after that applying the 1-D IFFT then applying the DWT to the resultant matrix for each row of the frame.

Most of the energy of the speech signal lies in the lower frequency bands. The other sub-bands contain more detailed information of



the signal and they are discarded, since the frequency band covered by these levels contains much noise and less necessary for representing the approximate shape of the speech signal. Hence take the approximation a3 and discard (d1, d2, d3). In the proposed work the DWT that used are Daubechies (Db1) and (Db4) type.

### 5.5.2 The Second Mixed Transform

In this proposed model the same preprocess and classification stages was used as in the first model, in feature extraction stage DMCT was used instead of DWT. The DMCT was applied to each frame of each version that results in 16 sub bands for each frame, each sub band treated independently to examine the recognition rate when each sub band used separately. Nine sub bands (sb1, sb2, sb3, sb5, sb6, sb7, sb9, sb10, sb11) which represent the approximation sub bands will be later represent the feature vector for the uterus and it will be ready to be used by the classifier, as it can be shown in **Fig. 6** where the shaded bands represent the detailed bands with a lowest recognition rate that can be ignored. **Fig. 7** shows the recognition steps using the second mixed transform.

### 5.6 Dynamic Time Warping Algorithm

After taking the mixed transform for all versions and represent each version by one feature vector, these feature vectors are different even in the same word, so these data are suitable to enter DTW classifier. The DTW algorithm allows a non-linear warping alignment of one signal to another by minimizing the distance between the two. This warping between two signals can be used to determine the similarity between them and thus it is very useful feature for recognition. The algorithm of DTW for classification of words is explained as follows:

**a.** Take fifteen version for each word and divide these versions, ten versions of each word ( $10 \times 40 = 400$  version) for basing, and five versions ( $5 \times 40 = 200$  version) for testing.

**b.** Calculate the distance value between each version from test with each version from base for all words.

The calculation of distance is done by finding the warping path between two versions and then calculate the global warp cost of the two versions defined by eq. (17)

## 6. RESULTS

In this work, the proposed systems have been applied on forty Arabic words. The number of versions of each word have been divided into two parts:

**a.** One part of these versions used for basing called “basing versions”, ten versions have been taken for each word.

**b.** The other part used for testing called “testing versions” five versions have been taken for each word. The test versions are tested on the DTW and their resultant error is used to give the measure of the generalization ability of this algorithm.

The proposed speech recognition system is done by different models two mixed transforms are used to recognize the speech signal. The first one consists of cascaded mixed transforms including (2D FFT, Radon transform, 1D IFFT) and followed by the DWT. The second mixed transform use the same first three stages as the first one, but differs in the last transform where DMCT is used. To compare the performance of each one of them, the accuracy or recognition rate has been computed as follows:

$$\text{Accuracy} = \frac{\text{Total number of correct recognition}}{\text{Total number of testing version}} \times 100\%$$

**Table 1** shows the comparison between the accuracy of different recognition system, while **Fig.8** shows the percentage of accuracy for each recognition system.

## 7. CONCLUSIONS

In this work, two mixed transforms are used to recognize the speech signal. The first one consists of cascaded mixed transforms including (2D FFT, Radon transform, 1D IFFT) and followed by the DWT that gave a recognition rate of 91%. The second mixed transform use the first as the first one, but differs in the last transform where DMCT is used, that gave a recognition rate of 93%. The mixed transform succeeded as a technique for combining features of speech recognition, since the coefficients pass through a cascaded transforms which enhance its low frequency component. The proposed mixed transform is a combination of multicircularlet transform with a 2D-FFT, Radon transform and 1D-IFFT to achieve better coefficient decomposition. The DMCT offers a good distribution of the signal in the frequency - spatial domain. It was shown that, this will result in a better decomposition of the coefficients, so it can be used as the extraction stage in the proposed speech recognition. DTW algorithm was used as a classifier to the features that are extracted by the mixed transform; this algorithm is a powerful tool to find the minimum distance between features of the same word, and there is no need to equalize their lengths. With all these advantages of using the proposed algorithm, the disadvantage of using the proposed mixed transform is the execution time because the complex computation of the proposed mixed

transforms that take more time of executing a single transform alone.

## 8. REFERENCES

- Abdulwahid ,H. " **Design And Simulation of A Multidimensional Radon-Based OFDM System** ", M.Sc. Thesis, Nahrain University, Communications Engineering Department, June 2010.
- Albert P. B. and Mikhael B. W. "A **Survey of Mixed Transform Techniques for Speech and Image Coding**", IEEE Xplor, pp.106-109,1999.
- Alubady,I. " **A Proposed Multicircularlet Mixed Transform and Its Application for Image Compression**", M.Sc. Thesis, University of Baghdad, Electrical Engineering Department, 2009.
- Chapaneri, S.V. " **Spoken Digits Recognition using Weighted MFCC and Improved Features for Dynamic Time Warping**", International J. of Computer Applications, Vol. 40, No.3, pp.6-12, February 2012.
- Furtuna, T.F., "Dynamic Programming **Algorithms in Speech Recognition**", Revista Informatica Economica, Vol.46, No.2, pp. 94-99, Bucharest, 2008.
- Geronimo, J., Hardin, D. & Massopust, P., "Fractal Function and Wavelet Expansion **Based on Several Functions**", J. Approx. Theory, Vol. 78, PP. 373-401, 1994.
- Holmes, J. and Holmes, W., "Speech **Synthesis and Recognition**", Second Edition, London and New York, 2001.
- Ibraheem, A. K., "Image **Reconstruction Using Hybrid Transform**", M.Sc. Thesis,





University of Baghdad, Electrical Engineering Department, 2010.

Li Dong, X., Kui Gu, C. & Ou Wang, "A **Local Segmented Dynamic Time Warping Distance Measure Algorithm for Time Series Data Mining**", Proceedings of the Fifth International Conference on Machine Learning and Cybernetics, Dalian, pp.1247-1252, August 2006.

Mutasher, S., "A **Multi Transform Based Dynamic Time Warping Isolated Word Speech Recognition System**", M.Sc. Thesis, University of Baghdad, Electrical Engineering Department, April, 2010.

Qassim, A., "Arabic Phonemes Recognition Using Hybrid Technique", M.Sc. Thesis,

University of Technology, Electrical and Electronic Engineering Department, January 2006.

Rabiner, L. and Juang, B. H., "Fundamentals of Speech Recognition", Prentice-Hall, New Jersey, 1993.

Strela, V. and Walden, A.T. "Orthogonal and Biorthogonal Multiwavelets for Signal Denoising and Image Compression" Proc. SPIE, 3391, pp.96-107, 1998.

Trivedi, N., Kumar, V., and Singh, S., "Speech Recognition by Wavelet Analysis", International J. of Computer Applications, Vol.15, No.8, pp.27-32, February 2011.

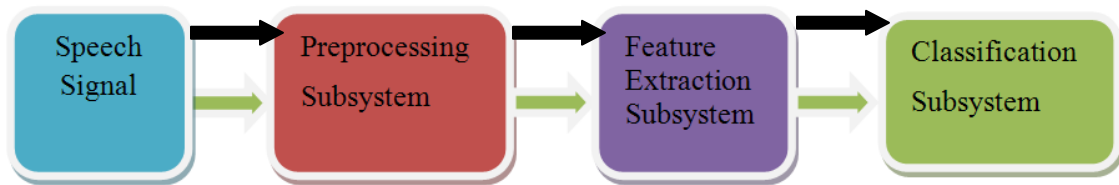


**Fig.1:** General block diagram of the speech recognition system

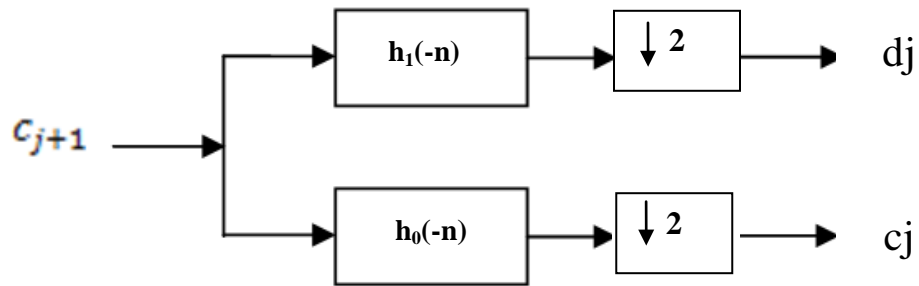


**Fig.2:-** Two-band filter bank .

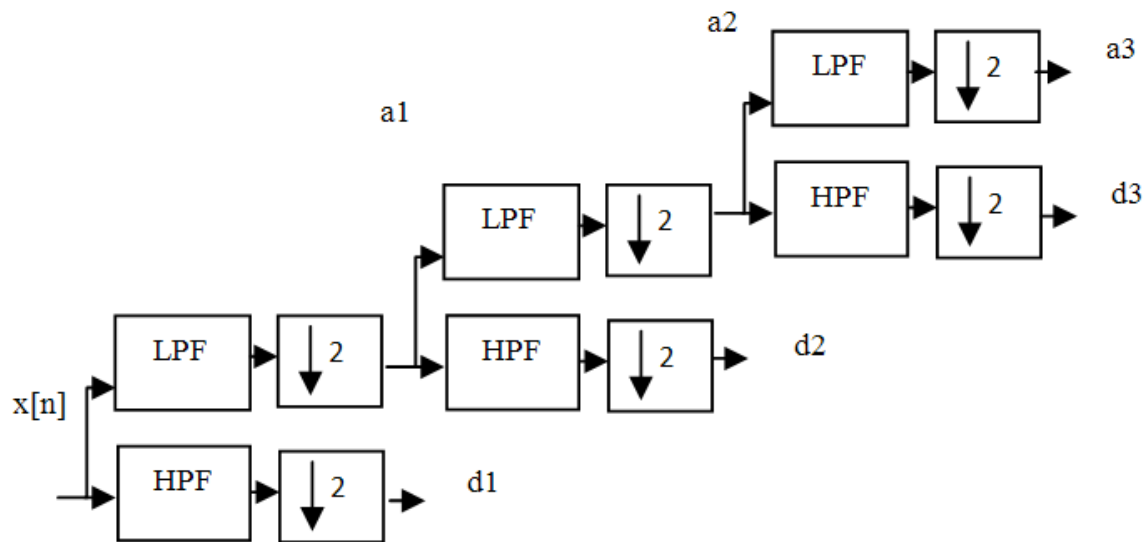
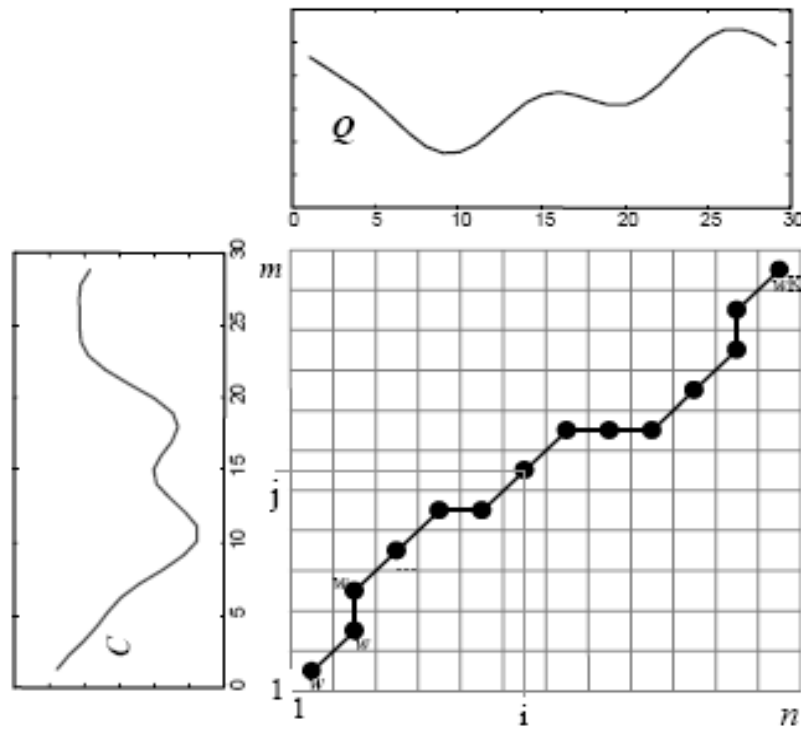


**Fig.3:-** 3-Levels of DWT



time series  $Q$  of length  $n$ ,  $Q = q_1, q_2, \dots, q_i, \dots, q_n$   
time series  $C$  of length  $m$ ,  $C = c_1, c_2, \dots, c_j, \dots, c_m$

**Fig.4:-** An example of warping path

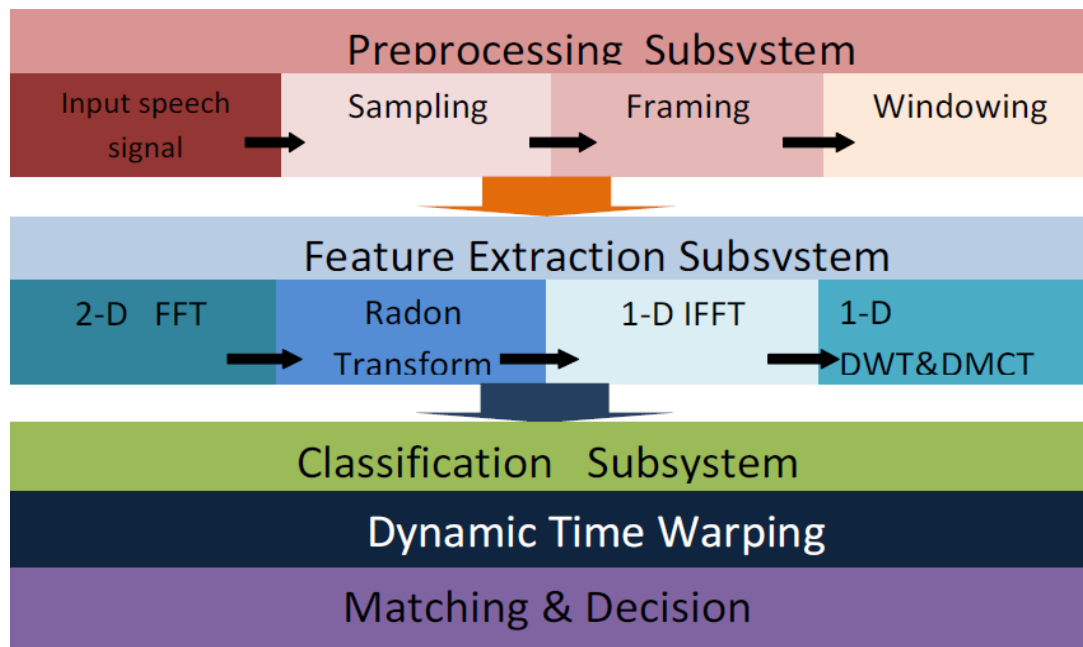


**Fig.5:-** Proposed speech recognition system

L1L1	L1L2	L1H1	L1H2
L2L1	L2L2	L2H1	L2H2
H1L1	H1L2	H1H1	H1H2
H2L1	H2L2	H2H1	H2H2

**Fig.6:-** The resultant MCT bands

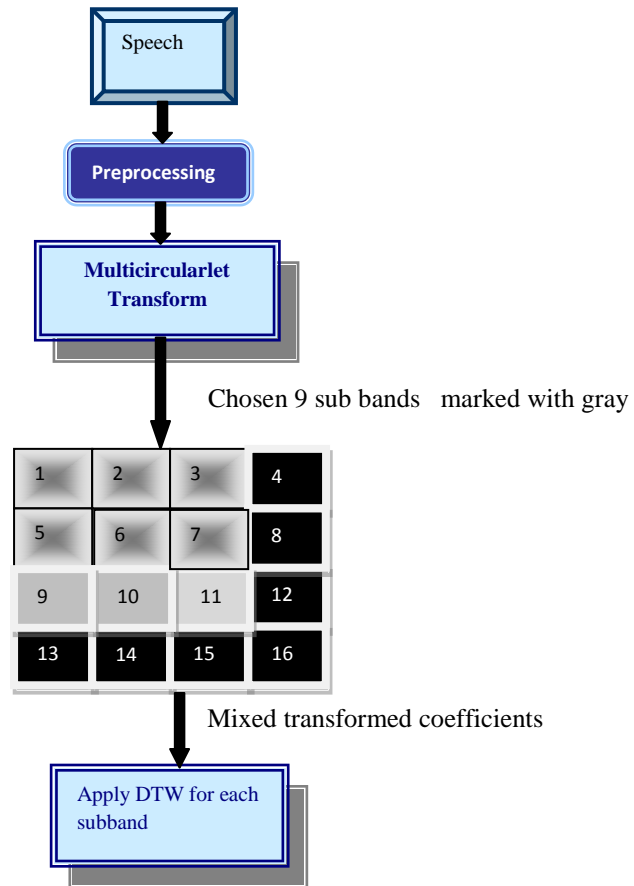


**Fig.7:-** The recognition steps using second mixed transform

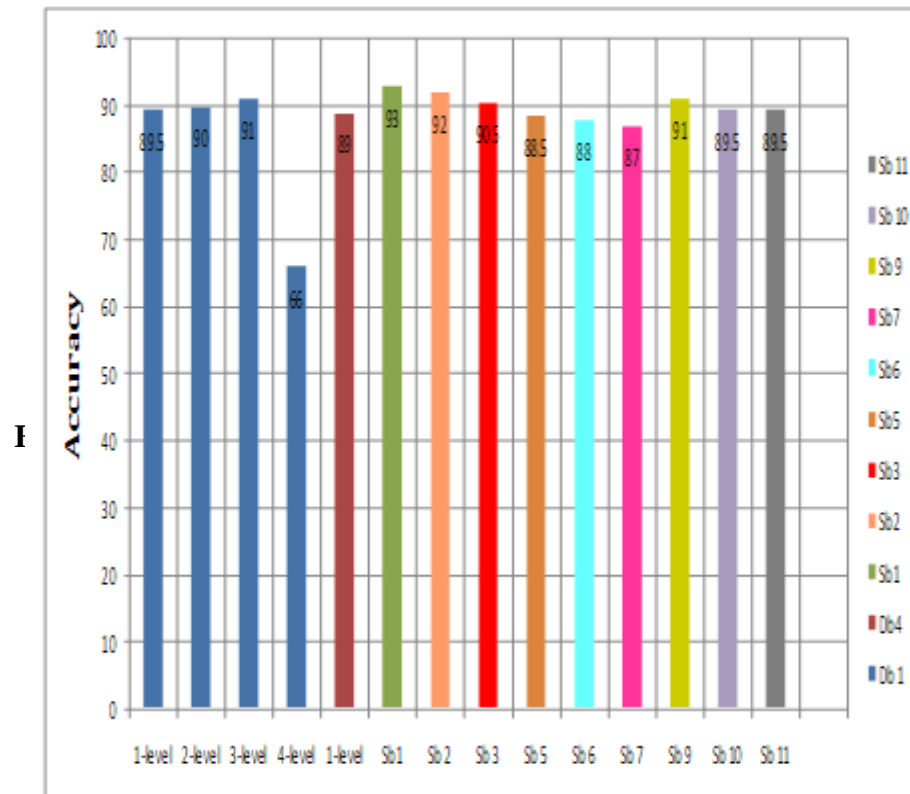


**Fig.8:-** The percentage of accuracy of each recognition system

**Table 1:** Comparison between the accuracy of different recognition system

Classification system	Total number of testing version	Total number of correct recognition	Accuracy
<u>First model</u>			
1-level Db1	200	179	89.5 %
2-level Db1	200	180	90 %
3-level Db1	200	182	91 %
4-level Db1	200	132	66 %
1-level Db4	200	178	89%
<u>Second model</u>			
sb1	200	186	93 %
sb2	200	184	92 %
sb3	200	181	90.5%
sb5	200	177	88.5%
sb6	200	176	88%
sb7	200	174	87%
sb9	200	182	91%
sb10	200	179	89.5%
sb11	200	179	89.5 %

# A Fuzzy Logic Controller Based Vector Control of IPMSM Drives

Asst. Prof. Afaneen Anwer Abbood

Electrical Engineering Department, University of Technology  
afaneenalkhazragy@yahoo.com

## ABSTRACT:

This paper explores a fuzzy-logic based speed controller of an interior permanent magnet synchronous motor (IPMSM) drive based on vector control. PI controllers were mostly used in a speed control loop based field oriented control of an IPMSM. The fundamentals of fuzzy logic algorithms as related to drive control applications are illustrated. A complete comparison between two tuning algorithms of the classical PI controller and the fuzzy PI controller is explained. A simplified fuzzy logic controller (FLC) for the IPMSM drive has been found to maintain high performance standards with a much simpler and less computation implementation. The Matlab simulink results have been given for different mechanical operating conditions. The simulated results confirmed that the FLC-PI has a lower ripple than the conventional PI controller.

**Keywords:** fuzzy logic controller, vector control, PID controller, IPMSM.

## محاكاة السيطرة باستخدام المنطق المضرب للمحركات التزامنية ذو المغناطيس الدائمي

أ.م.د. أفانين أنور عبود

قسم الهندسة الكهربائية / الجامعة التكنولوجية

### الخلاصة:

عرض هذا البحث وحدة تحكم السرعة في المكان التزامنية ذو مغناطيس الدائمي (PMSM) وفق سيطرة المتجه . ان وحدات تحكم السيطرة تستخدم PI التقليدي للسيطرة على سرعة المكان التزامنية ذو المغناطيس الدائمي. ان اساسيات خوارزميات المنطق المضرب قد تم تقديمها في هذا العمل لتحسين الاداء والحصول على تحكم بسرعة الماكينة بشكل افضل. حيث تم مقارنة كاملة بين المتحكم باستخدام PI الكلاسيكية مع المتحكم باستخدام قوانين المنطق المضرب. وكانت النتائج تبين ان المتحكم باستخدام المنطق المضرب ذو اداء عالي ناهيك عن بساطة تنفيذ الخوارزميات. هذا وقد أعطيت Matlab/SIMULINK نتائج جيدة لمحاكاة PI- FLC بعد ان تم تشغيل الموديل لظروف تشغيل ميكانيكية مختلفة .

### الكلمات الرئيسية:

المسيطر ذو المنطق المضرب، سيطرة المتجه، مسيطر PID، المكان التزامنية ذو المغناطيس الدائمي (PMSM).

## 1. INTRODUCTION

Power electronics system models are often ill-defined thus far. Even for a known plant there may be parameter variation problems. Vector or field- oriented control (FOC) of a drive can overcome this problem and it is very widely used for high performance PMSM drive applications as well; however an accurate vector control is quite difficult [Bilal, 2002]. The vector control is used to obtain the fast torque response for interior permanent magnet synchronous motor (IPMSM) drive, thus the current and speed controllers both play an important role for the drive performance [Blaschke, 1972].

PI controllers are mostly used for speed control due to their simple structure and also for providing a good performance over a wide speed range. However, tuning the PI controller is the main problem. The system parameters were changed through the operating conditions. In addition the PI control method is a linear control method and could not be worked with a discrete system.

A variety of control techniques have been developed to solve the aforementioned problems, offline PI and PID tuning, nonlinearity compensation, modeling, parameters estimation [Uddin et al. (2002), Rubaai (2002), Yubazaki (1993), Ko (1993), Wai (2001), Lin et al. (1998) and Jae et al. (2007)]. Among all of the control techniques Fuzzy Logic Control (FLC) was mostly utilized in industrial applications. FLC is an adaptive and nonlinear control method, which gives robust performance for a linear and nonlinear plant with parameter variation.

Recently, a fuzzy logic controller (FLC) has been widely applied in various drive applications including the speed control. The fault detection sensitivity is improved by using fuzzy logic controller [Quiroga et al., 2008]. Sometimes it is not easy to get a satisfied control characteristic by using normal linear PI controller because of the nonlinearity of the systems; hence an integral separated self-tuning fuzzy PI controller has been developed [Sun Qiang and Zhou, 2003]. The major feature of FLC's doesn't depend on the mathematical model of the plant

(which could be very complicated), but only on expert operator knowledge.

In this paper, a vector control scheme based on FLC for IPMSM drives is proposed. The control rules and the membership functions have been designed and explained.

## 2. PMSM MODELING

The space vector diagram is shown in Figure (1) the electrical equations for the IPMSM in the synchronously rotating frame (d-q) model are given as [Azizur Rahman et al., 2003]:

$$\begin{bmatrix} v_d \\ v_q \end{bmatrix} = R_s \begin{bmatrix} i_d \\ i_q \end{bmatrix} + \begin{bmatrix} L_d & 0 \\ 0 & L_q \end{bmatrix} \frac{d}{dt} \begin{bmatrix} i_d \\ i_q \end{bmatrix} + w_r \begin{bmatrix} -\lambda_q \\ \lambda_d \end{bmatrix} \quad (1)$$

$$\begin{bmatrix} \lambda_d \\ \lambda_q \end{bmatrix} = \begin{bmatrix} L_d & 0 \\ 0 & L_q \end{bmatrix} \begin{bmatrix} i_d \\ i_q \end{bmatrix} + \begin{bmatrix} -\lambda_m \\ 0 \end{bmatrix} \quad (2)$$

The electromagnetic torque  $T_e$  depends on the interlinkage flux and the difference between the d- and q-axis inductance ( $L_d$ - $L_q$ ) is given as:

$$T_e = \frac{3}{2} P [\lambda_m i_q - (L_q - L_d) i_d i_q] \quad (3)$$

The conventional control of IPMSM is done by linearizing the q-axis current expression by setting the d-axis current equal to zero. Then the electromagnet torque equation becomes:

$$T_e = \frac{3}{2} P \lambda_m i_q \quad (4)$$

$$\frac{dw_m}{dt} = (T_e - T_L - Bw_m) / J \quad (5)$$

$$\frac{d\theta_r}{dt} = w_r \quad (6)$$



### 3. SYSTEM DESCRIPTION

IPMSM is controlled by a Space vector PWM inverter [M.N. Uddin et al., 2000]. The motor drives a mechanical load characterized by moment of inertia (J), viscosity friction coefficient (B), and load torque (TL). The speed control loop uses a fuzzy logic controller instead of a simple proportional-integral PI controller to produce the quadrature-axis current (iq) which controls the motor torque whereas the motor flux is controlled by the direct-axis current (id). Figure (2) shows the block diagram of the standard PMSM drive system.

### 4. THE FUZZY CONTROLLER

Fuzzy logic is an extension of a multi-valued logic based on the theory with unshaped boundaries and in which membership is a matter of degree. The basic of fuzzy logic are linguistic variables, whose values are words rather than numbers [Dubois and Prade, 1980]. The first step for controller design is a determination of condition variable number and fuzzy partition of state space. From this, the membership function is given with the fuzzification. And then, a fuzzy inference is done by giving control input. Finally, defuzzification is needed to obtain the crisp control input. The coarse and fine rule tables given by off-line calculation are used to guarantee short sampling time. A rule in fuzzy logic can be based on the experience of experts and that it represents a combination of the operating system and quantitative knowledge of the motor conditions.

#### 4.1 Fuzzy Logic Controller Structure

FLC block diagram is illustrated in Fig.3 consists from four blocks:

- Fuzzification: transforms crisp to fuzzy input.
- Inference engine: decides which rules from knowledge base are fired.

-Defuzzification: transforms fuzzy output to crisp output.

-Knowledge base consists of rule base [Nguyen et al., 1995].

#### 4.1.1 Fuzzification

Fuzzification is the process of taking the numerical (crisp) value of a (crisp) variable and relating it to a fuzzy set through a membership function. In the FLC for PMSM drive, the error between the actual rotor speed and the reference speed command and the error during the sampling time are chosen for the condition variables.

The actual inputs to the fuzzy system are  $e_1$  and  $e_2$  which represent the speed error and the change in speed error respectively as defined by Eqs. (7) and (8). The gains  $G_1$  and  $G_2$  can be varied to tune the fuzzy controller for the desired performance [Uddin et al., 2002]. The output gain  $G_3$  can also be tuned.

$$\Delta \omega_r(n) = \omega_r(n) - \omega_r(n-1)$$

$$e_1(n) = G_1(\omega_r(n) - \omega_r(n-1)) \quad (7)$$

$$e_2(n) = G_2(\Delta \omega_r(n) - \Delta \omega_r(n-1))$$

$$e_2(n) = G_2(e_1(n) - e_1(n-1)) \quad (8)$$

In discrete form equation 8 becomes:

$$e_2(n) = G_2\left(\frac{e_1(n) - e_1(n-1)}{T_s}\right) \quad (9)$$

Using Z-transform

$$e_2(Z) = G_2\left(\frac{Z-1}{T_s Z}\right)e_1(Z) \quad (10)$$

Where  $T_s$  is the sampling time and  $G_1$  and  $G_2$  are the input scaling factors and  $k$  is the

output scaling factor. Their values affect the membership functions [10].

The output of the FLC is the torque producing current relating to the change in the torque producing current at the  $n$ -th sampling time, where  $k$  is the FLC gain as defined in Eq. (11) by:

$$i_q(n) = i_q(n-1) + k\Delta i_q(n) \quad (11)$$

In this system, the universe of discourse for  $e_1$ ,  $e_2$  as a control inputs are given as  $[-500 \ 500 \text{ rad/sec}]$ ,  $[-500 \ 500 \text{ rad/sec}^2]$ , respectively and the output variable as  $[-400 \ 400 \text{ A}]$ .

#### 4.1.2 Controller Linguistic Terms and Memberships Functions

A membership function is normally expressed graphically and tends to illustrate how completely a crisp variable belongs to a fuzzy set. Trapezoids and triangles are the two most popular membership functions. The ideal membership function is a bell-shaped curve with a Gaussian distribution. The trapezoid function comes fairly close to a bell-shaped curve and is a lot easier to implement and faster to execute. Five linguistic terms for each one of the input  $e_1(n)$ ,  $e_2(n)$  and the output  $\Delta i_q(n)$  are chosen. These terms are Negative Big(NB), Positive Big(PB), Negative Small(NS), Positive Small(PS), Zero(ZE). The memberships are shown in Fig.4 where the input  $e_1$  and  $e_2$  are normalized to the range  $[500,-500]$ . These memberships use a Gaussian membership function whereas a single spike is used for the output  $\Delta i_q(n)$  since the sugeno fuzzy system type is used to construct a fuzzy controller.

The fuzzy membership functions of the input variables and output variable are shown in Fig. 4a and 4b respectively, and the corresponding fuzzy logic rule is shown in Table (1).

The fuzzy rules have the form as :

Rule 1: IF is NB and is PB THEN is ZE ,

An easier way to visualize a 1<sup>st</sup> order system by defining the location of a moving singleton, means the singleton output spikes can move around linearly depending on the input signals (see Figure (5) which shown the ruler viewer). Nevertheless the control rules are contributed as follows [Jae et al., 2007]:

- a- When the actual rotor speed is lower than the reference value then  $\Delta i_q(n)$  should be large in order to bring the speed to the reference value.
- b- When the actual rotor speed is near to the reference speed then  $\Delta i_q(n)$  should be a little small.
- c- When the actual rotor speed approaching the reference speed is within a short time then  $\Delta i_q(n)$  should be kept constant so as to avoid the overshooting.
- d- When the actual rotor speed has the same value of the reference speed without a sensible changing then  $\Delta i_q(n)$  is required to be changed gradually to avoid the output from moving away.
- e- When the actual rotor speed reaches the reference value and remains steady then  $\Delta i_q(n)$  should remain unchanged.
- f- When the speed is higher than the reference speed  $\Delta i_q(n)$  should remain negative.

#### 4.1.3 Defuzzification

Defuzzification is the process of taking a fuzzy value and converting it into a numerical (crisp) value (quantifications). Defuzzification is required for generating a real-world output. Various methods have been used for defuzzification [Blaschke, 1972]. Among the defuzzification methods the sugeno method is very simple [Nguyen et al., 1995].

### 5. SIMULATION RESULTS

Table (2) shows the parameters of IPMSM which used in the simulation test. The



simulation has been carried out using Matlab/Simulink and Fuzzy Logic Toolbox. Speed and torque command transient responses to repetitive step changes in the speed command have been obtained for different load operating conditions and at nominal moment of inertia. The responses have been obtained for step speed commands (500rpm to -500rpm).

The FLC gains are affected on the membership functions, in this paper these gains are set  $G_1=2$ ,  $G_2=5$ ,  $G_3=150$ ,  $k=0.5$ ,  $T_s=100\mu\text{sec}$ . Under these values, a dequate response has been observed. The value of  $k$  affects the rise time while the small value of  $k$  increases the rise time. The dynamic response under different operating conditions is illustrated. Figures (6) and (7) show the step response of the speed and torque for the conventional PI controller for full-load and half-load operating conditions at nominal inertia for 500 to -500 rpm command. Figs. 8 and 9 show the step response of the FLC for full-load and half-load torque at nominal inertia for 500 to -500rpm. As shown in Figures (8) and (9), the dynamic response has a lower ripple than that for PI controller. It is obvious that also the proposed digital FLC system with FLC-PI is of better performance than the conventional PID controller. Furthermore, since the conventional PI speed controller is a linear controller the gain of the PI controller can not be varied. However, FLC is nonlinear can confirmed with the surface shown in Figs. 8c and Fig. 9c under half and full load operations.

## 6. CONCLUSION

This paper investigates the performance of a fuzzy logic controller (FLC) based on vector control method of an interior permanent magnet synchronous motor (IPMSM) for high performance industrial applications. The fundamentals of fuzzy logic algorithms as related to motor control applications are illustrated. The conventional control of IPMSM linearizes the q-axis current expression by setting the d-axis

current equal to zero. It is obvious from the simulated results that the proposed system with FLC is of better performance and be more robust for applications in IPMSM than the conventional PID controller. The simulation was done by using matlab/simulink.

## REFERENCES

- A. Rubaai, D. Rickattes, & M.D. Kankam, "Development and implementation of an adaptive fuzzy-neural network controller for brushless drives", IEEE Transactions on Industry Applications, 38 (2), 2002, 441–447.
- Bimal K. Bose, "Modern Power Electronic and AC Drives", ISBN 7-111-11296-2, Prentice Hall, Inc. 2002.
- D. Dubois, and H. Prade, Fuzzy Sets and Systems, "Theory and Applications", Academic Press, New York, 1980.
- F. Blaschke, "The principle of field orientation as applied to the new transvector closed-loop control system for rotating field machines", Siemens Review, 1972, 217–220.
- F.J. Lin & R.J. Wai, "Hybrid controller using a neural network for a PM synchronous servo-motor drive", IEE Proceedings Electric Power Applications, 145 (3), 1998, 223–230.
- H.T. Nguyen, M. Sugeno, R. Tong, & R.R. Yager, "Theoretical Aspects of Fuzzy Control", John Wiley & Sons, Inc., 1995.
- Jae-Sung Yu, Student, Sang-Hoon Kim, Byoung-Kuk Lee, Chung-Yuen Won, and Jin Hur, "Fuzzy-Logic-Based Vector Control Scheme for Permanent-Magnet Synchronous Motors in Elevator Drive Applications", IEEE TRANSACTIONS ON INDUSTRIAL ELECTRONICS, VOL. 54, NO. 4, AUGUST 2007.

J. Quiroga, Li Liu, and D. A. Cartes, "Fuzzy Logic based Fault Detection of PMSM Stator Winding Short under Load Fluctuation using Negative Sequence Analysis", 2008 American Control Conference USA, June 11-13, 2008.

J.S. Ko, J.G. Hwang, & M.J. Youn, "Robust position control of BLDD motors using integral-proportional plus fuzzy logic controller", Proc. IEEE IECON, 1993, 213–218.

M.N. Uddin, T.S. Radwan, & M.A. Rahman, "Performances of fuzzy logic based indirect vector control for induction motor drive", IEEE Transactions on Industry Applications, 38 (5), 2002, 1219–1225.

M. Azizur Rahman, D. Mahinda Vilathgamuwa, M. Nasir Uddin, and King-Jet Tseng, "Nonlinear Control of Interior Permanent-Magnet Synchronous Motor", IEEE TRANSACTIONS ON INDUSTRY APPLICATIONS, VOL. 39, NO. 2, MARCH/APRIL 2003.

M.N. Uddin, T.S. Radwan, G.H. George, & M.A. Rahman, "Performance of current-controllers for VSI-fed IPMSM drive", IEEE Transaction on Industry Applications, 36 (6), 2000, 1531–1538.

M. N. Uddin, T. S. Radwan, and M. A. Rahman, "Performances of fuzzy-logic-based indirect vector control for induction motor drive", IEEE Trans. Ind. Appl., vol. 38, no. 5, pp. 1219–1225, Sep./Oct. 2002.

N. Yubazaki, M. Otani, T. Ashida, & E. Kitamura, "Fuzzy motion drive method of induction motor using position sensor", Proc. IEEE IECON, 1993, 170–175.

R.J. Wai, "Development of intelligent position control system using optimal design technique", Power Electronics Specialists Conf., 2, 2001, 760–765.

Sun Qiang, Cheng Ming, and Zhou E, "Integral-Separated Self-Tuning Fuzzy PI Control of A Novel Doubly Salient Permanent Magnet Motor Drive", Electrical Machines and Systems, 2003. ICEMS 2003. Sixth International Conference on Volume 2, 9-11 Nov. 2003 Page(s), 570 – 573.

## LIST OF SYMBLES

$V_d, V_q$	Stator d-and q-axes voltages
$i_d, i_q$	Stator d-and q-axes currents
$\lambda_d, \lambda_q$	Stator d-and q-flux linkages
$\lambda_m$	Magnetic flux linkage
$R_s$	Stator resistance
$L_d, L_q$	Stator d-and q-axes inductances
$T_e, T_L$	Electromagnetic and load torque
$\omega_r$	Electrical rotor speed
$\omega_m$	Mechanical rotor speed
$P$	No. of pole pairs
$\theta_r$	Electrical rotor position
$J$	Rotary inertia
$B$	Friction coefficient
$T_s$	Samplingtime

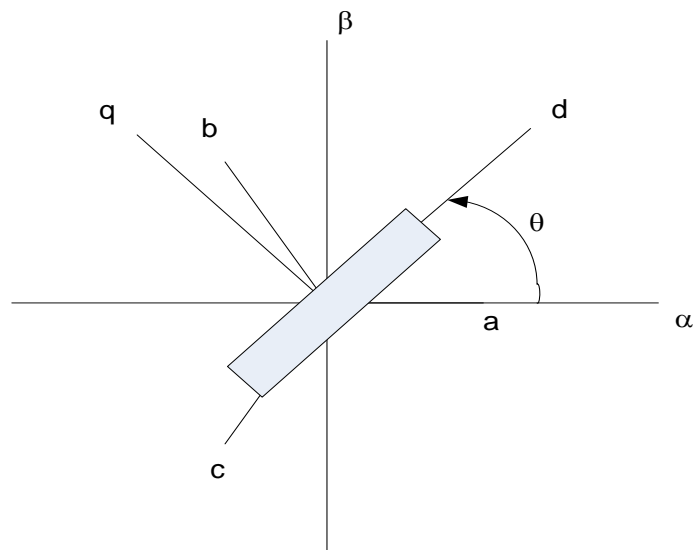


**Figure (1) Vector diagram of the PMSM**

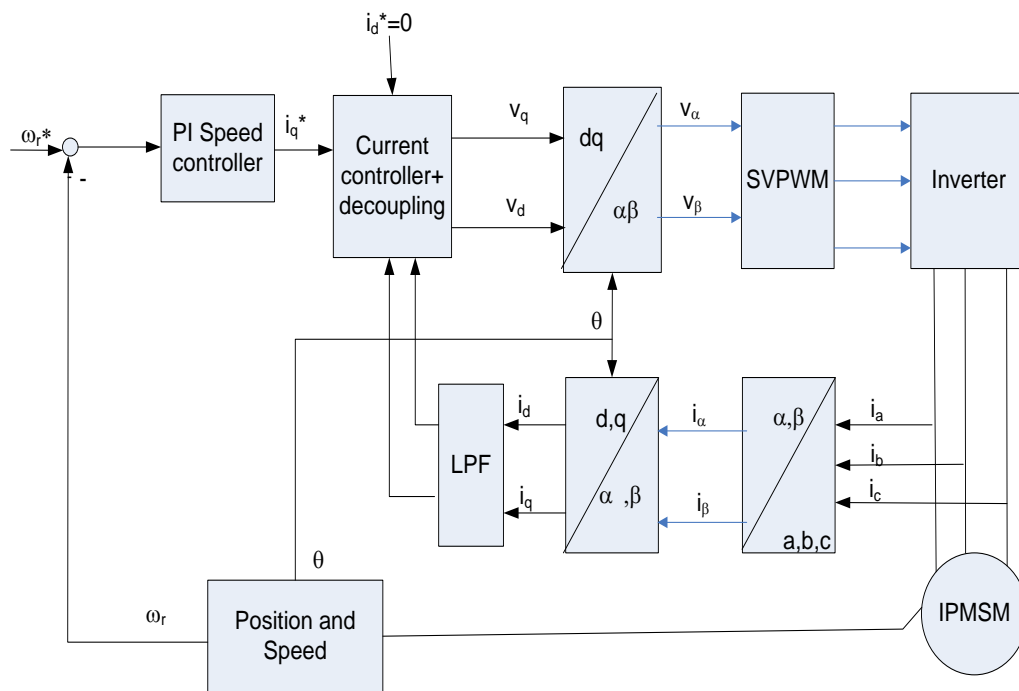
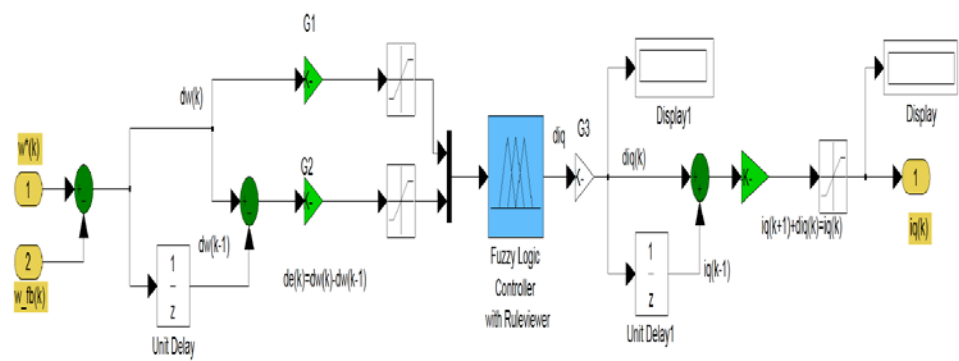
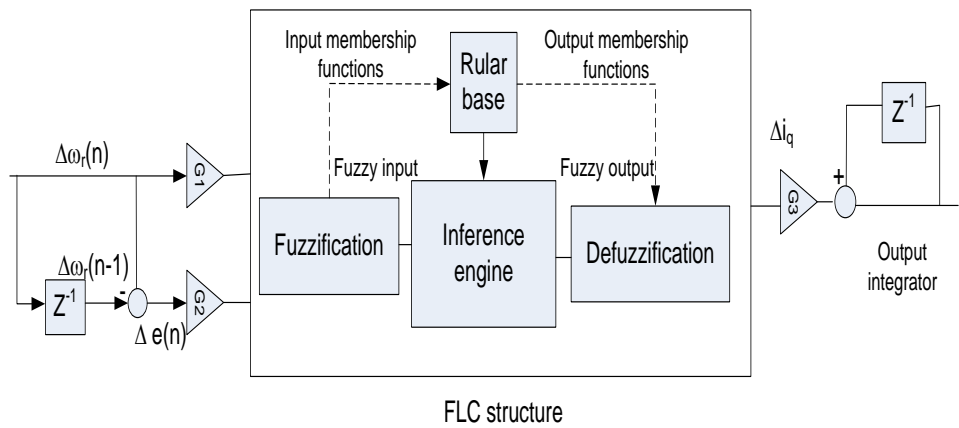


**Figure (2) Block diagram of standard PMSM control system**



(a) Matlab / Simulink for FLC



(b) FLC structure

Figure (3) FLC structure with Matlab/Simulink

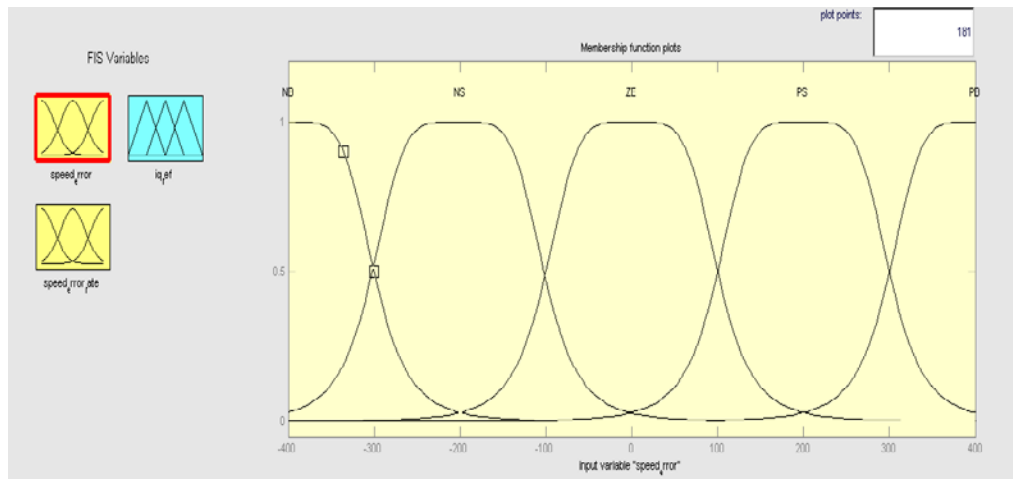


Figure (4, a) Input membership functions

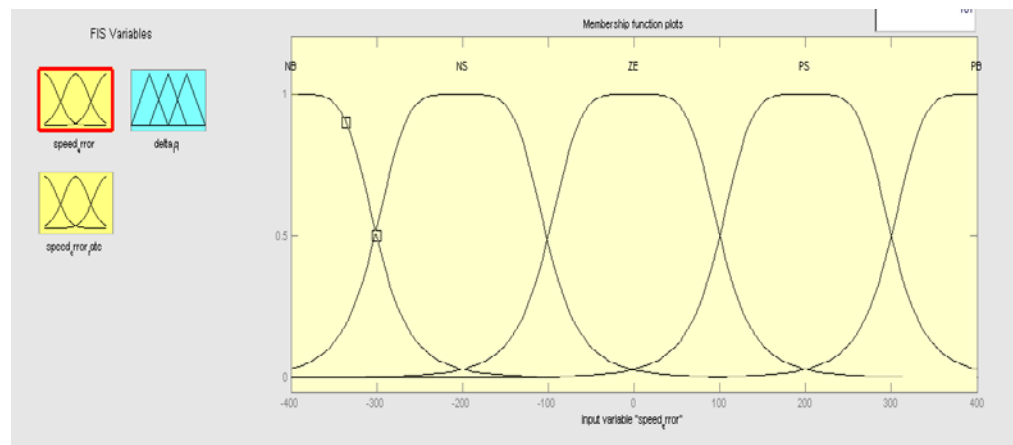


Figure (4, b) Output membership functions

Table (1) Fuzzy Controller Rules base

$\Delta i_q$		$e_1$				
		NB	NS	ZE	PS	PB
$e_2$	PB	ZE	PS	PS	PB	PB
	PS	NS	ZE	PS	PS	PB
	ZE	NS	NS	ZE	PS	PS
	NS	NB	NS	NS	ZE	PS
	NB	NB	NB	NS	NS	ZE

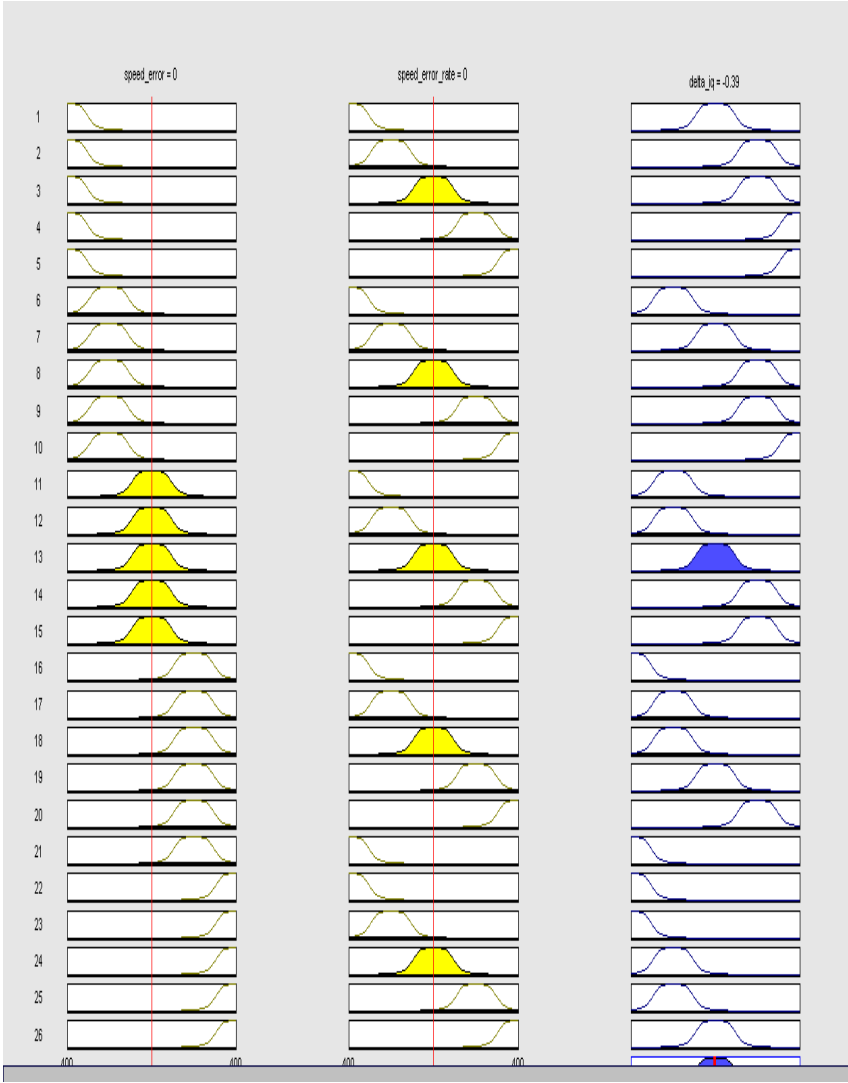
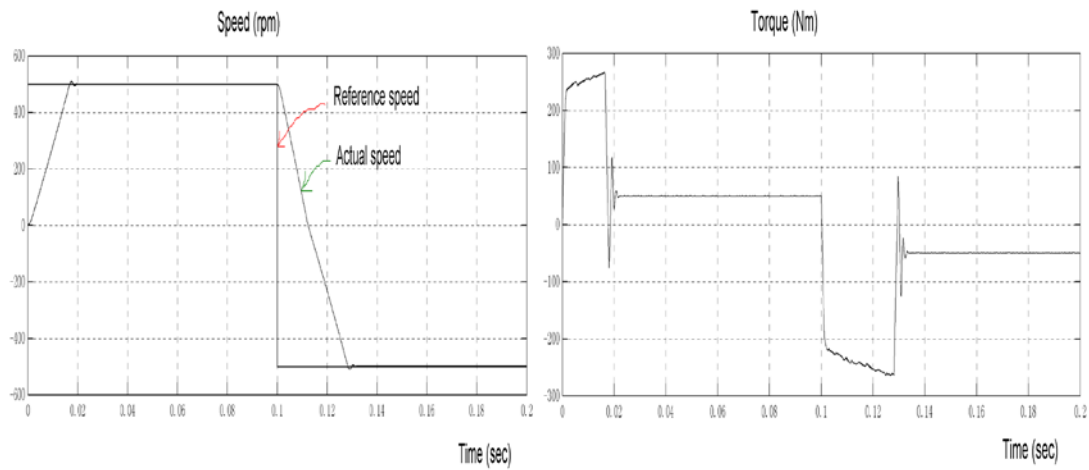


Figure (5) Ruler viewer

Table (2) IPMSM parameters

Pole-pairs	4	Stator resistance $R_s$	0.00402464 $\Omega$
d-axis inductance $L_d$	0.0986mH	Friction coefficient B	0.0001Nm/rad/sec
q-axis inductance $L_q$	0. 292723mH	Magnetic flux $\Phi_m$	0.0558537volts/rad/sec
Moment of inertia J	0.062kgm <sup>2</sup>		





**Figure (6) Conventional PI controller response for (500 to -500)rpm at 50%load. a-speed response, b-torque response c-idq currents.**

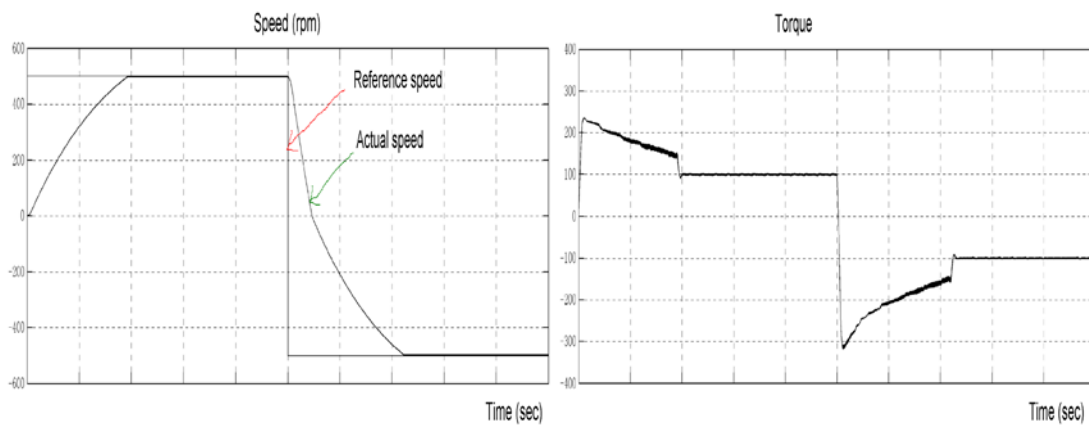


**Figure (7) Conventional PI controller response for (500 to -500) rpm at 100%load. a-speed response, b-torque response, c-idq currents.**

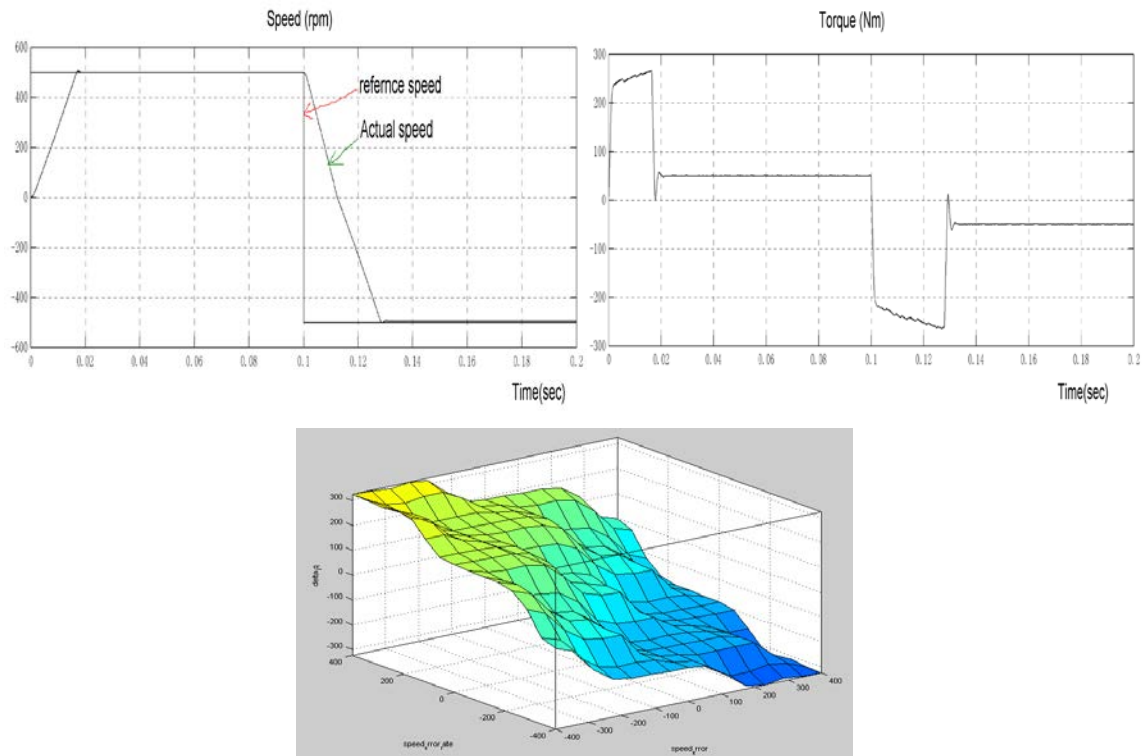


**Figure ( 8) The FLC responses for (500 to -500) rpm at 50% load torque. a- speed response, b-torque response, c-surface viewer**

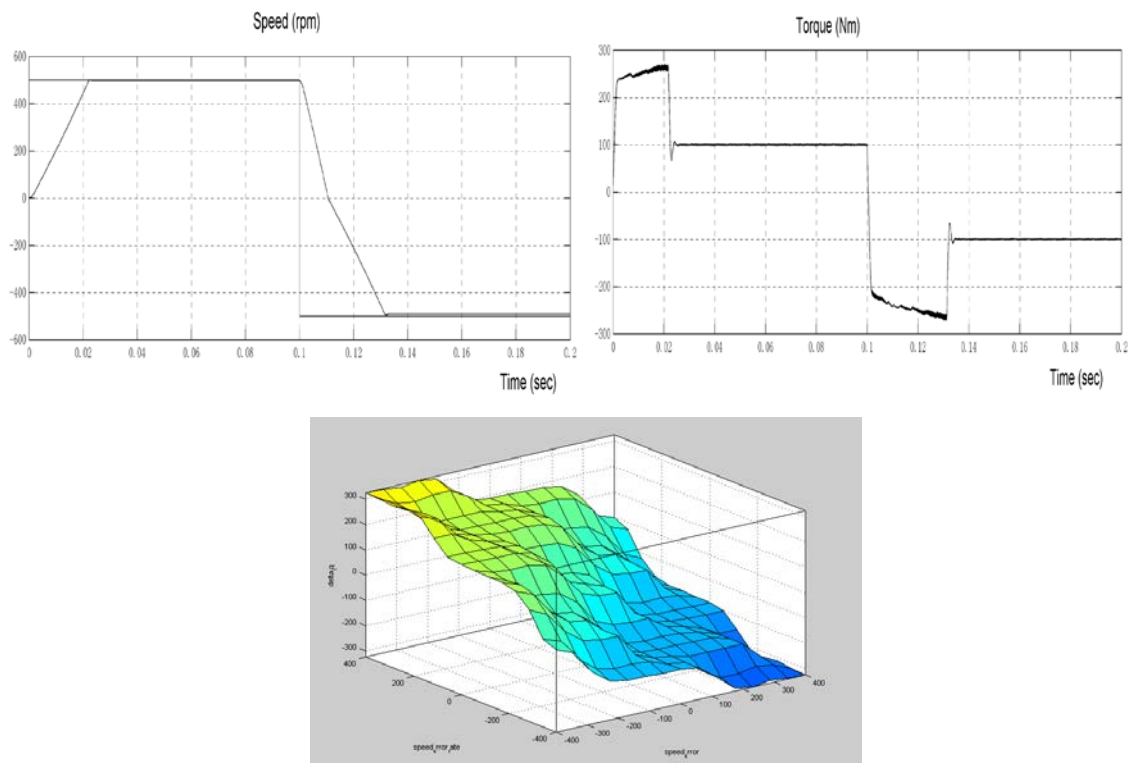


**Figure ( 9) The FLC responses at 100% load torque for (500 to -500) rpm. a- speed response, b-torque response, c-surface viewer**

## Simulation and Modeling of Detailed Load flow Analysis for the 400kVA and 132kVA Iraqi Grid

**Dr. Ahmed Abdul Sahib Hashim**

Computer Science Department

College of Science for Women, Baghdad University, Baghdad, Iraq

dreng.ahmed@yahoo.com

### ABSTRACT:

A load flow program is developed using MATLAB and based on the Newton–Raphson method, which shows very fast and efficient rate of convergence as well as computationally the proposed method is very efficient and it requires less computer memory through the use of sparsing method and other methods in programming to accelerate the run speed to be near the real time. The designed program computes the voltage magnitudes and phase angles at each bus of the network under steady–state operating conditions. It also computes the power flow and power losses for all equipment, including transformers and transmission lines taking into consideration the effects of off–nominal, tap and phase shift transformers, generators, shunt capacitors, shunt inductors, line reactors and bus reactors. Thus, overloaded transformers and transmission lines are identified, and remedial measure can be designed and implemented. It also provides the ability of tie lines, area splitting, and contingency analysis.

Any generator station(s) or busbar(s) that exceeds the specified operation limits will be automatically checked and flagged and then the program will automatically suggest the best solution to the problem. It also automatically checks whether the system is sub divided into sub areas or not. If yes, it will find the solution for each area separately. A complete report about the results and the state of the system (the violated generators, busbars, and transmission lines, the required modifications to overcome the violations, the names of the areas splitted,...) will be displayed in working window as well as generating a text file containing all details .

It is important to mention that this program is used by the national control center of the Ministry of Electricity and its efficiency was tested through applying the data of the two major Iraqi networks (400kV and 132kV), the program shows very accurate results and provides efficient notes about the status of the networks.

**KEYWORDS:** Load flow, tie lines, contingency analysis, Newton –Raphson method, MATLAB

### نمذجة ومحاكاة مفصلة لتحليل سريان الاحمال للشبكة العراقية 400kVA و 132kVA

د. أحمد عبدالصاحب هاشم

قسم علوم الحاسوب

كلية العلوم للبنات، جامعة بغداد، بغداد، العراق

#### المستخلص

تم بناء برنامج سريان الاحمال بأستعمال برنامج ماتلاب، وبالاغتماد على طريقة نيوتن رافسن (NR) لإيجاد الحل، والذي أظهر معدل سريع وفعال للتقارب وكذلك حسابيا فإن الطريقة المقترحة فعاله جدا وتتطلب ذاكرة حاسوب اقل من خلال استعمال التقانات الخاصه بالمصفوفات التي تحتوي عدد كبير من الازفار بالاضافه الى طرق اخرى في البرمجه لتسريع وقت التنفيذ لتقارب مع الوقت الحقيقي.

برنامج تدفق القدرة المصمم يقوم بحساب مقادير الجهد والطور في كل ناقل في الشبكة تحت ظروف تشغيل ثابتة. كما يقوم أيضا بحساب تدفق القدرة وخسائر القدرة في جميع المعدات، متضمناً المحولات وخطوط النقل آخذاً بنظر الاعتبار تأثير أنواع مختلفة من المحولات (off-nominal, tap, and phase-shift transformers)، المولدات، المتسعات، الملفات، رادات الخطوط وراتات النواقل. لهذا، فإن للبرنامج القدرة على تحديد المحولات وخطوط النقل التي تتجاوز حدود الحمل المحدد لها، مع إعطاء إجراءات علاجية ووقائية. إن البرنامج يتيح العمل والربط والتحليل للمناطق المنفصلة وتحليل حالات الطوارئ.

يقوم البرنامج بصورة أوتوماتيكية بالفحص والإعلام عن أي محطة توليد أو ناقلات كابلات تجتاز حدود التشغيل المحدده لها ومن ثم يقوم البرنامج باقتراح افضل الحلول البديلة للمشكلة. كما يقوم البرنامج أوتوماتيكا بفحص في ما اذا كانت المنظومة الكهربائية مؤلفة من منطقة واحدة أو مقسمة الى عدة مناطق. فإذا كانت مؤلفه من عدة مناطق يقوم بتحليل كل منطقة على حدة. البرنامج يقوم بعرض تقرير (بالإضافة الى توليد ملف) كامل عن النتائج وحالة النظام (أي تجاوزات للشروط المحدده للمولدات والناقلات وخطوط النقل والتغييرات المطلوبة لتلافي هذه التجاوزات بالإضافة الى إعطاء تسميات للمناطق المفصلة...)

أخيراً، من المهم ان نذكر ان البرنامج استعمل في مركز السيطره الوطني التابع لوزارة الكهرباء وإن كفاءة البرنامج تم اختبارها من خلال تطبيقها على منظومة اختبار قياسي وبعدها على أكبر شبكتين في العراق (400 كيلو فولت و 132 كيلو فولت). حيث أن البرنامج أعطى نتائج دقيقة وأعطى ملاحظات كفوءه عن حالة الشبكتين.

**كلمات البحث:** سريان الحمل، ربط التاي لاين، تحليل الطوارئ، نيوتن رافسون، ماتلاب

## 1. INTRODUCTION

Power flow analysis is the solution for the static operating condition of a power system [T. Gonen]. It is the most frequently performed of routine power network calculations in digital computers. Power flow analysis is used in power system planning, operational planning, and operations/control. It is also employed in multiple assessments, stability analysis, and system optimization [H. E. Brown].

The well-established power flow methods (Newton-Raphson N-R, Gauss-Seidel, and Fast-Decoupled) are all based on classical methodologies of applied mathematics. Classical computer programs for solving the power flow based on these methods have been in practical use for a relatively long number of years. All of these programs met with strict limitations to power network size and calculation speed [J. Mahseredjian]. With the development of object-oriented programming and operations methodology new boundaries are being set for power flow calculations [Bhabani Sankar Hota, Göran Andersson]. This paper presents fundamental concepts of applying object-oriented programming algebra to power system modeling of a package for the purposes of power flow, contingency, and tie line calculations.

This package is designed to perform a steady state analysis of a power transmission or distribution

network. The algorithm consists of an efficient and robust method based on the recursive solution of a full N-R AC Load flow. Because of the size and complexity of the problem much effort has been devoted to the improvement of convergence, reliability, accuracy, reduction of computation time and computer storage requirements.

This paper describes the implementation of N – R method to solve the load flow, contingency and tie lines problems using MATLAB software package all of them in one detailed program. It is subdivided into three parts; the first part presents the method used and the implementation of the algorithm. The second parts deals with the program structure and facilities. Finally the third part takes a case study to check the efficiency of the program with a given results and conclusions.

## 2. SOLUTION OF THE LOAD FLOW PROBLEM USING NEWTON-RAPHSON METHOD

The load flow problem can be solved by the Newton – Raphson (N-R) method using a set of nonlinear equations to express the specified real and reactive power in terms of bus voltages. The power at bus p is [T. Gonen , YongLi Zhu]:

$$P_p - jQ_p = E_p \times I_p \quad (1)$$

$$= E_p \times \sum_{q=1}^n Y_{pq} E_q \quad (2)$$

Where

$$E_p = e_p + jf_p, Y_{pq} = G_{pq} + jB_{pq}$$

Hence

$$P_p - jQ_p = (e_p - jf_p) \sum_{q=1}^n (G_{pq} + jB_{pq})(e_q + jf_q) \quad (3)$$

Separating the real and imaginary parts:

$$P_p = \sum_{q=1}^n \{e_p(e_q G_{pq} - f_q B_{pq}) + f_p(f_q G_{pq} + e_q B_{pq})\} \quad (4)$$

$$Q_p = \sum_{q=1}^n \{f_p(e_q G_{pq} - f_q B_{pq}) - e_p(f_q G_{pq} + e_q B_{pq})\} \quad (5)$$

The N-R method requires that a set of linear equations be formed expressing the relationship between the changes in real and reactive powers and the components of bus voltages.

Note that  $P_i$  and  $Q_i$  are functions of  $e_i$ ,  $e_j$ ,  $f_i$ , and  $f_j$ . For each PQ load bus,  $P_i$  and  $Q_i$  can be calculated from eq. (3), for some estimated values of  $e$  and  $f$ . After each iteration, the calculated values of  $P_p$  and  $Q_p$  are compared against the known (or specified) values of  $P_s$  and  $Q_s$ . also, for each PV generator bus, the magnitude of the bus voltage can be calculated from the estimated values of  $e$  and  $f$  as

$$|V_p|^2 = e_p^2 + f_p^2 \quad (6)$$

Then the calculated voltage magnitude is compared with its specified value. Therefore, the corrected values for the  $k^{\text{th}}$  iteration can be expressed as

$$\Delta P_p^{(k)} = P_s - P_p^{(k)} \quad (7)$$

$$\Delta Q_p^{(k)} = Q_s - Q_p^{(k)} \quad (8)$$

$$\Delta |V_p|^2 = |V_s|^2 - |V_p|^2 \quad (9)$$

The resultant values of  $\Delta P_p^{(k)}$ ,  $\Delta Q_p^{(k)}$ , and  $\Delta |V_p|^2$  can be used to determine the changes in the real and imaginary components of the bus voltages. Since the changes in  $P$ ,  $Q$ , and  $V^2$  are related to the changes in  $e$  and  $f$ , it is possible to express them in a general form as:

$$\begin{bmatrix} \Delta P_2^{(k)} \\ \vdots \\ \Delta P_n^{(k)} \\ \Delta Q_2^{(k)} \\ \vdots \\ \Delta Q_{m-1}^{(k)} \\ \Delta |V_m|^2 \\ \vdots \\ \Delta |V_n|^2 \end{bmatrix} = \begin{bmatrix} \frac{\partial P_2}{\partial e_2} & \cdots & \frac{\partial P_2}{\partial e_n} & \frac{\partial P_2}{\partial f_2} & \cdots & \frac{\partial P_2}{\partial f_n} \\ \vdots & \vdots & \vdots & \vdots & \vdots & \vdots \\ \frac{\partial P_n}{\partial e_2} & \cdots & \frac{\partial P_n}{\partial e_n} & \frac{\partial P_n}{\partial f_2} & \cdots & \frac{\partial P_n}{\partial f_n} \\ \frac{\partial Q_2}{\partial e_2} & \cdots & \frac{\partial Q_2}{\partial e_n} & \frac{\partial Q_2}{\partial f_2} & \cdots & \frac{\partial Q_2}{\partial f_n} \\ \vdots & \vdots & \vdots & \vdots & \vdots & \vdots \\ \frac{\partial Q_{m-1}}{\partial e_2} & \cdots & \frac{\partial Q_{m-1}}{\partial e_n} & \frac{\partial Q_{m-1}}{\partial f_2} & \cdots & \frac{\partial Q_{m-1}}{\partial f_n} \\ \frac{\partial |V_m|^2}{\partial e_2} & \cdots & \frac{\partial |V_m|^2}{\partial e_n} & \frac{\partial |V_m|^2}{\partial f_2} & \cdots & \frac{\partial |V_m|^2}{\partial f_n} \\ \vdots & \vdots & \vdots & \vdots & \vdots & \vdots \\ \frac{\partial |V_n|^2}{\partial e_2} & \cdots & \frac{\partial |V_n|^2}{\partial e_n} & \frac{\partial |V_n|^2}{\partial f_2} & \cdots & \frac{\partial |V_n|^2}{\partial f_n} \end{bmatrix} \times \begin{bmatrix} \Delta e_2^{(k)} \\ \vdots \\ \Delta e_n^{(k)} \\ \Delta f_2^{(k)} \\ \vdots \\ \Delta f_n^{(k)} \end{bmatrix} \quad (10)$$

Where the coefficient matrix is the jacobian and the 1<sup>st</sup> bus is the slack bus.

Equations for determining the elements of the jacobian can be derived from the bus power equations. The real and reactive power from eq.(4) and eq. (5) is:

$$Q_p = f_p(e_p G_{pp} - f_p B_{pp}) + e_p(f_p G_{pp} + e_p B_{pp}) + \sum_{q=1}^n \{f_p(e_q G_{pq} - f_q B_{pq}) - e_p(f_q G_{pq} + e_q B_{pq})\} \quad (11)$$

$$q \neq p, p = 1, 2, \dots, n-1$$

$$P_p = e_p(e_p G_{pp} - f_p B_{pp}) + f_p(f_p G_{pp} + e_p B_{pp}) + \sum_{q=1}^n \{e_p(e_q G_{pq} - f_q B_{pq}) + f_p(f_q G_{pq} + e_q B_{pq})\} \quad (12)$$

$$q \neq p, p = 1, 2, \dots, n-1$$

Differentiating the off-diagonal elements of eq. (11), and eq. (12) then:

$$\frac{\partial P_p}{\partial e_q} = e_p G_{pq} + f_p B_{pq} \quad q \neq p$$

$$\frac{\partial P_p}{\partial f_q} = -e_p B_{pq} + f_p G_{pq} \quad q \neq p$$

$$\frac{\partial Q_p}{\partial e_q} = -e_p B_{pq} + f_p G_{pq} \quad q \neq p$$

$$\frac{\partial Q_p}{\partial f_q} = -e_p G_{pq} - f_p B_{pq} \quad q \neq p \quad (13)$$

Differentiation the diagonal elements of eq. (11), and eq. (12) then:

$$\begin{aligned}\frac{\partial P_p}{\partial e_p} &= 2e_p G_{pp} - f_p B_{pp} + f_p B_{pp} + \sum_{\substack{q=1 \\ q \neq p}}^n (e_q G_{pq} - f_q B_{pq}) \\ \frac{\partial P_p}{\partial e_p} &= -e_p B_{pp} + 2f_p G_{pp} + e_p B_{pp} + \sum_{\substack{q=1 \\ q \neq p}}^n (f_p G_{pq} + e_p B_{pq}) \\ \frac{\partial Q_p}{\partial e_p} &= f_p G_{pp} - f_p G_{pp} - 2e_p B_{pp} - \sum_{\substack{q=1 \\ q \neq p}}^n (f_p G_{pq} + e_q B_{pq}) \\ \frac{\partial Q_p}{\partial f_p} &= e_p G_{pp} - 2f_p B_{pp} - e_p G_{pp} + \sum_{\substack{q=1 \\ q \neq p}}^n (e_p G_{pq} - f_q B_{pq})\end{aligned}\quad (14)$$

The equation for the current at bus p is:

$$I_p = c_p + j d_p = (G_{pp} + j B_{pp})(e_p + j f_p) + \sum_{\substack{q=1 \\ q \neq p}}^n (G_{pq} + j B_{pq})(e_q + j f_q) \quad (15)$$

Hence

$$c_p = e_p G_{pp} - f_p B_{pp} + \sum_{\substack{q=1 \\ q \neq p}}^n (e_q G_{pq} - f_q B_{pq}) \quad (16)$$

$$d_p = f_p G_{pp} + e_p B_{pp} + \sum_{\substack{q=1 \\ q \neq p}}^n (f_q G_{pq} + e_q B_{pq}) \quad (17)$$

Substituting eq.(16) and eq.(17) in eq.(11) and eq.(12), then:

$$\begin{aligned}P_p &= e_p c_p + f_p d_p \\ Q_p &= f_p c_p - e_p d_p\end{aligned}\quad (18)$$

and eq. (14) will be:

$$\begin{aligned}\frac{\partial P_p}{\partial e_p} &= e_p G_{pp} + f_p B_{pp} + c_p \\ \frac{\partial P_p}{\partial f_p} &= -e_p B_{pp} + f_p G_{pp} + d_p \\ \frac{\partial Q_p}{\partial e_p} &= -e_p B_{pp} + f_p G_{pp} - d_p \\ \frac{\partial Q_p}{\partial f_p} &= -e_p G_{pp} - f_p B_{pp} + c_p\end{aligned}\quad (19)$$

Given an initial set of bus voltages, the real and reactive powers are calculated from eq. (18). The change in power is the difference between the specified and calculated values:

$$\begin{aligned}\Delta P_p^k &= P_s - P_p^k & p = 1, 2, \dots, n-1 \\ \Delta Q_p^k &= Q_s - Q_p^k & p = 1, 2, \dots, n-1\end{aligned}\quad (20)$$

The estimated bus voltages and calculated powers are used to compute bus currents in order to evaluate the elements of the jacobian. The linear set of eq.(10) can be solved for  $\Delta f_p$  and  $\Delta e_p$ ,  $p=1, 2, \dots, n-1$ , by a direct or iterative methods. Then, the new estimates for bus voltages are:

$$e_p^{k+1} = e_p^k + \Delta e_p^k \quad (21a)$$

$$f_p^{k+1} = f_p^k + \Delta f_p^k \quad (21b)$$

The process is repeated until  $\Delta P_p^k$ ,  $\Delta Q_p^k$ , and  $|\Delta V_p|^2$  for all buses are within a specified limit.

### 3. PROBLEM FORMULATION

The Newton-Raphson method is a very powerful load flow solution technique that incorporates first-derivative information when computing voltage updates. Normally, only 3 to 5 iterations are required to solve the load flow problem, regardless of system size (It is generally quadratic in convergence) [Mbuli].

Typically the power flow is formulated to minimize the production cost and satisfy some constraints, including entire power flow equations, generation limits, voltage ranges and line transfer capability... etc.

The general steps for problem formulation are goes in the following sequence [M. delimar, Ian A. Hiskens]

1. Inputting the data
2. Converting the transformers (phase-shift transformers and tap transformers) to their  $\pi$  - equivalent.
3. Performing contingency analysis (removing transmission lines, busbars, and/or generators) if it is required.
4. Y-matrix formulation (admittance) for the area and for each area in case of area splitting.
5. Starting the iterative solving algorithm program (Newton Raphson method).
6. If the parameters converged within the specified tolerance then stop the iteration and print the results else continue with the iterative method of step 4.

7. Flagging the generators, that violated their reactive generation limit and then finding the correct operating voltage of the generators that maintain the reactive generation of the generators within the limit. This is can be done by converting the violated P-V busbars to P-Q busbars and the reactive power demand at these busbars are set equal to negative of the violated limit. The program (step 5) is run again to solve for the voltage magnitude at these busbars.
8. Flagging the busbars which violated their voltage magnitude limit then finding the required per unit MVAR that have to be connected at the violated busbars to bring the voltages back within the limits. Converting the violated P-Q busbars to P-V busbars, setting the violated busbars to the violated voltage limit, does this and the power generation at these busbars is set equal to zero. The program (step 5 for Newton Raphson method) is run again to solve for the generation reactive powers at these busbars.
9. Modifying the system (setting the new values of voltages for the violated P-V busbars and adding the MVAR to the violated P-Q busbars) the program will run again (step5) and finds the final results
10. Repeat step 4 for the next area in case of area splitting.
11. End

The program was written in a structured format. It asks the user to supply the name of the text file that contains the input data. The expected output will be two text files provide a record of all the results one for the flow results while the other for the bus results a third text file may be generated if we have tie lines. The sequence of steps for the load flow solution is shown in flowchart (see figure 1)

#### 4. PACKAGE STRUCTURE

The package has the following options:

##### I- Load Flow Analysis

This function starts the execution of the program without the facilities of contingency and tie line but with the optional system correction facility.

##### II- Contingency Analysis

This function starts the execution of the program without the facility of tie line but with the contingency and the optional system correction facilities. In this case the outage of branches, buses

(with all connected lines), and the outage of generation stations are permissible for the user through the execution of the program. For the purpose of planning, control, fault estimation...etc

#### III- Tie Line Analysis

This function starts the execution of the program without the facility of contingency but with the tie line and the optional system correction facilities.

Large-scale power systems usually consist of several, or perhaps many, individual electric utility companies. In these cases, each area may have a desired net input or output power to satisfy sales and purchase agreements. The area interchange feature in a load flow program sums the tie line lows into each area for a net area power input. If these nets are not the desired values, to within a few megawatts, then an area-control generator within the area is adjusted by the error amount. The sum of all input powers for all areas must, of course, be zero [De Oliveira].

#### 5. PACKAGE FACILITIES

Some of the important facilities of the package are

##### a) Input Data File

Is a text file, which contains detailed information about the network to be solved (buses, branches, capacitors, reactors, tap changers (for all types of transformers), cables).

##### b) Voltage and VAR Compensation

This paper looks at the problem of placing Static VAR Compensators (SVC) to provide maximum transfer capability for all possible generation mixes. The margin to low voltage limit is one of the quantities used to determine power system transfer capability. A fast method for finding the location of SVC systems that will have the greatest impact on the low voltage margin is used.

The program asks the user whether he wants the program automatically diagnose the network violations after convergence to the solution within the specified tolerance or not, if yes, it will check and flag any violation in busbars voltages (in case of load busbars) and generators reactive power (in case of generator busbars), after that it will automatically fix them and gives the best solution to the problem then repeat solving of the network with the suggested modification without clearing the previous (actual) results.



**c) Splitting (Self Insertion)**

This software is designed to automatically identify the electrical island and nodal connectivity of a network. It checks the network whether it is subdivided into areas or not and tell the user if yes with the display of the names of each area busbars, then tell the program to run each area alone with the monitoring of each area selected slack busbare.

**d) Multi Area**

The software takes into consideration the case of tie lines and the problem of power transfer between countries.

**e) Output Reports**

The output results consists of two reports (three in case of tie line) one for bus results showing generated and/or consumed power at each busbare, also shows the removed buses or transmission lines in case of contingency analysis and the results of each area in case of area splitting all of these information are shown before and after modification (compensation) in case of voltage or Q violation. The second report for the flow results showing the power flow and losses in the transmission lines, also shows and flag the overloaded transmission lines (lines that exceed the rated MVA of the line), all of these information are shown before and after modification (compensation) in case of voltage or Q violation. The third report is automatically generated in case of multi area (tie line), which contains information about the required modification on the areas regulating generators in order to give the specified power transfer.

**f) User Error Detection**

When the user inputs any invalid, or out of range data the program flags theses errors for example, in contingency analysis, when the user try to remove a branch and he enters the sending and receiving buses of not found branch, the program will flag this entrance error, also when the user try to remove a generation station, or part of the generation, the program display an error message when the entered busbare identifier is not generator busbare or when the required amount of generation is out of the generation capability, and so on.

**g) Visual Display**

The package provide a visual link with the user, for example, figure 2 shows the main menu of choices which appear for the user when he starts the execution of the program, clicking any one of these three choices will make the package execute the

corresponding program, when the user clicks "CONTINGENCY" bottom, another menu will appear (figure 3) asking him to choose which type of contingency he wants to done, if he clicks "REMOVING BUSBARS" for example, a third menu will appear (figure 4) asking him to enter the number of busbars he wants to remove, and so on.

**6. CASE STUDY**

To demonstrate the application of power for analyzing the performance of a power system, a 15-bus test system is considered [M. Kezunovic]. The one-line diagram of the test system is shown in figure 5. The system power base used is 100 MVA, and the voltage bases are selected to match the nominal voltages in various parts of the system. The input data file are provided in figure 6 in which transformer data of fixed-tap, which is set at 100%, and the percent resistances and reactances given are based on the device ratings, the system load data, and the system generator data are shown also. The generators at buses 1 and 4 represent in-feeds from the neighboring power system that is charged with the bulk-power generation and transmission in the region. The South generator is connected to bus 1, which is chosen as slack bus.

The transmission line parameters are calculated and converted to per unit based on the chosen bases. The transformer impedances are also automatically converted to per unit based on system bases. The load data and generator data are, likewise, automatically converted to system bases. The system input bus data are given in which a "flat voltage" start is assumed; that is, the voltage phase angle at each bus is set equal to zero, while the voltage magnitude at each load bus is set equal to 1.0 per unit. The voltage at each generator bus is held at the specified value provided the generator reactive power stays within specified minimum and maximum limits.

The test system was analyzed using the software package. A converged solution was reached in 3 iterations. The bus data from the converged solution are shown in figure 7. Figure 8 shows another results when bus 12 is removed through the application of contingency analysis program.

**7. RESULTS**

The program flagged the West generator as having violated its reactive generation limit. As can be seen from figure 6, the reactive power generated by the West generator is 1.18 per unit, exceeding its upper limit of 0.9 per unit. This means that the specified voltage at bus 13 is too high, and the

generator cannot maintain it at this level. To find the correct operating voltage of the generator, the P-V bus 13 is automatically (if we choose the correction facility of the package) converted to a P-Q bus and the reactive power demand at this bus is set equal to the negative of the violated limit  $Q_G^{\max}$ , or  $-0.90$  per unit. The program was run again to solve for the voltage magnitude at this bus. It was found to be 1.00 per unit.

The program also automatically checks all bus voltages and flags those that are less than 0.95 per unit or higher than 1.05 per unit. The voltages at load buses 14 and 15 are 0.935 and 0.922 per unit, respectively, which are both less than the minimum allowable level of 0.95 per unit. These P-Q buses are converted to P-V buses, with their power generations set equal to zero. The voltage magnitudes are set equal to the violated limit  $V_{\min}$ , or 0.95 per unit. The program is run again to find the generator reactive powers at buses 14 and 15. These are equal to the per-unit MVAR of the capacitors that have to be connected at the two buses to bring the voltages back within limits. These are 0.116 per unit and 0.139 per unit for buses 14 and 15, respectively.

Finally, with the generator voltage at bus 13 set to 1.00 per unit and capacitors of 0.116 and 0.139 per unit MVAR connected to buses 14 and 15, respectively, the program was run again. The final bus results are presented in figure 7 also. It may be noted that all previous constraint violations have been resolved. Another set of results (not shown in this paper) is available considering the power flow and losses through the transmission lines before and after correction of the system.

Figure 8 shows the results when we remove bus 12 from the network (see figure 5). The results show that due to the removal of this bus (with all its connections): bus 13 is disconnected from the circuit and hence removed from the analysis of the system (because it has no effect on the system) also the results show that the system is divided into two areas, the first one with first 11 buses and the second with two buses (14, 15). Here, the contingency analysis is performed without the facility of correction. Also there is another set of results (not shown in this paper) that show the power flow and losses through the transmission lines also shows the removed busbars.

## 8. CONCLUSION

In this paper effective power system operation requires power system engineers and operators to analyze vast amounts of information. In systems containing thousands of buses, a key challenge is to present this data in a form such that the user can assess the state of the system in an intuitive and quick manner. This is particularly true when trying to analyze relationships between actual network power flows, the scheduled power flows, and the capacity of the transmission system. With restructuring and the move towards having a single entity, such as an independent system operator or pool, operate a much larger system; this need has become more acute. This paper presents power system visualization technique to help in this task.

One contribution of the paper is introducing an efficient power flow model; obviously much computing time is saved. By observation, the time of computing the whole program running time. The efficiency is shown by comparison with a MATLAB based programming. The developed program based on Newton method is promising to be used to solve the load flow problem of large size practical power system because of its high efficiency in modeling power system and computing the Jacobian of power flows.

## REFERENCES

Bhabani Sankar Hota and Amit Kumar Mallick, "load flow study in power system", Thesis, National Institute of Technology, Rourkela, India, April 2011

De Oliveira,...*etal*, "Distribution power flow method based on a real quasi-symmetric matrix", Journal: Electric Power Systems Research, Volume: 95, 2013, P 148-159 provider: Elsevier

Göran Andersson, "Modelling and Analysis of Electric Power Systems", lecture 227-0526-00, ITET ETH Zürich, EEH - Power Systems Laboratory, ETH Zürich, September 2008

H. E. Brown, "Solution of Large Networks by Matrix Methods", 2nd edition, JOHN WILEY & SONS, INC, 1985.

Ian A. Hiskens, "Power Flow Analysis", Department of Electrical and Computer Engineering, University of Wisconsin – Madison, November 6, 2003

J. Mahseredjian, F. Alvarado, G. Rogers, and W. Long, "MATLAB's Power for Power Systems", IEEE Computer Applications in Power, Vol. 14, No. 1, Jan. 2001, P13 – 19.

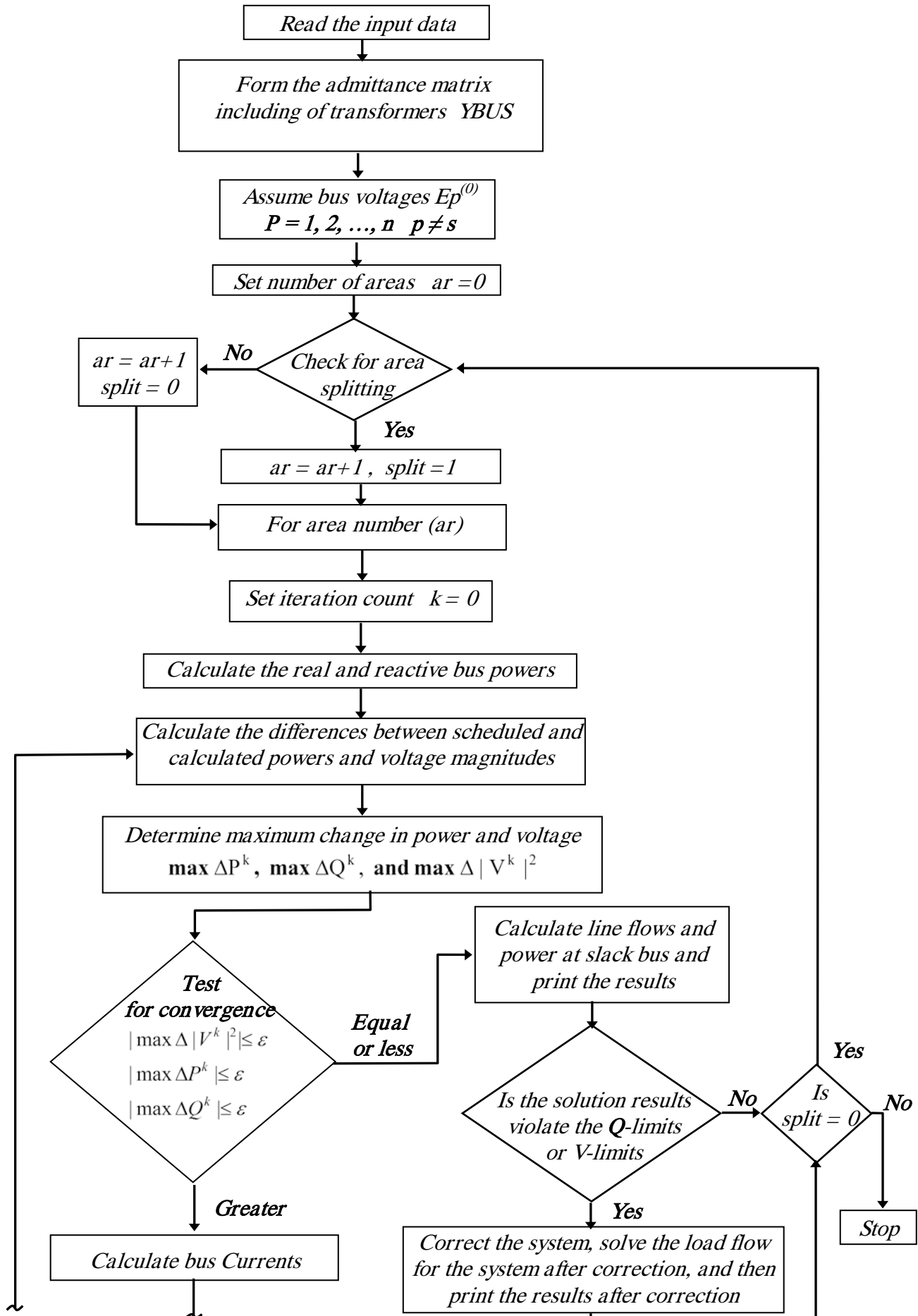
Mbuli, N., Pretorius, ...*etal*, " Network studies for the interconnection of a concentrating solar power plant in a weak distribution network in the Uington area", Journal: IEEE Africon vol. 11, 2011, P 1- 6

M. delimar, Z. Hebel, and I. Pavic, "Power System Modelling for Object – Oriented Power flow", International Journal for ENGINEERING MODELLING, Vol. 11, No. 1 – 2, 1998.

T. Gonen, "Modern Power System Analysis", JOHN WILEY & SONS, INC, 1988

YongLi Zhu and JianGuo Yao, " An Improved Newton Load Flow for Distributed Generation Based on Different Control Strategies", Journal: IEEE, Asia-Pacific Power and Energy Engineering Conference, 2011, P 1-5

M. Kezunovic, "Advanced Power Engineering Education Using Digital Simulation," CIGRE Workshop, 1998 CIGRE General Session, Paris, France, September 1998.



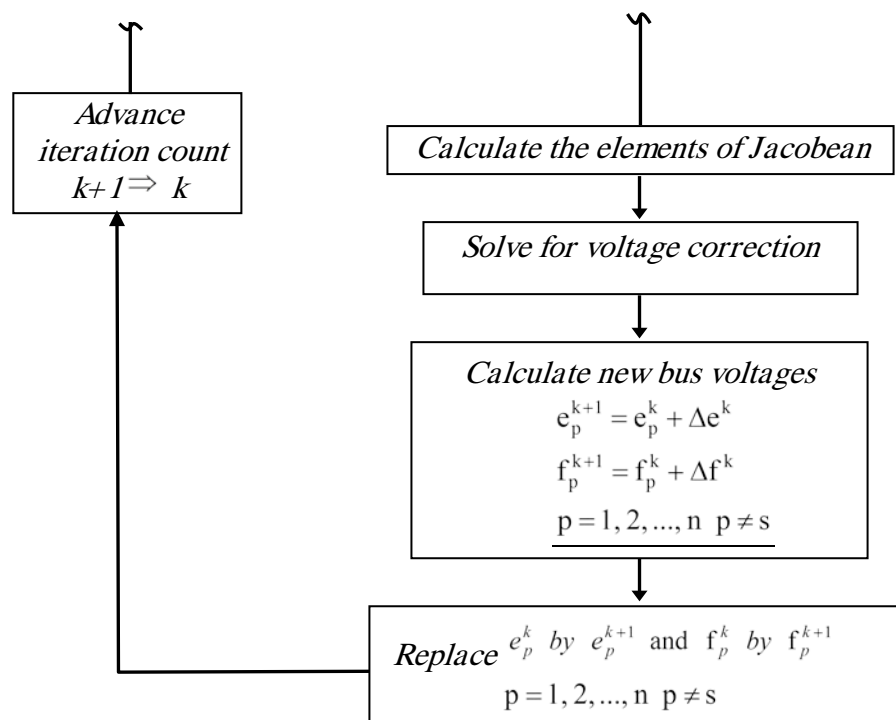


Figure 1 Flow chart of Newton – Raphson method

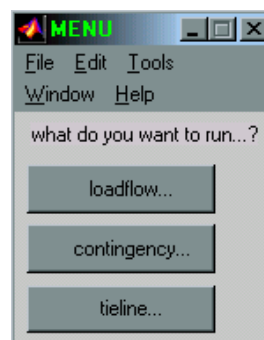


Figure 2 Software Main Menu of Choices

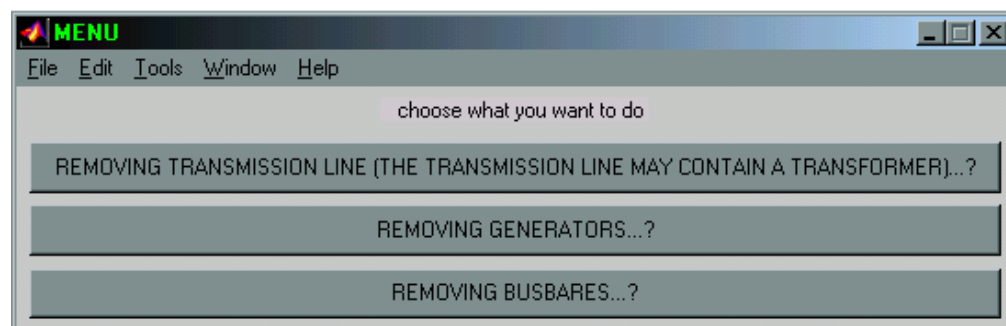


Figure 3 Contingency Main Menu

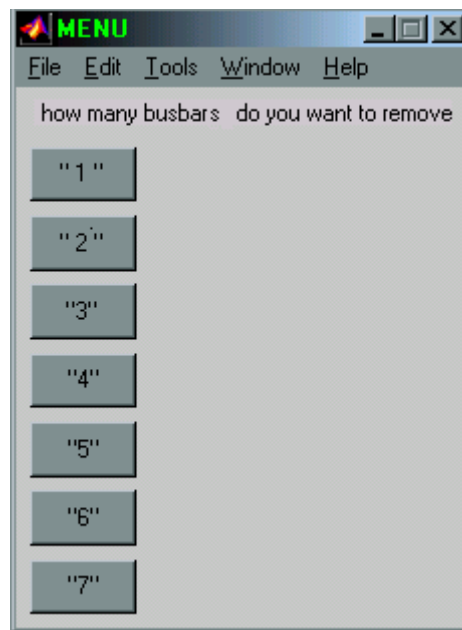


Figure 4 Contingency Analysis – Removing Busbars Main Menu

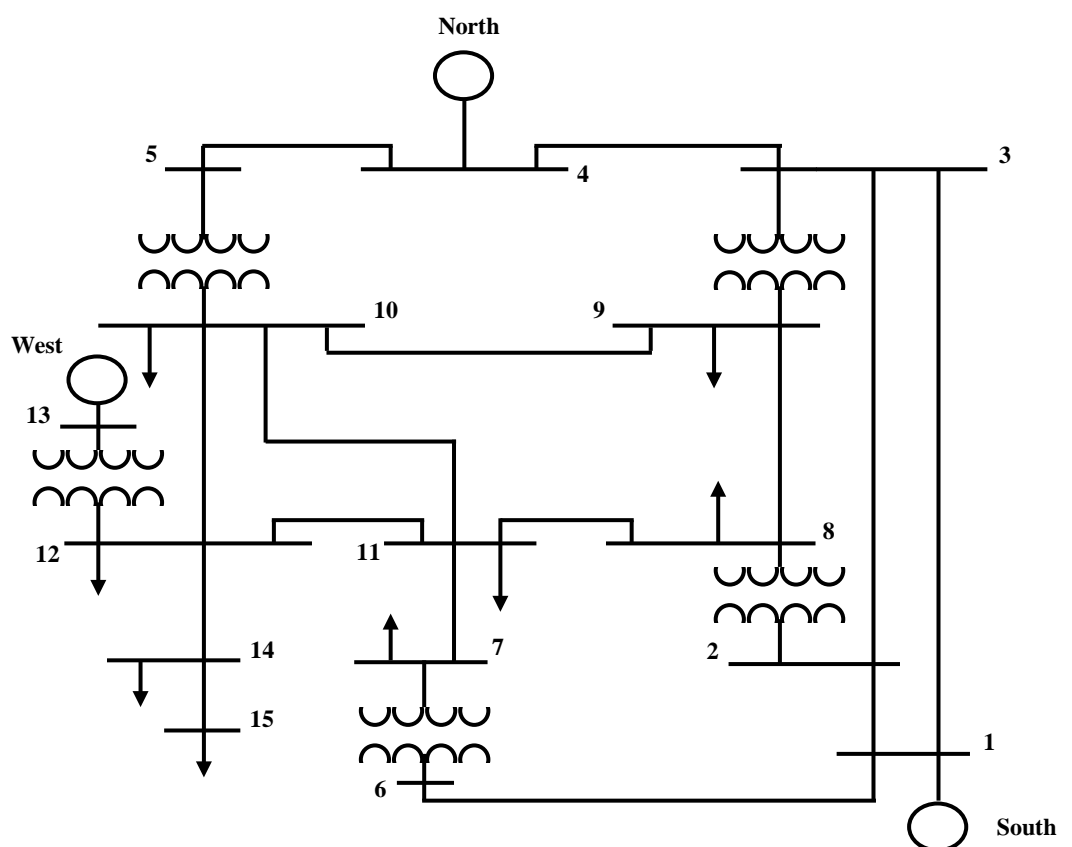


Figure 5 The One-Line Diagram of the Test System

MISMATCH VALUE 1e-5

NUMBER OF NODES 15

MVA BASE 100

BRANCH DATA

SEND.	NAME	REC.	NAME	RL(P. U)	XL(P. U)	GL	B(P. U)	REAC.(P.U.)	REF. TO	LIMIT
1	MICE	2	BASD	0.01	0.0528	0	0.1119	0	0	3
1	MICE	3	SENO	0.0233	0.1232	0	0.2611	0	0	3
1	MICE	6	LASS	0.0083	0.044	0	0.0933	0	0	3
2	BASD	3	RICE	0.0133	0.0704	0	0.1492	0	0	3
3	RICE	4	DIES	0.01	0.0528	0	0.1119	0	0	3
4	DIES	5	YORK	0.0066	0.0352	0	0.0746	0	0	3
7	TYRO	11	BRAZ	0.0277	0.1518	0	0.0271	0	0	3
8	YORB	9	SIDE	0.0332	0.1822	0	0.0325	0	0	3
8	YORB	11	NERO	0.0222	0.1214	0	0.0217	0	0	3
9	SIDE	10	DLHI	0.0277	0.1518	0	0.0217	0	0	3
10	DLHI	11	BRAZ	0.0277	0.1518	0	0.0217	0	0	3
10	DLHI	12	FORT	0.0222	0.1214	0	0.0217	0	0	3
11	BRAZ	12	FORT	0.0166	0.0911	0	0.0163	0	0	3
12	FORT	14	RICH	0.0222	0.1214	0	0.0217	0	0	3
14	RICH	15	HERO	0.0166	0.0911	0	0.0163	0	0	3
0	0	0	0	0	0	0	0	0	0	0

TAB-TRANSFORMER DATA

SEND.	NAME	REC.	NAME	RL(P.U)	XL(P.U)	TAP POSN
2	BASD	8	YORB	.0025	.03	0
3	RICE	9	SIDE	.0025	.03	0
5	YORK	10	DLHI	.0025	.03	0
6	LASS	7	TYRO	.002	.05	0
12	FORT	13	TETO	.0033	.0333	0
0	0	0	0	0	0	0

PHASE-SHIFT-TRANSFORMER DATA

SEND.	NAME	REC.	NAME	RL(P.U)	XL(P.U)	REAL-TAB POSN	IMAG-TAB POSN
0	0	0	0	0	0	0	0

SLACK NODE NUMBER

1

TIE LINES IDENTIFIERS

THE NO.OF AREAS IS 1

NOW YOU WILL ENTER THE TIE LINES CONNECTIONS AREAS

SEND. AREA	REC. AREA	SEN. BUS	REC. BUS	TIE LINE R(P.U)	TIE LINE X(P.U)	B (P.U)
0	0	0	0	0	0	0

AREA NO.	AREA DATA FILES	SPEC. POWER	REG.GEN.NO	NO. OF TIE LINES	TIE LINES AREA BUSBARES
0	0	0	0	0	0

SPECIFIED NODE VALUES

-FOR THE NONINTERESTING VARIABLE PUT ZERO ('0')

-IF THE NODE IS A LOAD FILL PS AND QS

-IF THE NODE IS GENERATOR FILL PS, VS, QMIN, QMAX

-IF THE NODE IS A SLACK FILL VS

-IF THE NODE IS A GENERATOR AND LOAD FILL PS, VS, QMIN AND QMAX FOR

THE GENERATOR AND QS AND PL FOR THE LOAD

BUS No.	NAME	BUS_REC	PL	QL	VS(MAG.)	VS(DEG)	QMIN	QMAX	PG	VMIN	VMAX	VOLTRAT
1	MICE	0	0	0	1.025	0	0	0	0	.95	1.05	230
2	BASD	0	0	0	1.00	0	0	0	0	.95	1.05	230
3	RICE	0	0	0	1.0	0	0	0	0	.95	1.05	230
4	DIES	0	0	0	1.025	0	-50	110	170	.95	1.05	230
5	YORK	0	0	0	1.0	0	0	0	0	.95	1.05	230
6	LASS	0	0	0	1.0	0	0	0	0	.95	1.05	230
7	TYRO	0	-25	-10	1.0	0	0	0	0	.95	1.05	115
8	YORB	0	-40	-20	1.0	0	0	0	0	.95	1.05	115
9	SIDE	0	-18	-10	1.0	0	0	0	0	.95	1.05	115
10	DLHI	0	-130	-40	1.0	0	0	0	0	.95	1.05	115
11	BRAZ	0	-160	-50	1.0	0	0	0	0	.95	1.05	115
12	FORT	0	-100	-30	1.0	0	0	0	0	.95	1.05	115
13	TETO	0	0	0	1.035	0	0	90	120	.95	1.05	13.8
14	RICH	0	-50	-20	1.0	0	0	0	0	.95	1.05	115
15	HERO	0	-24	-10	1.0	0	0	0	0	.95	1.05	115

SLACK NODE VOLTAGE

Figure 6 The Input Data File



LOAD FLOW BUS RESULTS						
Name	V	angle(deg)	PG(MW)	QG(MVAR)	PL(MW)	QL(MVAR)
MICE	235.75	0	269.79	7.981762	0	0
BASD	232.0589	-3.45218	0	0	0	0
RICE	233.9404	-3.68012	0	0	0	0
DIES	235.75	-3.32457	170	45.29895	0	0
YORK	230.3821	-6.22112	0	0	0	0
LASS	231.9283	-2.22981	0	0	0	0
TYRO	114.553	-4.91011	0	0	-25	-10
YORB	114.7307	-5.37925	0	0	-40	-20
SIDE	116.0614	-4.84473	0	0	-18	-10
DLHI	113.5732	-8.83897	0	0	-130	-40
BRAZ	111.2444	-11.05	0	0	-160	-50
FORT	114.2713	-12.0872	0	0	-100	-30
TETO	14.283	-10.0784	120	118.4851	0	0
RICH	107.55	-17.2546	0	0	-50	-20
HERO	105.9646	-18.6057	0	0	-24	-10
TOTAL		559.79	171.7658	-547	-190	
THE TOTAL AMOUNT OF SERIES LOSSES ARE 12.79-84.1853i						
THE TOTAL AMOUNT OF SHUNT LOSSES ARE 0+102.4194i						
AFTER CORRECTION						
Name	V	angle(deg)	PG(MW)	QG(MVAR)	PL(MW)	QL(MVAR)
MICE	235.75	0	269.3793	16.9437	0	0
BASD	231.6016	-3.43308	0	0	0	0
RICE	233.6063	-3.66511	0	0	0	0
DIES	235.75	-3.32051	170	58.0137	0	0
YORK	229.5934	-6.18764	0	0	0	0
LASS	231.542	-2.21096	0	0	0	0
TYRO	114.1388	-4.89541	0	0	-25	-10
YORB	114.3458	-5.36219	0	0	-40	-20
SIDE	115.7861	-4.82979	0	0	-18	-10
DLHI	112.8418	-8.81411	0	0	-130	-40
BRAZ	110.1602	-11.0374	0	0	-160	-50
FORT	112.1323	-11.9881	0	0	-100	-30
TETO	13.81438	-9.77439	120	68.3924	0	0
RICH	109.25	-17.5274	0	0	-50	-20
HERO	109.25	-18.965	0	0	-24	-10
TOTAL		559.3793	143.3498	-547	-190	
THE TOTAL AMOUNT OF SERIES LOSSES ARE 12.3793-81.0811i						
THE TOTAL AMOUNT OF SHUNT LOSSES ARE 0+102.0755i						
The added MVAR should be						
0.117063 at bus 14						
0.139495 at bus 15						

Figure 7 The Resulting Bus Data from the Converged Solution



DUE TO THE REMOVING OF THE SELECTED BUSBARS  
ANOTHER BUSBAR(S) IS (ARE) DISCONNECTED HENCE REMOVED THESE ARE  
'HERO'

THE SYSTEM IS SUBDIVIDED INTO AREAS

THIS AREA CONSISTS OF

MICE  
BASD  
RICE  
DIES  
YORK  
LASS  
TYRO  
YORB  
SIDE  
DLHI  
BRAZ

LOAD FLOW BUS RESULTS

Name	V	angle(deg)	PG(MW)	QG(MVAR)	PL(MW)	QL(MVAR)
MICE	235.75	0	210.4013	28.3677	0	0
BASD	231.4482	-2.6089	0	0	0	0
RICE	233.6047	-2.3528	0	0	0	0
DIES	235.75	-1.3833	170.0001	55.6411	0	0
YORK	229.7209	-3.8337	0	0	0	0
LASS	231.3491	-1.8783	0	0	0	0
TYRO	113.7655	-4.2004	0	0	-25	-10
YORB	114.0739	-4.284	0	0	-40	-20
SIDE	115.7493	-3.3494	0	0	-18	-10
DLHI	112.8215	-6.0956	0	0	-130	-40
BRAZ	108.9442	-9.147	0	0	-160	-50
TOTAL		380.4014	84.0088	-373	-130	

THE TOTAL AMOUNT OF SERIES LOSSES ARE 6.34032-34.1718i  
THE TOTAL AMOUNT OF SHUNT LOSSES ARE 0+94.8781i

THIS AREA HAS NO GENERATION STATIONS SO IT CAN NOT BE ANALYZED

RICH  
HERO

**Figure 8 Resulting Bus Data when Bus 12 is Removed Through the Application of Contingency Analysis Program**

## Hydrogenation of Nitrobenzene in Trickle Bed Reactor over Ni/SiO<sub>2</sub> Catalyst

Majid I. Abdulwahab

Chemical Engineering Department

College of Engineering

University of Baghdad

E-mail: [majid.abdulwahab@yahoo.co.uk](mailto:majid.abdulwahab@yahoo.co.uk)

### ABSTRACT

Trickle bed reactor was used to study the hydrogenation of nitrobenzene over Ni/SiO<sub>2</sub> catalyst. The catalyst was prepared using the Highly Dispersed Catalyst (HDC) technique. Porous silica particles (capped cylinders, 6x5.5 mm) were used as catalyst support. The catalyst was characterized by TPR, BET surface area and pore volume, X-ray diffraction, and Raman Spectra. The trickle bed reactor was packed with catalyst and diluted with fine glass beads in order to decrease the external effects such as mass transfer, heat transfer and wall effect. The catalyst bed dilution was found to double the liquid holdup, which increased the catalyst wetting and hence, the gas-liquid mass transfer rate. The main product of the hydrogenation reaction of nitrobenzene was aniline. Reaction operating conditions, i.e., temperature, liquid flow rate, and initial feed concentration were investigated to find their influences on the conversion and rate of nitrobenzene hydrogenation. Under normal conditions without bed dilution, the system was mass transfer controlled. In the diluted reactor, on the other hand, the resistance of mass transfer was nearly absent and the system became under surface kinetic control. The catalyst showed significant deactivation during the reaction period due to the adsorption of intermediate amine products on the surface of the catalyst. The kinetic study revealed that the reaction is zero order with respect to nitrobenzene concentration for the range of concentration between 0.58 to 1.17 mol/L while it was of positive order for the initial concentration less than 0.58 mol/L.

**KEY WORDS:** Hydrogenation, Trickle Bed, Nitrobenzene, Bed Dilution, Highly Dispersed Catalyst

### هدرجة النتروبنزين في مفاعل سيحي باستخدام النيكل/سيليك كعامل مساعد

أ.م.د. ماجد ابراهيم عبد الوهاب

قسم الهندسة الكيميائية

كلية الهندسة / جامعة بغداد

### الخلاصة

تم استخدام المفاعل السيحي لدراسة عملية هدرجة النتروبنزين على العامل المساعد نيكل/سيليك. تم تحضير العامل المساعد باستخدام تقنية الـ HDC. تم استعمال حبيبات السيليكا المسامية (شكل اسطواني 5.5x6) كمادة حاملة للعامل المساعد. تم ايجاد خواص العامل المساعد المحضر بفحص TPR و طريقة BET للمساحة السطحية و حجوم المسامات و التحليل الطيفي بطريقة انكسار اشعة اكس و كذلك التحليل الطيفي بجهاز رامان. تم شحن المفاعل بالعامل المساعد المخفف بكميات الزجاج الدقيقة و ذلك لخفض التأثيرات الخارجية كانتقال المادة و انتقال الحرارة و تأثير الجدار. و قد وجد ان استخدام الحبيبات الدقيقة مع العامل المساعد في المفاعل قد ادى الى مضاعفة محتوى السائل في المفاعل و الذي ادى بدوره الى زيادة درجة تبلل العامل المساعد و بالتالي زيادة معدل انتقال المادة للسائل و الغاز. كان المنتج الرئيسي من تفاعل هدرجة

النيترو بنزين هو الانيلين. تم ايجاد تأثير كل من الحرارة و معدل جريان السائل و التركيز الابتدائي للنيتروبنزين على مقدار التحول للنيتروبنزين و كذلك على سرعة التفاعل. في الظروف الطبيعية و بدون استخدام التخفيف بحبيبات الزجاج كان النظام تحت تأثير انتقال المادة. من جهة اخرى كانت مقاومة انتقال المادة في المفاعل المخفف بحبيبات الزجاج غائبة تقريبا و النظام تحت سيطرة التفاعل السطحي. كما لوحظ ان العامل المساعد يفقد فعاليته خلال فترة التفاعل بسبب امدصاص المواد الناتجة على السطح. بينت الدراسة ان تفاعل هدرجة النيتروبنزين من الدرجة الصفر نسبة الى تركيز النيتروبنزين في مدى التراكيز من 0.58 الى 1.17 مول/لتر بينما تصبح درجة التفاعل موجبة لمدى التراكيز اقل من 0.58 مول/لتر.

• الكلمات الرئيسية: هدرجة، مفاعل سيحي، نيتروبنزين، عمود مخفف، عامل مساعد كثيف التوزيع

## 1. INTRODUCTION

The catalytic hydrogenation of substituted aromatic compounds in the liquid phase is important in many processes and industries. Hydrogenation of nitrobenzene is used to produce aniline which is one of the most important chemicals and intermediates in the production of pharmaceuticals, dyes, pigments, and pesticides (Wang, et al., 2010). The majority of the reactors used to carry out this process are batch stirred reactors due to their simplicity and flexibility especially when used for small scale production. For the large scale production of some specific chemicals such as that used in fine chemicals industry, the trickle bed reactor is one of the suitable options due to its better selectivity control of the desired product, with no moving parts, and no need for the catalyst filtration (Hindle, et al, 2008). On the other hand, batch reactors can be effectively used to measure the kinetics with stable catalytic activity which is not affected by heat or mass transfer and axial dispersion. However, when the activity of catalyst gradually changes, the reaction process and the catalyst deactivation cannot be separated in batch-wise experiments. In such a case, trickle bed flow-type reactors are widely used for the kinetic measurements (Hiroshi, et al., 1999).

The problem with using trickle bed reactor for investigating the kinetics of reaction is that the superficial velocities in the lab-scale trickle bed reactor (TBR) are considerably lower than that of the industrial scale TBR, although the space velocities are in the same order which results in reduced catalyst wetting. Furthermore, the lab-scale TBR suffered of wall effect due to the small value of the bed to catalyst pellets ratio which

gives rise to incorrect kinetic data. This problem can be resolved by diluting the catalyst bed with fine inert particles. The dilution reduces axial dispersion substantially to the extent where plug flow can be established and much higher liquid hold-up improves the wetting contact efficiency at lower velocities of gas and liquid.

In the present work, the hydrogenation of nitrobenzene was carried out over Ni/SiO<sub>2</sub> catalyst in a trickle bed reactor. In this process, the aromatic nitro-group is reacted with three mole equivalents of hydrogen gas, in the presence of the catalyst, to produce the amine and water. This hydrogenation is usually carried out under relatively mild conditions and produces a low level of by-products and impurities (Qing, et al., 1997). The hydrogenation of nitrobenzene occurs rapidly over most metals and is often employed as a reference reaction to compare the activity of other hydrogenation catalysts and of new reactor systems (Hatziantoniou, et al., 1986).

Thermodynamically, the nitro group is one of the most easily performed of all functional group hydrogenations (Augustine, et al., 1976). The following thermodynamic data were evaluated for the hydrogenation of the nitrobenzene; the apparent activation energy is in the range of 12-104 kJ/mol, the estimated value of the equilibrium constant is about 1600 at standard temperature and pressure and indicates that reaction may be considered totally irreversible for all practical purposes. The reaction is exothermic with heat of reaction of 500 kJ/mol (Gelder, 2005). This means that dissipation of the exothermic heat of the reaction is very important in controlling the temperature during the hydrogenation reaction.

There have been many studies on the kinetics of the hydrogenation of nitrobenzene (Gelder, 2005, Holler, 2000), the majority of which were in the liquid phase carried out in batch-type reactors with a variety of kinetic proposals have been put forward. As expected from a hydrogenation reaction, a first order dependence on hydrogen concentration was widely reported. On the other hand, wide variations in the reaction order with respect to the nitrobenzene concentration have been reported in literature (Hatziantoniou, et al., 1986, Li, et al., 1994, Collins, et al., 1982). Like the hydrogen order, the value for nitrobenzene appears to be influenced by a high number of factors. Zero order reactions with respect to nitrobenzene, at different initial concentrations of nitrobenzene have been reported. (mostly greater than 0.1 mol/L). Holler, et al., 2000 stated a zero order reaction dependence at high nitrobenzene concentrations (greater than 0.1 mol/L), whereas, a first order reaction dependence when the nitrobenzene concentration was low. Conversely, Metcalfe and Rowden found that at concentrations below 0.15 mol/L the reaction proceeded with a zero order dependence on the nitrobenzene concentration (Metcalfe, et al., 1971). As with hydrogen, the order of reaction with respect to nitrobenzene is variable and appears to be sensitive to the specific reaction conditions.

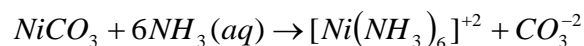
In the present work, it was aimed to study the performance of the trickle bed reactor when used for hydrogenation of nitrobenzene. The reactor bed dilution with fine inert particles was studied as a technique that can increase the liquid hold up in the bed which will has a useful effect in increasing the wetting efficiency of the catalyst particles in this type of reactors which are normally working at low liquid velocities. Nickel catalyst supported on silica particles were synthesised using HDC (Highly Dispersed Catalyst) preparation technique (Nele, et al, 1999, Martin Lok, et al., 2004). In the HDC method, the metals are precipitated from solution (precursor) onto the support in a similar way to the deposition-precipitation methods. The conversion of nitrobenzene, the effect of mass transfer, and

kinetics of the hydrogenation reaction were studied.

## 2. EXPERIMENTAL WORK

### 2.1 Preparation of nickel catalyst by HDC technique

The first step in preparation Ni/SiO<sub>2</sub> catalyst was the preparation of nickel hexamine solution. All materials, the ammonium carbonate chip, nickel hydroxy carbonate were purchased from Aldrich. The demineralised water was obtained from an internal supply. Calculated amounts of ammonia solution, water, ammonium carbonate chips and nickel hydroxycarbonate were used to prepare 2.5% of the hexamine solution. 25% ammonia solution (Sigma-Aldrich) was added to demineralised water in a 5 L conical flask with constant stirring by a magnetic stirrer. Ammonium carbonate chips were added to the solution with stirring. The solution was left until all the ammonium carbonate chips were dissolved. A certain amount of nickel hydroxyl carbonate (BDH) were divided into small portions, each portion was added to the above solution with constant mixing. After each addition, the solution was left for 45 minutes at constant stirring. The reaction was considered to complete when the solution colour changed from green to blue. When all carbonate dissolved, the solution was left overnight under constant stirring, and then filtered. The reaction of HDC catalyst preparation is:



Green

Blue

Calculated amount of the prepared hexamine solution was used with AEROSIL-200 silica pellets (capped cylinders of 6 x 5.5 mm dimensions) manufactured by Degussa, to prepare Ni catalyst of approximately 20% loading of nickel. The preparation was carried out in a 5 L rotating flask device (BÜCHI Rotavapor R-114) equipped with water condenser and connected to vacuum device (BÜCHI Vac V-511). The solution and support were put together in the flask. The

flask with its content was allowed to rotate inside a controlled-temperature water bath (BÜCHI Water bath B-480) at a rate of 250 rpm. The temperature was set at 30 °C to let slow evaporation under vacuum. The reaction mixture was refluxed until all ammonia had been distilled off and metal deposition on silica was complete. This was visible by the change in the colour of the solution from blue to green. The pH of the reaction mixture was monitored throughout the course of the reaction and following full deposition using a pH meter (Hanna Instrument-USA). The pH value decreased from 10.5 at the beginning of the process to 7.8 at the end. Reflux was continued for 15 minutes to age the reaction mixture. The product solution with coloured silica pellets was filtered via Buckner flask and washed with demineralised water many times, left for 30 minutes in air and then put in an oven with 110 °C temperature overnight to dry the catalyst pellets.

## 2.2 Characterisation of the catalyst

Temperature programmed reduction (TPR) of the newly synthesised HDC catalyst was performed to find the most efficient reduction conditions. This was measured using 0.1 g of catalyst in a Quantachrome Corporation TPR/TPD with 5% H<sub>2</sub> in N<sub>2</sub> as a reducing gas mixture and a linear heating rate of 5 deg/min over a temperature range of 293 to 1373 K.

The BET surface area and the pore volume of the prepared catalyst were measured in a Micromeritics ASAP 2400 gas adsorption analyser. The catalyst was outgased at 413 K in flowing nitrogen for one hour prior to the nitrogen absorption experiment at 77 K. Nitrogen adsorption and desorption isotherms were collected and used to derive the BET surface area, which quantifies the entire surface area of the catalyst, including the metal and the porous support material. The pore volume of each catalyst was also measured using a relative pressure of 0.98 on the desorption branch. The average pore diameter was also calculated using this method. **Table 1** shows the measurement results.

The UV-Vis Spectra analysis of the silica-supported catalyst was performed using a Varian Cary 500 scan UV-Vis-NIR spectrophotometer. Samples were run over a 200-1000 nm range with a scan rate of 200 nm/min and a resolution of 2 nm. Catalyst sample were ground for the suitability of the analysis.

Raman spectra analysis was performed on a LABRAM HR Raman spectrophotometer (HORIBA JOBIN YVON) using a green laser (532 nm, solid state, 10 mW). A range of 0-4000 cm<sup>-1</sup> was taken for the sample.

To investigate the crystallographic properties of the catalyst, X-ray diffraction (XRD) spectra of the catalyst were performed in a SIEMENS D 5000 X-ray diffractometer. Diffraction data were recorded using a continuous scanning starting at 5° and ending at 85° at a rate of 0.02°/s and a step of 0.02°.

## 2.3 Trickle bed reactor

The trickle bed reactor was a glass tube of 2.2 cm inner diameter and 35 cm height. The liquid was pumped to the reactor where a shower head distributor (6 tubes, 1 mm inner diameter each) was employed at the exit of the fluid stream allowing a more dispersed fluid distribution over the catalyst. The liquid flow rate was controlled by HPLC pump (Gilson-307, flow rate 0-10 cm<sup>3</sup>/min). The gas flow rate was controlled by a mass flow controller (Brooks, Model 5850, maximum pressure 100 bar, flow rate 0-100 cm<sup>3</sup>/min) connected to a gas flow monitor (BROSE, Model 5878). Hydrogen and nitrogen were both available as gas feed when required. The bed temperature was controlled using a hollow cylindrical furnace (WATLOW 425 W) fitted around the reactor wall and connected to a temperature controller (WEST 4400), accuracy ±1 K. Two thermocouples were used; the first was fitted inside the catalytic bed through a specially designed capillary glass tube, while the other thermocouple was fitted at the outside of the reactor wall at half length of the catalyst bed. **Fig. 1** shows the experimental rig of the hydrogenation experiments.

## 2.4 Experimental procedure

Hydrodynamic experiments were carried out at first to investigate the effect of diluting the catalytic bed on the liquid holdup in the bed. Glass beads (0.5-1.0 mm diameter) were used as fine particles. The void fractions were found by a measuring cylinder. The value of void fraction was 0.45 for the packed bed with coarse silica particles and 0.23 for the packed bed diluted with fines. Therefore, the void fraction in the diluted bed was nearly half of that in the undiluted bed. The packing technique of Al-Dahhan et al., 1995, was adopted for diluting the catalytic bed. 10 g of silica particles (catalyst support) were divided into 5 portions. The first portion of the coarse particles was loaded to the reactor with vibration. Then, fine glass bead particles were loaded gently with vibrating until the fine particles covered the top layer of coarse particles. This procedure was repeated for all portions. Liquid hold up was measured by quick closing of valves. Decalin solvent and nitrogen gas were used as liquid and gas, respectively. The gas and liquid were let to flow to the reactor and after the steady state conditions were achieved, the inlet and outlet valves were quickly closed. Then, the volume of liquid drained from the reactor was measured. Experiments were carried at room temperature and atmospheric pressure and for different values of liquid flow rate.

The hydrogenation of nitrobenzene experiments were carried out at different temperatures, liquid flow rates, and nitrobenzene feed concentrations. **Table 2** shows the values of the experimental variables used in hydrogenation experiments. 10 g of catalyst was packed with glass beads in the bed. The catalyst was reduced in a flow of 15 cm<sup>3</sup>/min of hydrogen gas according to the appropriate heating program pre-determined TPR data. The temperature ramped from 303 K to 723 K at a rate of 2K/min, holding at this temperature for 8 h, and then decreased to the required reaction temperature. The catalyst was then treated in hydrogen at a flow rate of 20 cm<sup>3</sup>/min at room temperature for 30 minutes. The hydrogen flow was then set to the required value and a flow of methanol solvent (2 cm<sup>3</sup>/min) was introduced for

10 minutes to wet the catalyst bed before the flow was switched to the feed solution of nitrobenzene in methanol at the required flow rate. After the steady state condition was achieved, samples (2.5 cm<sup>3</sup>) were collected and analysed.

The analysis of samples were performed using gas chromatography (FOCUS GC-Thermo Finnigan) fitted with a VF-5ms, 25 m capillary column. Throughout all sample analysis, the GC operating conditions were held constant. The injector temperature was set at 513 K. The column oven was initially kept at 353 K and was ramped to 493 K at a rate of 15 K/min and then held at 493 K for 10 minutes. Calibrations were carried out for nitrobenzene, aniline, and nitrozobenzene. Standard solutions for each of the components were made-up and a series of dilutions performed to obtain a series of solutions of known concentration.

## 3. RESULTS AND DISCUSSION

### 3.1 Change of pH during HDC catalyst preparation

The pH of the metal solutions was monitored throughout preparation of the HDC catalyst. The depositions were carried out under high pH conditions to facilitate a strong interaction between the positive nickel metal ions and the negatively charged alumina support material. **Figure 2** shows how the pH altered during preparation of the catalyst. The pH decreased fairly rapidly over the first 0-30 minutes of the deposition process as the ammonia was distilled off and then levelled off during the rest of the procedure after complete removal of the ammonia had occurred.

Although the HDC method of catalyst preparation has been used extensively in industry to prepare a range of commercial products, the majority of research into the technique and resultant catalysts has focused upon the precipitation of one metal ion from solution. The pH profile measured during synthesis of the catalyst (**Fig. 2**) showed a decrease in pH throughout reaction and was found to stabilize between at 8.5-7.7 indicating that

ammonia was being totally removed from solution by the distillation process and was not retained by the metal used.

### 3.2 Catalyst characterization

The Temperature Programmed Reduction profile of the catalyst was measured. The results showed that the initial and final temperatures were 360 °C and 880 °C respectively. The profile displayed one main reduction peak at 530 °C. This has been attributed to the reduction of the metal +2 ion down to the zero valent state, which is consistent with previous findings on similar catalyst systems published in the literature (Hoffer, et al., 2000).

Elemental weight analysis of the HDC catalyst was employed to confirm that the preparation had been performed successfully and that the precipitated metals were present in the intended quantities. The estimated nickel loaded on the silica support was 18.2%.

XRD tests showed that all the unreduced catalyst is amorphous and the reduced catalysts gave poorly crystalline nickel-containing phase on catalysts. The XRD patterns of reduced samples are displayed in **Fig. 3** which shows the XRD patterns for both silica and nickel-silica combination. The nearer matching of the catalyst structure is crystalline phase of Ni<sub>2</sub>SiO<sub>4</sub> (Liebenbergite).

Raman spectrum was collected for Ni/SiO<sub>2</sub> catalyst and compared with reference spectrum. The spectrum of silica support displayed a strong, sharp signal at around 500 cm<sup>-1</sup> that was also clearly visible in the Raman spectra of the prepared catalyst. The Raman spectrum of the 20 % Ni catalyst was compared to the spectra of its metal oxides. **Fig. 4** shows the Raman Spectra for silica particles and Ni/SiO<sub>2</sub> catalyst particles. The spectra of the silica support displayed a strong, signal at around 450 cm<sup>-1</sup> that was clearly visible in the Raman spectrum of the catalyst.

### 3.2 Liquid holdup

**Figure 5** shows the effect of liquid velocity on the liquid holdup for three kinds of beds; the

undiluted, diluted, and fine beds. The liquid holdup for the diluted bed packed with glass beads was higher than the holdup of the undiluted one and less than the holdup of beds packed with fine particles only. It is clear that diluting the coarse catalyst particles with inert fine glass beads will increase the liquid holdup by a factor two.

### 3.3 Hydrogenation of Nitrobenzene

The prepared Ni/SiO<sub>2</sub> was used for the hydrogenation of nitrobenzene in the diluted trickle bed reactor. Nitrobenzene (NB) was used as the inlet feed using methanol as solvent. Nitrobenzene and aniline were the only components visible on the GC chromatograms along with low levels of azobenzene (less than 1 % of the sample composition) were also detected in most of the reaction samples. Samples were collected from the reactor outlet at selected time intervals and analyzed. Each sample was analyzed using GC to identify and quantify each component. In all reactions performed, over the range of experimental conditions, a constant decrease in the nitrobenzene conversion was observed throughout the reaction which indicates a catalyst deactivation due to the adsorption of the intermediates and/or product aniline on the catalyst surface. During the early stages of hydrogenation, delays in the time the feed took to pass over the catalyst bed were sometimes experienced; leading to varying volumes of sample collected each interval, often much lower than expected. Towards the end of each catalytic run, the volume of sample obtained began to increase towards that expected from inlet rate and become more stable suggesting a more consistent performance could have been achieved if the reactions were left for a longer period of time. However, the catalyst displayed a loss in catalytic activity throughout the duration of the experiment and sampling was required in the early stages to ensure the reaction was monitored when the catalysts were most active. The reaction profile for typical initial concentration of nitrobenzene (0.5836 mol/L) and temperature of 323 K for different liquid feed flow rates is shown in **Fig. 6**. It can be shown a maximum of 19 % conversion of nitrobenzene to aniline in the exit samples after



1 hour reaction time. The activity then dropped off as the reaction progressed until about 13 % of the feed steam was composed of aniline after 10 hours.

When comparing with the previous works conducted on the same reaction using nickel catalyst prepared by wet impregnation method (Nele, et al, 1999), it is evident from the experimental results that the prepared HDC catalyst displayed less activity compared to catalysts prepared by wet impregnation method. The catalyst prepared appeared to be unsuitable for use as hydrogenation catalysts, with low percentages of aniline present in the exit streams. However, it should be noted that the large quantities of unreacted nitrobenzene exiting the reactor made detection of the products more difficult and exaggerated the poor activity of the catalysts. Examination of the reaction rates determined from these data shows that the levels of activity, although not approaching the precious metal catalysts, are not of an unreasonable level.

Three nitrobenzene initial concentrations (0.2926, 0.5853, and 1.1706 mol/L) were used to examine the dependence of the reaction rate on the nitrobenzene concentration at a temperature of 323 K. Experimental determination of the reaction order with respect to nitrobenzene, (**Fig. 7**), has revealed that at nitrobenzene concentration of 0.5853 and 1.1706 mol/L, the reaction appeared to be zero order with respect to nitrobenzene. Below this value (0.2926 mol/L), the reaction shifted to a positive order as the aniline amount decreased with the decrease in nitrobenzene concentration. If the adsorption of hydrogen is assumed to be the rate determining step in the nitrobenzene hydrogenation reaction (Gelder, 2005, Yao, et al., 1962), the shifting order can be explained with respect to the surface coverage of the catalyst. At low concentration of nitrobenzene, adsorption sites across the silica support become available for both hydrogen and nitrobenzene. This could affect an increase in the reaction rate by holding more nitrobenzene molecules adsorption on the catalyst. However, at high concentrations, nitrobenzene would be expected to saturate the

surface of the metal and support and inhibiting the further hydrogen adsorption.

To generate a rate of reaction, the following equation was used to determine the rate of reaction depending on the assumption of differential reactor (Gelder, et al., 2002).

$$\text{Rate of aniline formation} = \frac{F_{NB}x}{W} \quad (1)$$

Where,

$F_{NB}$ : Molar flow rate of nitrobenzene (mol/L)

W: Weight of catalyst bed (g)

x: Fractional conversion

The actual number of moles of aniline produced was used taking into account the volume of each sample. This gave a clear indication of the absolute quantity of aniline produced throughout hydrogenation. As the behavior at each experimental condition was slightly different, the maximum rate was selected as a comparison. These values are shown in **Table 3** and a plot of maximum rate with respect to the hourly space velocity is presented in **Fig. 8**.

The rate of reaction data at different temperatures were used to calculate the activation energy of the hydrogenation reaction using Arrhenius law. The average activation energy of the reaction is calculated as 31.78 kJ/mol which agrees with the values found in literature (Gelder, 2005). **Figure 9** shows the Arrhenius plot for the reaction carried out at WHSV of 9.75 h<sup>-1</sup>.

### 3.4 Mass Transfer Resistance

Experiments were carried out to check the resistance to mass transfer during the hydrogenation reaction for undiluted and diluted beds. The reaction was performed with two different liquid flow rates (1 and 2 ml/min) at constant weight hourly space velocity, WHSV of 9.75 hr<sup>-1</sup>. Different conversions of nitrobenzene were noticed for the undiluted reactor indicating external mass transfer control. The diluted bed showed nearly the same conversions for both liquid flow rates which can be interpreted as that



the dilution of the bed already increased the mass transfer coefficient inside the reactor. Figure 10 shows the mass transfer effect on the conversion of nitrobenzene for the two beds.

Pore diffusion was checked by the application of the method used by Weisz-Prater, 1954. Weisz-Prater relation correlates  $wp$  to the observed rate of the reaction and many other parameters as:

$$wp = \frac{r_{obs} \rho (d/6)^2}{D_e C_s} \quad (2)$$

Where  $r_{obs}$  is the observed rate of the reaction,  $\rho$  is the catalyst density,  $d$  is the average catalyst support diameter,  $D_e$  is the effective diffusivity, and  $C_s$  is the concentration of solute in solution. Weisz-Prater criterion states that the factor  $wp$  should be  $\ll 1$  for the internal resistance to be negligible.

The rate of reaction was obtained at temperature 323 K, liquid flow rate of 2 ml/min, gas flow rate of 135 ml/min and catalyst weight of 10 g. The diffusion coefficient was calculated by using Wilke equation (Wilke, et al., 1955), the solubility of hydrogen in methanol was taken from the data given by Young, 1981 as 0.0494 mol/L. For diluted beds,  $wp$  was calculated as 0.0102 for nitrobenzene as limiting species indicating the absence of internal mass transfer limitation.

The reaction rates at the steady state for the diluted bed are much higher than those for the undiluted bed. **Figure 10** shows the effects of liquid velocity on the reaction rate. In the case of the diluted bed, the reaction rate is independent of the liquid velocity. On the other hand, in the case of undiluted trickle bed, the reaction rates for lower liquid velocities are unstable and smaller than the rate without external effects. It was revealed from observations that some pellets of catalyst were completely dried. Therefore, they might make no contributions to the reaction.

## CONCLUSIONS

1. Trickle bed reactor can be used in the synthesis of fine chemicals. The catalyst

efficiency can be improved by dilution of the catalyst particles with fine inert particles to overcome the external mass transfer resistance.

2. Although the HDC method was successful in producing catalyst with a homogeneously distributed, well-dispersed monolayer of metals, the method was not gave advantages over alternative catalyst preparation routes for the synthesis of supported metal catalysts.
3. The diluted trickle bed reactor is suitable to obtain the reaction rate without external effects even if the liquid velocity is low.
4. The prepared catalyst was shown to deactivate over time due to the adsorption of the product aniline.
5. The reaction order of nitrobenzene hydrogenation reaction was zero with respect to nitrobenzene concentration for the values of nitrobenzene initial concentrations of 0.58 mol/L and more, while it is of positive order for the initial concentration less than 0.58 mol/L.

## REFERENCES

- Al-Dahhan, M. H., Wu, Y., and Dudukovik, M. P., *Reproducible Technique for Packing Laboratory-Scale Trickle-Bed Reactors with a Mixture of Catalyst and Fines*, Ind. Eng. Chem. Res. 1995, Vol. 34, pp 741-747.
- Augustine, R.L., *Organic Functional Group Hydrogenation*, in *Catalysis Reviews*, Science and Engineering, 1976, p. 285-313.
- Collins, D.J., Smith, A.D., and Davis, B.H., *Hydrogenation of nitrobenzene over a nickel boride catalyst*. Ind. Eng. Chem. Prod. Res. Dev., 1982, Vol. 21, pp. 279-281.
- Gelder, E.A., Jackson, S.D., and Lok, C.M., *A study of nitrobenzene hydrogenation over palladium/carbon catalysts*, Catal. Lett, 2002. Vol. 84(3-4), pp. 205-208.
- Gelder, E.A., *The Hydrogenation of Nitrobenzene over Metal Catalyst*, PhD Thesis, University of Glasgow, 2005.



Hatziantoniou, V., Andersson, B., and Schoon, N. H., *Mass transfer and selectivity in liquid-phase hydrogenation of nitro compounds in a monolithic catalyst reactor with segmented gas-liquid flow*, Ind. Eng. Chem. Process. Des. Dev., 1986, Vol. 25, pp. 964-970.

Hindle, K., Jackson, S. D., and Webb, G., *The hydrogenation of para-toluidine in a trickle bed reactor: mass transfer, product selectivity and catalyst deactivation*, Current Topics in Catalysis, 2008, Vol. 7, pp. 115-125.

Hiroshi Yamada, Takafumi Naruse, Shigeo Goto, *Trickle bed reactor diluted with fine particles and coiled tubular Flow-type reactor for kinetic measurements without external effects*, Catalysis Today, 1999, Vol. 48, pp. 301-306.

Hoffer, B.W., van Langeveld, A.D., Janssens, J.P., Bonné, R.L.C., Lok, C.M., Moulijn, J.A., *Stability of Highly Dispersed Ni/Al<sub>2</sub>O<sub>3</sub> Catalysts: Effects of Pretreatment*, J.Catal., 2000, Vol. 192(2), pp 432-440.

Holler, V., Wegricht, D., Yuranov, I., Kiwi-Minsker, L. and Renken, A., *Three-phase nitrobenzene hydrogenation over supported glass fiber catalysts: reaction kinetics study*. Chem. Eng. Technol, 2000. Vol. 23(3), pp. 251-255.

Li, C., Y.-W. Chen, and W.-J. Wang, *Nitrobenzene hydrogenation over aluminium borate-supported platinum catalyst*. Appl. Catal. A, 1994. Vol. 119, pp. 185-194.

Martin Lok, C., *Novel highly dispersed cobalt catalysts for improved Fischer-Tropsch productivity*, Studies in Surface Science and Catalysis, 2004, Vol. 147, pp. 283-288.

Metcalfe, A. and Rowden, M.W., *Hydrogenation of nitrobenzene over palladium-silver catalysts*, J. Catal, 1971. Vol. 22, pp. 30-34.

Nele, M., Vidal, A., Bhering, D. L., Pinto, J., and V. M. Salim, *Preparation of high loading silica supported nickel catalysts: simultaneous analysis of the precipitation and aging steps*, Appl. Catal. A, 1999, Vol.178, pp. 177-189.

Qing Z., Li F., Fang X., and Yao S., *Study on silica supported Cu-Cr-Mo nitrobenzene hydrogenation catalysts*. Appl. Catal. A, 1997. Vol. 161, pp. 129-135.

Wang, J., Yuan, Z., Nie, R., Hou, Z., and Zheng, X., *Hydrogenation of nitrobenzene to aniline over silica gel supported nickel catalysts*, Ind. Eng. Res., 2010, Vol. 49, pp. 4664-4669.

Weisz, B. P., and Prater, C. D., *Interpretation of measurements in experimental catalysis*, Advances in Catalysis, 1954, Vol. 6, VI, pp144-196.

Wilke, C. R., and Chang, P., *Correlation of diffusion coefficients in dilute solutions*, AIChE, 1955, V1, p 264.

Yao, H. C., and Emmett, P.H., *Kinetics of liquid phase hydrogenation. IV. Hydrogenation of nitrocompounds over raney nickel and nickel powder catalysts*, J. Am. Chem. Soc, 1961. 84: p. 1086-1091.

Young, C.L., *Solubility Data Series - Hydrogen and deuterium*, 1981, Vol. 5/6, Pergamon Press, Oxford.

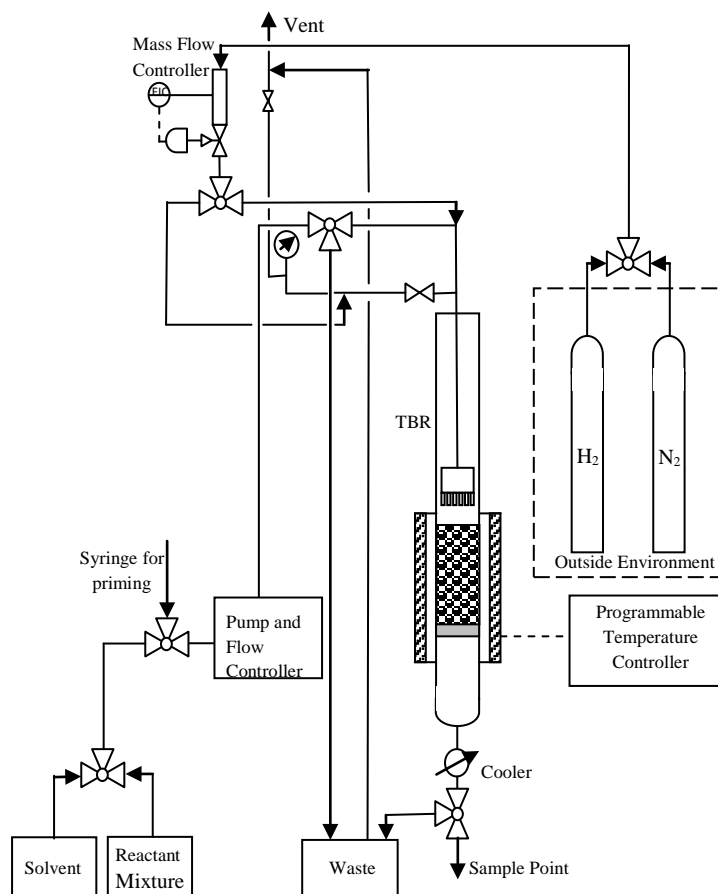


Fig. 1 Experimental apparatus

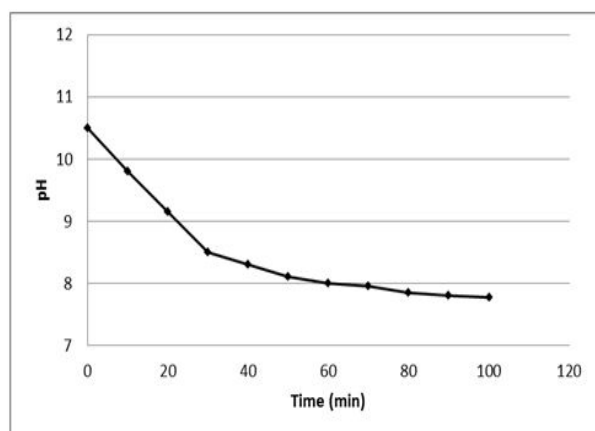


Fig. 2 Change in pH during synthesis of the nickel HDC catalyst

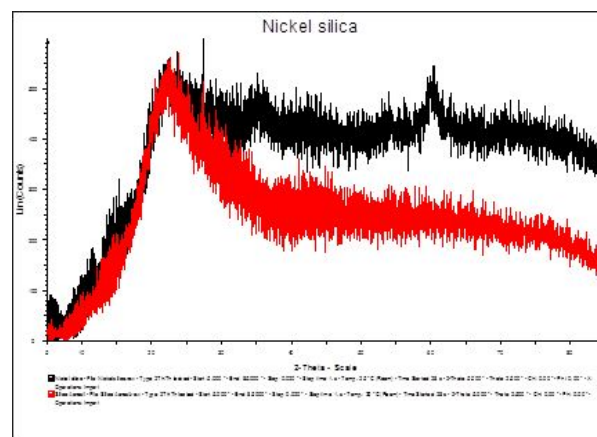


Fig. 3 XRD Patterns of Nickel/Silica Catalyst

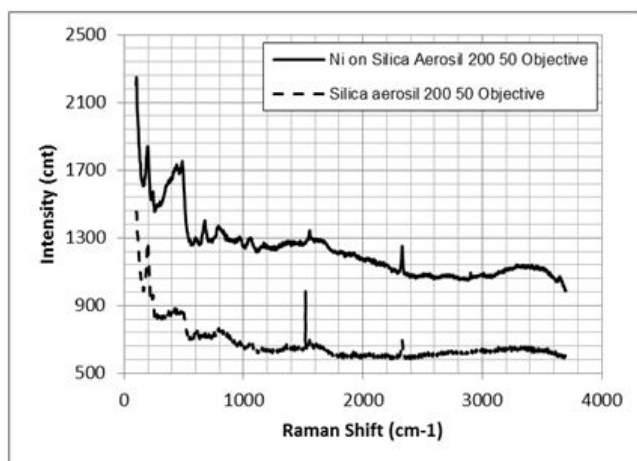


Fig.4 Raman Spectra for Silica particles and Nickel/Silica Catalyst

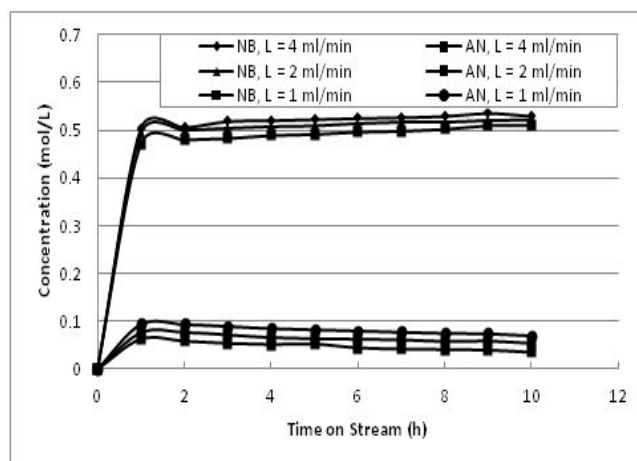


Fig 6. Typical reaction profile at different liquid flow rate, T=323 K,  $U_g$ =135 ml/min, Catalyst wt=10 g

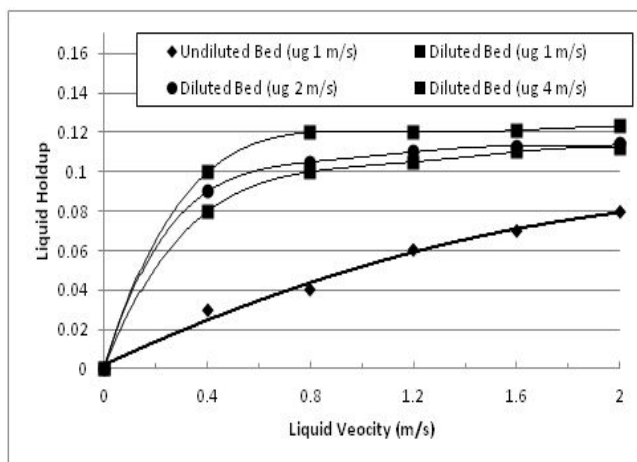


Fig 5. Liquid holdup for diluted and undiluted beds

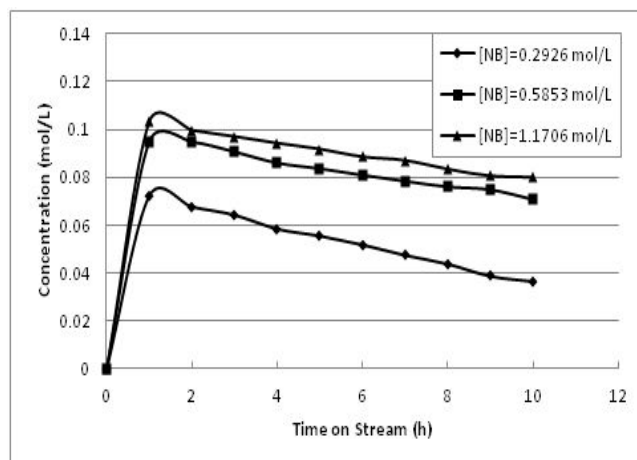


Figure 7 Outlet concentration of aniline vs. time on stream at WHSV = 4.87 h<sup>-1</sup>, T=323 K,  $U_g$  = 135 ml/min and different initial feed concentrations

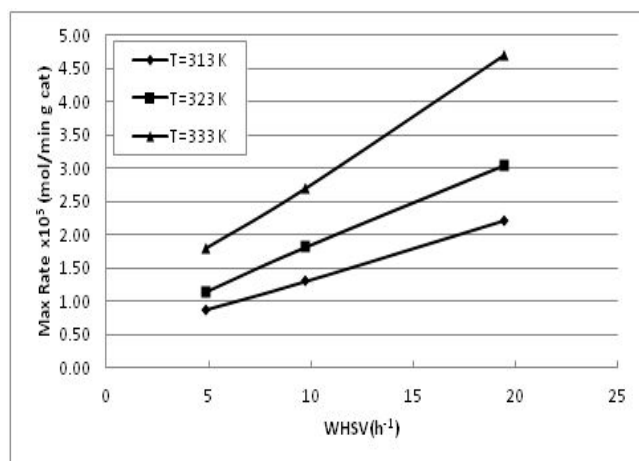


Fig. 8 Maximum rate of nitrobenzene hydrogenation vs. weight hourly space velocity at different temperatures at  $T=323$  K,  $U_g = 135$  ml/min

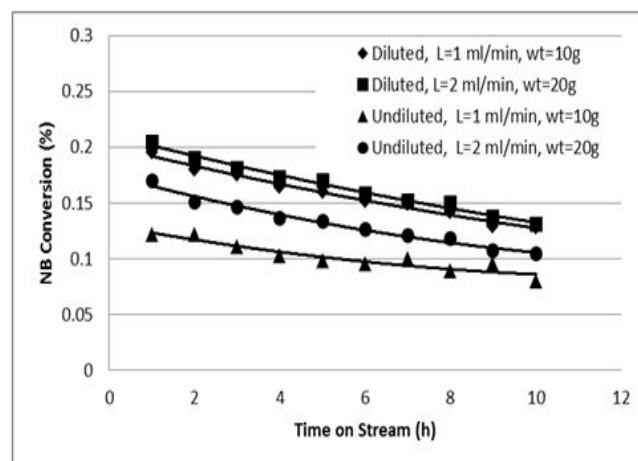


Fig. 10 Conversion of nitrobenzene vs. time on stream at  $WHSV = 9.75$  hr<sup>-1</sup>,  $T=323$ , and  $U_g = 135$  ml/min for undiluted and diluted beds

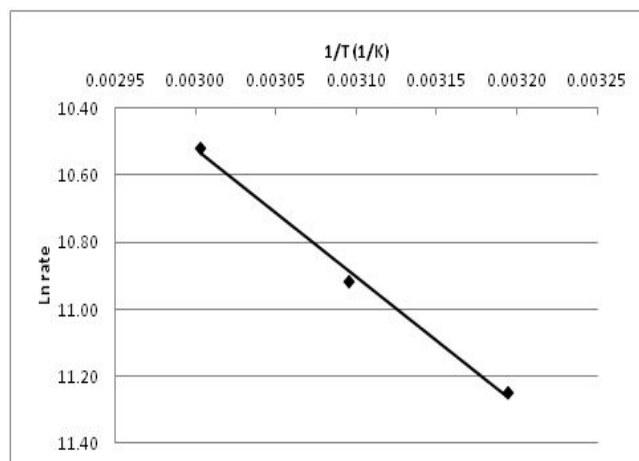


Fig. 9 Arrhenius plot for the reaction carried out at  $WHSV 9.75$  h<sup>-1</sup>,  $U_g = 135$  ml/min, catalyst wt=10g

**Table 1:** Values of the surface area and pore volume for the prepared Ni/SiO<sub>2</sub> catalyst

<b>Area</b>	
Single point surface area at P/Po = 0.285	238.782 m <sup>2</sup> /g
BET surface area	243.387 m <sup>2</sup> /g
BDH desorption cumulative surface area of pores between 17 and 3000 °A diameter	261.920 m <sup>2</sup> /g
<b>Volume</b>	
Single point total pore volume of pores less than 1070.5 °A diameter at P/Po = 0.981	0.589 cm <sup>3</sup> /g
BDH desorption cumulative pore volume of pores between 17 and 3000 °A diameter	0.594 cm <sup>3</sup> /g
<b>Pore Size</b>	
Average pore diameter (4V/A by BET)	96.944 °A
BDH desorption average pore diameter (4V/A)	90.764 °A

**Table 2** Experimental variables used in hydrogenation experiments

Experimental Variable	Range
Feed concentration (mol/L)	0.2926 - 1.1706
Liquid feed flow rate (ml/min)	1 - 4
Temperature (K)	313 - 333

**Table 3** Maximum rate of aniline formation with weight hourly space velocity and reaction temperature

WHSV (hr <sup>-1</sup> )	Maximum Rate x 10 <sup>5</sup> (mol/min g cat)		
	T = 313 K	T = 323 K	T = 333 K
4.87	0.88	1.14	1.80
9.75	1.30	1.81	2.70
19.49	2.2	3.04	4.70

## Removal of $\text{Cu}^{2+}$ , $\text{Pb}^{2+}$ , And $\text{Ni}^{2+}$ Ions From Simulated Waste Water By Ion Exchange Method On Zeolite And Purolite C105 Resin

Dr. Ahmed Abed Mohammed

Haidar Shukur Mahmood

Baghdad University/College of Eng.  
Environmental Engineering Dept.  
ahmed.abedm@yahoo.com

### ABSTRACT:

The removal of heavy metal ions from wastewater by ion exchange resins (zeolite and purolite C105), was investigated. The adsorption process, which is pH dependent, shows maximum removal of metal ions at pH 6 and 7 for zeolite and purolite C105 for initial metal ion concentrations of 50-250 mg/l, with resin dose of 0.25-3 g. The maximum ion exchange capacity was found to be 9.74, 9.23 and 9.71 mg/g for  $\text{Cu}^{2+}$ ,  $\text{Pb}^{2+}$ , and  $\text{Ni}^{2+}$  on zeolite respectively, while on purolite C105 the maximum ion exchange capacity was found to be 9.64, 8.73 and 9.39 for  $\text{Cu}^{2+}$ ,  $\text{Pb}^{2+}$ , and  $\text{Ni}^{2+}$  respectively. The maximum removal was 97-98% for  $\text{Cu}^{2+}$  and  $\text{Ni}^{2+}$  and 92-93% for  $\text{Pb}^{2+}$  on zeolite, while it was 93-94% for  $\text{Cu}^{2+}$ , 96-97% for  $\text{Ni}^{2+}$ , and 87-88% for  $\text{Pb}^{2+}$  on purolite C105. The obtained sorption affinity sequence was  $\text{Cu}^{2+} > \text{Ni}^{2+} > \text{Pb}^{2+}$  in both resins. Langmuir isotherm expressions were found to give better fit to the experimental data compared to Freundlich and BET models. Kinetic data correlated well with Lagergren first order kinetic model, indicating the reversible reaction with an equilibrium being established between liquid and solid phase.

**KEYWORDS:** ion exchange, heavy metals, wastewater, zeolite, purolite C105.

### ازالة ايونات النحاس، الرصاص والنيكل من المياه الملوثة بطريقة التبادل الايوني باستخدام راتنجات الزيولايت والبيورلايت

حيدر شكر محمود

احمد عبد محمد

### الخلاصة:

ازالة المعادن الثقيلة من مياه الصرف الصحي بواسطة راتنجات التبادل الايوني، مثل الزيولايت والبيورولايت تمت دراستها بطريقة الدفع. ، والتي تعتمد على الدالة الهيدروجينية ، يظهر الحد الأقصى لإزالة ايونات المعادن في درجة الحموضة بين 6 و 7 للزيولايت والبيورولايت لتركيز المعادن الأولية للايونات 50-250 ملغم / لتر ، مع جرعة من الراتنج من 0.25 الى 3 و تم التوصل إلى توازن في ساعتين. تم ايجاد السعة القصوى للتبادل الايوني لتكون 9.74 ملغم / غ للنحاس ، 9.23 ملغم / غ للرصاص و 9.71 ملغم / غ للنيكل على راتنج الزيولايت بينما على راتنج البيورولايت السعة القصوى للتبادل الايوني كانت 9.64 ملغم / غ للنحاس 8.73 ملغم / غ للرصاص و 9.39 ملغم / غ للنيكل . وان نسبة الازالة القصوى كانت 97-98% للنحاس و النيكل و حوالي 92-93% للرصاص على راتنج الزيولايت في حين كانت نسبة الازالة القصوى على راتنج البيورولايت حوالي 93-97% للنحاس و النيكل و 87-88% للرصاص. تم ايجاد ان تعبير لانكمير هو الملائم اكثر لتمثيل هذه البيانات المختبرية مقارنة بفريندلخ و بي اي تي . البيانات الحركية تبين انها ملائمة مع الدرجة الاولى، مشيرة الى ان التفاعل عكسي مع التوازن الذي يجري بين السائل و المادة الصلبة .

## 1. INTRODUCTION

Heavy metals are generally considered to be those whose density exceeds  $5 \text{ g/cm}^3$  (Nocito et al.,2007). Removal of heavy metals from industrial wastewater is of primary importance because they are not only causing contamination of water bodies but they are also toxic to many life forms. Industrial processes generate wastewater containing heavy metal contaminants. Since most of heavy metals are non degradable into nontoxic end products, their concentrations must be reduced to acceptable levels before discharging them into the environment. Otherwise they could pose threats to public health and/or affect the aesthetic quality of potable water (Aslam et al.,2004).

According to World Health Organization (WHO) the metals of most immediate concern are chromium, copper, zinc, iron, nickel, mercury and lead (WHO, 1984). The removal of heavy metal cations from aqueous solutions can be achieved by several processes, such as chemical precipitation, biosorption on marine algae, adsorption, solvent extraction, reduction, coagulation, oxidation, reverse osmosis, flotation, ultra filtration and ion exchange (Keane,1998; Rengaraj et al.,2004)

The most common method used for the removal of these heavy metals is ion exchange. The main advantages of ion exchange are recovery of metal value, cost-effective, selectivity and the meeting of strict discharge specifications. In ion exchange systems, polymeric resins are usually employed. The resin is a very complex material and there are several properties which are to be known and clearly understood before putting it to any particular application. Some of the important properties are: moisture content, particle size, cross linking, resin capacity, functional groups, resin selectivity, and distribution coefficient. In ion exchange, ions of positive and negative charges from an aqueous solution replace dissimilar ions of the same charge initially in the solid. The ion exchangers contain permanently bound functional groups of opposite charge type. Cation exchange resins generally contain bound sulfonic acid groups, carboxylic acid groups phosphonic acid groups, phosphinic acid groups and so on (Pehlivan and Altun,2006).Using Zeolite as an ion exchange for environmental

protection and other applications is stimulated by the good results obtained, the non toxic nature of these materials, their availability in many parts of the worlds, and the low cost (Campos et al.,2007). Removal and recuperation processes of heavy metals from aqueous solution by natural zeolite are commonly cyclic and take into account the recovery of the metals and the regeneration of the zeolite to be reused.

Additionally, the mineral stability of zeolites and their structural changes under treatment in various media play important roles in their potential utilization as ion exchangers (Sprynsky et al.,2006)

Weak cation acid(WAC) resins have very high selectivity for divalent cations, particularly  $\text{Pb}^{2+}$ ,  $\text{Cu}^{2+}$ ,  $\text{Cd}^{2+}$ , and  $\text{Ni}^{2+}$  ions. This makes them ideal candidates for the removal of various metals from wastewater streams. WAC resins offer extremely high capacity than strong cation resins, higher selectivity for divalent cations than chelating resins, especially at neutral to alkaline pH, have relatively low cost, and have lower kinetics, compared to chelating resins (Pehlivan and Altun,2007)

Ion exchange reaction is reversible interchange between solid phase (the ion exchange) and the solution phase, the ion exchanger being insoluble in the medium in which the exchange is carried out. If an ion exchanger  $\text{M}^+\text{A}^-$  carrying cations  $\text{A}^+$  as the exchanger ions, is placed in an aqueous solution phase containing  $\text{B}^+$  cations, an ion exchange reaction takes place which may be represented by the following equation:



The equilibrium represented by the above equation is an example of cation exchange, where  $\text{M}^-$  is the insoluble fixed anionic complement of ion exchanger  $\text{M}^+\text{A}^-$ , often called simply the fixed anion. The cations  $\text{A}^+$  and  $\text{B}^+$  are referred to counter- ions .whilst ions in the solution which bear the same charge as the fixed ion of the exchanger are called co-ions. In much the same way, anions can be exchanged provided that an anion-receptive medium is employed. An analogous representation of an anion exchange reaction may be written:





The equations above illustrate the essential difference between ion exchange and other sorption phenomena (Harland 1994).

The aim of the present work is to study the removal of  $Cu^{2+}$ ,  $Pb^{2+}$ , and  $Ni^{2+}$  from industrial waste water by ion exchange method using zeolite and purolite C105 resins. In addition, investigate the parameters that influence the ion exchange, such as contact time, pH, dose of resin, and initial concentrations. The isotherms models and kinetics parameters were also evaluated from the ion exchange measurements.

## 2 EXPERIMENTAL WORK AND PROCEDURE

The experimental work was performed in a batch mode by using synthetic zeolite and purolite C105 resins for the removal of heavy metal ions and making comparison between these resins in order to get the most efficient resin for heavy metals removal.

### 2-1 Materials

Analytical grade reagents were used. Solutions of certain molarities were prepared by dilution of chloride dehydrated, nickel sulfate hexahydrate and lead nitrate salts ( $CuCl_2 \cdot 2H_2O$ ,  $NiSO_4 \cdot 6H_2O$  and  $Pb(NO_3)_2$ ) from Merck company with double distilled water. Synthetic zeolite and Purolite C105 in hydrogen form UK were used, the properties of the resins are given in tables 1 and 2

### 2-2:Apparatus.

Atomic Absorption Spectrometer: AAS was used to measure concentrations of soluble copper, lead and nickel (Norwalk, Connecticut, U.S.A). The pH measurement was performed with pH bench meter (Type: HI 250, Bench model, USA). High-speed orbital shaker has an adjustable shaking range of 100 to 2200 rpm (Thermolyne, Maxi-Mix III, Type: 65800, USA) was used for ion exchange experiments.

## 2-3 Procedure

The resins were washed with 1M of NaOH and 1M HCl in order to remove possible organic impurities, then washed with distilled water to remove all excess acids and basics then dried for 24 hours.

The procedure involved filling number of flasks with 50 ml of heavy metal ions solution of 100 ppm concentration unless otherwise specified, and an amount of 0.25-3 g of adsorbent was added into different flasks. Resins and solution were mixed at 200 rpm, and then were allowed to reach equilibrium for 2 hrs in the shaker. The separation was performed using filter paper. The same measurements were repeated twice and the average value had been taken as the amount of the remaining metal in the solution phase.

## 3 RESULTS AND DISCUSSION

### 3-1 Effect of Contact Time

The effect of contact time on the ion exchange of metal ions by zeolite and purolite C105 was studied by adding 0.25 g of resin to 50 ml of metal solution in different flasks that were shaken for different time intervals. Figure (1-a) shows the effect of contact time on ion exchange of copper, lead, and nickel using zeolite, while figure (1-b) shows the effect of contact time using purolite C105. From these figures it can be seen that the percentage of metal ion sorbed increased with increasing time and it reached equilibrium at 2 hrs for zeolite and purolite C105. Further increase in contact time had no significant effect on copper, lead, and nickel removal. The kinetics of metal ions removal by the resin were relatively fast, which within 30 min uptake of 76.6% copper, 73.3% lead, 82.6% nickel on zeolite resin were achieved. While uptake on purolite C105 were 73% copper, 67.8 % lead, and 84% nickel were achieved at 30 min. The initial adsorption rate was very fast and this may be due to the existence of greater number of resin sites available for the adsorption of metal ions. As the remaining vacant surface sites decreased, the adsorption rate slowed down due to the formation of repulsive forces between the metals on the solid surface and in the liquid

phase (Yua et al.,2009). The increased uptake of metal ions with contact time can be due to the decrease mass transfer coefficient of the diffusion controlled reaction between resins and metal ions. This is a crucial parameter for an optimal removal of metal ions in waste water (Zaiter,2006). The ion exchange rate was faster and the equilibrium removal efficiency was higher for copper than that of lead and nickel in zeolite resin. While in purolite C105 the ion exchange rate was faster and the equilibrium removal efficiency of nickel was higher than that of copper and lead. The maximum removal efficiency was 99%, 94%, 98% and 94%, 93%, 98%, for copper, lead and nickel, on zeolite and purolite C105 respectively.

### 3-2 Effect of pH

pH affects both the surface charge of adsorbent and the degree of ionization of heavy metals in the solution (Shah et al.,2011). Equal quantity of resin 0.5 g was added to all reaction flasks and the solutions contain 100 mg/l heavy metal ions that were agitated for 2 hrs on zeolite and purolite C105 resins at 200 rpm speed. The maximum removal on zeolite were about 97%, 94%, and 96% for copper, lead, and nickel, respectively at pH ranges 5.5-8, as shown in figure (2-a) while for purolite C105 were about 92%, for copper and nickel and 91%,for lead , at pH ranges 6-9 as shown in figure (2-b). This may be attributed to the competition between hydrogen, sodium, and metal.

### 3-3 Effect of Resin Dose

The resin amount is an important parameter to obtain the quantitative uptake of metal ions (Rafati et al.,2010). The retention of the heavy metals was examined in the relation to the amount of resin used, 0.25 to 3 g of zeolite and purolite C105 that were tested and equilibrated for 2 hrs. The results plotted in figure (3) show that by increasing the resin amount, the sorption density, and the amount of adsorbed metal ion per unit mass increased. The retention of metals increased with increasing the amount of resin up to 0.5 g for both resins, this value was taken as the optimum amount for other trials. The increase in sorbent amount resulted in a decrease in the contact time required to reach equilibrium.

The results were expected because for a fixed initial metal concentration the resin provides greater surface area or ion exchange sites or adsorption site (Gupta and Bhattacharyya,2009). It is readily understood that the number of available sorption sites increases by increasing the resin amount. It may be concluded that by increasing the adsorbent dose, the removal efficiency increases but the ion exchange density decrease .The decrease in the ion exchange density can be attributed to the fact that some of ion exchange remains unsaturated during the sorption process whereas the number of ion exchange sites increases by an increase in sorbent dose and this results in an increase in the removal efficiency (Rafati et al.,2010). The optimum dose of 0.5g was observed enough to reach high removal efficiencies.

### 3-4Effect of Initial Metal Concentrations

Figure (4) shows the effect of varying metal concentrations 50-250 mg/L on the adsorption under the optimized conditions. It was found that the metal amounts retained were almost stable in the concentration ranges of copper, lead, nickel, and the two types of resins. Adsorption of metal ions was a bit higher in zeolite than in purolite C105. At high concentrations the removal efficiency decreased because of the slow motion of metal ions. The maximum removal efficiency on zeolite resin was obtained as 99.4%, 97%, and 98.5% for copper, lead and nickel respectively, while the maximum removal efficiency on purolite C105 was obtained as 98%, 93%, and 97% for copper, lead, and nickel respectively for 50 mg/l initial metals concentration.

## 4. SORPTION ISOTHERMS

Adsorption isotherms are very powerful tools for the analysis of adsorption processes. Adsorption isotherms establish the relationship between the equilibrium pressure or concentration and the amount of adsorbate adsorbed by the unit mass of adsorbent at a constant temperature. Langmuir, Freundlich, and BET isotherms models are widely used to investigate the adsorption process. The model parameters can be construed further, providing

the understanding of adsorption mechanisms, surface properties, and affinity of the adsorbent.

#### 4-1 Langmuir isotherm

Langmuir equation relates the coverage of molecules on a solid surface to the concentration of a medium above the solid surface at a fixed temperature. The isotherm is based on three assumptions, namely, adsorption is limited to monolayer coverage, all surface sites are alike and can only accommodate one adsorbed atom, and the ability of a molecule to be adsorbed on a given site is independent of its neighboring site's occupancy (Yua et al., 2009). The Langmuir equation was developed in the 1990s to describe the sorption of gas molecules on planer surfaces. This model was later extended to liquid systems, where species in solution are involved. The Langmuir model (Langmuir, 1916) suggests that sorption occurs on homogenous surfaces by monolayer sorption (sorption onto a surface with a finite number of identical sites), without interaction between sorbed molecules. Equation (1) describes the model

$$q_e = (q_m b C_e) / (1 + b C_e) \dots (1)$$

Where:  $b$  = constant related to the affinity of the binding site ( $L \text{ mg}^{-1}$ ),  $q_e$  = sorbed metal ions on the resin ( $\text{mg g}^{-1}$ ),  $C_e$  = metal ions concentration in the solution at equilibrium ( $\text{mg L}^{-1}$ ),  $q_m$  = maximum sorption capacity for a monolayer coverage ( $\text{mg g}^{-1}$ ) which is the maximum sorption amount of the metal ion per unit weight of biomass needed to form a complete monolayer on the surface.  $q_m$  represents a practical limiting sorption capacity when the surfaces are fully covered with metal ions and assists in the comparison of sorption performances. The sorption parameters ( $q_m, b$ ) can be determined from the linearized form by plotting  $C_e/q_e$  vs.  $C_e$  according to eq (2):

$$C_e/q_e = 1/(q_m b) + C_e/q_m \dots (2)$$

#### 4-2 Freundlich isotherm

The Freundlich isotherm describes equilibrium on heterogeneous surfaces and

hence, doesn't assume monolayer capacity and takes the following form for a single component adsorption (Freundlich, 1906)

$$q_e = K_F C_e^{1/n} \dots (3)$$

Where:  $K_F$  and  $n$  = the Freundlich constants

$K_F$  related to the adsorption capacity, the larger its value, the higher the capacity,  $n$  is the adsorption intensity or the heterogeneity of the sorbent; the more heterogeneous the surface, the larger its value. If  $1/n$  approaches 1, the equation becomes linear. If  $1/n$  value within 0.1 and 1 there is a favorable sorption of the sorbate on the given sorbent. The Freundlich relation is an exponential equation that assumes that the concentration of adsorbate on the adsorbent surface increases by increasing the adsorbate concentration in the liquid phase. Equation (4) can be linearized in logarithmic form and the Freundlich constants can be determined

$$\log q_e = (1/n) \log C_e + \log K_F \dots (4)$$

The values  $K_F$  and  $n$  can be estimated respectively from the intercept and slope of a linear plot of experimental data of  $\log q_e$  versus  $\log C_e$ . Freundlich isotherm provides no information on the monolayer adsorption capacity in comparison with the Langmuir model. This isotherm is widely recommended due to its accuracy. It gives more accurate results than the Langmuir isotherm for a wide variety of heterogeneous adsorption systems

#### 4-3 BET isotherm

The BET isotherm was developed by Brauner, Emmet and Teller. Unlike the Langmuir isotherm, BET type adsorption corresponds to multilayer adsorption. This isotherm indicates that more than one layer of adsorbate can accumulate at the surface, i.e. the first adsorbed layer serves as a site for adsorption of a molecule onto the second and so on. It also supposed that the adsorption/desorption occurs exclusively between the interface and the bulk, and the atoms are not allowed to move from one layer to other (Masel, 1996).

The Langmuir, Freundlich, and BET adsorption constants are evaluated from isotherms and their correlation coefficients are presented in tables 3, 4 and 5. The linearized Langmuir, Freundlich, and BET of copper, lead, and nickel for zeolite and purolite resins are given in figures 5, 6, and 7. The Langmuir model constants evaluated from isotherms and their correlation coefficients are presented in table 3. Ion exchange capacity of heavy metal cations listed in table 3 indicates the following selectivity sequence:  $\text{Cu}^{2+} > \text{Ni}^{2+} > \text{Pb}^{2+}$ . Since the adsorption phenomena depends on the charge density of cations, the diameter of hydrate cations is very important. The charges of the metal cation are the same (+2); therefore  $\text{Pb}^{2+}$  ions (the biggest diameter) have minimum adsorption while  $\text{Cu}^{2+}$  and  $\text{Ni}^{2+}$  ions (the least diameter) have maximum adsorption. The Langmuir model effectively described the sorption data with all  $R^2$  values  $> 0.97$  for each resin. According to the b parameter, sorption on zeolite and purolite C105 are produced following the sequence  $\text{Cu}^{2+} > \text{Ni}^{2+} > \text{Pb}^{2+}$ . The Freundlich model constants  $k_F$  and  $n$  on zeolite and purolite C105 are, respectively, obtained from the intercept and the slopes of the linear plot of  $\log q_e$  versus  $\log C_e$  according to equation 4 and their correlation coefficients for each resin are presented in table 4.

The BET isotherm has been used to describe sorption of metal ions on ion exchange resins as shown in eq. (5):

$$\frac{X}{q_s(1-X)} = \frac{1}{ab} + \frac{(b-1)}{ab} X \dots\dots (5)$$

Where:  $X = C_e/q_e$

The slope of the plot  $X/q_e(1-X)$  versus  $X$  gives  $(b-1)/ab$  and the intercept yields the sorption capacity  $1/ab$ . The plot of  $X/q_e(1-X)$  against  $X$  for metal ion sorption on zeolite and purolite C105 are shown in figure (7) respectively. The BET parameters for zeolite and purolite C105 are listed in table 5. It is clear that the Langmuir isotherm model provide an excellent represent to the equilibrium adsorption data, giving correlation coefficients of 0.984 for copper, 0.978 for lead, and 0.982 for nickel on zeolite resin. While giving correlation

coefficients of 0.970 for copper, 0.984 for lead, and 0.979 for nickel on purolite C105 resin.

## 5. ADSORPTION KINETICS

Kinetics of sorption describing the solute uptake rate, which is in turn governs the residence time of sorption reaction, is one of the important characteristics defining the efficiency of sorption (Pehlivan and Altun,2006). Several researchers have used different kinetic models to predict the mechanism involved in the sorption process. These include pseudo-first-order model, pseudo-second-order model, Webber and Morris sorption kinetic model, first-order reversible reaction model, external mass transfer model, Pseudo first order and second order kinetic models are widely used [(Pehlivan and Altun,2006,2007)

### 5-1 Pseudo first-order kinetics

Lagergren showed that the rate of adsorption of solute on the adsorbent followed a pseudo first-order equation. The non-linear form of pseudo first-order equation is given by

$$\log (q_e - q_t) = \log q_e - K_1 t / 2.303 \dots\dots(6)$$

Where:  $q_e$  and  $q_t$  = amounts of adsorption at equilibrium time.  $K_1$  = rate constant of the pseudo first-order adsorption operations.

### 5-2 Second order kinetics

Pseudo first-order kinetic equation differs from a true first order equation in two ways: The parameters  $K_1$  and  $(q_e - q_t)$  represent the number of available site. The parameter  $\log (q_e)$  is an adjustable parameter and often it is not equal to the intercept of the plot of  $\log(q_e - q_t)$  vs.  $t$ , whereas in a true first order  $\log q_e$  should be equal to the intercept. In such cases, applicability of the second order kinetics has to be tested with the rate equation given by eq. (7):

$$t/q_t = 1/h + (1/q_e)t \dots\dots(7)$$

Where:  $h = K_2 q_e^2$

Under such circumstances, plotting  $\log (q_e - q_t)$  against “ $t$ ” for zeolite and purolite C105



provides the first order rate constant ( $k_1$ ), while plotting  $t/q_t$  vs.  $t$  should give a linear relationship, which allows the computation of pseudo second order rate constant ( $K_2$ ),  $q_e$  and  $b$ , as listed in tables 6,7,8 and 9, respectively.

The values of correlation coefficient indicate a better fit of Lagergren first order model with the experimental data than pseudo second order model. In many cases the first order kinetic process is used for reversible reaction with an equilibrium being established between liquid and solid phases. Whereas, the second order kinetic model assumes that the rate limiting step may be chemical adsorption. Values of  $q_e$  calculated from the first order kinetic model agree very well with the experimental values, and the correlation coefficients were always more than 0.97 for all metal ions and on both resins.

## 6. CONCLUSIONS

1-Zeolite and purolite C105 are effective resins for the removal of copper, lead, and nickel from wastewater.

2-Zeolite is a better alternative than purolite C105 for removal of metal ions from wastewater at an optimum pH of about 6 and 7 onto zeolite and purolite C105 respectively.

3-It was observed that an increase of resin dosage resulted in a higher metal ions removal efficiency and by increasing the resin dosage the contact time required to reach equilibrium decreased.

4-The linear Langmuir, Freundlich, and BET isotherms were used to represent the experimental data, and the experimental data could be relatively well interpreted by Langmuir isotherm for both resins.

5-The monolayer adsorption capacity of copper, lead, and nickel calculated from Langmuir model was obtained 9.74, 9.23 and 9.71 mg/g on zeolite resin. While on purolite C105 resin the monolayer adsorption capacity of copper, lead, and nickel was 9.64, 8.73 and 9.39 mg/g respectively.

6-The sorption of metal ions on zeolite and purolite C105 resins followed first order reversible kinetics.

## REFERENCES

Aslam, M.M., Hassan, I., Malik, M., and Matin, A., "Removal of copper from industrial effluent by adsorption with economical viable material", *EJEAFChE*, Vol. 3, No. 2, pp. 658-664, (2004).

Campos, V., Morais, L. C., and Buchler, P. M., "Removal of chromate from aqueous solution using treated natural zeolite", *Environ. Geol.*, Vol. 52, No. 8, pp. 1521-1525, (2007).

Freundlich, H.M.F., Over the adsorption in solution. *J. Phys. Chem.* 57, 385-470, (1906).

Gupta, S. S., and Bhattacharyya, K. G., "Treatment of water contaminated with Pb (II) and Cd (II) by adsorption on koalinite, montmorillonite and their acid-activated forms", *Indian Journal of Chemical Technology*, Vol. 16, pp. 457-470, (2009).

Harland, C.E., "Ion exchange: theory and practice", Royal Society of Chemistry, 2<sup>nd</sup> ED., UK, (1994).

Keane, M. A., "The removal of copper and nickel from aqueous solution using zeolite ion exchangers", *Colloids Surfaces A: Physicochem. Eng. Aspects*, Vol. 138, pp. 11-20, (1998).

Langmuir, I., The constitution and fundamental properties of solids and liquids. *J. Am. Chem. Soc.* 38, 2221-2295, (1916).

Masel, R.I., Principles of adsorption and reaction on solid surfaces., John Wiley and Sons, Inc., (1996).

Nocito, F.F. Lancilli, C., Giacomini, B., and Sacchi, G. A., "Sulfur Metabolism and Cadmium Stress in Higher Plants", *Plant Stress*, Global Science Books, Vol. 1, No. 2, pp. 142-156, (2007).

Pehlivan, E., and Altun, T., "Ion exchange of  $\text{Pb}^{2+}$ ,  $\text{Cu}^{2+}$ ,  $\text{Zn}^{2+}$ ,  $\text{Cd}^{2+}$ , and  $\text{Ni}^{2+}$  from aqueous solution by Lewatit CNP 80", Journal of Hazardous Materials, Vol. 140, pp. 299 – 307, (2007).

Pehlivan, E., and Altun, T., "The study of various parameters affecting the ion exchange of  $\text{Cu}^{2+}$ ,  $\text{Zn}^{2+}$ ,  $\text{Ni}^{2+}$ ,  $\text{Cd}^{2+}$ , and  $\text{Pb}^{2+}$  from aqueous solution on Dowex50W synthetic resin", Journal of Hazardous Materials, Vol. 134, pp. 149 – 156, (2006).

Rafati, L., Mahvi, A. H., Asgari, A.R., and Hosseini, S. S., "Removal of chromium (VI) from aqueous solutions using Lewatit FO36 Nano ion exchange resin", Int. J. Environ. Sci. Tech., Vol. 7, No.1, pp.147-156, (2010)

Rengaraj, S., Kim, Y., Joo, C., Choi, K., and Yi, J., "Batch Adsorptive Removal of Copper Ions in Aqueous Solutions by Ion Exchange Resins: 1200H and IRN97H", Korean J. Chem. Eng., Vol. 21, No. 1, pp. 187-194, (2004).

Shah , B., Shah , A. V., and Shah , P. M., "Sorption Isotherms and Column Separation

of  $\text{Cu(II)}$  And  $\text{Zn(II)}$  Using Ortho Substituted Benzoic Acid Chelating Resins", Archives of Applied Science Research, Vol. 3, No. 3, pp. 327-341, (2011).

Sprynskyya , M., Buszewski , B., Terzyk , A.P., and Snik , J. N. "Study of the selection mechanism of heavy metal ( $\text{Pb}^{2+}$ ,  $\text{Cu}^{2+}$ ,  $\text{Ni}^{2+}$ , and  $\text{Cd}^{2+}$ ) adsorption on clinoptilolite", Journal of Colloid and Interface Science, Vol. 304, pp. 21–28, (2006).

World Health Organization, "Guidelines for drinking Water Quality", Geneva, (1984).

Yua, Z., Qia, T., Qua, J., Wanga, L., and Chua, J., "Removal of  $\text{Ca(II)}$  and  $\text{Mg(II)}$  from potassium chromate solution on Amberlite IRC 748 synthetic resin by ion exchange", Journal of Hazardous Materials, Vol. 167, pp. 406-412, (2009).

Zaiter, M. J., "Treatment of Low- and Intermediate- Level Radioactive Liquid Waste from Altwatha Site Using Iraqi Zeolite", M.S.c thesis, University of Baghdad, (2006).



**Table 1.** Properties of Purolite C105.

Polymer Matrix Structure	Acrylic Crosslinked with DVB
Physical Form and Appearance	Macroporous spherical beads
Whole Bead Count	95% min.
Functional Groups	R-COOH
Ionic Form ,as shipped	H
Total Exchange Capacity, H <sup>+</sup> form, wet, volumetric	4.2 eq/l min
Moisture Retention, H <sup>+</sup> form	45-52%
Particle Size Rang	+1.2 mm <5%, -0.3 mm <1%
Swelling Na <sup>+</sup> → H <sup>+</sup>	65% max.
Shipping Weight (approx.)	720-800 g/l
Specific Gravity, moist H <sup>+</sup> Form	1.18
pH Range, operating	4 - 14

**Table 2.** Physical properties of Zeolite pellets.

Dimension	Bulk Density	Particle Density	Void Fraction of Bed	Surface Area
2mm*2mm	0.58 g/cm <sup>3</sup>	2.38 g/cm <sup>3</sup>	0.3	7.82 m <sup>2</sup>

**Table 3.** Langmuir isotherm for ion exchange of metal ions on zeolite and purolite C105.

Metal	Zeolite			Purolite C105		
	Q <sub>m</sub>	b	R <sup>2</sup>	Q <sub>m</sub>	b	R <sup>2</sup>
Cu <sup>2+</sup>	12.195	0.410	0.984	10.526	0.785	0.970
Pb <sup>2+</sup>	10.52	0.257	0.978	6.94	0.304	0.984
Ni <sup>2+</sup>	11.76	0.298	0.982	10	0.31	0.979

**Table 4.** Parameters of Freundlich isotherm for ion exchange of metal ions on zeolite and purolite C105.

Metal	Zeolite			Purolite C105		
	k <sub>f</sub>	1/n	R <sup>2</sup>	k <sub>f</sub>	1/n	R <sup>2</sup>
Cu <sup>2+</sup>	6.745	0.127	0.811	6.194	0.119	0.593
Pb <sup>2+</sup>	5.321	0.139	0.716	4.764	0.123	0.554
Ni <sup>2+</sup>	6.266	0.129	0.700	5.147	0.116	0.638

**Table 5.** Parameters of BET isotherm for ion exchange of metal ions on zeolite and purolite.

Metal	Zeolite			Purolite C105		
	a	b	$R^2$	a	b	$R^2$
$\text{Cu}^{2+}$	76.923	13	0.584	28.571	1.522	0.60
$\text{Pb}^{2+}$	3.115	1.122	0.527	6.097	1.123	0.14
$\text{Ni}^{2+}$	27.778	1.636	0.690	7.875	1.165	0.68

**Table 6.** Adsorption rate constants, estimated  $q_e$  and coefficients of correlation associated to the Lagergren first order model for zeolite resin.

metal	$q_{e, \text{exp}}$ ( $\text{mg g}^{-1}$ )	$K_1 \times 10^3$ ( $\text{min}^{-1}$ )	$q_e$ ( $\text{mg g}^{-1}$ )	$R^2$
$\text{Cu}^{2+}$	9.74	11	8.414	0.985
$\text{Pb}^{2+}$	9.23	12	9.715	0.999
$\text{Ni}^{2+}$	9.71	11	9.247	0.989

**Table 7.** Lagergren first order model for purolite C105 resin.

metal	$q_{e, \text{exp}}$ ( $\text{mg g}^{-1}$ )	$K_1 \times 10^3$ ( $\text{min}^{-1}$ )	$q_e$ ( $\text{mg g}^{-1}$ )	$R^2$
$\text{Cu}^{2+}$	9.64	11	9.016	0.985
$\text{Pb}^{2+}$	8.73	10	9.099	0.979
$\text{Ni}^{2+}$	9.39	8	9.12	0.995

**Table 8.** adsorption rate constants, estimated  $q_e$  and coefficients of correlation associated to the Lagergren second order model for zeolite resin.

metal	$q_{e, \text{exp}}$ ( $\text{mg g}^{-1}$ )	$K_2 \times 10^{-3}$ ( $\text{g/mg.min}$ )	$q_e$ ( $\text{mg g}^{-1}$ )	h	$R^2$
$\text{Cu}^{2+}$	9.74	3.689	12.82	0.35	0.99
$\text{Pb}^{2+}$	9.23	2.348	15.873	0.2	0.93
$\text{Ni}^{2+}$	9.71	2.864	14.084	0.27	0.97



**Table 9.** adsorption rate constants, estimated  $q_e$  and coefficients of correlation associated to the Lagergren second order model for purolite C105 resin.

metal	$q_{e,exp}$ ( $\text{mg g}^{-1}$ )	$K_2 \times 10^{-3}$ ( $\text{g/mg.min}$ )	$q_e$ ( $\text{mg g}^{-1}$ )	$h$	$R^2$
$\text{Cu}^{2+}$	9.64	3.659	12.5	0.34	0.99
$\text{Pb}^{2+}$	8.73	2.493	14.08	0.19	0.93
$\text{Ni}^{2+}$	9.39	3.17	12.66	0.28	0.98

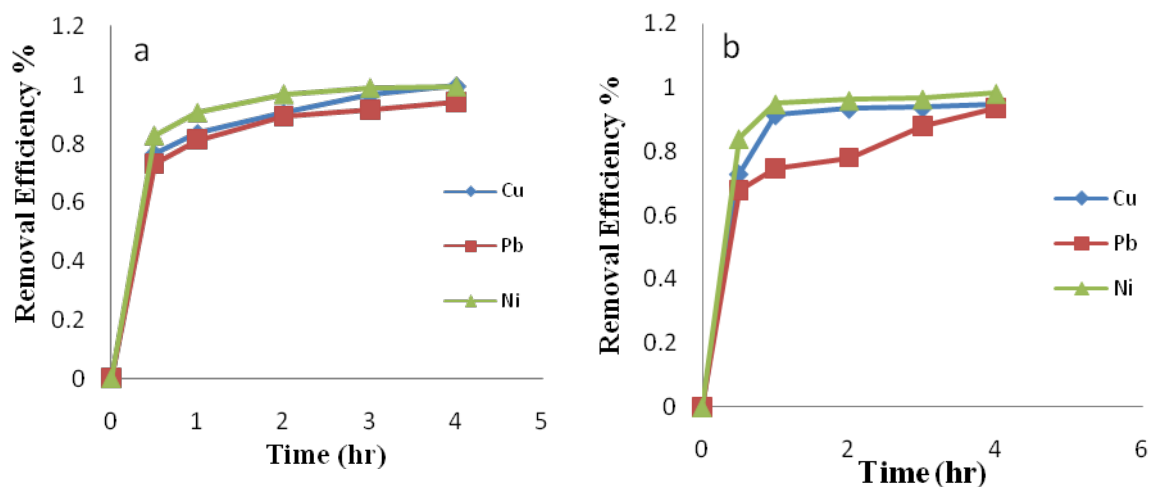


**Fig. 1.** Effect of contact time on removal of heavy metals on (a)zeolite,(b) purolite C105. (pH 6;  $m=0.5$  g; 200 rpm;  $C_0=100$  mg/L).

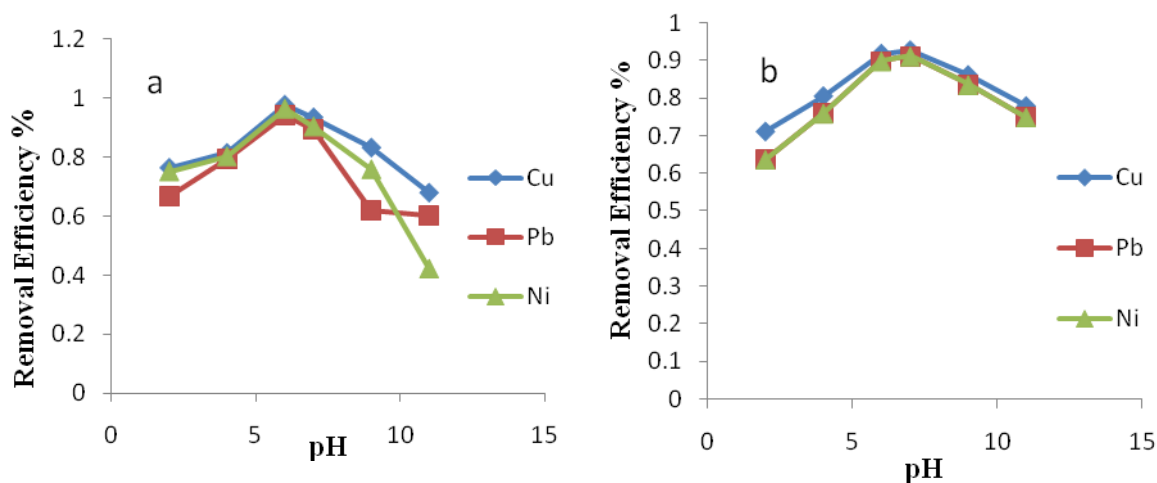


**Fig. 2.** Effect of pH on removal of heavy metals on (a) zeolite (b) purolite C105. (2hrs,  $m=0.5$  g; 200 rpm;  $C_0=100$  mg/L).

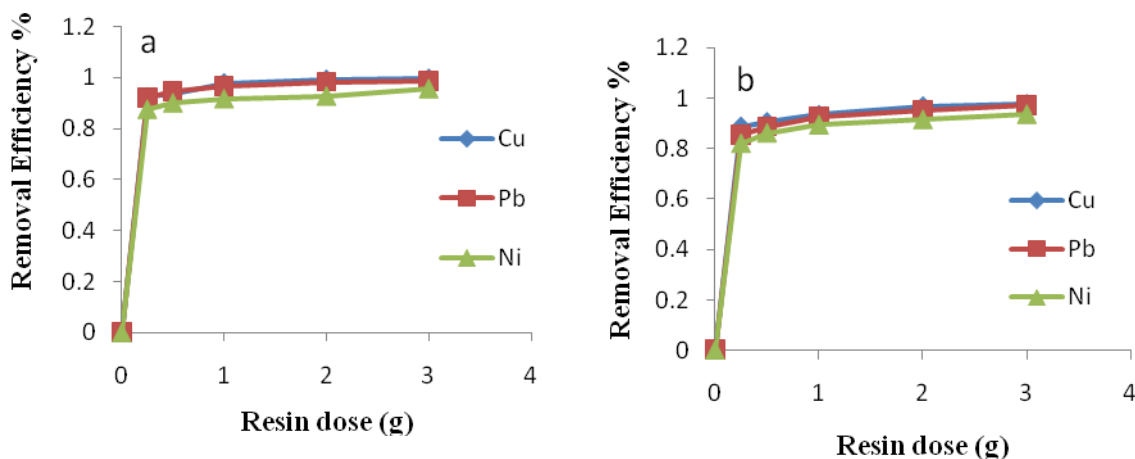


**Fig. 3.** Effect of resin dose on removal of heavy metals on (a) zeolite, (b) purolite C105. (2 hrs, pH 6, 200 rpm,  $C_0=100$  mg/L).

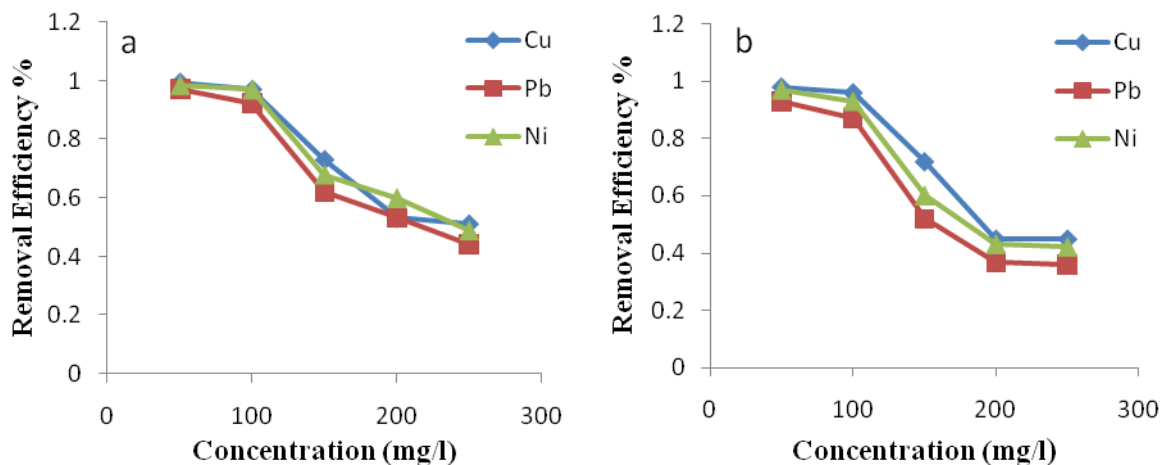


**Fig. 4.** Effect of initial concentration on removal of heavy metals on (a) zeolite, (b) purolite C105 resin (pH 6,  $m=0.5$  g, 200 rpm, 2 hrs).

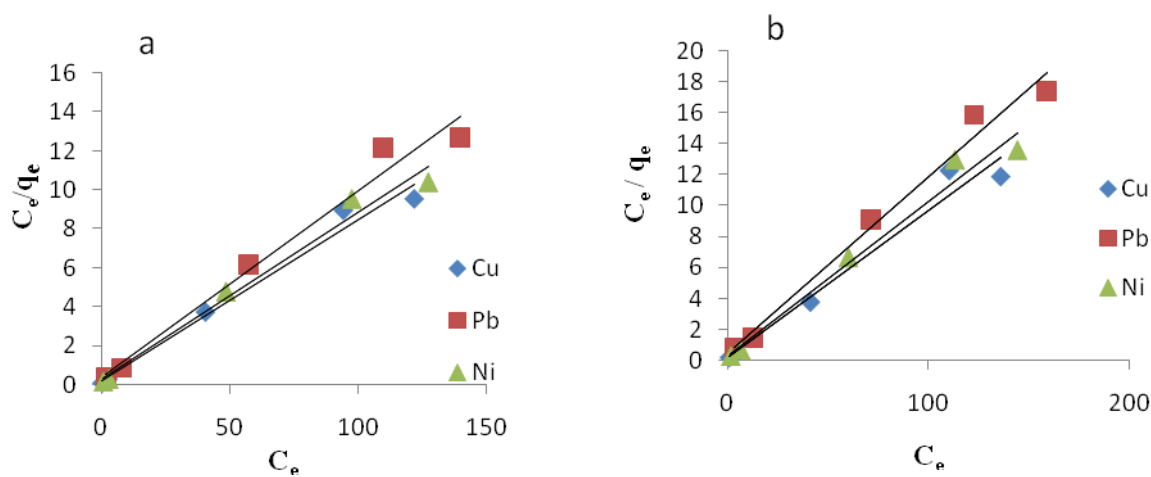


**Fig. 5.** Langmuir isotherm for ion exchange of copper, lead, and Nickel on (a) zeolite,(b) puroliteC105 (pH 6; 200rpm; m= 0.5g).

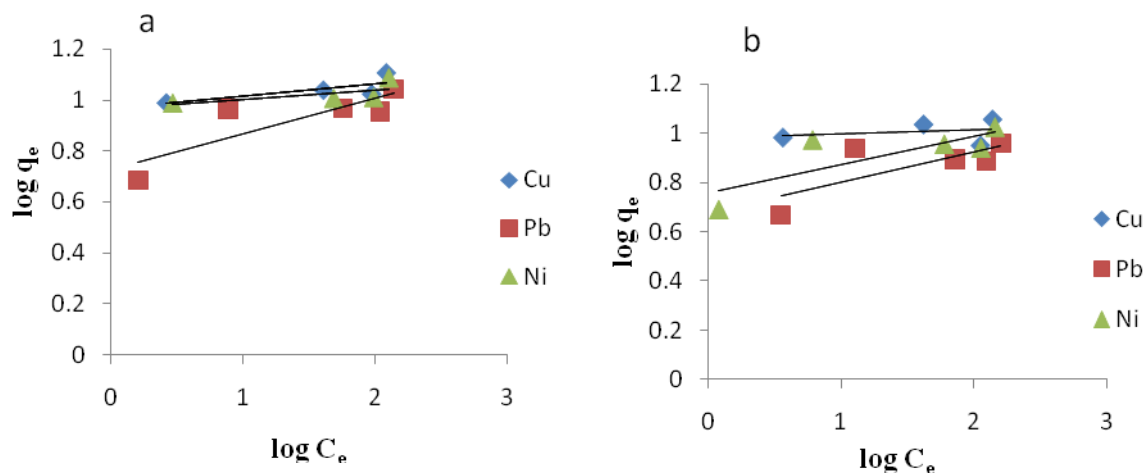


**Fig. 6.** Freundlich isotherm for ion exchange of copper, lead and Nickel on(a) zeolite,(b) purolite C105 (pH 6; 200 rpm; m= 0.5g).

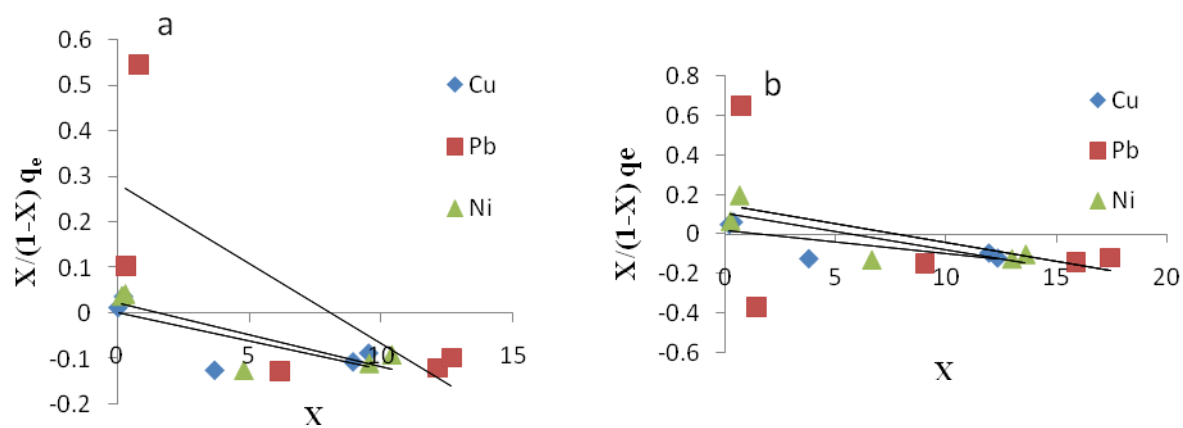


**Fig. (7):** BET isotherm for ion exchange of copper, lead, and Nickel on (a) zeolite,(b) purolite C105 (pH7, 200rpm; m=0.5g).

## Neural Network Geometric Correction Method for High Resolution Satellites Images

Alaa Soud Mahdi  
College of Science  
University of Baghdad  
dralaa\_smahdi@yahoo.com

Bushra Hassan Ali  
College of Engineer  
University of Baghdad  
bushraalaa37@yahoo.com

### ABSTRACT

Most remotely sensed data required the geometric correction process due to the geometric errors associated with the satellite images. Therefore the geometric process become important and essential in most remote sensing application. In the high resolution imagery, the geometric process will be more critical and many accurate measurements were required, the allow able the Total Root Mean Square Error (TRMSE) in the different remote sensing applications is less than the half of pixel . In the present work, many geometric correction algorithms and models have been implemented to improve the assessment of the geo-results. Two high resolution satellite imagery have been used as raw data, Ikonos 1m panchromatic, and QuickBird 0.6 m panchromatic. The evaluation in this research is carried out using GCPs and check point coordinates measurements, these coordinates were collected using the DGPS, (Leica GPS 1200). In this paper , we applied Neural Network Geometric Correction Method by using Multi Layers Perceptron (MPL) . The result obtained shows that the image using Quick bird Satellite is better than the image using IKONOS Satellite , in which the TRMSE are (0.39m) and (0.46m) respectively .

**KEYWORDS :** Geometric Correction , ANN ( Artificial Neural Network ) , Multi Layers Perceptron , Geometric Rectification , Satellite Imagery .

### طريقة الشبكة العصبية لتصحيح الهندسي الخاصة بالصور الفضائية عالية الدقة

علاء سعود مهدي، و بشرى حسن علي

#### الخلاصة

معظم بيانات التحسس النائي تتطلب عملية تصحيح هندسي نتيجة الأخطاء الهندسية المرتبطة بصور الأقمار الصناعية؛ لذا فإن العمليات الهندسية أصبحت مهمة وضرورية في معظم تطبيقات التحسس النائي . تكون العمليات الهندسية في الصور الفضائية عالية الدقة حاسمة ، وتتطلب العديد من القياسات الدقيقة . إن جذر مربع معدل الخطأ الكلي المسموح به في تطبيقات التحسس النائي المختلفة هو أقل من نصف بكسل .

في البحث الحالي ، العديد من خوارزميات ونماذج التصحيح الهندسية طبقت من أجل تحسين دقة النتائج ، حيث كانت منطقة الدراسة في جامعة بغداد .

تم استخدام صورتين فضائيتين عاليتي الدقة كبيانات أولية : الأولى صورة Ikonos بدقة (1) متر من نوع أحادية الطيف، والثانية هي صورة للقمر QuickBird بدقة (0.6) متر من نوع أحادية الطيف . تم تقييم نتائج العمل باستخدام قياسات نقاط الضبط الأرضي GCPs وإحداثيات نقاط التدقيق وتم جمع هذه الإحداثيات باستخدام جهاز DGPS (لايكا GPS 1200).

في هذا البحث تم تطبيق طريقة الشبكة العصبية لتصحيح الهندسي باستخدام طريقة الطبقات المتعددة . تم الحصول على النتائج التي أوضحت بأن الصورة المستحصلة بواسطة قمر QuickBird هي أفضل من الصورة المستحصلة بواسطة القمر IKONOS ، وكان مقدار معدل مربع الجذر الكلي (0.39م) و (0.46م) على التوالي .

## INTRODUCTION :

The preprocessing of remotely sensed image consists of geometric and radiometric characteristics analysis. By realizing these features , it is possible to correct image distortion and improve the image quality and readability.

Radiometric analysis refers to mainly the atmosphere effect and its corresponding terrain feature's reflection, while geometric analysis refers to the image geometry with respect to sensor system with the launch of various commercial high-resolution earth observation satellites, such as India Remote Sensing Satellite IRS-IC/ID, the Space Imaging Ikonos system, Spot 5 and QuickBird system, precise digital maps generated by satellite imagery are expected in the spatial information industry. In the last decade, many studies and researches performed with rigorous and non-rigorous mathematical models to rectify the satellite line scanner imagery such as SPOT, MOMS-02 and IRS-IC.

One of the main goals of these researches is to find an appropriate mathematical model with precise and accurate results. The geometric accuracy of data products is terminated by the knowledge of precise imaging geometry, as well as the capability of the imaging model to use this information. The precise imaging geometry in its turn is established by knowledge of orbit, precise altitude, precise camera alignments with respect to the spacecraft and precise camera geometry .

In this paper, we'll use Neural Network Geometric Correction Method using IKONOS and Quickbird Satellite Images , ( Lillesand, 2001 ) .

## THE AIM OF STUDY

- 1- The aim of research is to evaluate the accuracy of geometric correction processes for high resolution imagery through studying and investigating different techniques.
- 2- Compare the results with many ground control and check points.
- 3- Implementing simple application to the corrected image by using GIS Program .

## STUDY AREA AND AVAILABLE DATA

Study area located in the middle of Iraqi country (i.e. Baghdad University), Latitude ( $33^{\circ} 16' 55.6''$ ) to ( $33^{\circ} 16' 4.5''$ ) N, Longitude ( $44^{\circ} 22' 11.8''$ ) to ( $44^{\circ} 23' 20.4''$ ) E. The major features in this area are buildings of different heights; representing the colleges and their departments, some green (bush) areas and trees.

The region can describe as thick density urban and the Tigris river divide the region into two parts. Some vegetation can be found in the region, where the region elevation is 36 m (DEM).

The following sources of information are used in the study area:

- 1- Satellite images of high resolution such as Ikonos and QuickBird.
- 2- GPS measurements. (Leica GPS 1200), appendix D show specification of GPS 1200 .
- 3- ISBA CORS Station information data

One of the best available data is QuickBird satellite image of 0.6 spatial resolutions, shown figure (1).



**Figure (1): The image of the studied area (Baghdad University)**

## ARTIFICIAL NEURAL NETWORK

A neural network is a powerful data modeling tool that is able to capture and represent complex input/output relationships. The motivation for the development of neural network technology stemmed from the desire to develop an artificial system that could perform " intelligent " task similar to those performed by the human brain. Neural networks resemble the human brain in the following two ways :

1. A neural network acquires knowledge through learning .
2. A neural network's knowledge is stored within inter-neuron connection strengths known as synaptic weights .

The true power and advantage of neural networks lies in their ability to represent both linear and non-linear relationships and in their ability to learn these relationships directly from the data being modeled. Traditional linear models are simply inadequate when it comes to modeling data that contains non-linear characteristics. In particular, they can form a model from their training data (or possibly input data) alone, this is particularly useful with sensor data, or with data from a complex (e.g. chemical, manufacturing, or commercial) process. There may be an algorithm, but it is not known, or has too many variables. It is easier to let the network learn from examples . A great deal of research is going on in neural networks worldwide, (Nada,2007).

The tasks to which artificial neural networks are applied tend to fall within the following broad categories :

1. Function approximation, or regression analysis, including time series prediction and modeling .
2. Classification, including pattern and sequence recognition, novelty detection and sequential decision making .
3. Data processing, including filtering, clustering, blind source separation and compression.

Neural computing is one of the fastest growing areas of artificial intelligence. The reason of this growth is that neural nets hold great promise for solving problems that have proven to be extremely difficult for standard

digital computers. There are two key differences between neural computers and digital computers. First, neural nets are inherently parallel machines and as a result they can solve problems much faster than a serial digital computer. Secondly, and perhaps more importantly, many neural nets have the ability to " learn ". Rather than programming these nets, one presents them with a series of examples. From these examples the net learns the governing relationships involved in the training database . Since nonlinear governing relationships can be handled by neural nets, the nets may offer a cost effective approach to modeling chemical process systems, (Bhat,1990).

The main advantages of (ANN) are economy, fast computing, easy realization, and independence from physical model compared with the traditional methods, such as experiment and numerical simulation, (You,2003).

## TRANSFER FUNCTION (ACTIVATION FUNCTION) :

As we defined the transfer function (activation) in section three, the choice of it determines the neuron model, such that, there are different kinds of the transfer function, for examples (Paul,1997) :

1. *Hyperbolic tangent sigmoid transfer function*: a squashing function of the form shown below that maps the input to the interval (1,-1)

$$f(n) = 2/(1 + \exp(-2 * n)) - 1 \quad (1)$$

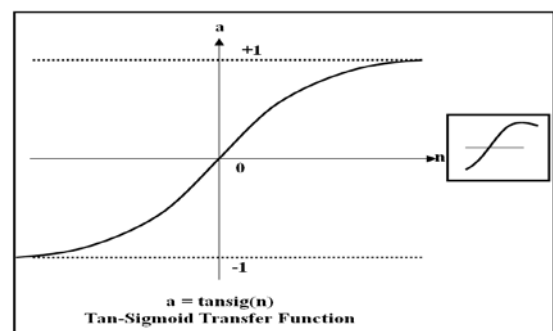


**Figure (2): Tangent-Sigmoid Transfer Function**



2. *Positive linear transfer function*: a transfer function that produces an output of zero for negative inputs and an output equal to the input for positive input.

$$f(n) = \begin{cases} n & \text{if } n \geq 0 \\ 0 & \text{if } n < 0 \end{cases} \quad (2)$$

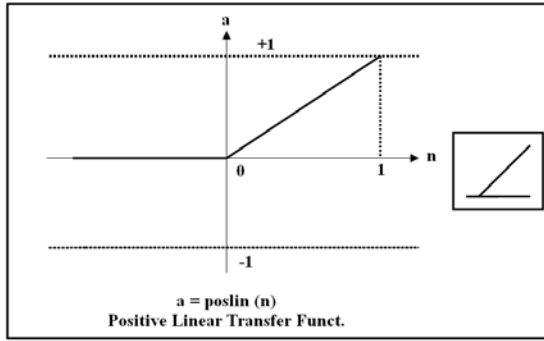


Figure (3): Positive Linear Transfer Function

3. *Log-sigmoid transfer function*: a squashing function of the form shown below that maps the input to the interval (0,1) .

$$f(n) = \frac{1}{1 + \exp^{-n}} \quad (3)$$

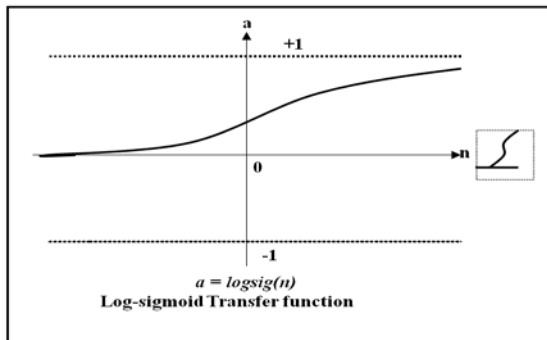


Figure (4): Log-sigmoid Transfer Function

4. *Linear transfer function*: a transfer function that produces its input as its output .

$$f(n) = n \forall n \quad (4)$$

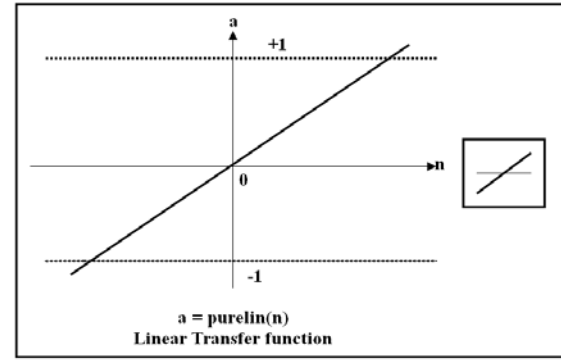


Figure (5): Linear Transfer Function

5. *Hard limit transfer function* : a transfer that maps inputs greater-than or equal-to 0 to 1, and all other values to 0.

$$f(n) = \begin{cases} 1 & \text{if } n \geq 0 \\ 0 & \text{otherwise} \end{cases} \quad (5)$$

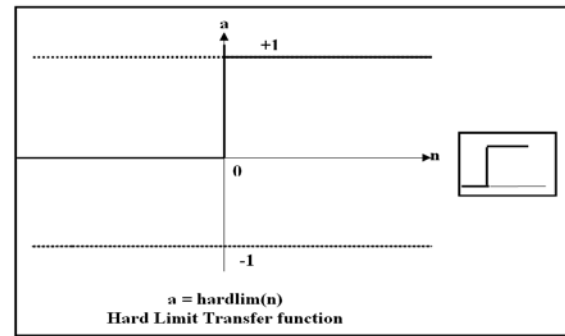


Figure (6): Hard Limit Transfer Function

## NEURONS LAYERS :

A one layer network with  $R$  input elements and  $S$  neurons is shown below in the following figure (7)

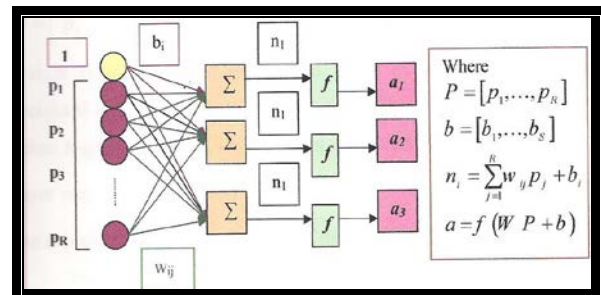
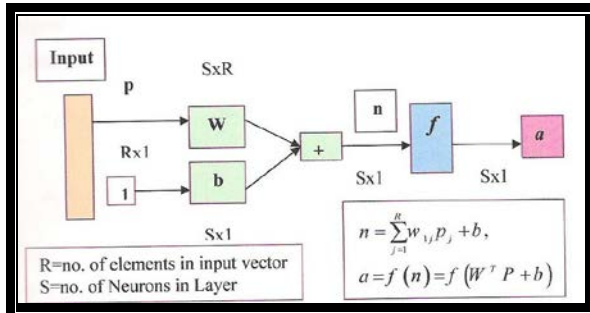


Figure (7): One Layer Neural Network



The S neuron R input one layer network also can be drawn in abbreviated notation.



**Figure (8): One Layer Neural Network**

In this network, each element of in the input vector  $P = [P_1 P_2 \dots P_R]$  is connected to each neuron input through the weight matrix  $W$ . The  $i$ th neuron has a summand that gathers its weighted inputs and bias to form its own scalar output  $n_i$ . The various  $n_i$  taken together form an  $S$ -element net input vector  $n$ . Finally, the neuron layer outputs from a column vector  $a = [a_1 a_2 \dots a_S]^T$ . We show the expression for  $a$  at the bottom of the figure (8). The input vector elements enter the network through the weight matrix  $W$ .

$$W = \begin{pmatrix} w_{1,1} & w_{1,2} & \dots & w_{1,R} \\ w_{2,1} & w_{2,2} & \dots & w_{2,R} \\ \vdots & \vdots & \ddots & \vdots \\ w_{S,1} & w_{S,2} & \dots & w_{S,R} \end{pmatrix} \quad (6)$$

Note that the row indices on the elements of matrix  $W$  indicate the destination neuron of the weight and the column indicates which source is the input for the weight. Thus, the indices in  $w_{1,2}$  say that the strength of the signal from the second input element to the first (and only) neuron is  $w_{1,2}$ . Such that :

$$n_i = \sum_{j=1}^R w_{ij} p_j, \text{ for } i=1,2,\dots,S \quad (7)$$

$$a_i = f\left(\sum_{j=1}^R w_{ij} p_j\right) \text{ for } i=1,2,\dots,S \quad (8)$$

### Multiple Layer of Neurons :

The following is the architectures of multilayered neural network, figure (3.13) shows the notations of 3-layer neural network where the network can have several layers. Each layer has a weight matrix  $W$ , a bias vector  $b$ , and an output vector  $a$ . To distinguish between the weight matrices, output vectors, etc., for each of those layers in our figures, we will append the number of the layer as a superscript to the variable of interest.

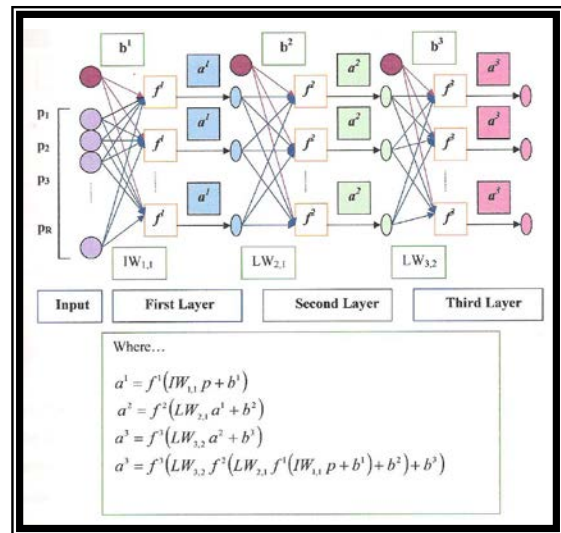


**Figure (9) : Three Layer Neural Network**

The same three layer network discussed previously also can be drawing using our abbreviated notation.

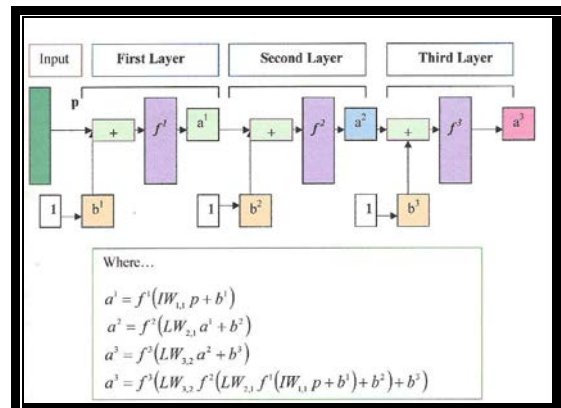


**Figure (10): Three Layer Neural Network**

In figures (9), (10), the first layer is called the *Input layer* which connected with the inputs of the network, the third layer is called the *output layer* referring to the fact that it produces the output of the network, and the second layer is known as the *hidden layer* since it is in some sense hidden between the external inputs  $[p_1, p_2, p_3]$  and the output layer.

Note that the outputs of each intermediate layer are the inputs to the following layer. Thus  $a^1$  is the output of the *input layer* (first layer)

$$a^1 = f^1(IW_{1,1}p + b_1) \quad (9)$$

where  $a^1$  will be the input to the *hidden layer* (second layer), and  $a^2$  will be the output of the hidden layer

$$a^2 = f^2(LW_{2,1}a^1 + b_2) \quad (10)$$

where  $a^2$  will be the input of the *output layer* (third layer), and  $a^3$  will be the output of the network

$$a^3 = f^3(LW_{3,2}a^2 + b_3) \quad (11)$$

such that the mathematical formula expressing that is going on in the three-layer network takes the form

$$a^3 = f^3(LW_{3,2}f^2(LW_{2,1}f^1(IW_{1,1}p + b_1) + b_2) + b_3) \quad (12)$$

## TYPES OF NEURAL NETWORKS: FEEDFORWARD NEURAL NETWORK

The feedforward neural networks are the first and arguably simplest type of artificial neural networks devised. In this network, the information moves in only one direction, forward, from the input nodes, through the hidden nodes (if any) and to the output nodes. There are no cycles or loops in the network.

### 1. Single-layer perceptron

The earliest kind of neural network is a single-layer perceptron network, which

consists of a single layer of output nodes; the inputs are fed directly to the outputs via a series of weights. In this way it can be considered the simplest kind of feed-forward network. The sum of the products of the weights and the inputs is calculated in each node, and if the value is above some threshold (typically 0) the neuron fires and takes the activated value (typically 1); otherwise it takes the deactivated value (typically -1). Neurons with this kind of activation function are also called McCulloch-Pitts neurons or threshold neurons. In the literature the term perceptron often refers to networks consisting of just one of these units. They were described by Warren McCulloch and Walter Pitts in the 1940s.

A perceptron can be created using any values for the activated and deactivated states as long as the threshold value lies between the two. Most perceptrons have outputs of 1 or -1 with a threshold of 0 and there is some evidence that such networks can be trained more quickly than networks created from nodes with different activation and deactivation values. Perceptrons can be trained by a simple learning algorithm that is usually called the delta rule. It calculates the errors between calculated output and sample output data, and uses this to create an adjustment to the weights, thus implementing a form of gradient descent. A single-layer neural network can compute a continuous output instead of a step function. A common choice is the so-called logistic function:

$$y = \frac{1}{1 + e^{-x}} \quad (13)$$

With this choice, the single-layer network is identical to the logistic regression model, widely used in statistical modeling. The logistic function is also known as the sigmoid function. It has a continuous derivative, which allows it to be used in backpropagation. This function is also preferred because its derivative is easily calculated:

$$y' = y(1 - y) \quad (14)$$

## 2. Multi-layer perceptron

The most common neural network model is the multilayer Perceptron (MLP). This type of neural network is known as a supervised network because it requires a desired output in order to learn. The goal of this type of network is to create a model that correctly maps the input to the output using historical data so that the model can then be used to produce the output when the desired output is unknown. A graphical representation of an MLP is shown in Fig (11), (Nada,2007).

This class of networks consists of multiple layers of computational units, usually interconnected in a feed-forward way. Each neuron in one layer has directed connections to the neurons of the subsequent layer. In many applications the units of these networks apply a sigmoid function as an activation function.

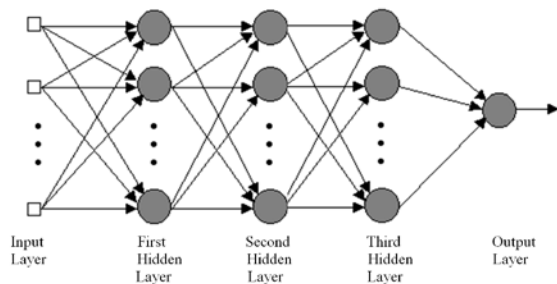


**Figure (11): Block diagram of a three hidden layer multilayer Perceptron (MLP)**

Multi-layer networks use a variety of learning techniques, the most popular being *back-propagation*. Here the output values are compared with the correct answer to compute the value of some predefined error-function. By various techniques the error is then fed back through the network. Using this information, the algorithm adjusts the weights of each connection in order to reduce the value of the error function by some small amount. After repeating this process for a sufficiently large number of training cycles the network will usually converge to some state where the error of the calculations is small. In this case one says that the network has *learned* a certain target function. To adjust

weights properly one applies a general method for non-linear *optimization task* that is called *gradient descent*. For this, the derivative of the error function with respect to the network weights is calculated and the weights are then changed such that the error decreases (thus going downhill on the surface of the error function). For this reason back-propagation can only be applied on networks with differentiable activation functions.

## THE WORK ANALYSIS :

The neural geometric correction was performed using 54 GCPs, also well distributed over the Baghdad university camp. The map coordinates of all GCPs were collected through the DGPS (Leica GPS 1200). The selection of GCPs was accurate targets as more as possible, but due to the DGPS signals limitation, many GCPs were selected not in road intersection or building corners. The 54 GCPs locations were shown in figure (12) projected on the Quick-Bird input satellite images.

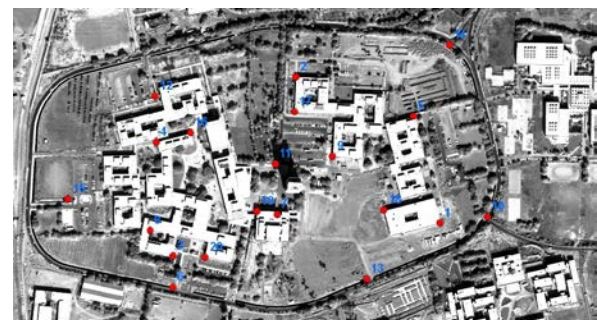


**Figure (12): The 54 GCPs used In Neural Geometric Correction, Quick-Bird Input Satellite Image .**

The geodic parameters used in DGPS coordinates characteristics and the images information can given in table (1), this information was used in this method .

The original image of Quickbird which is shown in figure (13) is used in correction process, noting that the same steps was implemented for QuickBird image , while figure (14) shows the corrected image using Neural Network Geometric Correction Method .

**Table (1): The Used Geodetic Parameters and Images Information**

Parameter	Ikonos	Quick-Bird
Image type	Panchromatic	Panchromatic
Spatial Resolution	1m	0.6m
Map Projection	UTM	UTM
Datum	WGS 84	WGS 84
Zone Number	38	38
Acquisition Time	2003	2004
File Format	Geo TIFF	Geo TIFF
Measurement Method	DGPS	



**Figure (13) : Quickbird Image before correction**



**Figure (14) : Neural Network corrected Quickbird image**

## NEURAL NETWORK TRANSFORM RESULTS

The neural network algorithms were used through evaluation of special subroutine (Matlab environment facility), these algorithms were conclude in the table (2). The No. of GCPs used was 54 well distributed among The university camp. The transformation results obtained were between 0.46 m for Ikonos, and 0.39 m thorough the best algorithm (LM), the best neural training algorithm for geometric process. The transformation details illustrated in tables (3),

**Neural Network Geometric Correction Method for High Resolution Satellites Images** and (4) for Ikonos and Quick-Bird respectively. The procedure of programming can be explained in figure (15) and summarize as following;

1. Load the data from external file.
2. Create a net work of type newff (Feed forward Neural Network).
3. Construct a net work for each layer.
4. Fix some values for the variables, show, Ir, Ir\_inc, epochs, goal, max\_fail.
5. Train the net work to reach the goal.
6. Evolution of simulation to examine the output values accuracy.
7. Display the results.

**Table (2): Training Algorithms Names and Symbols**

Symbol	Algorithm Name
GDA	Back propagation training with an adaptive learning rate
GDX	adaptive learning rate with momentum training
RP	Resilient Back propagation
CGF	Fletcher-Powell Conjugate Gradient
CGP	Polak-Ribière Conjugate Gradient
LM	Levenberg-Marquardt
BFG	BFGS Quasi-Newton
SCG	Scaled Conjugate Gradient
CGB	Conjugate Gradient with Powell/Beale Restarts
OSS	One Step Secant

After preparing Matlab program using Neural Network (MLP) to correct both images (IKONOS and QuickBird images) , then after implementation of the program , we got the interface of Neural Network Training as shown in figures (16) and (17) .

To implement the Geometric Correction Process by using multilayer Perceptron , we can use Train Algorithm :

- Train LM : Levenberg-Marquardt Like the quasi-Newton methods .

This algorithm appears to be the fastest method for training moderate-sized feedforward neural networks (up to several hundred weights). It also has a very efficient MATLAB implementation, since the solution of the matrix equation is a built-in function, so its attributes become even more pronounced in a MATLAB setting.

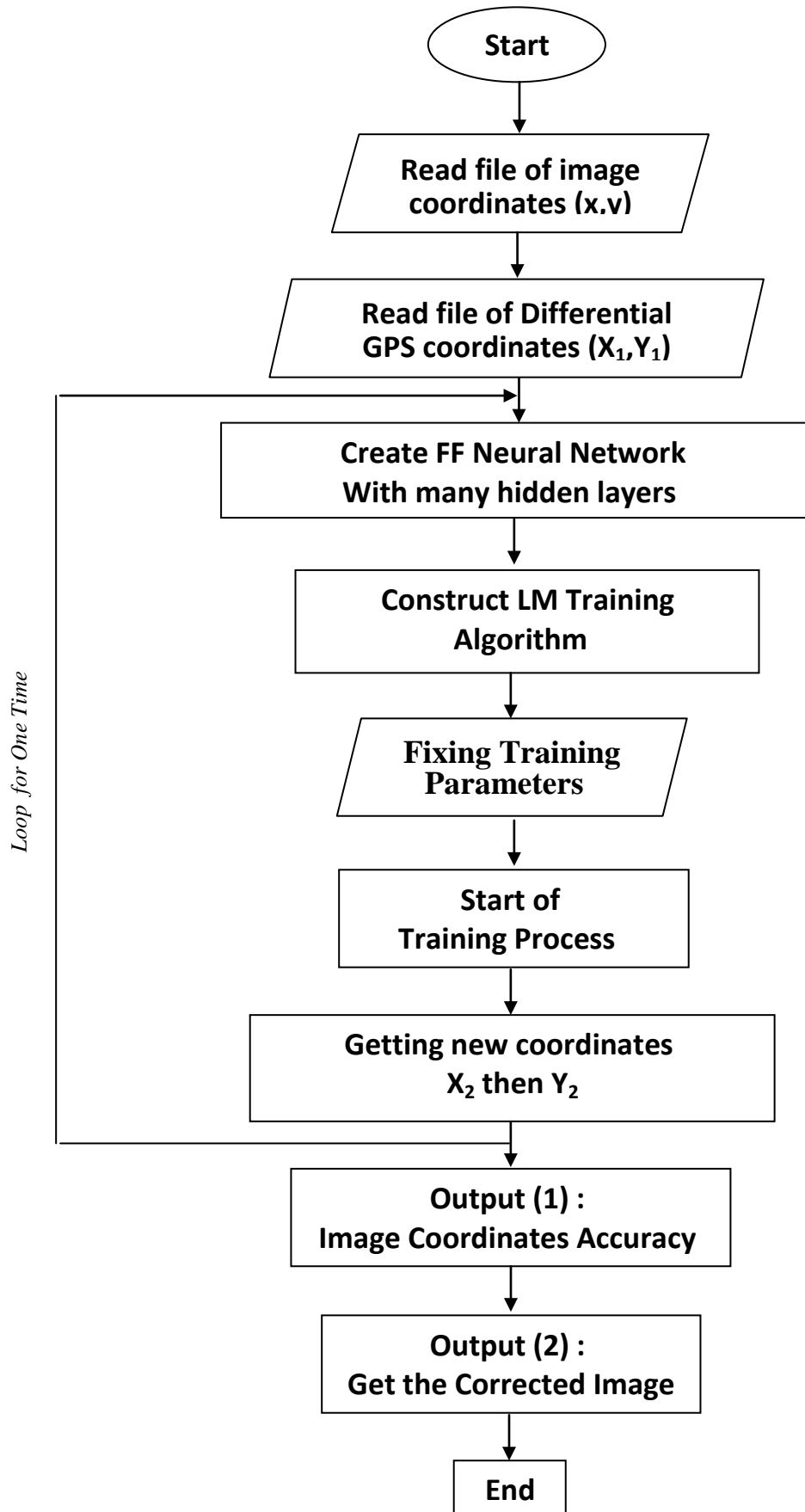


**Figure (15) : Flowchart of Neural Network Model**

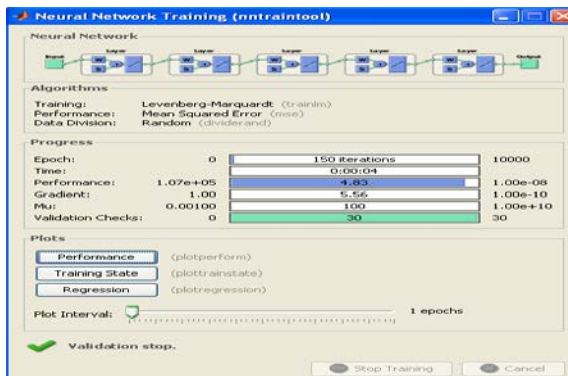


Figure (16) : IKONOS Image interface of Neural Network Training .

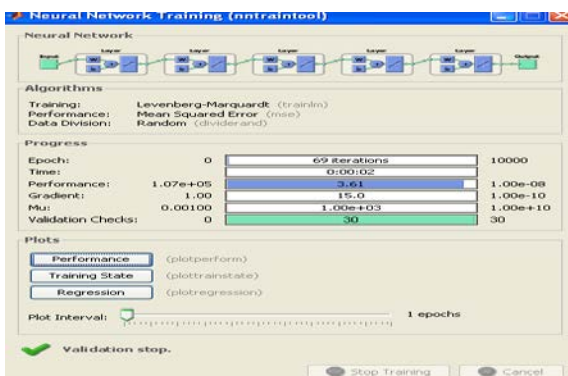


Figure (17) : QuickBird Image interface of Neural Network Training .

When we click on (regression) button on above interfaces , we got the following plots , figures (18) and figure (19) , that showed the equivalently of target with the output. We noticed that  $R_{(IKONOS)} = 0.99979$  and  $R_{(Quickbird)} = 0.99982$  that proved that there is a very small difference between the images .

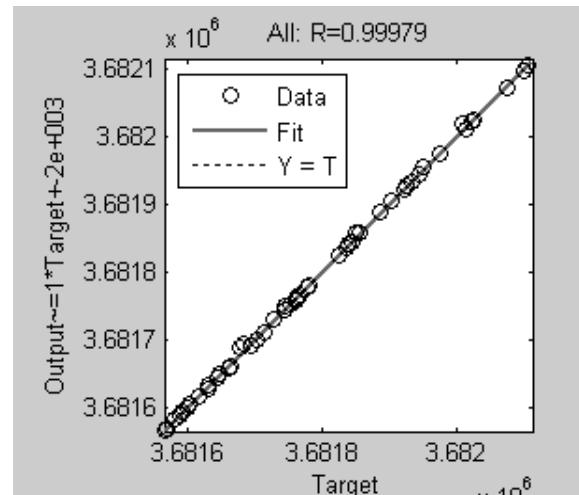


Figure (18) : Plot Regression of IKONOS Image .

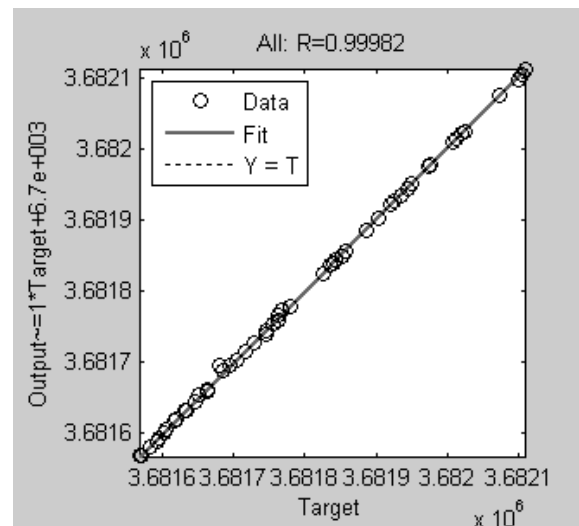


Figure (19) : Plot Regression of QuickBird Image .





Table (3): Ikonos by Neural (Matlab), LM Algorithm

No.	Image Coordinates (pixel)		Measured Coordinates Map (meter )		Computed Coordinates Map (meter )by Neural		Residuals errors	
	X	y	E	N	E'	N'	V <sub>x</sub>	V <sub>y</sub>
1	164	554	441656.81	3681630.51	441656.62	3681630.18	-0.19	-0.33
2	227	567	441721.58	3681617.03	441721.41	3681617.27	-0.17	0.25
3	302	583	441792.66	3681602.21	441792.97	3681602.63	0.31	0.43
4	341	592	441833.56	3681593.70	441833.81	3681593.35	0.25	-0.35
5	400	604	441892.64	3681581.44	441892.64	3681581.58	0.00	0.14
6	458	616	441945.66	3681570.39	441945.44	3681570.07	-0.22	-0.31
7	529	619	442021.85	3681566.64	442021.54	3681566.77	-0.31	0.13
8	680	568	442174.39	3681618.11	442174.60	3681618.16	0.21	0.05
9	766	532	442252.53	3681649.55	442252.39	3681649.94	-0.14	0.38
10	851	498	442340.43	3681685.04	442340.61	3681685.17	0.18	0.12
11	915	446	442408.11	3681745.73	442408.18	3681745.66	0.07	-0.07
12	932	338	442424.00	3681851.53	442424.99	3681851.81	0.99	0.28
13	890	180	442385.02	3682008.00	442385.98	3682007.88	0.96	-0.12
14	842	113	442340.85	3682074.76	442340.34	3682074.92	-0.52	0.16
15	779	92	442271.29	3682101.16	442271.31	3682101.11	0.02	-0.05
16	657	84	442151.70	3682106.47	442151.14	3682106.96	-0.56	0.49
17	482	80	441975.62	3682111.69	441975.20	3682111.42	-0.43	-0.27
18	450	86	441942.00	3682106.02	441942.10	3682106.07	0.10	0.05
19	127	164	441621.20	3682026.19	441621.64	3682026.69	0.44	0.51
20	55	210	441543.91	3681975.45	441543.43	3681975.73	-0.48	0.28
21	35	490	441532.40	3681678.76	441532.39	3681678.64	-0.01	-0.12
22	350	540	441840.62	3681646.81	441840.30	3681646.36	-0.32	-0.45
23	413	552	441906.22	3681633.05	441906.22	3681633.57	-0.01	0.51
24	400	596	441897.21	3681591.04	441897.75	3681591.33	0.54	0.29
25	338	579	441831.65	3681604.58	441831.95	3681604.65	0.30	0.06
26	440	408	441962.80	3681780.38	441962.63	3681780.24	-0.17	-0.14
27	470	428	441962.07	3681763.43	441962.20	3681763.82	0.13	0.39
28	502	428	441994.09	3681761.96	441994.22	3681761.98	0.13	0.02
29	502	409	441994.81	3681778.95	441994.36	3681778.20	-0.45	-0.75
30	97	412	441594.42	3681768.11	441594.65	3681768.36	0.23	0.25
31	97	419	441594.63	3681761.35	441594.62	3681761.77	-0.02	0.42
32	175	167	441665.03	3682021.55	441665.10	3682021.65	0.07	0.10
33	190	236	441683.26	3681949.30	441683.44	3681950.07	0.18	0.77
34	268	212	441761.31	3681975.10	441761.19	3681976.31	-0.12	1.21
35	503	345	441998.47	3681844.01	441998.21	3681844.16	-0.27	0.15
36	602	352	442091.11	3681836.24	442091.49	3681835.47	0.37	-0.77
37	716	435	442207.39	3681754.05	442207.91	3681754.38	0.52	0.33
38	824	460	442316.28	3681728.09	442316.10	3681728.95	-0.18	0.86
39	727	483	442219.87	3681704.20	442219.04	3681704.52	-0.84	0.31
40	784	350	442276.38	3681839.21	442276.43	3681839.08	0.05	-0.13
41	716	267	442209.07	3681921.44	442209.47	3681921.24	0.40	-0.20
42	772	253	442264.88	3681935.22	442264.14	3681935.80	-0.74	0.58
43	615	332	442106.19	3681856.65	442106.38	3681856.35	0.19	-0.29
44	616	263	442109.20	3681926.08	442109.14	3681926.20	-0.06	0.12
45	540	245	442031.97	3681944.09	442031.99	3681944.93	0.01	0.83
46	543	175	442035.01	3682013.49	442035.53	3682012.73	0.52	-0.77
47	364	526	441856.39	3681662.90	441856.41	3681662.85	0.02	-0.05
48	301	526	441792.77	3681663.91	441792.47	3681663.49	-0.30	-0.43
49	257	472	441748.54	3681716.01	441748.51	3681716.15	-0.03	0.15
50	278	362	441770.35	3681826.56	441770.18	3681826.14	-0.18	-0.42
51	270	302	441761.42	3681886.77	441761.49	3681886.70	0.07	-0.07
52	337	285	441828.86	3681903.56	441828.49	3681903.32	-0.37	-0.24
53	505	443	441996.59	3681745.10	441996.20	3681745.12	-0.39	0.02
54	463	493	441954.62	3681695.37	441954.76	3681695.23	0.14	-0.14

TRMSE = 0.46 m

**Table (4) :Quick Bird by Neural (Matlab), LM Algorithm**

No.	Image Coordinates (pixel)		Measured Coordinates Map (meter )		Computed Coordinates Map (meter )by Neural		Residuals errors	
	X	y	E	N	E'	N'	Vx	Vy
1	292	858	441656.81	3681630.51	441656.50	3681630.90	-0.31	0.38
2	399	880	441721.58	3681617.03	441721.68	3681617.08	0.09	0.05
3	520	909	441792.66	3681602.21	441792.56	3681602.28	-0.10	0.08
4	587	919	441833.56	3681593.70	441833.57	3681593.91	0.01	0.21
5	685	939	441892.64	3681581.44	441892.61	3681581.44	-0.03	0.00
6	784	960	441945.66	3681570.39	441945.64	3681570.67	-0.02	0.29
7	901	965	442021.85	3681566.64	442021.36	3681566.49	-0.49	-0.15
8	1151	879	442174.39	3681618.11	442174.51	3681618.38	0.12	0.27
9	1291	823	442252.53	3681649.55	442252.64	3681649.37	0.11	-0.18
10	1440	761	442340.43	3681685.04	442340.38	3681685.56	-0.05	0.52
11	1545	677	442408.11	3681745.73	442408.15	3681745.69	0.04	-0.04
12	1571	496	442424.00	3681851.53	442424.12	3681851.32	0.11	-0.22
13	1504	238	442385.02	3682008.00	442385.03	3682007.52	0.02	-0.47
14	1438	134	442340.85	3682074.76	442340.86	3682074.46	0.00	-0.30
15	1322	85	442271.29	3682101.16	442271.36	3682101.51	0.07	0.34
16	1115	76	442151.70	3682106.47	442151.63	3682106.25	-0.07	-0.22
17	826	64	441975.62	3682111.69	441975.69	3682111.52	0.06	-0.17
18	774	72	441942.00	3682106.02	441942.01	3682106.60	0.01	0.58
19	230	207	441621.20	3682026.19	441621.22	3682026.47	0.03	0.28
20	113	281	441543.91	3681975.45	441543.60	3681975.88	-0.31	0.43
21	77	749	441532.40	3681678.76	441532.60	3681678.58	0.20	-0.18
22	602	834	441840.62	3681646.81	441840.67	3681646.68	0.05	-0.13
23	705	854	441906.22	3681633.05	441906.11	3681633.95	-0.12	0.89
24	691	929	441897.21	3681591.04	441897.26	3681591.55	0.05	0.50
25	585	898	441831.65	3681604.58	441831.61	3681604.51	-0.04	-0.08
26	802	613	441962.80	3681780.38	441962.69	3681780.58	-0.10	0.20
27	802	641	441962.07	3681763.43	441962.83	3681763.07	0.76	-0.36
28	854	647	441994.09	3681761.96	441994.04	3681761.71	-0.05	-0.26
29	855	615	441994.81	3681778.95	441994.80	3681778.55	0.00	-0.40
30	179	621	441594.42	3681768.11	441594.38	3681768.98	-0.04	0.87
31	182	631	441594.63	3681761.35	441594.58	3681761.10	-0.06	-0.25
32	310	214	441665.03	3682021.55	441665.07	3682021.45	0.04	-0.10
33	334	324	441683.26	3681949.30	441683.34	3681949.21	0.08	-0.09
34	466	291	441761.31	3681975.10	441761.23	3681975.85	-0.08	0.75
35	857	509	441998.47	3681844.01	441998.38	3681844.97	-0.10	0.96
36	1019	522	442091.11	3681836.24	442091.20	3681836.62	0.08	0.38
37	1210	658	442207.39	3681754.05	442207.34	3681754.32	-0.05	0.28
38	1393	699	442316.28	3681728.09	442316.22	3681728.69	-0.06	0.61
39	1231	745	442219.87	3681704.20	442219.85	3681704.24	-0.02	0.03
40	1325	515	442276.38	3681839.21	442276.52	3681839.78	0.14	0.57
41	1213	379	442209.07	3681921.44	442209.07	3681921.25	0.00	-0.19
42	1307	355	442264.88	3681935.22	442264.77	3681935.25	-0.11	0.03
43	1042	486	442106.19	3681856.65	442106.27	3681856.46	0.08	-0.18
44	1047	371	442109.20	3681926.08	442109.16	3681926.63	-0.03	0.56
45	918	340	442031.97	3681944.09	442031.93	3681944.23	-0.05	0.14
46	923	225	442035.01	3682013.49	442034.51	3682013.64	0.51	0.15
47	625	811	441856.39	3681662.90	441856.26	3681662.44	-0.13	-0.46
48	520	806	441792.77	3681663.91	441792.68	3681663.35	-0.09	-0.57
49	446	721	441748.54	3681716.01	441748.35	3681716.60	-0.19	0.59
50	482	537	441770.35	3681826.56	441770.21	3681826.94	-0.14	0.38
51	467	436	441761.42	3681886.77	441761.44	3681886.09	0.02	-0.68
52	580	409	441828.86	3681903.56	441828.20	3681903.93	-0.66	0.37
53	861	672	441996.59	3681745.10	441996.15	3681745.12	-0.44	0.02
54	790	755	441954.62	3681695.37	441954.63	3681695.99	0.01	0.62

TRMSE = 0.39 m





## CONCLUSIONS :

From the experimental results obtained by this research , the final conclusions can be given as :

1. The best results was acquired by using Neural Network (MLP) applied to QuickBird Satellite Image.
2. ANN model has strong error-tolerant capability, which can automatically inhibit the impact of the control point with large error so that it can improve efficiency in practical geometry correct application .
3. ANN model for the geometric correction completely dependent on the accuracy of the number of control points, as the increasing control point number significantly improved accuracy.
4. ANN are economy, fast computing and easy realization .

## REFERENCE :

- Bhat N., and McAvoy T.J., (1990). **“Use of neural nets for dynamic modeling and control of chemical process system “** Computers Chem.Eng. Vol.14,No.4/5,pp.573-583 .
- Lillesand, T. M., and Kiefer, R. W.,(2000). **“ Remote Sensing And Image Interpretation ”** , 4<sup>th</sup> edition, John Wiley & Sons, New York.
- Nada S. A.,(2007). **“The prediction of heat transfer coefficient in bubble column using artificial neural Network “** , Doctoral Thesis University of Baghdad / Iraq .
- Paul, J. Werbos.,(1997). **“ Handbook of Neural Computation”**., IOP Publishing Ltd and Oxford University Press., 1997 .
- You X.Y. and Yang Z.S.,(2003). **“Estimating the Relative Tray Efficiency of Sieve Distillation Trays by Applying Artificial Neural Networks”**, Chem. Biochem. Eng. Q.17 (2) pp. (153-158).